

Springer Theses

Recognizing Outstanding Ph.D. Research

Craig S. Slater

Studies of
Photoinduced
Molecular
Dynamics Using
a Fast Imaging
Sensor

 Springer

Springer Theses

Recognizing Outstanding Ph.D. Research

Aims and Scope

The series “Springer Theses” brings together a selection of the very best Ph.D. theses from around the world and across the physical sciences. Nominated and endorsed by two recognized specialists, each published volume has been selected for its scientific excellence and the high impact of its contents for the pertinent field of research. For greater accessibility to non-specialists, the published versions include an extended introduction, as well as a foreword by the student’s supervisor explaining the special relevance of the work for the field. As a whole, the series will provide a valuable resource both for newcomers to the research fields described, and for other scientists seeking detailed background information on special questions. Finally, it provides an accredited documentation of the valuable contributions made by today’s younger generation of scientists.

Theses are accepted into the series by invited nomination only and must fulfill all of the following criteria

- They must be written in good English.
- The topic should fall within the confines of Chemistry, Physics, Earth Sciences, Engineering and related interdisciplinary fields such as Materials, Nanoscience, Chemical Engineering, Complex Systems and Biophysics.
- The work reported in the thesis must represent a significant scientific advance.
- If the thesis includes previously published material, permission to reproduce this must be gained from the respective copyright holder.
- They must have been examined and passed during the 12 months prior to nomination.
- Each thesis should include a foreword by the supervisor outlining the significance of its content.
- The theses should have a clearly defined structure including an introduction accessible to scientists not expert in that particular field.

More information about this series at <http://www.springer.com/series/8790>

Craig S. Slater

Studies of Photoinduced Molecular Dynamics Using a Fast Imaging Sensor

Doctoral Thesis accepted by
University of Oxford, UK

 Springer

Author

Dr Craig S. Slater
Physical and Theoretical Chemistry
Laboratory
University of Oxford
Oxford
UK

Supervisor

Prof. Mark Brouard
Physical and Theoretical Chemistry
Laboratory
University of Oxford
Oxford
UK

ISSN 2190-5053

Springer Theses

ISBN 978-3-319-24515-7

DOI 10.1007/978-3-319-24517-1

ISSN 2190-5061 (electronic)

ISBN 978-3-319-24517-1 (eBook)

Library of Congress Control Number: 2015951798

Springer Cham Heidelberg New York Dordrecht London

© Springer International Publishing Switzerland 2016

This work is subject to copyright. All rights are reserved by the Publisher, whether the whole or part of the material is concerned, specifically the rights of translation, reprinting, reuse of illustrations, recitation, broadcasting, reproduction on microfilms or in any other physical way, and transmission or information storage and retrieval, electronic adaptation, computer software, or by similar or dissimilar methodology now known or hereafter developed.

The use of general descriptive names, registered names, trademarks, service marks, etc. in this publication does not imply, even in the absence of a specific statement, that such names are exempt from the relevant protective laws and regulations and therefore free for general use.

The publisher, the authors and the editors are safe to assume that the advice and information in this book are believed to be true and accurate at the date of publication. Neither the publisher nor the authors or the editors give a warranty, express or implied, with respect to the material contained herein or for any errors or omissions that may have been made.

Printed on acid-free paper

Springer International Publishing AG Switzerland is part of Springer Science+Business Media
(www.springer.com)

Parts of this thesis have been published in the following journal articles:

Covariance Imaging Experiments Using a Pixel Imaging Mass Spectrometry Camera

C.S. Slater, S. Blake, M. Brouard, A. Lauer, C. Vallance, J.J. John, R. Turchetta, A. Nomerotski, L. Christensen, J.H. Nielsen, M.P. Johansson, and H. Stapelfeldt, *Phys. Rev. A*, **89**, 011401(R) (2014)

Dynamic Stark Control of Torsional Motion by a Pair of Laser Pulses

L. Christensen, J.H. Nielsen, C.B. Brandt, C.B. Madsen, L.B. Madsen, C.S. Slater, A. Lauer, M. Brouard, M.P. Johansson, B. Shepperson, and H. Stapelfeldt, *Phys. Rev. Lett.*, **113**, 073005 (2014)

Coulomb-explosion imaging using a pixel-imaging mass-spectrometry camera

C.S. Slater, S. Blake, M. Brouard, A. Lauer, C. Vallance, C.S. Bohun, L. Christensen, J.H. Nielsen, M.P. Johansson, and H. Stapelfeldt, *Phys. Rev. A*, **91**, 053424, (2015)

Three-dimensional imaging of carbonyl sulfide and ethyl iodide photodissociation using the Pixel Imaging Mass Spectrometry camera

K. Amini, S. Blake, M. Brouard, M.B. Burt, E. Halford, A. Lauer, C.S. Slater, J.W. L. Lee, and C. Vallance, *Rev. Sci. Instrum.*, *Manuscript accepted*

Supervisor's Foreword

Over the past decade or so, advances in fast imaging sensors have revolutionised the study of gas-phase chemical dynamics and have unlocked the door to a huge array of new experimental possibilities. This thesis provides an excellent introduction to the principles and techniques that underpin the contemporary study of gas-phase photochemical dynamics and presents a detailed yet accessible account of a range of experiments that have significantly advanced the field.

Undoubtedly, the most impressive achievement of this work is the recording of a molecular 'movie', in which the motion of a substituted biphenyl molecule is imaged in real-time using a table top apparatus. The individual frames of the 'film strip' are separated by mere femtoseconds and the images recorded reveal the inherently quantum mechanical nature of motion on this scale. The measurements of molecular motion are intertwined with a study of the complicated dynamics of the Coulomb explosion process used to probe the instantaneous molecular structure. These experiments are particularly impressive for the relative simplicity of the approach and for the detail and complexity of the information revealed.

Work has already begun on extending the principles and techniques detailed in this thesis to new and exciting applications, and I have no doubt that many future studies will be inspired to follow in the same vein. I would highly recommend this thesis to anyone who is interested in the field of molecular dynamics and who would like to learn more about some of the exciting new possibilities in the field.

July 2015

Prof. Mark Brouard

Acknowledgements

First and foremost, I would like to thank my supervisor, Prof. Mark Brouard. His enthusiasm for research has been an inspiration throughout my time with the group, especially after a few ‘refreshments’ on a Friday evening. He has been a constant source of support and guidance during my time in the group, and I cannot thank him enough for the trust he has placed in the work I have undertaken.

I would also very much like to thank Prof. Henrik Stapelfeldt and his group for allowing us to collaborate with them on some truly exciting experiments, and for their excellent hospitality during our visits to Denmark. Much of the work in this thesis would not have been possible without the efforts of Henrik and the Aarhus team. In particular, I would like to thank Lauge Christensen, who has been an absolute pleasure to work with.

I also extend my thanks to the members of the PImMS collaboration, both past and present. I am especially grateful to Jaya John John, who has always been willing to offer help and advice when asked, and to Jason Lee for his efforts on the camera software development.

I am also indebted to Prof. Ben Whitaker, who was kind enough to invite me to work in his laboratory for a month and to host me during my time there. Although these experiments have not made it into this thesis, they laid the groundwork for the coincidence work performed in Aarhus, and I am thankful to him and his group.

A final collaboration that I would like to mention is the ‘Maths in Chemistry’ study group. Dr Claire Vallance and I gained more from working with the mathematicians in a few short days than we ever expected, and their contribution to the development of the ion trajectory codes is duly acknowledged. I would particularly like to thank Dr Sean Bohun and Dr Ian Hewitt for their contributions in this regard, and Dr Claire Vallance for all her help.

Over the past few years, I have become rather too familiar with the small stretch of South Parks Road outside the CRL, having crossed it to seek help from the electronics and workshop teams with a frequency only bettered by Benjamin Winter. I would like to express my gratitude to all those in the workshops and electronics department who have offered their help during the course of my D.Phil.

A particularly large thank you is reserved for Andy Green, who has devoted many hours to my personal projects and has been an outstanding help.

My time in the Brouard group has been truly enjoyable, and I would like to express my thanks to those who I have been fortunate enough to overlap with for their friendship and support over the years. It has been a genuine pleasure to work alongside such a fantastic group of people, and I leave with many fond memories.

On a personal note, I would like to thank my parents, my family, and my friends for their help and encouragement. I hope this thesis goes some way to explaining what I have been doing for the past 4 years.

Lastly, but by no means least, I would like to thank Sophie for her love, friendship, and unwavering support.

Contents

1	Introduction and Motivation	1
1.1	Motivation	2
1.2	Photoinduced Molecular Dynamics	4
1.2.1	Molecular Photodissociation	5
1.2.2	Coulomb Explosion	6
1.3	Femtochemistry	7
1.3.1	Strong Field Control of Molecular Motion	9
1.4	Position-Sensitive Coincidence Spectroscopy	10
1.5	Ion Imaging	12
1.5.1	Velocity-Mapping	13
1.6	Fast Detectors in Ion Imaging	14
1.6.1	Microchannel Plates	14
1.6.2	Anode Readout Technologies	15
1.6.3	Pixelated Silicon Detectors	18
1.7	Outline of This Thesis	21
	References	22
2	Experimental Techniques and Methods of Data Analysis	27
2.1	Experimental Principles	27
2.2	The Oxford VMI Spectrometer	28
2.2.1	Overview	28
2.2.2	Ion Optics	30
2.2.3	Detector	31
2.2.4	Optical Systems	31
2.2.5	Reagent Sources	32
2.3	The Aarhus VMI Spectrometer	33
2.3.1	Overview	33
2.3.2	Molecular Beam Source	34
2.3.3	Electrostatic Deflector	34
2.3.4	Optical Systems	35

2.3.5	Nanosecond Laser System	36
2.3.6	Femtosecond Laser System	37
2.3.7	Reagent Source	38
2.4	Velocity-Map Image Analysis	39
2.5	The PImMS Camera	41
2.5.1	CMOS Technology	41
2.5.2	PImMS Pixel Architecture and Functionality	42
2.5.3	Post-Processing.	44
2.5.4	Characterisation and Performance	50
	References	52
3	Three-Dimensional Velocity-Map Imaging	55
3.1	Imaging the Newton-Sphere	55
3.1.1	Ion Extraction Methods	58
3.2	Simulations.	59
3.3	Experimental Results	62
3.3.1	Experimental Conditions	62
3.3.2	PImMS Data Processing	63
3.3.3	PImMS Images.	64
3.4	Discussion	67
	References	69
4	Pulsed-Field Electron-Ion Imaging	71
4.1	Introduction	71
4.2	Simulations.	73
4.3	Experimental Images	78
4.3.1	CCD Images	79
4.3.2	PImMS Images.	81
4.4	Measurement of the Detection Efficiency	83
4.5	Discussion	85
	References	86
5	Principles of Coulomb Explosion Imaging	87
5.1	Background and Motivation	87
5.2	Coulomb Explosion Imaging.	88
5.2.1	Methods of Ionisation	90
5.2.2	Ionisation by Intense Laser Fields.	92
5.3	Molecular Alignment.	94
5.3.1	Principles of Laser-Induced Alignment	95
5.3.2	Non-adiabatic Alignment	99
5.3.3	3D Alignment	99
5.4	Summary	100
	References	100

6	Investigations of Coulomb Explosion Dynamics	103
6.1	Introduction	103
6.1.1	The Molecule	104
6.1.2	Experimental Details	105
6.2	Adiabatic Alignment	106
6.3	Time-of-Flight Spectra	109
6.3.1	General Details of the Spectra	110
6.3.2	Ion Yields	111
6.3.3	Time-of-Flight Covariance	114
6.4	Recoil Frame Covariance Images	120
6.4.1	Overview of Covariance Images	122
6.4.2	Detailed Analysis of Selected Covariance Images	126
6.5	Classical Simulations of Coulomb Explosion	131
6.5.1	Computational Details	132
6.5.2	Details of the Ion Trajectories	134
6.5.3	Comparison to Experimental Data	137
6.6	Simulation of Experimental Data	142
6.6.1	Details of the Simulations	143
6.6.2	Simulation Results	145
6.7	Summary	152
	References	154
7	Time-Resolved Studies of Induced Torsional Motion	155
7.1	Introduction	155
7.2	Experimental Details	160
7.3	Single Kick Torsional Dynamics	161
7.3.1	Theoretical Treatment	161
7.3.2	Alignment Dynamics	162
7.3.3	Time-Resolved Torsional Motion	165
7.3.4	Torsional Dynamics of 1D Prealigned Molecules	169
7.4	Double Kick Torsional Dynamics	172
7.5	Summary and Outlook	177
7.5.1	Towards Larger Amplitude Torsional Motion	178
7.5.2	Prospects for Photoinduced Deracemisation	179
	References	182
	Appendix A: Calculated Structural Parameters	185

Chapter 1

Introduction and Motivation

Few experimental techniques have found such a diverse range of applications as has ion imaging. The field of chemical dynamics is constantly advancing, and new applications of ion imaging are being realised with increasing frequency. This thesis is concerned with the application of a fast pixelated imaging sensor, the Pixel Imaging Mass Spectrometry (PImMS) camera, to ion imaging applications. The experimental possibilities of such a marriage are exceptionally broad in scope, and this thesis reports the development of a selection of velocity-map imaging applications within the field of photoinduced molecular dynamics.

The capabilities of the PImMS camera in three-dimensional and slice imaging applications are investigated, wherein the product fragment Newton-sphere is temporally stretched along the time-of-flight axis, and time-resolved slices through the product fragment distribution are acquired. Through experimental results following the photodissociation of ethyl iodide ($\text{CH}_3\text{CH}_2\text{I}$) at around 230 nm, the PImMS camera is demonstrated to be capable of recording well-resolved time slices through the product fragment Newton-sphere in a single experiment, without the requirement to time-gate the acquisition. The various multi-hit capabilities of the device represent a unique and significant advantage over alternative technologies.

The details of a new experiment that allows the simultaneous imaging of both photoelectrons and photoions on a single detector during each experimental acquisition cycle using pulsed ion extraction are presented. It is demonstrated that it is possible to maintain a high velocity resolution using this approach through the simultaneous imaging of the photoelectrons and photoions that result from the (3 + 2) resonantly enhanced multi-photon ionisation of Br atoms produced following the photodissociation of Br_2 at 446.41 nm. Pulsed ion extraction represents a substantial simplification in experimental design over conventional photoelectron-photoion coincidence (PEPICO) imaging spectrometers and is an important step towards performing coincidence experiments using a conventional ion imaging apparatus coupled with a fast imaging detector. The performance of the PImMS camera in this application is investigated, and a new method for the determination of the photofragment detection efficiencies based on a statistical fitting of the coincident photoelectron and photoion data is presented.

The PImMS camera is applied to laser-induced Coulomb explosion imaging (CEI) of an axially chiral substituted biphenyl molecule. The multi-hit capabilities of the device allow the concurrent detection of individual 2D momentum images of all ionic fragments resulting from the Coulomb explosion of multiple molecules in each acquisition cycle. Correlations between the recoil directions of the fragment ions are determined through a covariance analysis. In combination with the ability to align the molecules in space prior to the Coulomb explosion event, the experimental results demonstrate that it is possible to extract extensive information pertaining to the parent molecular structure and fragmentation dynamics following strong field ionisation. Preliminary simulations of the Coulomb explosion dynamics suggest that such an approach may hold promise for determining elements of molecular structure on a femtosecond timescale, bringing the concept of the ‘molecular movie’ closer to realisation.

Finally, the PImMS camera is applied to the imaging of laser-induced torsional motion of axially chiral biphenyl molecules through femtosecond Coulomb explosion imaging. The target molecules are initially aligned in space using a nanosecond laser pulse, and torsional motion induced using a femtosecond ‘kick’ pulse. Instantaneous measurements of the dihedral angle of the molecules are inferred from the correlated F^+ and Br^+ ion trajectories following photoinitiated Coulomb explosion at various time delays after the initial kick pulse. The technique is extended to include a second kick pulse, in order to achieve either an increase in the amplitude of the oscillations or to damp the motion, representing a substantial degree of control of the system. Measurements out to long kick-probe delays (200 ps) reveal that the initially prepared torsional wave packet periodically dephases and rephases, in accordance with the predictions of recent theoretical work.

1.1 Motivation

The field of chemistry is exceptionally broad, ranging from the study of bulk industrial processes through to the innately quantum nature of electrons in a chemical bond. These apparently disparate areas of research are unified by a common motivation: to understand the forces and principles that determine structure and drive chemical change. The physical world we observe is composed of barely more than 100 chemical elements, each of which may be broken down into three subatomic particles: the proton, the neutron, and the electron. The rich variety of chemical structure and reactivity is a consequence of the intricate and nuanced interactions between these fundamental units of construction. Despite the limited basis set from which chemical systems are composed, the inherently quantum nature of matter on the atomic and molecular scale poses a significant challenge to the formulation of theoretical descriptions of chemical behaviour. Although the quantum mechanical framework within which atoms and molecules are described is formulated precisely, with the exception of atomic hydrogen (the simplest chemical system, composed of a single electron and a single proton), an exact quantum mechanical description of

chemical systems is mathematically intractable. The study of chemistry is therefore concerned with the application of suitable approximations, or models, to describe the experimentally observed behaviour of chemical systems, with the level of theory tailored to the scale and complexity of the system.

At a macroscopic level, chemistry may be described in terms of bulk thermodynamic and kinetic properties, allowing predictions to be made concerning the effect of various environmental perturbations on the system. In this way, it is possible to control the physical conditions under which a reaction is performed in order to manipulate the yields of the desired products. However, such descriptions are unable to account for the mechanisms of chemical change, which are of fundamental importance to our understanding of the rich tapestry of chemical reactivity.

The first serious attempt to rationalise reaction rates on a molecular level considered the relationship between the thermally averaged rate constant and frequency of molecular collisions in the gas phase [1]. Although ‘collision theory’, as it became known, provided a crude understanding of rates of reaction in the gas phase in terms of reaction cross sections and ‘steric factors’, a model based on the interaction of hard spheres is necessarily limited in providing a satisfactory mechanistic description of chemical reactivity. In the solution phase, a pragmatic but useful model of the chemical reactivity of organic compounds is the so-called ‘curly arrow’ approach [2], where each covalent bond is considered to consist of a pair of electrons, which migrate around the molecule subject to the constraints of atomic valence and various qualitative rules of thumb. While useful as a predictive tool for the synthetic chemist hoping to discover possible new synthesis routes, such a description ignores the complicated nature of electronic structure in polyatomic molecules, providing a rather unsatisfying description of chemical reactivity at the fundamental level.

The study of molecular dynamics is the pursuit of a fundamental and detailed understanding of the processes that govern chemical reactions and molecular transformations. By preparing a system in a well-defined initial state and measuring the signatures of a chemical process in terms of experimentally accessible observables, such as the scattering trajectories, internal energies, and angular momentum polarisation of the products, a precise description of the dynamical processes is sought on a molecular level. Although the complexities and intricacies of molecular structure pose significant challenges to gaining a complete understanding of even the most simple of chemical processes, great advances have been made in our fundamental understanding of molecular dynamics over the past few decades, especially in the case of small systems comprising only a few atoms. Through a more detailed appreciation of the underlying mechanics of such processes, the enticing prospect of gaining precise control over the outcome of a chemical reaction is brought closer to reality.

This thesis explores the experimental possibilities for studying photoinduced molecular dynamics using a novel fast imaging sensor combined with a velocity-map ion-imaging spectrometer. The following sections serve as an introduction to the important experimental and theoretical concepts that underpin this work.

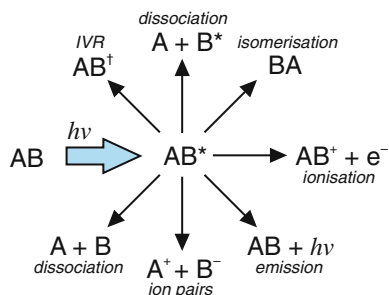
1.2 Photoinduced Molecular Dynamics

Photochemical processes, whereby chemical change is induced through the interaction of an atom or molecule with light, are of fundamental importance in chemistry and physics [3, 4] and are essential for the existence of life on Earth. For example, photosynthesis (the process through which carbon dioxide is converted into carbohydrate, and oxygen liberated into the atmosphere) is driven by photoabsorption [5]. Many atmospheric processes that shield the Earth from harmful ultraviolet radiation proceed via photochemical mechanisms, with a particularly well-known example being the formation of ozone in the lower stratosphere [6]. Photochemistry is also crucial in a variety of technological applications, including photography [7], organic synthesis [8], and energy production [9].

The quantum nature of molecules gives rise to a complex spectrum of discrete internal energy levels, defined by the electronic, vibrational, and rotational character of the system, described in terms of quantum numbers. The absorption of light resonant in energy with a transition between two such levels may promote the system to an energetically excited state, following which a variety of fates may befall the molecule, depending on the nature of the excitation and the precise conditions of the experiment, as illustrated by Fig. 1.1.

The rapid development of laser technology over recent decades [10] has driven huge advances in our understanding of photochemical processes. The use of intense, coherent, and tunable light sources allows both the state-specific preparation and the monitoring of chemical systems under precisely controllable laboratory conditions. A particularly powerful technique, combining the complementary abilities of lasers to both prepare and monitor specific quantum states of chemical systems in a precisely time-controlled manner, is that of the ‘pump-probe’ experiment, pioneered by Norrish and Porter in the late 1940s [11, 12], for which they received (in part) the Nobel Prize in Chemistry in 1967 [13]. The general principle of a pump-probe experiment is attractively simple: a chemical system is photochemically prepared in a desired state using a short pulse of light, whereafter, at a well-defined time delay, the system is probed by a second pulse of light through some observable photochemical processes, such as photoabsorption, resonant multiphoton ionisation, or laser-induced fluorescence, for example. The pump-probe time delay may be con-

Fig. 1.1 Some of the possible fates of an electronically excited molecule, AB^* , following photoabsorption in the ground state



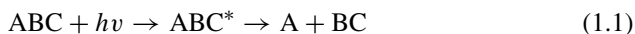
trolled and the experiment repeated to yield a time-resolved picture of the evolution of the system under study. Alternatively, the wavelength of the probe pulse may be scanned in order to monitor the various products or components of the system in turn. The original experiments by Norrish and Porter used flashlamp light sources, which discharged on a millisecond (10^{-3} s) timescale [11]: revolutionary at the time, and worthy of a Nobel Prize. Today's lasers are capable of generating light pulses with durations of attoseconds (10^{-18} s) [14], a timescale one million billion times faster than the light sources used by Norrish and Porter, and which is commensurate with the timescale of electron motion in chemical systems.

The scope of photochemistry is vast, essentially encompassing all possible interactions of chemical systems with light. This thesis is concerned with the development of experimental techniques that facilitate the study of dynamical processes that ultimately result in the production of ionic product fragments from an initially bound parent molecule. Of particular interest are the processes of molecular photodissociation and Coulomb explosion.

1.2.1 Molecular Photodissociation

Of all the possible fates that may befall a molecule following absorption of light, photodissociation represents one of the most fascinating from a dynamical perspective. If a molecule gains sufficient energy through the absorption of one or more photons, electronic excitation may result [15]. If the electronically excited state is repulsive in character, the previously chemically bound species will dissociate to yield product fragments. In practice, the term photodissociation encompasses a wide variety of processes, each being initiated by electronic excitation following photon absorption and resulting in bond cleavage [16]. Figure 1.2 illustrates various photodissociation schemes involving both repulsive and bound excited electronic states.

Photodissociation represents one of the simplest chemical reactions and has therefore received much attention from both experimentalists and theorists. The process is often referred to as a 'half-collision', highlighting the similarity of photodissociation to bimolecular reactions, with the excited states reached through photon absorption (Eq. 1.1) resembling those of excited state collision complexes (Eq. 1.2) [16]:



The study of photodissociation can therefore often be complementary to the study of the dynamics of full reactive collisions. Photodissociation also has the advantage that, by carefully selecting the experimental conditions, excited state complexes may be generated with a very narrow spread of rovibrational states, representing a level of control over the system that is unparalleled in more complex reaction schemes.

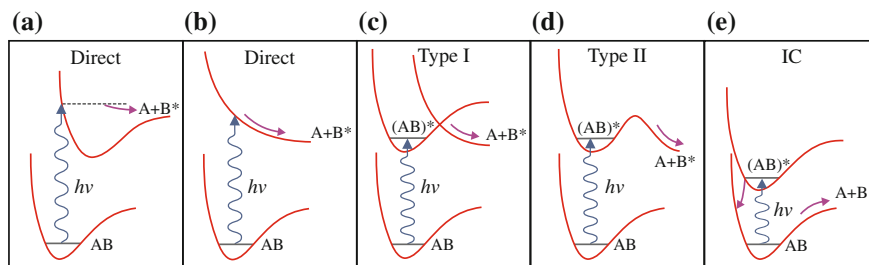


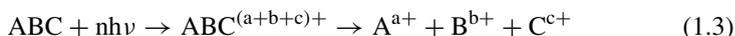
Fig. 1.2 Possible photodissociation pathways following electronic excitation: **a** direct photodissociation via a bound excited state; **b** direct photodissociation via a repulsive excited state; **c** Herzberg type I (or electronic) predissociation, where the molecule undergoes a transition from a bound to a dissociative excited state potential; **d** Herzberg type II predissociation, whereby the molecule undergoes a transition to a quasi-bound excited state, which may be overcome either through IVR or tunnelling through the barrier; **e** predissociation following non-radiative IC onto the ground electronic state in a rotationally or vibrationally excited state. (Figure adapted from Ref. [17])

Following photoabsorption, the evolution of the system is determined by the topology of its potential energy surface(s), or PES(s) [16–18]. Each electronic state has an associated PES, which represents the energy of the system as a function of the nuclear coordinates. Within the adiabatic regime, the PES(s) are constructed by solving the Schrödinger equation within the framework of the Born-Oppenheimer approximation [19] for various nuclear coordinates, with the final PES approximated by interpolating between these points. By studying the dynamics of photodissociation, in terms of quantities such as quantum state populations, angular scattering, speed distributions, and angular momentum polarisation of the product photofragments, a clearer understanding of the influence of the PES(s) on the dynamics of the system may be sought. In particular, in the cases where the Born-Oppenheimer approximation breaks down, the signatures of non-adiabatic couplings between the adiabatic PESs of the system are often evident in the scattering distributions and angular momentum polarisation of the product photofragments [20–22].

1.2.2 Coulomb Explosion

The irradiation of molecules by intense laser fields may lead to a variety of interesting dynamical phenomena, including molecular alignment [23–25], optical trapping [26], bond softening [27], and ionisation [28–30]. Of particular importance to the work presented in this thesis is the process of strong field ionisation to produce a highly charged molecular ion [31–35]. The subsequent energetic dissociation of the resultant ion is termed a Coulomb explosion, as the final kinetic energies of the atomic ions are principally determined by the classical electrical potential associated with the internuclear separation of the ionised nuclei immediately prior to molecular break up. The concept of Coulomb explosion was first proposed to explain the

fragmentation of methyl iodide following inner shell X-ray photoionisation [36], and the study of such processes has since become a research field in its own right. An example of such a process is illustrated by Eq. 1.3:



The behaviour of small molecules, consisting of a few atoms, in intense laser fields has been the subject of much study in recent years [28, 29]. If the ionisation of the target molecules occurs on a timescale that is short compared to the process of molecular break up, it can be assumed that the initial atomic coordinates are mapped onto the final velocities of the detected ion photofragments. Thus, by recording the asymptotic velocities of the ionic fragments following Coulomb explosion, it should be possible, in theory, to determine the starting coordinates of each ion, and therefore the structure of the molecule immediately prior to Coulomb explosion. Over recent years, a number of experiments have sought to investigate the validity of these assumptions (see for example Refs. [35, 37–40]). While the precise details of each experiment differ, in general they demonstrate that it is possible to determine the initial geometry, and even the chirality [33], of small molecules by measuring the final recoil velocities of the ionic fragments following Coulomb explosion. The principles of Coulomb explosion imaging (CEI), as this approach is known, are described in detail in Chap. 5, before the Coulomb explosion dynamics of a large polyatomic system are investigated in Chap. 6. Finally, the torsional motion of a biphenyl molecule is monitored in real-time using CEI as a probe of molecular structure in Chap. 7.

1.3 Femtochemistry

The study of chemical dynamics has undergone a revolution in recent years, with the advent of ultrashort light sources in the 1980s and 90s [41, 42] opening the door to time-resolved measurements on the order of femtoseconds (fs). Since processes such as molecular break-up and vibrational motion occur on timescales on the order of tens of femtoseconds, it is necessary to make measurements on an ultrafast timescale if the temporal evolution of these phenomena is to be probed in detail. Whereas more traditional studies of reaction dynamics rely on the preparation of target molecules in a well-defined initial state and the measurement the asymptotic states of the products in order to infer the mechanistic details of the processes undergone, time-resolved studies performed on an ultrafast timescale allow ‘snapshots’ of the system to be taken as the reaction unfolds. Such experiments generally employ the pump-probe technique [13], in which a pump laser first initiates a photochemical process, whereafter the evolution of the system is probed at well-defined time intervals using a probe laser pulse, which creates some observable quantity containing information on the system at that precise moment in time. Ultrafast time-resolved measurements using the pump-probe technique were first explored by Ahmed Zewail [43], who was

awarded the Nobel Prize in Chemistry in 1999 for his pioneering work in establishing the field of femtochemistry. The unparalleled insight that may be gained through performing ultrafast spectroscopy of this sort has resulted in an explosion of activity in the field during the past couple of decades, with applications ranging from the study of simple bond breaking [44], through to charge transfer [45, 46] and molecular motion [47].

A central concept in femtochemistry is that of the ‘wave packet’. As the duration of a laser pulse becomes comparable to the characteristic timescale of the system, the spectral bandwidth broadens sufficiently to cover excitation to several eigenstates of the system. Due to the ultrashort pulse envelope, these eigenstates are coherently superimposed to create a non-stationary, spatially localised wavefunction, known as a wave packet [48]:

$$\Psi(x, t) = \sum_n c_n \psi_n(x) \exp[-i(\omega_n t - \phi_n)], \quad (1.4)$$

where $\psi_n(x)$ is the eigenfunction of the n th eigenstate, and ω_n , c_n , and ϕ_n are the transition frequency, amplitude, and phase of the state, respectively. Since the phase of each term in Eq. 1.4 oscillates at a frequency characteristic of the energy of the eigenstate, ω_n , the patterns of constructive and destructive interference evolve as a function of time, giving rise to the time-dependent condition of the system. This illustrates a subtle and highly important consequence of the time-energy uncertainty principle [49]: it is the combination of the ultrashort pulse envelope and the broad spectral bandwidth of the laser pulse that results in the preparation of a non-stationary state. Without the coherent superposition of several eigenstates the excited system would exist in a single, stationary wavefunction, and the notion of time-dependent behaviour would become meaningless, regardless of the duration of the pulse envelope.

During the preparation of the wave packet, the phases and amplitudes of the various frequency components contained within the spectral bandwidth of the pump laser pulse are transferred onto the corresponding eigenstates that compose the wavefunction. Therefore, by altering the amplitudes and phases of the various frequency components of the laser pulse, it is possible to manipulate the patterns of constructive and destructive interference between the various eigenstates, allowing control over the temporal evolution of the system to be achieved. Such ‘coherent control’ strategies represent a powerful means of manipulating molecular dynamics on an ultrafast timescale. Various coherent control schemes have been developed over the last few decades [50–54] demonstrating control over many dynamical processes, in particular photoionisation and photodissociation. More recently, pulse shaping technology has been combined with intelligent learning algorithms [55–57] to achieve control over increasingly complex systems, such as large polyatomic molecules and those in the condensed phase.

1.3.1 Strong Field Control of Molecular Motion

The control and manipulation of molecular motion has long been a goal of femtochemistry. One of the simplest examples of strong field control is the phenomenon of non-adiabatic laser-induced alignment of molecules [23–25]. In this process, irradiation by a moderately intense laser pulse of short duration with respect to the natural rotational timescale of the system populates a broad, coherent superposition of rotational levels through non-resonant stimulated Raman processes [58], resulting in the creation of a rotational wave packet. The evolution of this coherent superposition depends intrinsically upon the phase relations between the rotational eigenstates, causing a transient alignment of the molecules, at a time delay that is characteristic of the prepared system. Following this initial alignment, the rotational wave packet periodically dephases and rephases, resulting in a pattern of transient alignment revivals at predictable time delays after the initial laser pulse. This predictable and recurrent alignment allows the possibility of performing experiments on aligned molecules in the absence of an external laser field and has received much experimental and theoretical attention in recent years.

The rotational control of molecules by short, intense laser pulses has been extensively studied with an impressive degree of success over recent years. However, the strong field control of molecular motion is by no means limited to rotational motion. Similar excitation schemes may be applied to the internal vibrational modes of diatomic and polyatomic molecules [37, 38, 59–61] (see Fig. 1.3), where the pendular motion of the system is modulated by the wave packet revival structure. Additionally, by exploiting the polarisability interaction between the external electric field of the laser pulse and the molecular system, control of the translational motion of molecules has been realised, giving rise to a range of interesting phe-

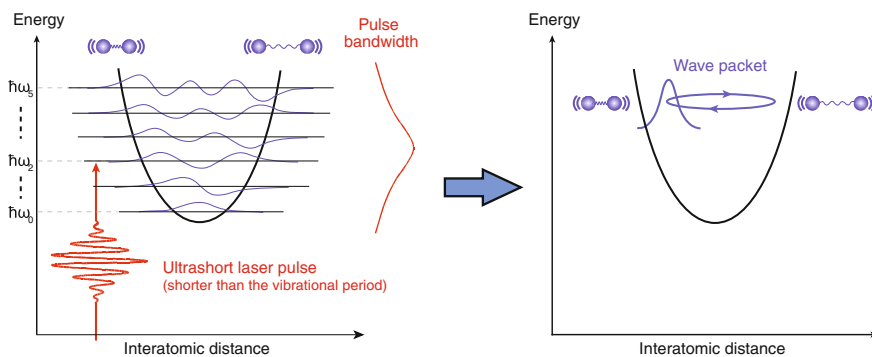


Fig. 1.3 Schematic illustration of the preparation of a vibrational wave packet by an ultrashort laser pulse. As the pulse duration becomes shorter than the vibrational period, the spectral bandwidth becomes broad enough to coherently excite the system to a superposition of several excited vibrational eigenstates. The resulting time-dependent wavefunction is called a wave packet and oscillates back and forth at the characteristic vibrational frequency. (Figure adapted from Ref. [48])

nomena, such as molecular focussing [62–64], optical trapping [26], deflection [65, 66], reflection [67], and filtering [63, 68]. Such optical control strategies allow an unprecedented level of control over the spatial manipulation of molecules and are proposed as potential routes towards achieving highly accurate nanoscale material processing (deposition, etching, doping, filtering, etc.).

Chapter 7 of this thesis investigates the control of torsional motion in an axially chiral substituted biphenyl molecule using CEI as a probe of molecular geometry on a femtosecond timescale. Torsional modes represent a fascinating intermediary between overall molecular rotation and internal vibration, often characterised by shallow potential energy surfaces and timescales comparable to those normally expected of rotational motion. Exhibiting complex time-dependent dynamics due to their unique energy eigenvalue spectra, which derive characteristics from both rotational and vibrational motion, torsional modes are of significant fundamental interest. Practically, torsional modes have been observed to influence a wide range of interesting chemical phenomena, including charge transfer [69], energy flow and redistribution [70], electrical conductivity of molecular junctions [71–73], and molecular chirality [74–80]. The time-resolved control of torsional motion in polyatomic molecules therefore offers a possible route towards gaining influence over a variety of fundamental molecular processes.

1.4 Position-Sensitive Coincidence Spectroscopy

Many photochemical processes, particularly those considered within the scope of this thesis, result in the production of two or more product fragments. If experimentally detected fragments can be unambiguously assigned to individual reactive events, then it is often possible to obtain a more complete picture of the dynamics of the processes involved in their production. Experimentally, this can be achieved by detecting fragments simultaneously and recording coincidences between them. Coincidence spectroscopy was originally developed by Walther Bothe [81], who received the Nobel Prize in Physics in 1954 for his application of the coincidence method to a range of phenomena, including nuclear reactions, the Compton effect, and the wave-particle duality of light. Later, the application of coincidence spectroscopy to the study of chemical dynamics was pioneered by McCulloh et al. in the 1960s, who first applied the method to the Coulomb explosion of small gas phase molecules following electron impact [82]. Coincidence techniques are a powerful experimental tool, having the potential to yield a wealth of valuable information about the product fragment distributions and how they relate to one another, thereby allowing the experimentalist a greater insight into the underlying molecular dynamics.

Position sensitive coincidence (PSCO) experiments, wherein a position sensitive detector is coupled with a time-of-flight apparatus, can reveal correlations between the angular and velocity distributions of the product fragments. Such information is often hidden when using more conventional experimental approaches in which the various product fragments are measured without reference to one another. Much

position sensitive coincidence work has been concerned with the Coulomb explosion of small diatomic [37, 38] and triatomic molecules [39, 40, 83, 84]. PSCO techniques have also been successfully employed to investigate reactive dynamics. In particular, much work has been performed on the reactions of small molecular dications with neutral molecules [85], where coincidence spectroscopy has proved to be a powerful probe of the reactivity of such species.

The most direct pathway to determining correlations between photofragments is to perform experiments under very low count rates, yielding far fewer than one reactive event per experimental cycle (typically on the order of ~ 0.01 events per cycle). By carefully collecting data in such a way, and by ensuring that certain additional criteria are met, one can ensure that any fragments detected within a single shot are in fact related to one another, in the sense that they originate from the same event. If higher count rates are employed, in which several events occur in each laser shot, it is inevitable that the coincident detection of fragments from different reactive events will occur. These ‘false’ coincidences have the potential to confuse data interpretation and it is therefore desirable to minimise their effect or eliminate them all together.

Although the low count rate approach represents a rigorous measurement of photofragment correlations, there are a number of situations in which such a strategy becomes experimentally impractical. For example, due to the necessarily low signal levels, where the repetition rate of the experiment is modest, the low count rate approach results in data acquisition timescales that are impractically long. Furthermore, it is often a considerable experimental challenge to achieve background signal levels that are low enough to perform such measurements. This issue becomes increasingly acute as the target system increases in size, as it becomes impossible to discriminate between genuine and false coincidences using secondary filters such as calculations of momentum conservation. In any case, where nonselective ionising radiation sources are used (such as strong field, VUV, or X-ray), it is often the case that signal from the ionisation of background gas overwhelms that from the target system. In order to overcome these limitations, Frasinski et al. demonstrated the possibility of performing a statistical measurement of photofragment correlations in the high count rate regime [86]. Following the Coulomb explosion of small molecules, Frasinski et al. used the covariance as a statistical measure of linear correlation between the fragment ion signals. The covariance between two random variables X and Y is given by

$$\text{Cov}(X, Y) = \langle (X - \langle X \rangle)(Y - \langle Y \rangle) \rangle \quad (1.5)$$

which may be rewritten as

$$\text{Cov}(X, Y) = \langle XY \rangle - \langle X \rangle \langle Y \rangle \quad (1.6)$$

where $\langle \rangle$ denotes the arithmetic mean over all samples. If the two variables X and Y tend to vary together, in the sense that when one of the variables is above its expected value then the other variable is too, then the covariance will be positive. Conversely, if one of them tends to be above its expected value when the other variable is below

its expected value, then the covariance between the two variables will be negative. If there is no correlation between the two variables then the covariance will be zero.

Recently, a formal theory has been developed to interpret the covariance values extracted from such experiments [87, 88]. In the case of an experiment operating under Poisson statistics (i.e. the shot-to-shot conditions of the experiment remain constant), the covariance values reproduce perfectly the correlations between the various product fragments, as would be obtained from a conventional, low count rate coincidence experiment. However, where deviations from Poisson statistics arise, the covariance data are expected to contain false artefacts, which result from the inevitable correlation of all channels with one another. Various partial covariance strategies have been developed to address these shortcomings [89–91], which depend on the measurement of additional experimental parameters, such as the shot-to-shot laser power. However, in the case of a well-behaved Poisson experiment, the covariance represents a convenient measure of photofragment correlation, affording data convergence many orders of magnitude faster than is possible using conventional coincidence strategies. Covariance mapping has proved invaluable in a diverse range of applications relating to the study of chemical dynamics, including molecular Coulomb explosion [92–94], multi-photon ionisation [95], and the time-resolved motion of polyatomic molecules [47].

1.5 Ion Imaging

The technique of ion imaging [96] was pioneered by Chandler and Houston in 1987, and has since been adapted to applications in an exceptionally broad range of fields, becoming the experimental tool of choice in the study of molecular dynamics. Ion imaging has proved an invaluable tool to experimentalists in areas as diverse as molecular photodissociation [97], inelastic and reactive scattering [85, 98], Coulomb explosion [40], molecular alignment [99], the structure and reactivity of gas phase transition metal clusters [100], and the study of molecular motion [47]. This list is by no means exhaustive, and the horizons of ion imaging continue to expand into new and exciting fields of research.

The technique is illustrated schematically in Fig. 1.4. Typically, the sample gas is supersonically expanded into the experiment through a pulsed valve and is collimated by one or more skimmers to form a rotationally cold (typically <25 K) molecular beam. The molecular beam is then intersected by one or more focussed laser pulses to induce a structural or chemical change in the target molecules, and to cause photoionisation of the resultant photofragments. The nascent ions are then accelerated and focussed down a flight tube by an electric field onto a two-dimensional detector, generally consisting of a stack of microchannel plates (MCPs) coupled to a readout capable of determining simultaneously the position and time of the ion impact on the detector.

The most common readout employed is that of a phosphor screen and a camera. In this arrangement, the phosphor screen is mounted directly behind the MCPs. The

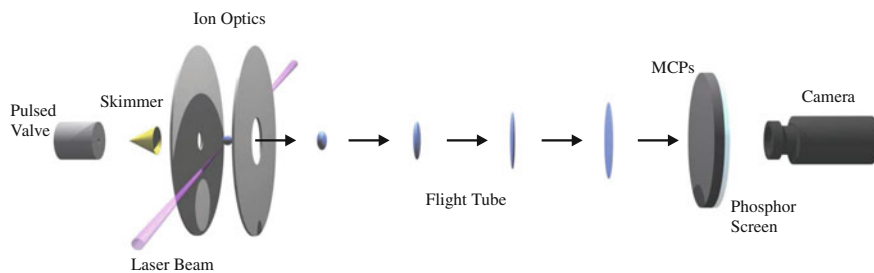


Fig. 1.4 Illustration of an ion imaging experiment showing the principal components. The Newton-Sphere is shown at various times during its flight towards the detector

shower of electrons from the MCPs is accelerated by a potential difference onto the phosphor screen, causing localised flashes of light that are imaged by the camera, thereby identifying the position of the ion impact on the detector. A consequence of the use of an electric field to effect ion extraction is that the ions are separated temporally at the detector according to their mass-to-charge (m/z) ratio, with ions carrying a lower m/z ratio arriving earlier than those with a higher m/z ratio. In this way some information about the chemical identity of the detected ion may be inferred from its time-of-flight.

1.5.1 Velocity-Mapping

Although the technique of ion imaging was introduced by Chandler and Houston in 1987, it was not until a decade later, and the development of velocity-mapping by Eppink and Parker [97], that the technique began to mature into the powerful experimental tool it has since become. Whereas Chandler and Houston used grid-based electrodes to extract the ions onto the detector [96], Eppink and Parker employed open electrodes to achieve a similar result. In addition to allowing 100% transmission of the ions, the use of open electrodes allows the focussing of the ions onto the detector such that the final impact coordinate on the detector is determined uniquely by the initial velocity of the photofragment in the detector plane, and is crucially independent of the initial position of formation of the ion. This removes the blurring of the ion images caused by the finite size of the interaction region, where the overlap of the molecular beam and the ionising radiation is sufficient to produce ions. What results, therefore, is a ‘velocity-map’ of the ion fragments on the detector, which is a two-dimensional representation of the asymptotic velocities of the product photofragments resulting from the photochemical process under investigation. If the position of ion-impact on the detector is expressed in polar coordinates, the radius from the centre of the image is proportional to the magnitude of the velocity in the detector plane, and the polar angle representative of the direction of travel.

1.6 Fast Detectors in Ion Imaging

Velocity-map ion imaging combines traditional time-of-flight spectrometry with two-dimensional positional information. The ideal detector should therefore be capable of recording both the ion arrival time and the spatial coordinates of ion impact on the detector with a high degree of precision, in order that the maximum amount of information about the particle may be determined. The simplest method of capturing this information is to accelerate the electrons from the back of the MCPs onto a transparent screen coated with a phosphorescent material. The electrons exit the back of the MCPs in localised showers and are accelerated onto a phosphor screen through a potential of a few kilovolts, resulting in excitation of the scintillator material and subsequent relaxation and fluorescence to produce a flash of light. This flash of light is then imaged by a camera and the images transferred to a computer for post-processing.

It is possible to time-gate either the detector or the camera to achieve exposure times below 10 ns [101], providing a time-selective acquisition window. While it is possible, in principle, to take successive measurements at different times using such a detector, it is far more favourable to employ a detector that combines precise time-resolution with continuous acquisition throughout the experiment. With a sufficient time-resolution it then becomes possible to determine the x , y , and t coordinates of each event, providing a complete data set in a single acquisition. The obvious advantage of this deterministic measurement scheme, versus a selective approach, is the reduction in data acquisition time where several fragments of different mass-to-charge ratio must be imaged. By recording all masses simultaneously, the data acquisition time is reduced by a factor equal to the number of different masses to be imaged. A more nuanced, but potentially more powerful, advantage lies in the ability to measure correlations between particles arriving at different times, affording the ability to perform position sensitive coincidence experiments, as discussed in Sect. 1.4. It is also possible, when using certain ion extraction fields [102, 103], to determine the z -velocity of each photofragment from its precise time-of-flight, thus yielding a three-dimensional velocity-map image the full Newton-sphere. (Such three-dimensional imaging applications are explored in more detail in Chap. 3.) For these reasons, several detection and readout schemes have been developed to provide full three-dimensional information for each ion detected. The technologies may broadly be divided into two main types: those based upon anode readouts, and those utilising pixelated silicon-based sensors. In each case the ion signal is initially amplified by a stack of microchannel plates.

1.6.1 Microchannel Plates

The first stage of charged particle detection in ion imaging is almost universally the amplification of the incident signal by microchannel plates (MCPs). MCPs are

constructed from thin plates of silica, each containing millions of pores with typical diameters of 8–25 μm . The pores are equally spaced in a close-packed arrangement to give open area ratios (OAR) on the order of 50–60 %. For an ion to be detected it must first impact on the inside of one of these microscopic pores. If the impact of the ion occurs with a sufficient kinetic energy, several secondary electrons are liberated from the surface of the silica, which are drawn through the pores by an electrical potential applied across the MCPs. The microchannels are angled at approximately 12° to the surface normal of the MCPs, which ensures that the electrons impact upon the inside of the pores as they are drawn through. This results in the release of further secondary electrons, causing a cascade effect. For each ion that impacts on the MCPs approximately 10^6 electrons are produced, representing a substantial amplification of the initial ion signal. The electrons exit the back of the MCPs in localised showers and are subsequently detected using one of the detection schemes described in the following sections.

1.6.2 Anode Readout Technologies

While the more emergent fast imaging technologies are pixelated silicon-based sensors, anode readouts have traditionally been the detector of choice for time-resolved imaging applications over the past years. Although this thesis is principally concerned with the application of the PImMS camera (a pixelated silicon-based detector) to ion imaging experiments, it is important to review the capabilities and limitations of anode readout systems in this context.

1.6.2.1 Wedge and Strip Anodes

Wedge and strip anodes (WSAs) exist in many different forms [104], but the general principle relies on a differential coverage of the surface of the detector by three or more independent anodes. Figure 1.5a illustrates schematically one of the most commonly used arrangements [104, 105], consisting of three coplanar anodes, named the wedge, strip, and meander anodes due to their shape. When a shower of electrons from the back of an MCP hits a wedge and strip anode, the charge is distributed between the three anodes according to the geometry at the point of detection. The charge on each electrode is measured independently, and the x - and y -coordinates are determined according to

$$x = \frac{Q_S}{Q_W + Q_S + Q_M} \quad (1.7)$$

$$y = \frac{Q_W}{Q_W + Q_S + Q_M}, \quad (1.8)$$

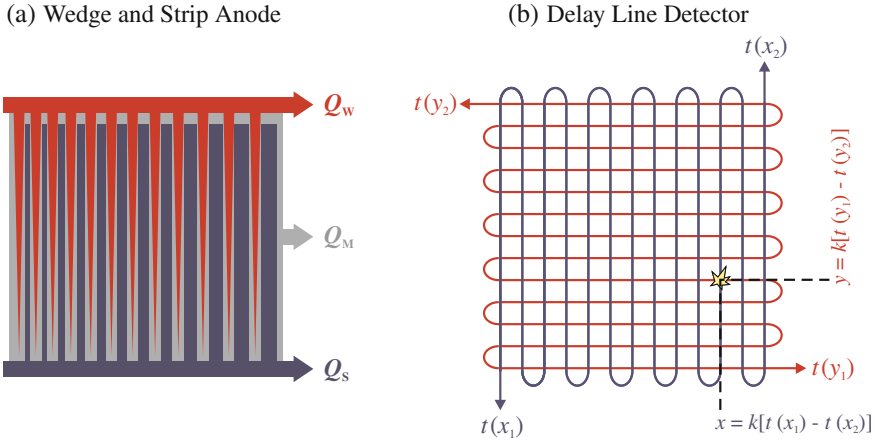


Fig. 1.5 Schematic illustrations of the principle components of **a** a wedge and strip anode, and **b** a delay line detector (DLD). The wedge and strip anode detector consists of three anodes, electrically insulated from one another. The surface coverage of strip anode (blue) increases linearly from left to right (x -direction), the surface coverage of the wedge anode (red) increases linearly from bottom to top (y -direction), and the meander anode (grey) fills the space between the wedge and strip anodes. The DLD consists of two perpendicularly wound electrodes, terminated by amplification and timing electronics. $t(x_1)$, $t(x_2)$, $t(y_1)$, $t(y_2)$ denote the pulse arrival times at the four wire terminals

where Q_w , Q_s , and Q_M are the measured charges on the wedge, strip, and meander anodes, respectively. Wedge and strip anodes offer a very good spatial resolution (40–100 μm), but only a moderate time-resolution ($>6\text{ ns}$) due to the speed of the read-out and signal processing electronics [105]. A further drawback of WSAs is their failure when multiple events occur simultaneously. Such an occurrence results in a break-down of the validity of Eqs. 1.7 and 1.8, resulting in a single, false event being recorded by the detector.

1.6.2.2 Crossed Wire Detectors

Crossed wire detectors (CWDs) consist of two sets of equally spaced parallel wires arranged perpendicular to one another along the x - and y -axes. The wires are electrically insulated and the signal from each is processed independently. If an electron cloud from the MCPs hits a crossing point between two wires, coincident electrical signals are generated in both anodes, allowing the x - and y -coordinates and time of the event to be recorded straightforwardly.

While conceptually simple, crossed wire detectors suffer from an inability to detect multiple particles simultaneously. Furthermore, the spatial resolution of such detectors is limited by the substantial readout electronics required, which increases proportionally with the number of anodes present in the detector. In practical applications this limits the spacing of adjacent wires to 0.5 mm or greater [106], which

represents a relatively poor spatial resolution when compared to a typical MCP pore size (8–25 μm). Although crossed wire detectors offer an impressive time-resolution (~ 200 ps) [102, 106], they have largely been superseded by delay line detectors in most practical applications due to the superior time- and spatial-resolutions afforded by delay line technology.

1.6.2.3 Delay Line Detectors

Delay line anodes were first developed into spatially resolved detectors by Eland in the early 1990s [107, 108] and have since become widely used in coincidence and 3D imaging applications due to their high spatial and temporal resolution and short dead time [109, 110]. In their simplest form, delay line detectors (DLDs) generally consist of two orthogonally wound anodes, each consisting of a pair of wires separated by approximately 0.5 mm and biased with a small voltage (~ 30 V). Electrons from the MCPs induce an electrical signal in each delay line pair, which propagates to the wire terminals, where it is amplified and recorded. The spatial coordinates of the ion hit may therefore be determined from the difference between the time of arrival of the signal at the ends of the two anodes. Specifically, in the case of two orthogonally wound anodes, each event produces two pairs of times at the wire terminals, $t(x_1)$, $t(x_2)$, and $t(y_1)$, $t(y_2)$. The x - and y - coordinates of the event are therefore proportional to $(x_1 - x_2)$, and $(y_1 - y_2)$, respectively, with the time of the event normally calculated as $t = [t(x_1) + t(x_2) + t(y_1) + t(y_2)]/4$. Additionally, the calculation of the time of the event by the two independent delay lines must coincide in the case of a genuine signal, hence the condition $t(x_1) + t(x_2) = t(y_1) + t(y_2)$ must also be satisfied. This constraint allows false events to be discriminated against and discarded from the final data set.

The principal advantages of the delay line detector are highly accurate spatial and temporal information, coupled with a low dead time between successive events. Typically, spatial resolutions are on the order of $100\mu\text{m}$, with the time recorded to an accuracy of approximately 100 ps [110]. However, a fundamental limitation of the delay line detector lies in the severely restricted multi-hit capabilities of the technology. If two or more events occur simultaneously the signals corresponding to the different events become difficult to distinguish from one another, limiting the technology to the detection of isolated events. Recent advances, such as those described in Ref. [111], have improved the situation somewhat, allowing a limited multi-hit capability to be achieved. Hexanodes, based on three delay lines wound in a hexagonal geometry, are capable of recording up to two or three particles simultaneously when specific conditions on the relative coordinates of the events are satisfied. Although certainly an improvement over conventional delay line technologies, the situation is still not entirely satisfactory as the total number of particles that may be detected simultaneously is still restricted to the low single figures. Furthermore, the constraints imposed on the relative coordinates of simultaneous events may lead to a systematic bias in the data recorded.

1.6.3 Pixelated Silicon Detectors

A common disadvantage of anode-based readout technologies is their failure to record multiple events simultaneously. These limitations are not particularly serious in the case of experiments operating under conditions of low signal and high repetition rates as such occurrences are rare. However, in more general imaging applications, and for experiments in which it is impossible to maintain a low count rate, this represents a serious shortcoming of anode readouts. For example, when using lower repetition rate laser systems it is simply not practical to operate under low count rate conditions as it would take a prohibitively long time to record a sufficient quantity of data. Similarly, when studying rare photochemical processes with small absorption cross sections, the ionisation of background gas may cause false signal to become problematic. A further complication arises when the fragmentation of large molecules containing many atoms of the same type is to be studied. In this case, it is highly likely that several ions will reach the detector almost simultaneously, making these systems unsuitable for measurement by anode-based readouts.

Recent advances in silicon imaging technologies have led to the development of new devices capable of recording multiple events simultaneously. Pixelated imaging sensors, based on charge coupled device (CCD) [112, 113] or, more recently, complementary metal-oxide semiconductor (CMOS) [114, 115] technology, overcome this disadvantage through the independent detection of events by each pixel, practically eliminating the restrictions on the maximum number of events that may be recorded simultaneously. The difficulty, however, lies in the efficient handling of the large amounts of data, which must be either stored or read out at high speed for high frequency acquisition.

1.6.3.1 Parallel Readout

Parallel readout sensors operate at an increased frame rate by increasing the number of data readout channels. The multiple readouts may be operated either in parallel or alternate mode. In parallel mode the data are divided between the multiple readout channels to increase the rate of data transfer, and therefore the maximum possible frame rate of the device. Alternatively, by alternating between readout channels, data acquisition and readout may be performed concurrently, removing the requirement for a dedicated acquisition dead time in which data are transferred from the device, and allowing for a continuous acquisition. The main advantage of using parallel readout is that there is no fundamental limit to the number of consecutive frames that may be acquired, as data are continuously transferred from the device. The majority of commercially available fast imaging sensors rely on parallel readout, with the most advanced devices operating at frame rates of up to 1 Mega-frames per second (Mfps) [116]. This frame rate is indeed fast when compared to conventional CCD and CMOS sensors, but the exposure time of $1\ \mu\text{s}$ to which this relates is rather uncompetitive when compared to the time-resolutions offered by anode-based

detectors. Furthermore, high frame rates come at the expense of pixel count. For example, the parallel readout sensor in Ref. [116] is restricted to only 64×16 pixels at a frame rate of 1 Mfps, compared to a maximum pixel resolution of 1024×1024 at 1 kfps. This illustrates the main drawback of parallel readout sensors: that the limited capacity of data readout necessarily requires a trade off between the pixel count and frame rate.

1.6.3.2 In Situ Storage Imaging Sensors

An alternative to fast data readout is to store the signal in situ during acquisition, followed by a slower readout from the chip once the acquisition is complete [112, 117]. In this way, the frame rate is not limited by the data transfer rate, allowing shorter exposure times to be realised. The maximum frame rate of in situ devices is instead determined by the rate of charge transfer from the charge collection regions of the chip to the storage buffers. Calculations based on simulations performed by Son et al. [118] suggest a maximum theoretical frame rate of 100 Mfps for in situ storage, corresponding to an exposure time of 10 ns. Furthermore, since each pixel contains its own set of charge storage buffers, there is no fundamental limit on the maximum pixel count. The primary disadvantage of in situ storage lies in the limited number of memory buffers that can be incorporated into a single pixel, which restricts the total number of frames that can be stored on-chip before readout to an external memory register becomes necessary. This data readout requires a dedicated dead time, during which no further acquisition can occur. However, for most time-of-flight experiments this is not problematic, since readout can occur at the end of the experimental duty cycle.

1.6.3.3 Time Stamping Detectors

Both parallel readout and in situ detectors suffer from the large volume of data that must be either stored on the chip or transferred to an external memory when high frame rates are required. However, in photofragment imaging experiments it is unnecessary and inefficient to record entire images, as the majority of the data will be null and of no value at the data processing stage. In most cases the majority of frames will contain no events whatsoever, and even when an event does occur, the useful information content is confined to only a tiny fraction of the overall number of pixels. In this case, it is far more efficient to employ an event-oriented approach, in which data are recorded only when an event is detected, in a similar manner to the anode readout technologies discussed previously. The pixels of time stamping detectors therefore only record data when a predetermined signal threshold is exceeded. When this condition is satisfied, the value of an internal, synchronised clock is recorded in an internal memory buffer, thereby providing the time of the event [115]. The spatial information is provided by the pixel coordinates. The timing resolution of an event counting sensor is therefore determined by the frequency of the internal clock, and

Table 1.1 Table summarising the typical performance of various fast imaging technologies, including wedge and strip anodes (WSA), crossed wire detectors (CWD), delay line detectors (DLD), fast framing CCD (FF-CCD), and time stamping CMOS (TS-CMOS)

Technology	Multi-hit capability	Resolution		Rate	References
	Events/Dead time	mm	ns	kHz	
WSA	1	0.04–0.1	6	0.4–150	[105]
CWD	1/(3–5 ns)	2.5	0.2	1000	[119]
DLD	<3/~100ns	0.1	0.1	20–1000	[110]
FF-CCD	>100	16 × 16 pixels	10	0.05	[113]
TS-CMOS	>100	512 × 512 pixels	10	0.2	[114]

not by charge transfer or data readout. Similarly, the effective number of ‘frames’ is limited only by the maximum number of time intervals in a full clock cycle. For example, a 12-bit counter provides 4096 unique time codes in a full clock cycle (Table 1.1).

The advantage of the time stamping approach, in terms of the quantity of data that must be stored and transferred, when compared to conventional fast framing is illustrated in Fig. 1.6. As with in situ storage, time stamping detectors require an acquisition dead time, in order that the data stored in the pixel memory buffers may be read out to an external storage. A current example of such a detector is the TimePix sensor [114], which is a CMOS-based pixelated detector comprising of an array of 256×256 pixels with an internal clock cycle as low as 10ns. However, the TimePix family of detectors contain only a single memory buffer in each pixel, limiting the sensor to the detection of a maximum of a single event per pixel during a full acquisition cycle. While this may be sufficient for applications in which low count rates are expected, and for those in which the signal is well distributed amongst

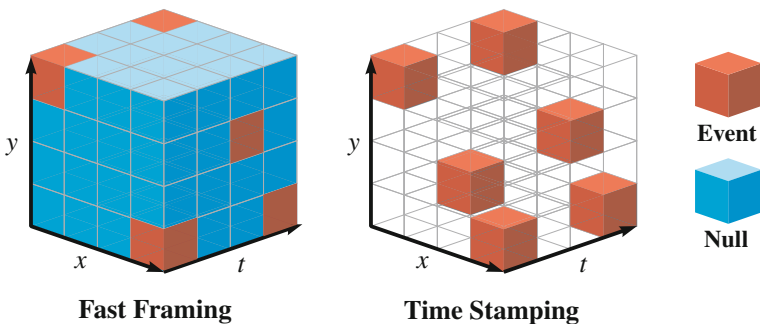


Fig. 1.6 Illustration of the reduced size of time stamping data sets when compared to fast framing acquisition. In the fast framing case the value of each pixel is stored regardless of the data content, resulting in a dense data array. Time stamping devices, on the other hand, only record events, ignoring the overwhelming majority of null data. (Figure adapted from Ref. [121])

the many pixels of the detector, it will become problematic when imaging congested data sets in which there is an appreciable probability of recording multiple events at the same spatial coordinate during a single acquisition cycle. Under these conditions it is likely that earlier peaks in the time-of-flight spectrum will ‘shadow’ those at later times, causing a systematic bias in the data.

The recently developed PImMS sensor addresses this shortcoming with the inclusion of an additional three memory registers per pixel, taking the total number to four [115]. Simulations and practical experience have shown that for most ion imaging applications this is sufficient to capture the vast majority of events in each acquisition cycle [120]. The prototype PImMS1 sensor consists of an array of 72×72 pixels, with a clock cycle down to 12.5 ns. The second generations sensor, known as PImMS2, is currently undergoing testing and consists of a 256×256 pixel array. It is anticipated that the clock cycle of the PImMS family will be capable of reaching 6.25 ns, but this is yet to be demonstrated.

1.7 Outline of This Thesis

This thesis is concerned with the application of a new fast imaging sensor to studies of photoinduced molecular dynamics in the gas phase. The unique capabilities of the PImMS camera open the door to new experimental possibilities, some of which are investigated in the following chapters. The experimental apparatus are described in detail in Chap. 2, whereafter data characterising some elements of the performance of the PImMS camera are presented, particularly in relation to the interfacing of the device with a time-of-flight ion imaging apparatus. Chapters 3 and 4 present proof of principle experiments demonstrating the versatility of the PImMS camera when combined with a conventional ion imaging apparatus, providing perspectives on possible future applications of the device. Specifically, Chap. 3 investigates the possibilities for using the camera in slice and 3D imaging applications, using the photodissociation of ethyl iodide at around 230 nm as the target system. Chapter 4 demonstrates the simultaneous velocity-map imaging of both ions and electrons on a single detector, transforming a conventional ion imaging apparatus into a PEPICO spectrometer when combined with the PImMS camera. Chapter 5 introduces the principles of Coulomb explosion imaging (CEI) as an ultrafast probe of molecular structure, before the Coulomb explosion dynamics of a substituted biphenyl derivative are investigated in detail in Chap. 6. In Chap. 7 the principles of CEI are used to probe the torsional motion of axially chiral substituted biphenyl derivatives following torsional excitation by a single femtosecond ‘kick’ pulse. This approach is extended to include a second kick pulse, in order that the induced torsional motion may be amplified or damped, depending on the precise time delay between the two kick pulses.

References

1. W.C.McC. Lewis, *J. Chem. Soc. Trans.* **113**, 471 (1918)
2. W.O. Kermack, R. Robinson, *J. Chem. Soc. Trans.* **121**, 427 (1922)
3. M.A. Gilbert, J.E. Baggott, *Essentials of Molecular Photochemistry* (Blackwell Scientific Publications, Oxford, UK, 1991)
4. N.J. Turro, V. Ramamurthy, J.C. Scaiano, *Principles of Molecular Photochemistry* (University Science Books, Sausalito, CA, USA, 2009)
5. I. Asimov, *Photosynthesis* (Basic Books, New York, NY, USA, 1968)
6. R.P. Wayne, *Chemistry of Atmospheres* (Oxford University Press, Oxford, UK, 2000)
7. D. Rogers, *Chemistry of Photography* (Royal Society of Chemistry, Cambridge, UK, 2007)
8. N.J. Turro, V. Ramamurthy, J.C. Scaiano, *Modern Molecular Photochemistry of Organic Molecules* (University Science Books, Sausalito, CA, USA, 2010)
9. H.P. Garg, J. Prakash, *Solar Energy: Fundamentals and Applications* (Tata McGraw-Hill, Noida, UP, India, 1997)
10. K.F. Renk, *Basics of Laser Physics: For Students of Science and Engineering* (Springer, New York, NY, USA, 2012)
11. R.G.W. Norrish, G. Porter, *Nature* **164**, 658 (1949)
12. G. Porter, *Proc. R. Soc. Lond. A.* **200**, 284 (1950)
13. G. Porter, *Nobel Lectures in Chemistry 1963–1970* (Elsevier Publishing Company, Amsterdam, Netherlands, 1972)
14. K. Zhao, Q. Zhang, M. Chini, Y. Wu, X. Wang, Z. Chang, *Opt. Lett.* **37**, 3891 (2012)
15. G. Herzberg, *Molecular Spectra and Molecular Structure: III, Electronic Spectra and Electronic Structure of Polyatomic Molecules* (David Van Nostrand Company, Princeton, USA, 1967)
16. R. Schinke, *Photodissociation Dynamics* (Cambridge University Press, Cambridge, UK, 1993)
17. Mark Brouard, Claire Vallance, *Tutorials in Molecular Reaction Dynamics* (Royal Society of Chemistry, Cambridge, UK, 2010)
18. R.N. Zare, *Faraday Discuss. Chem. Soc.* **67**, 7 (1979)
19. M. Born, R. Oppenheimer, *Zur Quantentheorie der Molekeln* **84**, 457 (1927)
20. Y. Tang, W.-B. Lee, Z. Hu, B. Zhang, K.-C. Lin, *J. Chem. Phys.* **126**, 064302 (2007)
21. T.P. Rakitzis, T.N. Kitsopoulos, *J. Chem. Phys.* **116**, 9228 (2002)
22. A.J. Johnsen, A.B. Alekseyev, G.G. Balint-Kurti, M. Brouard, A. Brown, R.J. Buenker, E.K. Campbell, D.B. Kokh, *J. Chem. Phys.* **136**, 164310 (2012)
23. T. Seideman, E. Hamilton, *Adv. Atom. Mol. Opt. Phys.* **52**, 289 (2005)
24. H. Stapelfeldt, T. Seideman, *Rev. Mod. Phys.* **75**, 543 (2003)
25. Y. Ohshima, H. Hasegawa, *Int. Rev. Phys. Chem.* **29**, 619 (2010)
26. B. Friedrich, D. Herschbach, *Phys. Rev. Lett.* **74**, 4623 (1995)
27. P.H. Bucksbaum, A. Zavriyev, H.G. Muller, D.W. Schumacher, *Phys. Rev. Lett.* **64**, 1883 (1990)
28. H. Niikura, V.R. Bhardwaj, F. Légaré, I.V. Litvinyuk, P.W. Dooley, D.M. Rayner, M. Yu Ivanov, P.B. Corkum, D.M. Villeneuve, *Springer Series in Optical Sciences* **134**, 185 (2009)
29. J.H. Posthumus, *Rep. Prog. Phys.* **67**, 623 (2004)
30. M. Schmidt, P. DOLiveira, P. Meynadier, D. Normand, C. Cornaggia, *J. Nonlinear Opt. Phys. Mat.* **4**, 817 (1995)
31. K. Codling, L. Frasninski, *J. Phys. B* **26**, 783 (1993)
32. J. Gagnon, K.F. Lee, D.M. Rayner, P.B. Corkum, V.R. Bhardwaj, *J. Phys. B* **41**, 215104 (2008)
33. M. Pitzer, M. Kunitski, A.S. Johnson, T. Jahnke, H. Sann, F. Sturm, L.P.H. Schmidt, H. Schmidt-Böcking, R. Dörner, J. Stohner, J. Kiedrowski, M. Reggelin, S. Marquardt, A. Schießer, R. Berger, M.S. Schöffler, *Science* **341**, 1096 (2013)
34. A. Hishikawa, A. Iwamae, K. Hoshina, M. Kono, K. Yamanouchi, *Chem. Phys. Lett.* **282**, 283 (1998)

35. J.H. Sanderson et al., *Phys. Rev. A* **59**, R2567 (1999)
36. T.A. Carlson, R.M. White, *J. Chem. Phys.* **44**, 4510 (1966)
37. A. Rudenko, Th Ergler, B. Feuerstein, K. Zrost, C.D. Schröter, R. Moshhammer, J. Ullrich, *Chem. Phys.* **329**, 193 (2006)
38. T. Ergler, A. Rudenko, B. Feuerstein, K. Zrost, C.D. Schröter, R. Moshhammer, J. Ullrich, *Phys. Rev. Lett.* **97**, 193001 (2006)
39. F. Légaré, K.F. Lee, I.V. Litvinyuk, P.W. Dooley, S.S. Wesolowski, P.R. Bunker, P. Dombi, F. Krausz, A.D. Bandrauk, D.M. Villeneuve, P.B. Corkum, *Phys. Rev. A* **71**, 013415 (2005)
40. H. Hasegawa, A. Hishikawa, K. Yamanouchi, *Chem. Phys. Lett.* **349**, 57 (2001)
41. R.L. Fork, B.I. Greene, C.V. Shank, *Appl. Phys. Lett.*, **38**, 671 (671)
42. D.E. Spence, P.N. Kean, W. Sibbett, *Opt. Lett.* **16**, 42 (1991)
43. A.H. Zewail, *Science* **242**, 1645 (1988)
44. J.A. Davies, R.E. Continetti, D.W. Chandler, C.C. Hayden, *Phys. Rev. Lett.* **84**, 5983 (2000)
45. A. Zewail, *J. Phys. Chem.* **100**, 12701 (1996)
46. P. Cheng, D. Zhong, A. Zewail, *J. Chem. Phys.* **105**, 6216 (1996)
47. J.L. Hansen, J.H. Nielsen, C.B. Madsen, A.T. Lindhardt, M.P. Johansson, T. Skrydstrup, L.B. Madsen, H. Stapelfeldt, *J. Chem. Phys.* **136**, 204310 (2012)
48. K. Ohmori, *Annu. Rev. Phys. Chem.* **60**, 487 (2009)
49. J.S. Briggs, *J. Phys.: Conf. Ser.* **99**, 012002 (2008)
50. M. Shapiro, P. Brumer, *J. Chem. Phys.* **84**, 4103 (1986)
51. D.J. Tannor, S.A. Rice, *J. Chem. Phys.* **83**, 5013 (1985)
52. L. Zhu, V. Kleiman, X. Li, S.P. Lu, K. Trentelman, R.J. Gordon, *Science* **270**, 77 (1995)
53. E.D. Potter, J.L. Herek, S. Pedersen, Q. Liu, A.H. Zewail, *Nature* **355**, 66 (1992)
54. N.F. Scherer, R.J. Carlson, A. Matro, M. Du, A.J. Ruggiero, V. Romero-Rochin, J.A. Cina, G.R. Fleming, S.A. Rice, *J. Chem. Phys.* **95**, 1487 (1991)
55. R.S. Judson, H. Rabitz, *Phys. Rev. Lett.* **68**, 1500 (1992)
56. A. Assion, T. Baumert, M. Bergt, T. Brixner, B. Kiefer, V. Seyfried, M. Strehle, G. Gerber, *Science* **282**, 919 (1998)
57. V.I. Prokhorenko, A.M. Nagy, S.A. Waschuk, L.S. Brown, R.R. Birge, R.J.D. Miller, *Science* **313**, 1257 (2006)
58. T. Seideman, *J. Chem. Phys.* **103**, 7887 (1995)
59. B. Kohler, V.V. Yakovlev, J. Che, J.L. Krause, M. Messina, K.R. Wilson, N. Schwentner, R.M. Whitnell, Y.J. Yan, *Phys. Rev. Lett.* **74**, 3360 (1995)
60. Ch. Warmuth, A. Tortschanoff, F. Milota, M. Shapiro, Y. Prior, ISh Averbukh, W. Schleich, W. Jakubetz, H.F. Kauffmann, *J. Chem. Phys.* **112**, 5060 (2000)
61. H. Katsuki, K. Hosaka, H. Chiba, K. Ohmori, *Phys. Rev. A* **76**, 013403 (2007)
62. T. Seideman, *Phys. Rev. A* **56**, 17 (1997)
63. T. Seideman, *J. Chem. Phys.* **107**, 10420 (1997)
64. M. Artamonov, T. Seideman, *Nano Lett.* **10**, 4908 (2010)
65. H. Stapelfeldt, H. Sakai, E. Constant, P. Corkum, *Phys. Rev. Lett.* **79**, 2787 (1997)
66. H. Sakai, A. Tarasevitch, J. Danilov, H. Stapelfeldt, R. Yip, C. Ellert, E. Constant, P. Corkum, *Phys. Rev. A* **57**, 2794 (1998)
67. T. Seideman, *J. Chem. Phys.* **111**, 4397 (1999)
68. B. Suk Zhao, H. Sung Chung, K. Cho, S. Hyup Lee, S. Hwang, J. Yu, Y. Ahn, J. Sohn, D. Kim, W. Kyung Kang, D. Chung, *Phys. Rev. Lett.* **85**, 2705 (2000)
69. M. Maus, W. Rettig, *J. Phys. Chem. A* **106**, 2104 (2002)
70. F. Sterpone, R. Martinazzo, A.N. Panda, I. Burghardt, *Z. Phys. Chem.* **225**, 541 (2011)
71. L. Venkataraman, J. Klare, C. Nuckolls, M. Hybertsen, M. Steigerwald, *Nature* **442**, 904 (2006)
72. D. Vonlanthen, A. Mishchenko, M. Elbing, M. Neuburger, T. Wandlowski, M. Mayor, *Angew. Chem. Int. Ed.* **48**, 8886 (2009)
73. A. Mishchenko, D. Vonlanthen, V. Meded, M. Burkle, C. Li, I. Pobelov, A. Bagrets, J. Viljas, F. Pauly, F. Evers, M. Mayor, T. Wandlowski, *Nano Lett.* **10**, 156 (2010)
74. D. Kroner, B. Klaumunzer, T. Klamroth, *J. Phys. Chem. A* **112**, 9924 (2008)

75. F. Grossmann, L. Feng, G. Schmidt, T. Kunert, R. Schmidt, *Europhys. Lett.* **60**, 201 (2002)
76. B. Dietzek, B. Brüggemann, T. Pascher, A. Yartsev, *Phys. Rev. Lett.* **97**, 258301 (2006)
77. S. Belz, T. Grohmann, M. Leibscher, *J. Chem. Phys.* **131**, 034305 (2009)
78. M. Parker, M.A. Ratner, T. Seideman, *Mol. Phys.* **110**, 1941 (2012)
79. C.B. Madsen, L.B. Madsen, S.S. Viftrup, M.P. Johansson, T.B. Poulsen, L. Holmegaard, V. Kumarappan, K.A. Jorgensen, H. Stapelfeldt, *Phys. Rev. Lett.* **102**, 073007 (2009)
80. C.B. Madsen, L.B. Madsen, S.S. Viftrup, M.P. Johansson, T.B. Poulsen, L. Holmegaard, V. Kumarappan, K.A. Jorgensen, H. Stapelfeldt, *J. Chem. Phys.* **130**, 234310 (2009)
81. W. Bothe, *Nobel Lectures in Physics 1942–1962* (Elsevier Publishing Company, Amsterdam, Netherlands, 1964)
82. K. McCulloh, T. Sharp, H. Rosenstock, *J. Chem. Phys.* **42**, 3501 (1965)
83. A. Hishikawa, A. Iwamae, K. Yamanouchi, *J. Chem. Phys.* **11**, 8871 (1999)
84. R.K. Kushawaha, S.S. Kumar, I.A. Prajapati, K.P. Subramanian, B. Bapat, *J. Phys. B* **42**, 105201 (2009)
85. S.D. Price, *Int. J. Mass. Spectrom.* **260**, 1 (2007)
86. L.J. Frasinski, K. Codling, P.A. Hatherly, *Science* **246**, 1029 (1989)
87. J. Mikoscha, S. Patchkovskii, *J. Mod. Opt.* **60**, 1426 (2013)
88. J. Mikoscha, S. Patchkovskii, *J. Mod. Opt.* **60**, 1439 (2013)
89. T.W. Anderson, *An Introduction to Multivariate Statistical Analysis* (Wiley, New York, NY, USA, 2003)
90. L.J. Frasinski, A.J. Giles, P.A. Hatherly, J.H. Posthumus, M.R. Thompson, K. Codling, *J. Electron Spectrosc. Relat. Phenom.* **79**, 367 (1996)
91. L.J. Frasinski et al., *Phys. Rev. Lett.* **111**, 073002 (2013)
92. K. Codling, C. Cornaggia, L.J. Frasinski, P.A. Hatherly, J. Morellec, D. Normand, *J. Phys. B: At. Mol. Opt. Phys.* **24**, L593 (1991)
93. P.A. Hatherly, M. Stankiewicz, K. Codling, L.J. Frasinski, G.M. Cross, *J. Phys. B: At. Mol. Opt. Phys.* **27**, 2993 (1994)
94. J.H. Posthumus, A.J. Giles, M.R. Thompson, K. Codling, *J. Phys. B: At. Mol. Opt. Phys.* **29**, 5811 (1996)
95. V. Zhaunerchyk et al., *J. Phys. B: At. Mol. Opt. Phys.* **46**, 164034 (2013)
96. D.W. Chandler, P.L. Houston, *J. Chem. Phys.* **87**, 1445 (1987)
97. A.T. Eppink, D.H. Parker, *Rev. Sci. Instrum.* **68**, 3477 (1997)
98. M. Brouard, H. Chadwick, C.J. Eyles, B. Hornung, B. Nichols, J.M. Scott, F.J. Aoiz, J. Klos, S. Stolte, X. Zhang, *Mol. Phys.* **111**, 1759 (2013)
99. L. Holmegaard, J.H. Nielsen, I. Nevo, H. Stapelfeldt, F. Filsinger, J. Kpper, G. Meijer, *Phys. Rev. Lett.* **102**, 023001 (2009)
100. W.S. Hopkins, A.P. Woodham, R.J. Plowright, T.G. Wright, S.R. Mackenzie, *J. Chem. Phys.* **132**, 214303 (2010)
101. I. Wilkinson, B.J. Whitaker, *J. Chem. Phys.* **129**, 154312 (2008)
102. A.I. Chichinin, K.-H. Gericke, S. Kauczok, C. Maul, *Int. Rev. Phys. Chem.* **28**, 607 (2009)
103. M.N.R. Ashfold, N.H. Nahler, A.J. Orr-Ewing, O.P.J. Vieuxmaire, R.L. Toomes, T.N. Kitsopoulos, I.A. Garcia, D.A. Chestakov, S.-M. Wu, D.H. Parker, *Phys. Chem. Chem. Phys.* **8**, 26 (2006)
104. C. Martin, P. Jelinsky, M. Lampton, R.F. Malina, H.O. Anger, *Rev. Sci. Instrum.* **52**, 1067 (1981)
105. O. Jagutzki, J.S. Lapington, L.B.C. Worth, U. Spillman, V. Mergel, H. Schmidt-Böcking, *Nucl. Instrum. Meth. Phys. Res. A* **477**, 256 (2002)
106. N. Saito, F. Heiser, O. Hemmers, K. Wieliczek, J. Viehhaus, U. Becker, *Phys. Rev. A* **54**, 2004 (1996)
107. J.H.D. Eland, *Meas. Sci. Technol.* **1**, 36 (1990)
108. J.H.D. Eland, *Meas. Sci. Technol.* **5**, 1501 (1994)
109. I. Ali, R. Dörner, O. Jagutzki, S. Nuttgens, V. Mergel, L. Spielberger, K. Khayyat, T. Vogt, H. Bräuning, K. Ullmann, *Nucl. Instrum. Methods Phys. Res. B* **149**, 490 (1999)

110. O. Jagutzki, V. Mergel, K. Ullmann-Pfleger, L. Spielberger, U. Spillmann, R. Dörner, H. Schmidt-Böcking, *Nucl. Instrum. Methods Phys. Res. A* **477**, 244 (2002)
111. O. Jagutzki, A. Cerezo, A. Czasch, R. Dörner, M. Hattas, M. Huang, V. Mergel, U. Spillmann, K. Ullmann-Pegeter, T. Weber, H. Schmidt-Böcking, G. Smith, *I.E.E.E.T. Nucl. Sci.* **49**, 2477 (2002)
112. T.G. Etoh, D. Poggemann, G. Kreider, H. Mutoh, A.J.P. Theuwissen, A. Ruckelshausen, Y. Kondo, H. Maruno, K. Takubo, H. Soya, K. Takehara, T. Okinaka, Y. Takano, *I.E.E.E. Trans. Electron.* **50**, 144 (2003)
113. L. Lazovsky, D. Cismas, G. Allan, D. Given, *Proc. SPIE* **5787**, 184 (2005)
114. X. Llopart, R. Ballabriga, M. Campbell, L. Tlustos, *Nuc.Inst. Meth. Phys. Res.*, **581**, 485 (2007)
115. J.J. John, M. Brouard, A. Clark, J. Crooks, E. Halford, L. Hill, J.W.L. Lee, A. Nomerotski, R. Pisarczyk, I. Sedgwick, C.S. Slater, R. Turchetta, C. Vallance, E. Wilman, B. Winter, W.H. Yuen, *J. Inst.* **7**, C08001 (2012)
116. <http://www.photron.com>
117. W.F. Kosonocky, G. Yang, R.K. Kabra, Z. Pektas, C. Ye, J.L. Lowrance, V.J. Mastrocola, F.V. Shallcross, V. Patel, *IEEE Trans. Electron.* **44**, 1617 (1997)
118. D.V.T. Son, T.G. Etoh, M. Tanaka, N.H. Dung, V. Le Cuong, K. Takehara, T. Akino, K. Nishi, H. Aoki, J. Nakai, *Sensors* **10**, 16 (2010)
119. J. Becker, K. Beckord, U. Werner, H. Lutz, *Nucl. Instrum. Meth. Phys. Res. A* **337**, 409 (1999)
120. A.T. Clark, J.P. Crooks, I. Sedgwick, R. Turchetta, J.W.L. Lee, J.J. John, E.S. Wilman, L. Hill, E. Halford, C.S. Slater, B. Winter, W.-H. Yuen, S.H. Gardiner, M.L. Lipciuc, M. Brouard, A. Nomerotski, C. Vallance, *J. Phys. Chem. A* **116**, 10897 (2012)
121. W.H. Yuen, *Ion Imaging Mass Spectrometry*, PhD thesis, University of Oxford (2012)

Chapter 2

Experimental Techniques and Methods of Data Analysis

This chapter details the experimental methods and apparatus used in the work presented in this thesis. The experiments were performed in two separate laboratories: that of Prof. Mark Brouard at the University of Oxford, and that of Prof. Henrik Stapelfeldt at the University of Aarhus. Both apparatus are variants of a conventional velocity-map ion imaging (VMI) spectrometer. The fundamental principals of velocity-map ion imaging were introduced in Sect. 1.5 and are reviewed briefly here, whereafter each spectrometer is described in detail. The Pixel Imaging Mass Spectrometry (PImMS) camera, which is central to the work undertaken in this thesis, is introduced and the design and function of the device are described in detail. Experimental results are presented characterising the performance and characteristics of the device. In addition to experimental methods, this chapter also describes the various data analysis routines used to extract scientifically pertinent information from the experimental data.

2.1 Experimental Principles

The data presented in this thesis were collected using variants of a conventional velocity-map ion imaging experiment, as illustrated in Fig. 1.4. Although such apparatus differ in their details, the general construction is similar in each case. The apparatus generally consist of a series of chambers kept under high ($<10^{-5}$ Torr) or ultra-high ($<10^{-8}$ Torr) vacuum conditions, typically through the use of turbomolecular and/or diffusion pumps. The sample gas is supersonically expanded into the experiment through a pulsed valve and subsequently passes through one or more skimmers to produce a collimated and rotationally cold (typically <25 K) molecular beam. The molecular beam is then intersected by one or more focussed laser pulses to induce a structural or chemical change in the target molecules, and to

cause photoionisation of the resultant photofragments. The nascent ions are then accelerated and focussed down a flight tube onto a two-dimensional detector by an electric field, tuned such that velocity-mapping of the ions takes place, as discussed in Sect. 1.5.1. A further consequence of the use of an electric field to extract the ions onto the detector is that the ions are separated temporally at the detector according to their mass-to-charge (m/z) ratio. The detector consists of a set of microchannel plates (MCPs) and a phosphor screen. The impact of the ions onto the detector causes flashes of light to be emitted by the phosphor screen, which are imaged by a camera.

2.2 The Oxford VMI Spectrometer

The Oxford spectrometer was used for the PImMS characterisation experiments (Sect. 2.5.4), the three-dimensional imaging experiments (Chap. 3), and the proof-of-principle electron-ion pulsed extraction experiments (Chap. 4). The experiment is located in the laboratory of Prof. Mark Brouard in the Chemistry Research Laboratory at the University of Oxford.

2.2.1 Overview

The experiment comprises three main vacuum chambers: the source chamber, the reaction chamber, and the flight tube. A schematic of the experiment is shown in Fig. 2.1. The sample gas is introduced to the source chamber by way of a supersonic expansion through a pulsed (10 Hz) General Valve (Series 9) at a backing pressure of approximately 0.5–2 bar, supplied from an external stainless steel sample reservoir fitted with a two-stage regulator. The General valve is mounted in such a way that it is possible to translate the valve orifice fully in three-dimensional space relative to the fixed position of the skimmer, allowing for optimisation of the experimental signal. The rotational temperature of the molecular beam has been measured previously to be approximately 25 K [1]. The source chamber is pumped by a 3700 l s^{-1} water-cooled diffusion pump (Varian VHS-250), backed by a rotary pump (Leybold Trivac D40V). The diffusion pump is fitted with a water-cooled baffle located between the pump and the chamber in order to minimise contamination of the apparatus by the diffusion pump oil vapour. Background pressures in the source chamber are typically around 1×10^{-6} Torr, rising to approximately 2×10^{-5} Torr when the molecular beam is in operation.

The source chamber is separated from the reaction chamber by a skimmer with an orifice of 1 mm diameter (BeamDynamics Inc.), through which the supersonic expansion passes in order to produce a collimated molecular beam. The reaction chamber contains the ion optics assembly (see Sect. 2.2.2) and is differentially pumped by a 510 l s^{-1} turbomolecular pump (Pfeiffer, Vacuum TMH-521P), backed by a rotary pump (Leybold, Trivac D40V), to a typical background pressure of around

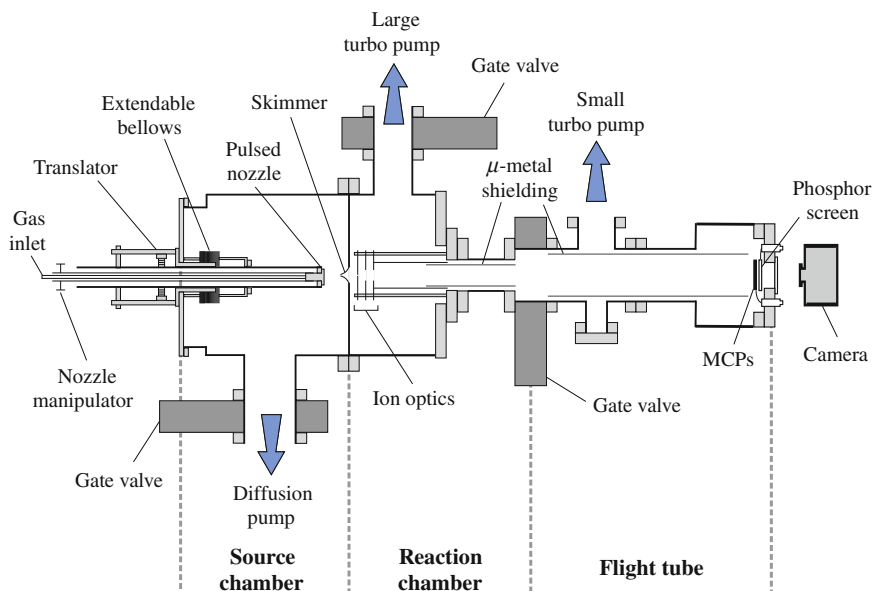


Fig. 2.1 Schematic illustration of the Oxford velocity-map ion imaging spectrometer

2×10^{-7} Torr. The laser beams enter through fused silica windows on either side of the reaction chamber to intersect the molecular beam in a perpendicular geometry between the repeller and extractor electrodes of the ion optics assembly. The windows are fitted internally with home-built light baffles to minimise the amount of scattered light entering the chamber. Each of the baffles consists of a stack of copper rings contained within a stainless steel housing. The surfaces of the copper rings were oxidised in an alkaline solution of potassium persulphate [2] to increase their absorbance in the visible and UV wavelength range, and to diffuse the small amount of reflected light.

The flight tube is separated from the reaction chamber by a gate valve and is pumped by a small turbomolecular pump with a capacity of 60 l s^{-1} (Pfeiffer, Vacuum TMU 071P) backed by the same Leybold Trivac D40V rotary pump as the reaction chamber turbomolecular pump. The background pressure of the flight tube is of a similar order to that in the reaction chamber. The gate valve allows the reaction and source chambers to be vented while maintaining a vacuum in the flight tube, thereby protecting the detector from exposure to atmospheric gases. The flight tube is shielded along its length by a double-layered, cylindrical μ -metal magnetic shield in order to neutralise the effect of stray magnetic fields on the trajectories of the ions and electrons in the field-free drift region.

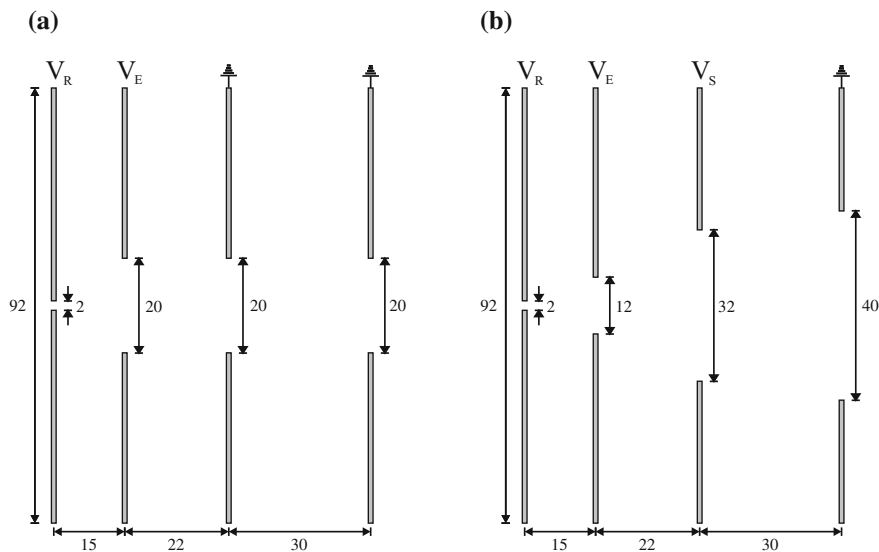


Fig. 2.2 Schematic representation of the two variants of ion optics arrangements used in the Oxford spectrometer. The ion optics consist of four disc shaped electrodes, each with a central aperture. The electrodes are referred to as (from *left*) the repeller, extractor, slice, and ground electrodes. The values V_R , V_E , and V_S refer to the voltages applied to the repeller, extractor, and slice electrodes, respectively. All measurements are in mm. **a** Crush velocity map imaging. **b** dc slice velocity map imaging

2.2.2 Ion Optics

The ion optics assembly is mounted on the main flange of the reaction chamber by four threaded stainless steel rods, as illustrated in Fig. 2.1. The ion optics consist of a stack of circular stainless steel plates of thickness 1 mm, each possessing a central aperture of a carefully selected diameter, through which the ions are accelerated. The ion optics are separated from one another and insulated from the stainless steel mounting rods by MACOR[®] spacers. Depending on whether crush or dc slice imaging is to be effected (see Chap. 3), one of two alternative ion optics arrangements may be used (see Fig. 2.2). The final electrode was held at ground in each case in order to shield the flight tube from the potentials applied to the focussing lenses.

The electrostatic lenses were supplied with high voltages through three independent high-voltage MOSFET switches (Behlke, HTS 121, 12kV, 30A) so that the magnitude and polarity of the voltages may be switched on a short timescale (~ 40 ns). In order to reduce the capacitance of the system, and therefore the rise-time upon switching, the unit containing the Behlke switches is attached directly to the high voltage feedthroughs (SHV-10), which are mounted on a DN40 conflat (CF) flange fitted to the external wall of the reaction chamber.

2.2.3 *Detector*

The detection assembly consists of a pair of 78 mm chevron-stacked MCPs coupled to a P47 phosphor screen (Burle Technologies Inc.). The MCPs have a pore diameter of $25\ \mu\text{m}$ and a pitch of $32\ \mu\text{m}$, giving a theoretical open area ratio of 55.4%. The MCPs are fitted with a fine nickel mesh (Precision Eforming, MN4) with a pitch of 1.27 mm and a transmittance of 95%. The mesh covers the front face of the MCPs and is located approximately 2 mm from the surface of the detector. The nickel mesh allows voltages to be applied to the front face of the detector while maintaining a field-free drift region in the flight tube. A photomultiplier tube fitted with a liquid light guide is used to measure the signal from the phosphor screen and provide a time-of-flight trace on an oscilloscope. Events on the phosphor screen are recorded by either an intensified CCD camera (Photonic Science, 576×768 pixels) or the PImMS camera, which is described in detail in Sect. 2.5. The intensifier in the CCD camera is time-gated to allow the acquisition of images corresponding to individual peaks in the time-of-flight spectrum.

The high voltages required for operation are supplied through individual transformer units, which allows an additional pulse of up to 300 V to be independently applied to each face of the MCPs and the scintillator screen at independently determined times after the Q-switch trigger of the Nd:YAG laser. This allows for pulsing of the detector, to achieve a stepped gain profile during the course of each acquisition cycle. By altering the gain of the MCPs between the arrival times of the photoelectrons and photoions it is possible to optimise the detection efficiencies of each species. Since the gain profile of an MCP detector depends on the mass, kinetic energy, and chemical identity of the charged particle being detected [3], this is crucial to the success of the single detector photoelectron-photoion correlation experiments proposed in Chap. 4.

2.2.4 *Optical Systems*

The experiments performed using the Oxford VMI spectrometer were all of a single colour, that is that the pump and probe processes are at the same wavelength; therefore a single laser system was required in each case. The 446.41 nm radiation used for the experiments involving the photodissociation of molecular bromine was produced by a dye laser system (Lambda Physik, LPD 3000) pumped by the third harmonic (355 nm) of an Nd:YAG laser (Continuum, Powerlite Precision II) operating at 10 Hz. The third harmonic pulse energy of the Nd:YAG laser was approximately 420 mJ at full power, although this was attenuated to the desired level by increasing the time delay between the flashlamps and the Q-switch. The dye solution used was Coumarin 450 (also known as Coumarin 2) dissolved in ethanol, at a concentration of $0.2\ \text{g l}^{-1}$ in the oscillator and one third of that in the amplifier, producing a peak power output of ~ 10 mJ per pulse. The output of the dye laser was steered to the experiment using optical prisms and focussed into the reaction chamber by a 30 cm focal length lens.

For the experiments involving the photodissociation of ethyl iodide at around 245 nm the laser radiation was again provided by a dye laser system (Sirah, Cobra Stretch) pumped by the third harmonic of an Nd:YAG laser (Continuum, Powerlite Precision II). The maximum pulse energy of the third harmonic output was approximately 300 mJ, which was again attenuated by altering the delay between the flashlamps and the Q-switch of the laser. The dye solution used was Coumarin 503 (also known as Coumarin 307) dissolved in ethanol, at a concentration of 0.2 g l^{-1} in the oscillator and one fifth of that in the amplifier, giving a peak power output of $\sim 23 \text{ mJ}$ per pulse at the fundamental wavelength. The frequency doubled output was produced using a BBO type I crystal (SHG 220) and was separated from the fundamental by a set of four Pellin-Broca prisms. The beam was then steered to the experiment using optical prisms and focussed into the reaction chamber using a 30 cm focal length lens.

2.2.5 Reagent Sources

Both bromine and ethyl iodide are liquid at room temperature and pressure, and were prepared in the gas phase following the procedures outlined below. Both reagents have a tendency to form clusters in the gas phase unless the pressures and concentrations are kept sufficiently low.

2.2.5.1 Bromine

Liquid bromine was supplied from Fisher Scientific at a purity of 99 % and was decanted in small quantities into a sealed glass flask. The bromine was expanded into the stainless steel sample reservoir until it reached its vapour pressure. The bromine vapour was then successively diluted with helium to the appropriate concentration (<1 %). Backing pressures of approximately 2 bar were used to supply the General Valve.

2.2.5.2 Ethyl Iodide

Ethyl iodide was supplied from Sigma-Aldrich at a purity of 99 % and was decanted in small quantities into a stainless steel 'cold finger'. The cold finger was cooled with liquid nitrogen and the residual atmospheric gases pumped off. The ethyl iodide was then allowed to warm to room temperature and expanded into the stainless steel sample reservoir until it reached its vapour pressure. The ethyl iodide vapour was then successively diluted with helium until the appropriate concentration was reached (approximately 5 %). Backing pressures of approximately 0.8 bar were used to supply the General Valve.

2.3 The Aarhus VMI Spectrometer

The Aarhus spectrometer was used in the study of the Coulomb explosion dynamics and torsional motion of the substituted biphenyl molecules 3,5-dibromo-3',5'-difluoro-4'-cyanobiphenyl and 3,5-dibromo-3',5'-difluoro-4-cyanobiphenyl presented in Chaps. 6 and 7. The experiment is located in the laboratory of Prof. Henrik Stapelfeldt at the University of Aarhus.

2.3.1 Overview

The experiment comprises three main vacuum chambers: the source chamber, the deflection chamber, and the reaction chamber. An illustration of the experiment is shown in Fig. 2.3. The molecular beam is introduced into the source chamber by way of a supersonic expansion through a high pressure Even-Lavie pulsed valve (see Sect. 2.3.2). The molecular beam is skimmed twice at distances of 14 and 38 cm from the nozzle in order to collimate the expansion. The first skimmer is located at the junction between the source and deflection chambers, and has a relatively large orifice (3 mm, Beam Dynamics Inc.) so as not to attenuate the signal too strongly. The second skimmer is fitted immediately before an electrostatic deflector and has a 1 mm orifice to ensure that the supersonic expansion is well collimated to form a cold molecular beam.

The molecular beam then travels through a 15 cm long electrostatic deflector (see Sect. 2.3.3), which acts to separate the molecules with respect to their rotational quantum states, thereby improving the degree of adiabatic alignment achievable using the nanosecond laser pulse.

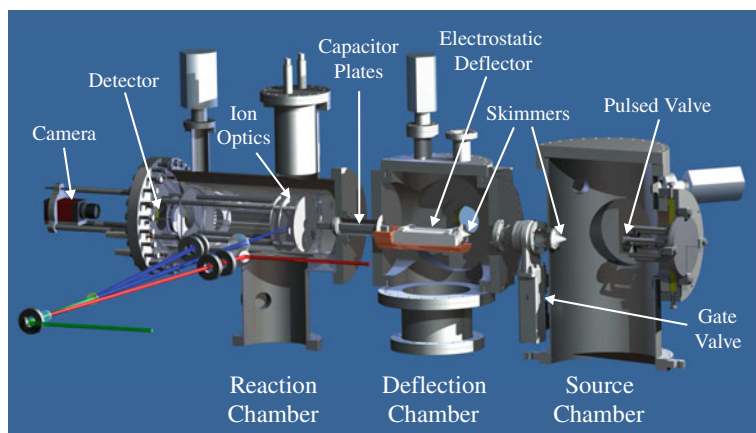


Fig. 2.3 A three-dimensional model of the Aarhus VMI spectrometer. The principal components are identified and labelled

The molecular beam then passes into the reaction chamber, which contains the ion optics assembly and the field-free drift region. The ion optics consists of three open electrodes, which act as an electrostatic lens. The first two electrodes are supplied with high voltages optimised to effect velocity-map imaging, while the third electrode is electrically grounded, which acts both to focus the ions and to isolate the field-free drift region from the potentials applied to the first two plates. The laser pulses enter the experiment through a fused silica window on one side of the reaction chamber, intersecting the molecular beam in a perpendicular manner between the repeller and extractor electrodes of the ion optics assembly. The ion optics and drift region are surrounded by a single cylindrical μ -metal shield in order to isolate the spectrometer from external magnetic fields, which could influence the trajectories of the ions.

The ions are detected by a pair of chevron-stacked MCPs coupled to a P47 phosphor screen (EI-Mul Technologies Ltd., B050V, ScintiMaxTM). The events on the phosphor screen are captured using a PImMS camera, which is described in detail in Sect. 2.5.

2.3.2 Molecular Beam Source

The molecular beam is produced by a supersonic expansion through a high pressure Even-Lavie pulsed valve (E.L.-7-4-2005-HRR) [4, 5]. The valve is mounted such that it can be translated in the xy -plane (perpendicular to the propagation direction of the molecular beam) relative to the skimmer. The temperature of the molecular beam has been measured previously to be on the order of 1 K [6]. The pulsed valve has a maximum repetition rate of 1 kHz, but this was limited to 20 Hz in the experiments described in this thesis due to the repetition rate of the Nd:YAG laser system used to align the target molecules (see Sect. 2.3.4). The valve incorporates a thermocouple combined with a resistive heater, which allows operational temperatures in the range of 30–250 °C. This allows the relative concentration of the sample gas to carrier gas to be optimised when sublimation of a solid sample is required to produce a gas-phase mixture. Solid samples are introduced to the valve on a small glass fibre filter, which is inserted into an internal sample reservoir.

2.3.3 Electrostatic Deflector

The deflection system is based on that of Chamberlain et al. [7] and comprises a polished rod-shaped electrode with a radius of 3.0 mm, which nests inside a trough-shaped electrode with an inner radius of curvature of 3.2 mm. The rod electrode is separated from the trough electrode by two 0.9 mm MACOR[®] spacers. The geometry of the deflector ensures that, when a large electrostatic potential is applied to the rod electrode (up to 10 kV), a field which is strongly inhomogeneous along the y -axis (vertical, perpendicular to the propagation of the molecular beam) but is almost

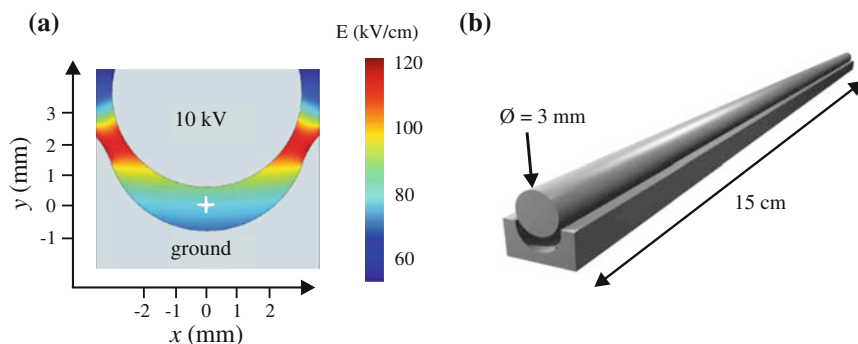


Fig. 2.4 Panel a shows a cross section of the deflector, illustrating the electric field used to deflect the molecules according to their rotational quantum states. Panel b shows a three-dimensional illustration of the deflector. Panel a is adapted from Ref. [8]

perfectly homogeneous along the x -axis (horizontal, perpendicular to the propagation of the molecular beam) results. This is illustrated in Fig. 2.4a, where a colour scale is used to map the electrostatic field gradient between the two electrodes. Polar molecules entering the deflector therefore experience a force in the y -direction, due to the potential gradient, but not in the x -direction. The extent and direction of deflection of a molecule depends on its effective dipole moment, which is, in part, determined by the rotational quantum state of the molecule. The deflection system employed in this apparatus ensures that molecules in high-field-seeking quantum states are deflected upward, whereas those in low-field-seeking states are deflected downward. The molecules are therefore spatially separated in the y -direction according to the magnitude and direction of their rotation, thus resulting in prealignment of the target molecules. By focussing the laser beams into the appropriate part of the deflected molecular beam it is therefore possible to select molecules that are prealigned and rotationally cold.

The electrostatic deflector is immediately followed by a parallel plate capacitor comprising two 17 cm long polished stainless steel plates separated by two 2.7 mm MACOR[®] spacers. The plates are aligned parallel to the direction of deflection and ensure a non-zero potential gradient in the region between the electrostatic deflector and the electrostatic lenses of the ion optics assembly. The presence of a non-zero potential gradient helps to minimise Majorana transitions between individual M quantum states, which are degenerate in zero-field.

2.3.4 Optical Systems

The optical system comprises two main parts: a nanosecond Nd:YAG laser, used to adiabatically align the molecules; and a Ti:Sapphire femtosecond system, used to

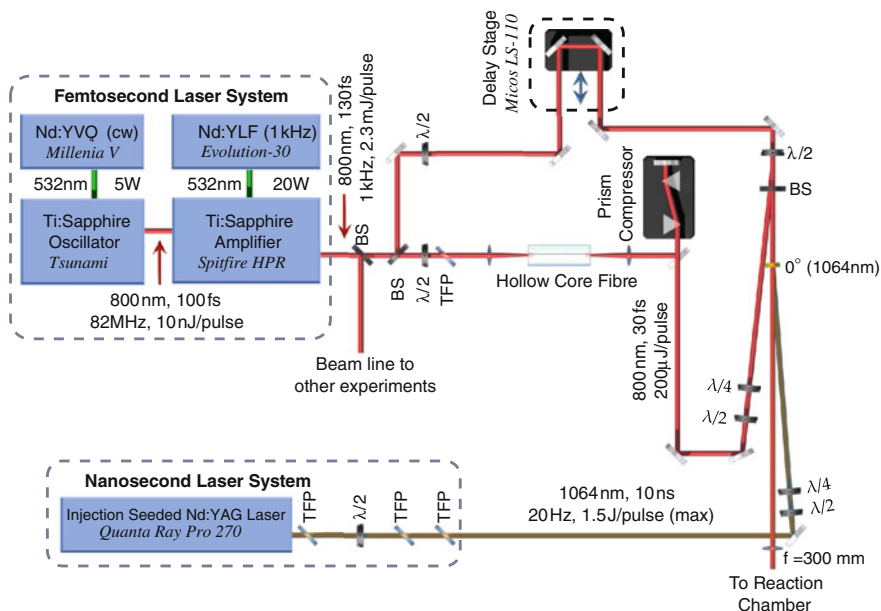


Fig. 2.5 Diagram of the optical systems coupled to the Aarhus spectrometer. See text for further details. Figure adapted from Ref. [8]

initiate torsional motion in the target molecules, and to induce non-resonant multiphoton ionisation and Coulomb explosion. An overview of the optical set-up is shown in Fig. 2.5.

2.3.5 Nanosecond Laser System

The nanosecond laser system consists of an injection seeded Q-switched Nd:YAG laser (Spectra-Physics, Quanta Ray Pro 270) with a maximum repetition rate of 20Hz and a maximum pulse energy of 1.5J. The laser is operated to output at the fundamental wavelength of 1064nm and has a pulse duration of 10ns. The pulses delivered to the experiment are attenuated to the desired energy (~ 150 mJ) following output by a combination of three thin film polarisers (TFPs) and a half waveplate (HWP). The first TFP is located immediately after the Nd:YAG laser system and acts to clean the polarisation of the laser output, whereafter the axis of polarisation may be rotated by a HWP. The HWP is followed by two further TFPs, with the extent of transmission being determined by the angle of the axis of polarisation of the incident light. A shift of 0° corresponds to full transmittance, whereas a shift of 90° corresponds to complete attenuation. The final TFP acts to clean the polarisation of the transmitted light. The final polarisation of the laser pulse is controlled by sending the beam through a further HWP and a quarter waveplate (QWP) prior to introduction into the reaction chamber.

The combination of low photon energy (1.17 eV) and long pulse duration relative to the molecular rotational period ($\tau_{\text{YAG}} \gg T_{\text{rot}}$) makes these laser pulses ideal for adiabatically aligning [9] the target molecules prior to interaction with the femtosecond pump and probe laser pulses.

2.3.6 Femtosecond Laser System

The femtosecond laser system is based upon the output of a regenerative, chirped pulse amplified Ti:Sapphire laser comprising two main parts: an oscillator and an amplifier. The oscillator (Spectra-Physics, Tsunami) is pumped by the intra-cavity doubled output of a diode pumped Nd:YVO₄ cw laser (Spectra-Physics, Millennia V), providing an energy of >5 W at 531 nm. The Ti:Sapphire oscillator generates sub-100 fs pulses at a peak wavelength of 800 nm through Kerr lens mode-locking [10] at a repetition rate of 82 MHz, giving a pulse energy of <10 nJ.

The output of the oscillator passes into a Ti:Sapphire amplifier (Spectra-Physics, Spitfire-HPR) operating at 1 kHz, where it is regeneratively amplified in an optically excited Ti:Sapphire crystal. The amplification crystal is excited by the output of a 1 kHz Q-switched Nd:YFL laser (Coherent, Evolution-30) and provides amplification to energies of approximately 20 mJ at a wavelength of 527 nm. The repetition rate of the Nd:YFL laser limits the repetition rate of the amplification system to 1 kHz. Pulses entering the Ti:Sapphire amplifier are temporally stretched by positive Group Velocity Dispersion in a grating stretcher to avoid damaging the amplifier optics and must therefore be recompressed upon exiting the amplifier system. Recompression is achieved through a grating compressor, resulting in a final output of pulses with a peak wavelength of 800 nm, and a pulse energy of up to 2.3 mJ, at a repetition rate of 1 kHz. The amplifier output is then split into several beam lines by beam splitters, two of which are used for the pump (kick) and probe beam lines described in the following sections.

2.3.6.1 Kick Pulse

The first femtosecond beam line (~ 600 mJ) is used to initiate torsional motion in the aligned biphenyl molecules. The 130 fs pulse duration produced by the Ti:Sapphire amplifier is sufficiently short compared to the torsional period of the biphenyl molecules (~ 1.2 ps) that it acts impulsively to induce coherent torsional motion across the ensemble of target molecules. In order that the time delay between the kick pulse and the probe pulse may be accurately controlled, the kick pulse is directed through a computer-controlled delay stage (Micos, LS-110). A HWP allows for control of the linear polarisation of the kick pulse. The power of the kick pulse is kept sufficiently low such that ionisation and subsequent Coulomb explosion of the target molecules is very unlikely.

2.3.6.2 Probe Pulse

The second femtosecond beam line is used to probe the molecular structure of the biphenyl target molecules through Coulomb explosion. In order that the deformation of the molecular skeleton is minimised on the timescale of multiple ionisation, the probe pulse must be short compared to the timescales of molecular motion. For this reason, it is necessary to temporally compress the probe pulse duration from the 130 fs output of the Ti:Sapphire amplifier. Compression also has the effect of increasing the intensity of the probe pulse, which is another prerequisite for achieving Coulomb explosion of the target molecules. The compression of the probe pulse is achieved in a two-step process. First, the beam is focussed by an $f = 60$ cm lens into an argon-filled hollow core fibre mounted within a plexiglass tube at an overpressure of ~ 1.3 bar. As the pulse travels through the hollow-core fibre, the process of self-phase modulation [10] causes the broadening of the spectral bandwidth of the pulse from ~ 10 to ~ 50 nm. Upon leaving the hollow-core fibre the beam is recollimated by an $f = -100$ cm concave lens. The second step involves the temporal compression of the spectrally broadened pulse. This is achieved by passing the beam through a prism compressor, providing flat-phase pulses with a temporal width of 30 fs. Once focussed into the reaction chamber, the beam provides peak intensities of up to $5 \times 10^{14} \text{ W cm}^{-2}$, which is sufficient to induce Coulomb explosion of the target molecules. Before reaching the reaction chamber, the probe beam is passed through a HWP, allowing for control of the linear polarisation of the pulse.

2.3.7 Reagent Source

Gas phase samples of both 3,5-dibromo-3',5'-difluoro-4'-cyanobiphenyl ($\text{C}_{13}\text{H}_5\text{F}_2\text{Br}_2\text{N}$, DBrDFCNBph) and 3,5-dibromo-3',5'-difluoro-4-cyanobiphenyl ($\text{C}_{13}\text{H}_5\text{F}_2\text{Br}_2\text{N}$, DFDBrCNBph) were formed by heating less than 50 mg of solid sample to 170°C in a high pressure atmosphere (90 bar) of helium within the internal sample reservoir of the Even-Lavie valve. Both chemicals are commercially unavailable and were synthesised specially for the experiment (for the procedure see the Appendix in Ref. [11]). It should be noted that the purity of DFDBrCNBph ($\sim 99\%$) was determined to be superior to that of the isomer DBrDFCNBph ($\sim 95\%$). The major contaminant found in the sample of DBrDFCNBph was identified as the byproduct in which both phenyl rings are F-substituted. Despite the higher vapour pressure of the impurity relative to that of DBrDFCNBph, it was not observed as a major contaminant in the ion images recorded. This is likely due to the larger deflection of the impurity by the electrostatic deflector causing its concentration in the interaction region to fall below detectable levels.

2.4 Velocity-Map Image Analysis

In a typical velocity-map ion imaging experiment, the three-dimensional product fragment Newton-sphere is projected onto a two-dimensional detector and the signal integrated over the time-of-flight coordinate. What results, therefore, is a two-dimensional projection of the full three-dimensional photofragment velocity distribution. Chapter 3 of this thesis explores an alternative approach to a variant of ion imaging that allows slices through the product fragment Newton-sphere to be extracted directly from the experiment, but in the more general case it is often necessary to invert the resulting two-dimensional image to recover the unintegrated velocity distribution of the nascent photofragments. The following sections provide a brief overview of the various approaches that have been developed to address this problem.

Inverse Abel Transform

In the case of cylindrical symmetry, the most common approach to the problem of image inversion is to perform an inverse Abel transform [12] of the data to extract a representation of the meridional slice of the Newton-sphere. If $P(x, z)$ is the two-dimensional projection of the three-dimensional distribution $I(r, z)$ on the detector plane (x, z) then the two are related by the Abel integral [13],

$$P(x, z) = 2 \int_{|x|}^{\infty} \frac{r I(r, z)}{\sqrt{r^2 - x^2}} dr. \quad (2.1)$$

The quantity of interest is the laboratory frame distribution $I(r, z)$, which can in theory be evaluated from $P(x, z)$ by the inverse Abel transform [14],

$$I(r, z) = -\frac{1}{\pi} \int_r^{\infty} \frac{[dP(x, z)/dx]}{\sqrt{x^2 - r^2}} dx. \quad (2.2)$$

While Eq. 2.2 describes precisely the relationship between the projected and laboratory frame distributions, it is unfortunately numerically impractical to handle directly. The most commonly used approach for solving the inverse Abel transformation is the Fourier-Hankel reformulation [15]. Unfortunately, the Fourier-Hankel method is notoriously sensitive to noise, which collects towards the central line of the reconstructed image, degrading the fidelity of the image inversion. A further issue is encountered when using the Fourier-Hankel method to reconstruct images that contain sharp, intense features, as these are often found to leave false artefacts in the inverted images, which are dependent on the exact Fourier-Hankel formulation employed.

Alternative Approaches

An alternative to the inverse Abel transformation is the onion-peeling method [16], which inverts the image by treating the photofragment distribution as a series of concentric spheres. The algorithm proceeds by iteratively removing the contributions

from each ‘layer’ in turn, starting from the largest kinetic energy and progressively working towards the centre of the image. While relatively straightforward to implement and computationally inexpensive, this approach often leads to an overestimation of the contribution made by the fastest particles and is prone to cumulative error problems. For this reason, the experimental ion images are typically smoothed using a suitable algorithm before the Abel inversion is performed.

Rather than inverting the experimentally acquired ion images, the method of Vrakking [17] relies on a forward convolution of an assumed photofragment velocity distribution, which is then compared to the experimental data. The initial assumed distribution is iteratively refined until an acceptable agreement between the fitted image and the experimental image is achieved. This method introduces significantly less noise than the Abel inversion and onion-peeling methods, and has the advantage that the noise accumulates towards the centre of the image, rather than down the axis of polarisation, due to the polar formulation of the method. The obvious disadvantage is that some prior knowledge of the distribution is must be assumed for the fit to converge at an acceptable speed.

pBASEX

Perhaps the most successful approach to image inversion is that of Powis et al. [18], who have developed a method of solving the Abel inversion problem by fitting a set of radial forward basis functions that correspond to analytical inverse Abel transforms. The method is a reformulation in polar coordinates of the method of Dribinski et al. [19] and relies on fitting the kinetic energy distribution with a discrete number of Gaussian functions of a given width, σ . Within this approximation, the laboratory frame distribution may be described by

$$I(r, z) = \sum_{k=0}^{k_{max}} \sum_{l=0}^{l_{max}} c_{kl} f_{kl}(R, \Theta), \quad (2.3)$$

with

$$f_{kl}(R, \Theta) = e^{-(R-R_k)^2/\sigma} P_l(\cos \theta), \quad (2.4)$$

where θ is measured with respect to the axis of cylindrical symmetry, P_l is the Legendre polynomial of order l , and R_n represents the mean radius of the n th radial Gaussian function. The method relies on fitting the experimental image to the Abel integrated versions of these basis functions to yield the radial and angular distributions of the nascent photofragments in the laboratory frame. As is also the case for the forward convolution method of Vrakking, the noise accumulates towards the centre of the inverted image, which is usually unimportant in image analysis. This method is known as pBASEX (polar basis set expansion), and is the primary image inversion algorithm used in the processing of the ion images presented in this thesis.

2.5 The PImMS Camera

Central to the work presented in this thesis is the Pixel Imaging Mass Spectrometry (PImMS) Camera [20]. The device has been developed by a collaboration between research groups based in the Departments of Chemistry and Physics at the University of Oxford, and researchers working at the Rutherford Appleton Laboratory (RAL) in Harwell, Oxfordshire. The camera is a time stamping device based upon a complementary metal-oxide-semiconductor (CMOS) sensor incorporating novel INMAPS technology [21]. The device used in the work presented in this thesis was fitted with the prototype PImMS1 sensor, which has a resolution of 72×72 pixels. A second generation sensor (PImMS2) with a resolution of 324×324 pixels is currently in testing and will be available for experiments in the near future. This section describes the architecture, performance, and characterisation of the PImMS camera, preceded by a brief discussion of the principles behind CMOS and INMAPS technology.

2.5.1 CMOS Technology

Complementary metal-oxide-semiconductor (CMOS) technology was first developed in the 1960s and has since become very popular in a broad range of semiconductor applications. CMOS technology is found in a variety of imaging technologies, with applications in particle and nuclear physics [22, 23], X-ray medical imaging [24], electron microscopy [25], commercial digital cameras, and more recently in a variety of imaging mass spectrometry applications [26, 27]. The technology of monolithic active pixel sensors (MAPS) using CMOS technology has been advancing rapidly over recent years, with the notable development of INMAPS, where the ‘IN’ prefix stands for ‘Isolated N-well’. CMOS offers several advantages over the more conventional charge-coupled device (CCD) technologies traditionally employed in the manufacture of digital imaging sensors, such as reduced cost and power consumption. However, the principal advantage of CMOS over CCD technology for scientific applications lies in the ability of CMOS to support a large number of transistors on each pixel, providing valuable logic and processing power local to the light collection diodes.

2.5.1.1 INMAPS

Figure 2.6 illustrates the principles of MAPS and INMAPS [21] CMOS technologies. In each case the CMOS wafer consists of a P-doped epitaxial layer supported on a P-doped substrate. Incident charged particles or photons create electron-hole pairs in the P-doped epitaxial layer, which act as minority carriers. The photoelectrons migrate to the N-doped diodes at the surface of the epitaxial layer, where they are collected. Since the photoelectrons are repelled by the small potential created at the

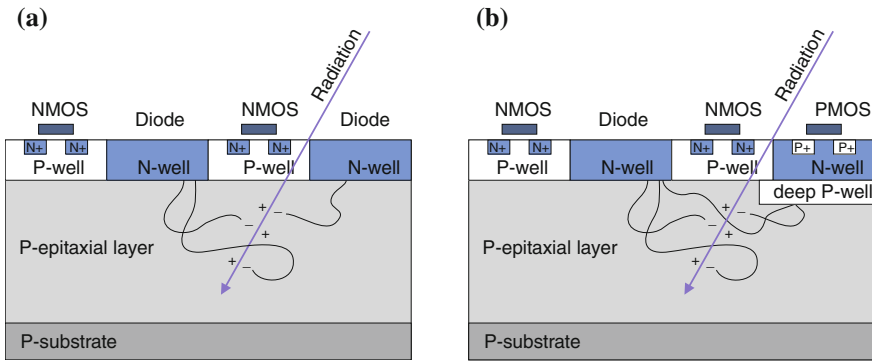


Fig. 2.6 Diagram illustrating how radiation is detected by MAPS and INMAPS CMOS sensors. In the MAPS sensor, charge is collected by all N-type wells, limiting logic to NMOS transistors only. In the INMAPS sensor, the N-wells are shielded from the charge carriers in the P-epitaxial layer by a deep P-implant, allowing PMOS transistors to be included on the surface of the pixel. **a** MAPS. **b** INMAPS

junction between differently doped P-substrates, a 100% collection efficiency by the diodes should be expected, provided the lifetime of the electron-hole pairs is long enough for them to diffuse to the P-N junction. A 100% collection efficiency will, however, only be possible if the P-N junctions present in the pixel are exclusively those between the diodes and the P-epitaxial layer. This condition necessarily limits the electronics in the pixel to exclusively N-type (NMOS) transistors, significantly reducing the complexity of electronic processing that can occur on the pixel. INMAPS technology solves this problem of parasitic charge collection by P-type (PMOS) transistor supporting N-wells by inserting deep P-wells to shield the N-wells from the P-doped epitaxial layer. This allows the presence of both NMOS and PMOS transistors on the surface of the sensor, vastly increasing the electronic processing potential of each pixel in the monolithic array without reducing the charge collection efficiency.

2.5.2 PImMS Pixel Architecture and Functionality

The PImMS1 sensor comprises an array of 72×72 pixels, each with dimensions of $70 \times 70 \mu\text{m}$, surrounded by the associated configuration and readout circuitry around the periphery of the chip. The sensor is mounted in a camera housing and light focussed onto the pixels using a commercial camera lens affixed to the camera body faceplate by either an F- or C-mounting fixture. The camera works on the principle of ‘time stamping’, wherein pixels independently record and store the value of an internal timer whenever an event with an intensity greater than a predetermined threshold level occurs. Each event recorded by the camera is therefore stored as a set of coordinates in x, y, t space, resulting in a compact data set containing the same

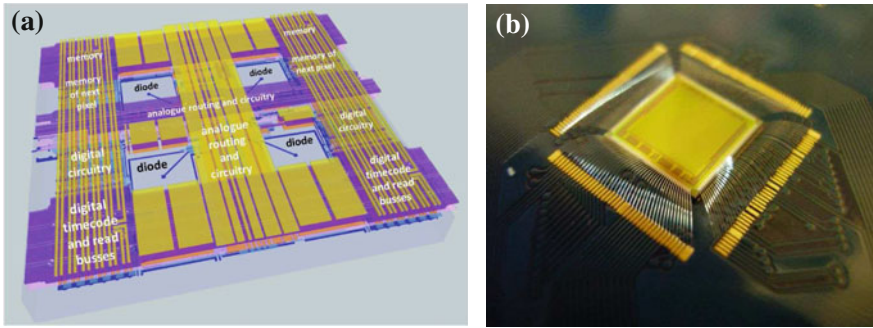


Fig. 2.7 Panel **a** shows the PImMS pixel architecture, showing the four charge collection photodiodes and the supporting circuitry. Panel **b** shows a photograph of a PImMS sensor bonded to the sensor board. Adapted from Ref. [20]

information as afforded by frame-based imaging. This efficient approach to event-based image acquisition is made possible by the considerable processing power of each pixel. Each PImMS pixel contains over 600 individual transistors, a remarkably high number only permitted by the incorporation of INMAPS technology.

The pixel architecture is illustrated in Fig. 2.7, alongside a photograph of a complete PImMS1 sensor comprising an array of 72×72 such pixels and the associated circuitry. Light is collected by four photodiodes contained within each pixel, corresponding to an active area of 16.9%. The remaining area of the pixel is occupied by the necessary onboard circuitry, which blocks the transmission of light to these regions.

Figure 2.8 shows a schematic of the pixel circuitry, illustrating the operation of the PImMS sensor. At the start of each acquisition cycle, an internal global 12-bit timer is triggered. The 12-bit timer permits the experimental period to be divided into 4095 equal time slices of width ≥ 12.5 ns. The value of zero is reserved to signify the absence of signal throughout the acquisition window. When a flux of photons from the phosphor screen impacts on a pixel, charge is collected by the four photodiodes, which is passed to an integrating pre-amplifier. The analogue signal is read out at this stage and integrated to give a measure of the total signal recorded by the pixel over the course of the acquisition window. A CR-RC shaper then produces two pulses representing the signal in differential form, which are passed to a comparator trim block. Since each pixel in the PImMS sensor is independent, each has a slightly different photon response curve. In order to provide a more consistent sensitivity over the whole sensor array, the response curve of each pixel may be shifted by four trim bits, allowing for 16 possible steps of adjustment. The comparator trim block applies this trim and thresholds the signal. The signal is then passed to a comparator, which determines whether an event over threshold has occurred. Positive events are then processed by the digital control logic, which stores the time code of the 12-bit global timer in one of four in-built 12-bit memory registers. At the end of an acquisition cycle, the data are read out from the memory buffers of the pixels and

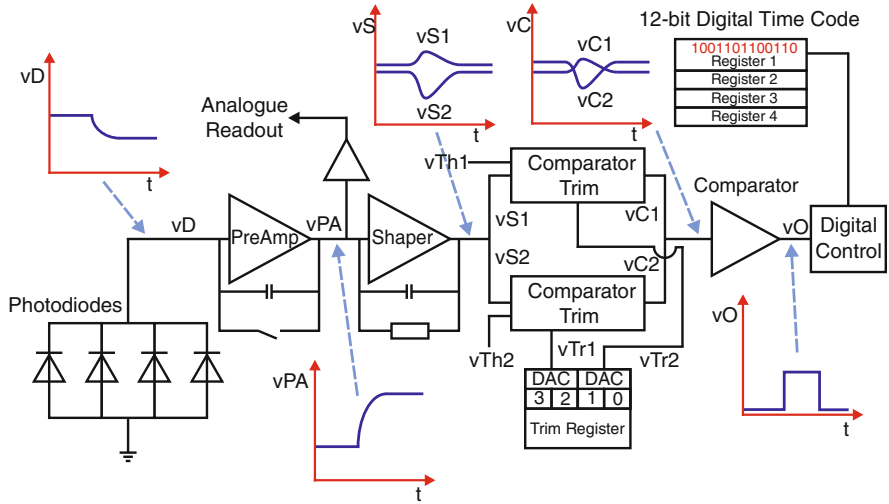


Fig. 2.8 Schematic of the PImMS pixel circuitry. See text for details

transferred to a PC via a USB 2.0 connection, where they are processed by custom built software (aSpect Systems). The data are stored as a list of events, with the data comprising the x - and y -coordinates of the pixel, the value of the 12-bit timer when the event was recorded, the acquisition cycle number, and the number of the register in which the event time stamp was stored. The PImMS1 camera repetition rate is limited by the USB data readout to a maximum of 550 Hz.

The data presented in this thesis were recorded using the PImMS1 sensor, which was designed as a prototype device and has a relatively modest pixel resolution when compared to conventional CCD cameras. The second generation (PImMS2) sensor has been developed during the course of this thesis and is currently undergoing testing. The PImMS2 sensor has a 324×324 pixel array and offers a more precise calibration of the pixel-to-pixel sensitivity than the PImMS1 sensor through a more consistent trim response.

2.5.3 Post-Processing

The PImMS camera interfaces with a velocity-map ion imaging experiment by collecting signal in the form of photon flux from the phosphor screen. The performance of the device is therefore intrinsically related to the operating parameters of the MCP-phosphor detector, which must be optimised to yield the highest quality experimental data.

Each ion event, amplified by the MCPs, results in a cascade of electrons hitting the phosphor screen, causing a flash of light, which is detected by the PImMS camera.

Each flash on the phosphor screen typically illuminates several pixels, resulting in a cluster of pixels corresponding to each ion detected. The intensity profile of each flash on the phosphor screen is expected to be somewhat Gaussian, with a higher brightness towards the centre of the cluster, where the highest density of electrons impact upon the phosphor, and dimmer towards the edges of the cluster. For an event to be recorded, the charge build-up within the diodes of an individual pixel must be sufficient to exceed an externally chosen threshold value. Pixels that lie towards the centre of a cluster will be subject to a higher photon flux, and should therefore be expected to go over threshold at an earlier time than those towards the edge of a cluster. Since the earliest pixel can detect an ion event is the actual time of the ion hit on the detector, the earliest time codes present within a cluster are necessarily the most accurate.

2.5.3.1 Centroiding

With these considerations in mind, the PImMS data were post-processed to reduce each cluster down to a single pixel and a single time code, a process known as centroiding. The centroiding algorithm identifies clusters through eight-fold connectivity (8 nearest neighbours), and determines the coordinate of the cluster centre through a weighted average of the coordinates of each pixel belonging to the cluster. The weighting factor for each pixel is determined by the time code of the event recorded, with earlier time codes corresponding to a larger weighting factor. In this way, the time code information is used as a surrogate for the absent intensity information. The event coordinate is given by

$$C = \frac{\sum_{i=1}^N r_i t_i^{-1}}{\sum_{i=1}^N t_i^{-1}}, \quad (2.5)$$

where r_i is the coordinate of the i th pixel and t_i is the time of the event, given by

$$t_i = T_i - T_0 + 1, \quad (2.6)$$

where T_i is the time code of the event and T_0 is the time code of the earliest event recoded in the cluster.

Since recorded events occur with both a two-dimensional Cartesian coordinate and a time code, limits must be placed on the maximum temporal range of the events contributing to each cluster. The processing algorithm searches the data for events by working through the time codes sequentially from the first to the last. When an event is identified, the algorithm searches for further events spatially connected to the seed pixel by eight-fold connectivity and within a predefined number of time codes after the seed event, known as the ‘time window’. If further events fulfilling

these conditions are found, the algorithm continues to extend the search in the spatial domain using eight-fold connectivity, but retains the same limits on the maximum temporal range explored. When the algorithm fails to identify further events satisfying the required conditions of connectivity, the event coordinate is calculated using Eq. 2.5, and the time code of the event is taken to be T_0 . Since the event coordinate is a non-integer value, it is possible to bin the events into a pixel array of greater fineness than that of the original sensor, thereby increasing the effective resolution of the device. This approach is known as ‘megapixeling’.

2.5.3.2 Cluster Characterisation

In order to optimise the centroiding algorithm, it was necessary to characterise the data recorded by the PImMS camera. Figure 2.9 compares data from several otherwise identical experiments, in which the MCP gain was kept constant and the phosphor voltage varied. The voltage across the MCPs was kept at 1750 V, with the voltage between the back face of the MCPs and the phosphor screen taking values in the

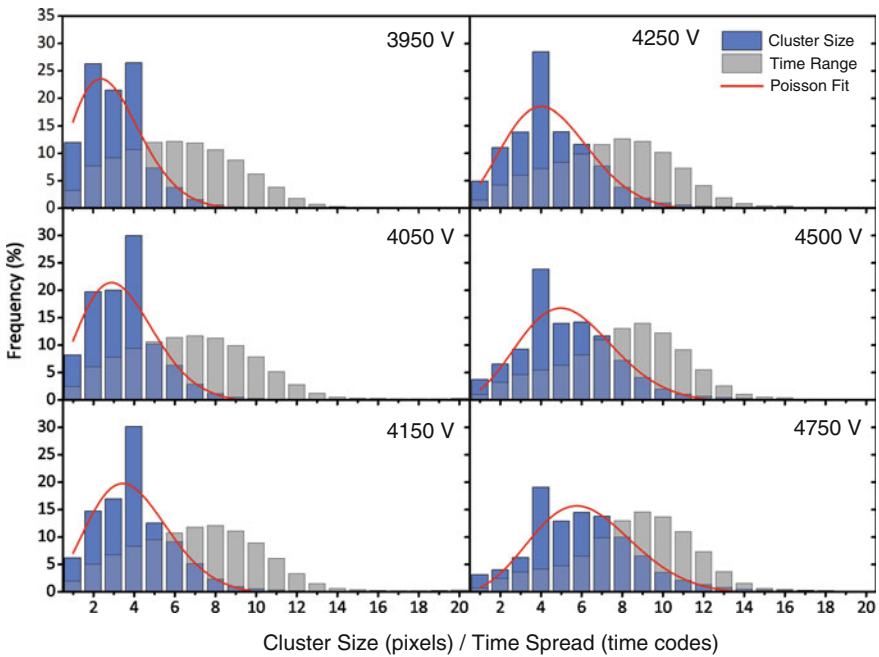


Fig. 2.9 Histograms of the cluster size (*blue bars*) and the range of time codes present within a cluster (*grey bars*) for various phosphor screen voltages. The MCPs were operated with a potential of 1750 V across the two plates. The time spread is calculated as $T_{\max} - T_0 + 1$, where T_{\max} is the latest time code and T_0 the earliest time code present in a cluster. The *red curves* are Poisson fits to the cluster size data

range 2200–3000 V. The ions detected are from the Coulomb explosion of a biphenyl molecule (see Chap. 6) and were accelerated by a potential of 7500 V applied to the repeller electrode. The data show that as the voltage bias between the MCPs and the phosphor is increased the average cluster size also increases. The general distribution in each case may be modelled reasonably well by Poisson statistics (red curves), as should be expected for a largely statistical process. Deviations from Poisson statistics are caused by averaging over a large fragment mass range ($m = 1\text{--}80\text{ Da}$), and the sampling of approximately circular phosphor flashes on a square pixel array. The latter effect is particularly pronounced for clusters of 4 pixels in size, which are significantly over-represented in the data. This is thought to be caused by the favourable overlap between a circular phosphor flash and a 2×2 pixel cluster.

Characterising the range of time codes present within a typical cluster is crucially important to the effective implementation of the centroiding algorithm. Figure 2.9 demonstrates that the maximum time range remains almost constant across all operating voltages at approximately 15 time codes (187.5 ns), with the distribution peaking towards higher values as the phosphor voltage increases. The observed time range is reasonably consistent with the decay lifetime of a P47 phosphor screen ($\sim 70\text{ ns}$ [28]). This result suggests that it should be possible to apply a universal time window to the centroiding algorithm as the time range is characteristic to the camera, and not to the operating voltages of the detector.

The data in Fig. 2.9 suggest that a time window of 15 time codes should be sufficient to capture all pixels within the majority of clusters. To test this assertion, data from the Coulomb explosion of a biphenyl molecule were processed through the centroiding routine with different time windows applied. The resulting time-of-flight spectra are shown in Fig. 2.10. The data illustrate the two conflicting pressures on the centroiding algorithm: firstly, that the time window must be long enough that it is unlikely that any pixels belonging to a cluster fall beyond the maximum time code permitted, and secondly, that the time window is not so long as to cause a significant number of pixels belonging to later, distinct events becoming included in earlier clusters. Using a time window that is too short results in ‘ghost peaks’ appearing in the time-of-flight spectrum. These ghost peaks are caused by the trailing events within a cluster being missed by the algorithm and therefore being counted as separate clusters in their own right. This effect can be seen in the time-of-flight spectra processed with time windows of 10 and 15 time codes in Fig. 2.10. The ghost peaks are most pronounced following the most intense signals in the spectrum, and occur at a time afterwards corresponding to the length of the time window. These ghost peaks therefore move in the time-of-flight spectrum, depending on the length of the time window used, and are therefore easily identified. Conversely, if the time window used is too long, larger peaks in the time-of-flight spectrum have a parasitic effect on those that follow. This effect can be seen in the time-of-flight spectrum corresponding to a time window of 30 time codes in Fig. 2.10, in which the peak at approximately time code 455 is reduced in intensity due to the shadowing by the

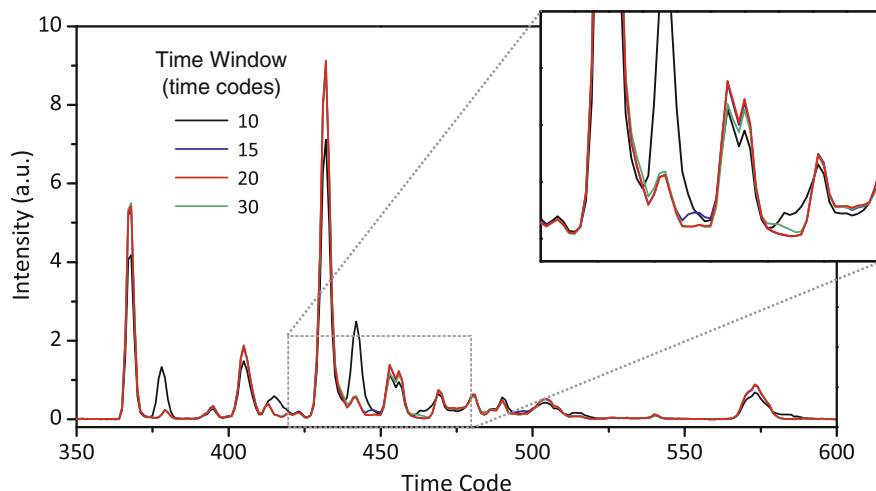


Fig. 2.10 Time-of-flight traces following data processing using various ‘time windows’ in the centroiding algorithm, measured in 12.5 ns PIMMS time codes. The time-of-flight spectrum is that recorded following Coulomb explosion of a substituted biphenyl molecule, as described in detail in Chap. 6. See text for details

intense signal centred on time code 430. After a careful analysis of the data, it was found that a time window of 20 time codes resulted in the optimum performance of the centroiding algorithm.

2.5.3.3 Centroiding Performance

Figure 2.11 illustrates the image processing scheme. The improvement in image resolution upon centroiding is clear, with each of the centroided images displaying a marked improvement compared to the raw data. Figure 2.11 also demonstrates the effect of megapixelising the data. It is clear that centroiding events to a pixel array with twice the original sensor dimensions does indeed afford an improvement in the spatial resolution. However, increasing the size of the pixel array beyond twice that of the original sensor does not seem to be beneficial as regular patterns begin to appear in the images. The arrows in Fig. 2.11 illustrate the processing scheme used for the images presented in Chaps. 3 and 4 of this thesis. The data are first centroided and the events binned to a pixel array with twice the dimensions of the original sensor (144×144). The centroided images are then centred and symmetrised appropriately along the horizontal and vertical axes ready for image analysis.

The images presented in this thesis that were recorded following the Coulomb explosion of substituted biphenyl target molecules (Chaps. 6 and 7) were not megapixelised or symmetrised due to the broader features of the ion images and the tendency of the fastest ions to overspill the detector in an asymmetric fashion. Instead, the data were centroided onto a 72×72 pixel array and the resulting images

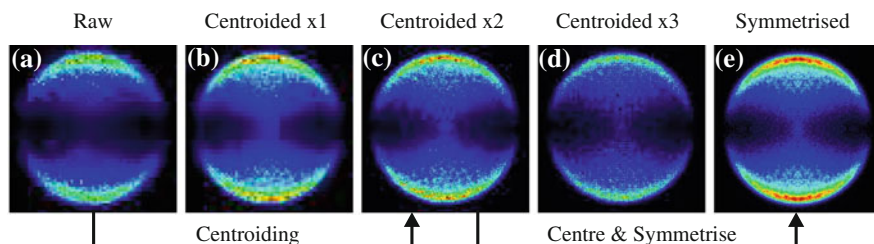


Fig. 2.11 Panel a shows a raw image of the I^+ ions resulting from the photodissociation of EtI at 245.36 nm (see Chap. 3 for details). Panels b–d show the centroided data binned into pixel arrays with dimensions of $1\times$, $2\times$, and $3\times$ that of the original sensor, respectively. Panel e shows the data in Panel c after centring and symmetrisation along the horizontal and vertical axes

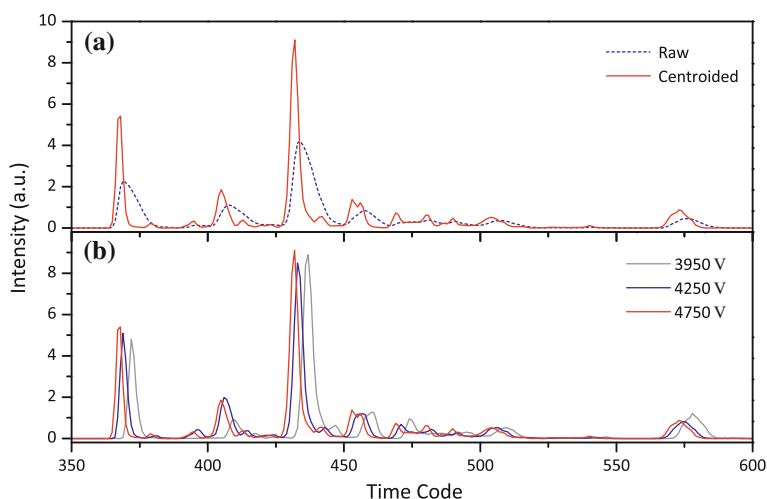


Fig. 2.12 Panel a compares the raw time-of-flight trace with that following centroiding of the data. Panel b compares the centroided time-of-flight spectra collected using three different phosphor voltages. The time-of-flight spectrum is that recorded following Coulomb explosion of a substituted biphenyl molecule, as described in detail in Chap. 6

smoothed using a moving average of the 9×9 cluster centred on the pixel of interest in order to reduce the effects of incomplete data convergence and the variable pixel-to-pixel sensitivity of the PImMS sensor.

Panel (a) of Fig. 2.12 illustrates the effect of the centroiding algorithm on the time-of-flight information. The time-of-flight spectrum shown is that recorded following the Coulomb explosion of a biphenyl molecule, which is described in detail in Chap. 6. The broken blue trace shows the time-of-flight spectrum obtained by integrating over all pixels before post-processing, whereas the red trace shows the time-of-flight spectrum after post-processing. The improvement in the sharpness of the spectrum upon post-processing is striking; the broad features in the raw data are reduced to well-resolved mass peaks, with the full 12.5 ns time-resolution of the internal clock being utilised.

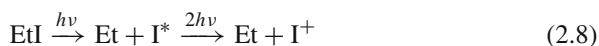
Panel (b) of Fig. 2.12 demonstrates the varying performance of the centroiding algorithm when using different phosphor voltages, while maintaining the same gain over the MCPs. In each case a voltage of 1750 V was applied across the MCPs, with a potential of 2200 V (grey), 2500 V (blue), and 3000 V (red) maintained between the MCPs and the phosphor screen. Upon increasing the voltage applied to the phosphor screen, the time-of-flight spectrum shifts to earlier time codes and noticeably sharpens. This is due to the increased brightness of the flashes produced by the phosphor screen upon increasing the kinetic energy of the electrons from the MCPs, which results in the threshold value of the PImMS pixels being exceeded at an earlier, and more accurate, time code. In order to maximise the time-resolution of the data, the detector was generally operated under conditions of high gain when interfaced with the PImMS camera.

2.5.4 Characterisation and Performance

The PImMS camera interfaces with a VMI spectrometer by simply replacing the standard CCD camera conventionally used to record images. While the PImMS camera significantly enriches the data available, the prototype PImMS1 sensor suffers from a relatively modest pixel resolution when compared to conventional CCD cameras. With this in mind, experimental images were recorded with both the PImMS1 camera and a conventional CCD camera (Photonic Science, 576×768 pixels), and the parameters extracted from the images compared.

2.5.4.1 Photodissociation of Ethyl Iodide at Around 245 nm

At around 245 nm, direct photodissociation is observed via the A band to form atomic iodine in either the ground ($^2P_{3/2}$) or first excited ($^2P_{1/2}$) electronic states [29]. The ground and excited state atomic photofragments may subsequently become ionised via either a three- or two-photon process, respectively, to form I^+ ions:



Alternatively, EtI molecules excited to the A band may absorb a further photon, resulting in parent ionisation. Absorption of a further photon at the same wavelength results in bond fission to form neutral Et fragments and I^+ ions:



At 245.00 nm the ion image consists of two principal components: a broad hourglass-shaped feature towards the centre of the image, and a narrower ring at higher

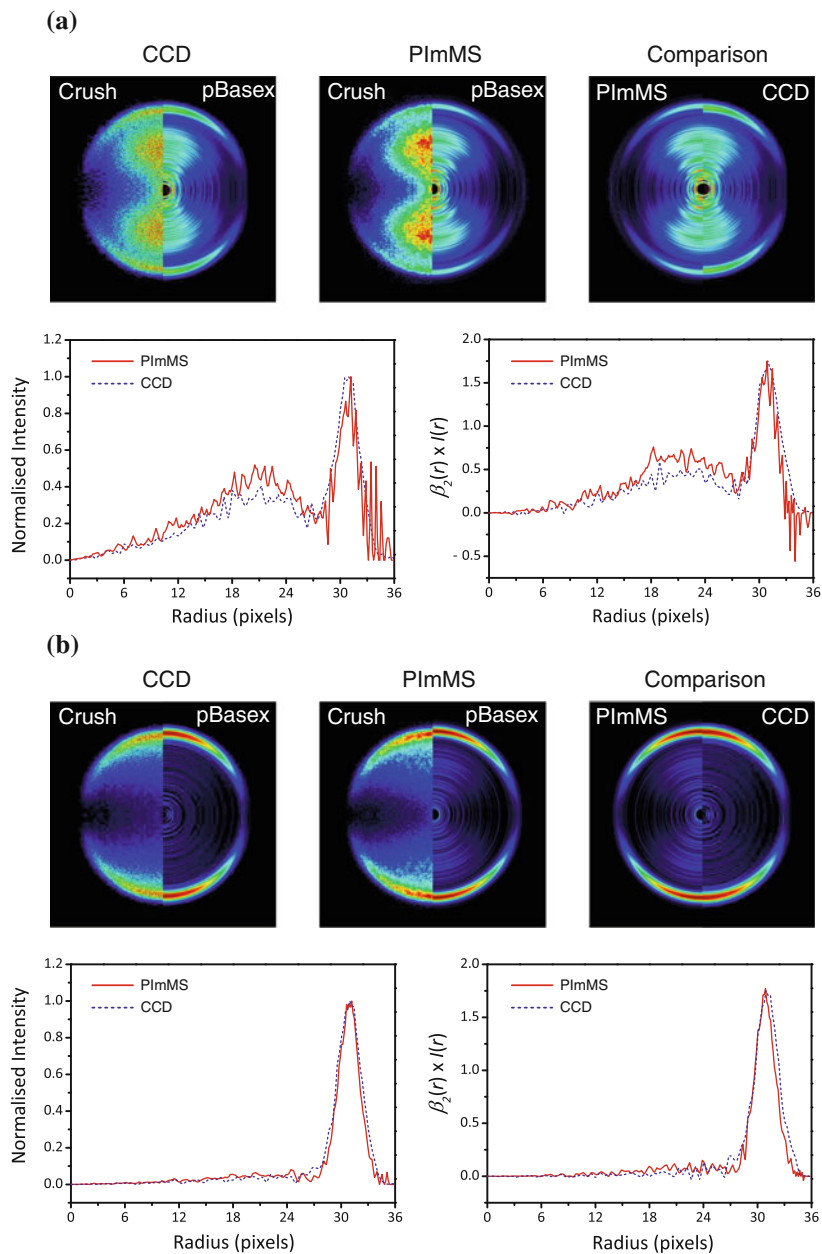


Fig. 2.13 A comparison of the ion images recorded using the PImMS camera and a conventional CCD camera following the photodissociation of ethyl iodide at 245.00 and 245.36 nm. From *left to right*, the images presented are those recorded using the conventional CCD camera, the PImMS camera, and a comparison of the pBASEX inverted images collected using the two devices, as labelled. Beneath the images are the corresponding speed (*left*) and weighted anisotropy parameters (*right*), extracted using the pBASEX image inversion algorithm. See text for further details. **a** 245.00 nm. **b** 245.36 nm

fragment velocities (see Fig. 2.13). The sharp ring corresponds to two-photon ionisation of I^* photofragments resulting from the photodissociation of ethyl iodide via the A band (Eq. 2.7). The broad hourglass-shaped feature at lower fragment velocities has been assigned by Tang et al. [29] to dissociative ionisation of the parent molecule (Eq. 2.9). Ionisation of the ground state atomic iodine fragments produced following dissociation of ethyl iodide via the A band is not observed as this requires the absorption of a further photon, which is uncompetitive at the pulse energies used in these experiments.

At 245.36 nm a significant enhancement of the outer ring is observed, causing it to dominate the ion image. Since there are no resonant transitions from either the ground or first excited states of atomic iodine at this wavelength, this is proposed to be caused by a two-photon resonance from the I^* level to an auto-ionising electronic state, causing a significant enhancement of the ionisation probability of the excited state atomic iodine photofragments:

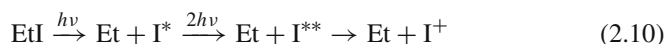


Figure 2.13 compares the images, velocity distributions, and anisotropy parameters measured at both 245.00 and 245.36 nm. The speed distribution and anisotropy parameters were extracted using the pBASEX algorithm, as described in Sect. 2.4. It should be noted that the anisotropy parameter (β_2) has been multiplied by the normalised speed distribution in order to enhance the important features. The parameters extracted from both cameras are in good agreement. This result is perhaps surprising when it is noted that the pixel count of the CCD camera is almost two orders of magnitude greater than that of the PImMS1 sensor. The images taken at 245.36 nm are in almost perfect agreement, with the speed and angular parameters measured by the two devices almost indistinguishable from one another. The agreement at 245.00 nm is once again very strong, with a slightly different relative intensity of the features corresponding to the two product channels. This difference can be attributed to the fluctuating laser power in the experiment, causing differential enhancement of the two channels, and is not thought to be caused by any differences between the two cameras.

References

1. A. Johnsen, Ion imaging, applications and extensions. Ph.D. thesis, University of Oxford (2010)
2. P. Richharia, *Sol. Energ. Mater.* **20**, 199 (1990)
3. M. Krems, J. Zirbel, M. Thomason, R.D. DuBois, *Rev. Sci. Instrum.* **76**, 093305 (2005)
4. U. Even, J. Jortner, D. Noy, N. Lavie, C. Cossart-Magos, *J. Chem. Phys.* **112**, 8068 (2000)
5. M. Hillenkamp, S. Keinan, U. Even, *J. Chem. Phys.* **118**, 8699 (2003)
6. F. Filsinger, J. Kpper, G. Meijer, L. Holmegaard, J.H. Nielsen, I. Nevo, J.L. Hansen, H. Stapelfeldt, *J. Chem. Phys.* **131**, 064309 (2009)
7. G.E. Chamberlain, J.C. Zorn, *Phys. Rev.* **129**, 677 (1963)

8. J.L. Hansen, Imaging molecular frame dynamics using spatially oriented molecules. Ph.D. thesis, Aarhus University (2012)
9. H. Stapelfeldt, T. Seideman, *Rev. Mod. Phys.* **75**, 543 (2003)
10. C. Rulliere, *Femtosecond Laser Pulses: Principles and Experiments*, 2nd edn. (Springer, New York, 2004)
11. J.L. Hansen, J.H. Nielsen, C.B. Madsen, A.T. Lindhardt, M.P. Johansson, T. Skrydstrup, L.B. Madsen, H. Stapelfeldt, *J. Chem. Phys.* **136**, 204310 (2012)
12. B.J. Whitaker, *Imaging in Chemical Dynamics* (Oxford University Press, Oxford, 2000)
13. F.B. Hildebrand, *Methods of Applied Mathematics* (Prentice-Hall, Englewood Cliffs, 1952)
14. R.N. Bracewell, *The Fourier Transform and its Applications* (McGraw-Hill, New York, 1978)
15. L.M. Smith, D.R. Keefer, S.I. Sudharsanan, *J. Quant. Spectrosc. Radiat. Transf.* **39**, 367 (1988)
16. S. Manzhos, H.-P. Looock, *Comput. Phys. Commun.* **154**, 76 (2003)
17. M.J.J. Vrakking, *Rev. Sci. Instrum.* **72**, 4084 (2001)
18. G.A. Garcia, L. Nahon, I. Powis, *Rev. Sci. Instrum.* **75**, 4989 (2004)
19. V. Dribinski, A. Ossadtchi, V.A. Mandelshtam, H. Reisler, *Rev. Sci. Instrum.* **73**, 2634 (2002)
20. J.J. John, M. Brouard, A. Clark, J. Crooks, E. Halford, L. Hill, J.W.L. Lee, A. Nomerotski, R. Pisarczyk, I. Sedgwick, C.S. Slater, R. Turchetta, C. Vallance, E. Wilman, B. Winter, W.H. Yuen, *JINST* **7**, C08001 (2012)
21. J.A. Ballin, J.P. Crooks, P.D. Dauncey, A.-M. Magnan, Y. Mikami, O.D. Miller, M.N., V. Rajovic, M. Stanitzki, K. Stefanov, R. Turchetta, M. Tyndel, E.G. Villani, N.K. Watson, J.A. Wilson, *Sensors* **8**, 5336 (2008)
22. K. Arndt, G. Bolla, D. Bortoletto, K. Giolo, R. Horisberger, A. Roy, T. Rohe, *Nucl. Instrum. Methods Phys. Res. A* **511**, 106 (2003)
23. C. Gemme, *Nucl. Instrum. Methods Phys. Res. A* **501**, 87 (2003)
24. S.E. Bohndiek, E.J. Cook, C.D. Arvantis, A. Olivo, G.J. Royle, A.T. Clark, M.L. Prydderch, R. Turchetta, R.D. Speller, *Phys. Med. Biol.* **53**, 655 (2008)
25. A.R. Faruqi, R. Henderson, *Curr. Opin. Struct. Biol.* **17**, 549 (2007)
26. C. Vallance, M. Brouard, A. Lauer, C.S. Slater, E. Halford, B. Winter, S.J. King, J.W.L. Lee, D. Pooley, I. Sedgwick, R. Turchetta, A. Nomerotski, J.J. John, L. Hill, *Phys. Chem. Chem. Phys.* **16**, 383 (2014)
27. A.T. Clark, J.P. Crooks, I. Sedgwick, R. Turchetta, J.W.L. Lee, J.J. John, E.S. Wilman, L. Hill, E. Halford, C.S. Slater, B. Winter, W.-H. Yuen, S.H. Gardiner, M.L. Lipciuc, M. Brouard, A. Nomerotski, C. Vallance, *J. Phys. Chem. A* **116**, 10897 (2012)
28. G.F. Knoll, *Radiation Detection and Measurement*, 4th edn. (Wiley, Hoboken, 2010)
29. Y. Tang, W.-B. Lee, Z. Hu, B. Zhang, K.-C. Lin, *J. Chem. Phys.* **126**, 064302 (2007)

Chapter 3

Three-Dimensional Velocity-Map Imaging

In this chapter the capabilities of the PImMS camera in three-dimensional and slice imaging applications are investigated, in which the product fragment Newton-sphere is temporally stretched along the time-of-flight axis, and time-resolved slices through the product fragment distribution are acquired. Through experimental results following the photodissociation of ethyl iodide ($\text{CH}_3\text{CH}_2\text{I}$) at around 230 nm, the PImMS camera is demonstrated to be capable of recording well-resolved time slices through the product fragment Newton-sphere in a single experiment, without the requirement to time-gate the acquisition.

3.1 Imaging the Newton-Sphere

In conventional velocity-map ion imaging experiments, the three-dimensional Newton-sphere is projected onto a two-dimensional detector, resulting in a loss of information on the initial z -velocities (where the z -axis coincides with the time-of-flight axis) of the nascent photofragments. In the case of a cylindrically symmetric product fragment distribution, it is possible to analytically reconstruct the full three-dimensional distribution from the two-dimensional image (see Sect. 2.4). While it is indeed the case that for many photoinitiated processes cylindrical symmetry will necessarily be present in the photofragment distribution, there are many applications of ion imaging in which no such constraints on image symmetry exist [1]. Even where cylindrical symmetry does exist, the various image inversion routines unavoidably introduce noise, and in some cases artificial artefacts, to the data, reducing the fidelity of the extracted parameters. Additionally, in the case of coincidence spectroscopy, it is highly desirable, and often crucial, that the full three-dimensional momenta of the product fragments are known, such that a kinematically complete picture of each reactive event may be unambiguously determined.

For these reasons, many experimental techniques have been developed to allow either the full three-dimensional product fragment distribution, or exclusively the meridional slice, to be determined directly from the experiment, without the requirement for image inversion (Fig. 3.1). With the exception of optical slicing methods, which will not be explored here but are described in detail in Refs. [2–6], the common strategy relies on temporally stretching the Newton-sphere, such that the time of arrival at the detector corresponds to the initial z -velocity of the photofragments. By using a detection system capable of recording both the time of arrival and the spatial coordinates of the ion impact on the detector with a sufficiently high accuracy, it then becomes possible to extract the full three-dimensional fragment momenta [1]. An alternative approach is to time-gate the detector to record only the central slice of the Newton-sphere, which, in the case of cylindrical symmetry, is sufficient to completely describe the velocity distribution of the photofragments. Such a strategy relies on the time-gate being sufficiently narrow that the central slice recovered may be considered as infinitely narrow when compared to the temporal width of the Newton-sphere. When this approximation is not valid, it may be necessary to correct the sliced images according to the finite slice width [7].

The major challenges of such a strategy are two-fold. Firstly, ion extraction must be performed in such a way that three conditions are satisfied: (i) that the initial z -component of the photofragment velocity, v_z , has a well-defined relationship to the arrival time at the detector, t ; (ii) that the spread in arrival times at the detector (Δt) between the most forward-scattered and most backward-scattered photofragments of the Newton-sphere is sufficiently large compared to the time-resolution of the detector; (iii) that the ions are extracted under velocity-mapping conditions, such that the initial x - and y -components of the photofragment velocity may be determined from the position of impact on the detector. A number of different ion extraction schemes have been devised to satisfy these three conditions, a selection of which are reviewed in the following section.

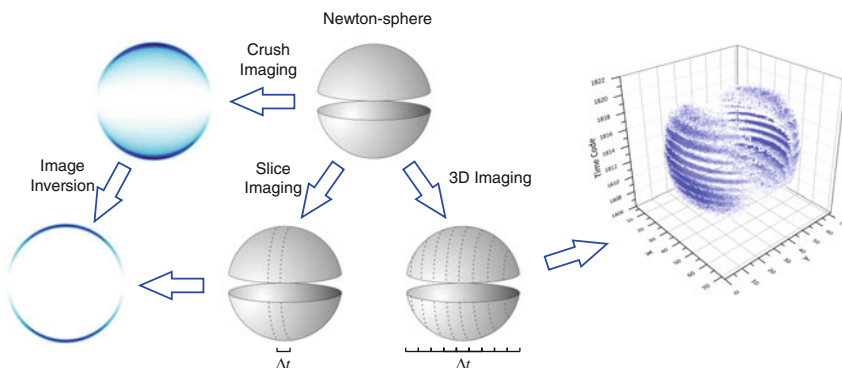


Fig. 3.1 Figure illustrating the relationship between crush, slice, and 3D imaging

The second major challenge is the development of a detection system that is capable of simultaneously recording both the time and spatial coordinates of ion impact with sufficiently high resolution that three-dimensional imaging becomes viable. Commonly, these conditions are met using an anode readout system, such as a delay line, wedge and strip anode, or crossed wire detector. However, recent advances in silicon technology have resulted in the development of pixelated fast imaging sensors, which hold much promise for 3D imaging applications. Each of these technologies is discussed in Sect. 1.6 and will not be reviewed in detail here. For slice imaging applications, in which only the meridional slice of the Newton-sphere is required, the most common approach is to use an MCP-phosphor detector coupled with a CCD camera, and to time-gate either the detector or the image intensifier in the CCD camera itself. Following this approach, time-gates on the order of 10 ns are typically achieved [8], which is usually sufficient for most slice imaging applications. If the goal is to achieve true 3D imaging of the full product fragment distribution, it becomes necessary for the time-resolution of the detector to afford a resolution of v_z on the order of that to which v_x and v_y may be determined by the spatial resolution of the device. For this condition to be realised, it is generally necessary for the time-resolution of the readout system to be ≤ 1 ns, which is satisfied by the use of delay line or crossed wire detectors.

Pixelated silicon-based detectors, such as PImMS [9] and TimePix [10], fall somewhere between the requirements for slice imaging and full 3D imaging. The spatial resolution of the PImMS1 camera has been demonstrated in Sect. 2.5.4 to be sufficient to provide good quality velocity-map imaging data, with the information extracted comparing favourably to that obtained using a conventional CCD camera. With the imminent arrival of PImMS2, which has a pixel resolution of 324×324 , and the current availability of other CMOS-based detectors offering comparable pixel counts, the spatial resolution of these devices is comfortably sufficient for slice and 3D imaging applications. The current time-resolution of the PImMS1 sensor (12.5 ns) compares favourably to time-gating approaches using MCP detector pulsing, but the ultra-high time precision of delay line detectors is presently beyond capabilities of the technology. However, TimePix currently operates with a clock cycle of 10 ns, and it is expected that the PImMS family of sensors will soon achieve a 6.25 ns time-resolution. Furthermore, with the integration of single-pixel avalanche diodes (SPADs), it has been demonstrated that CMOS technologies are capable of time-resolutions below 1 ns [11], competitive with that offered by delay line detectors and crossed wire detectors.

Despite the reduced time-resolution when compared to delay line and crossed wire detectors, the PImMS camera nonetheless confers some advantages over these technologies. Most notably, the PImMS camera is capable of simultaneous multi-particle detection, which is problematic for anode-based readouts. The PImMS camera may also be trivially integrated with the conventional MCP-phosphor detector arrangement most commonly used in ion imaging applications, and offers the further advantage that the image on the phosphor screen may be focussed onto the sensor to make the most efficient use of the active area of the sensor.

Attractively, the PImMS camera also offers advantages over the time-gating approach conventionally used to achieve slice imaging. A major drawback of traditional slice imaging is that the majority of the ion signal is simply discarded, since only the small fraction that constitutes the central slice is recorded. For processes with a low ion yield, or for geometries in which only a small fraction of the total ion flux is directed into the central slice, this can become problematic, resulting in low signal levels and poor data convergence. This problem becomes increasingly acute as the time-gate is narrowed, resulting in an ever diminishing fraction of the total signal being recorded. The PImMS camera offers the advantage that all ions that are amplified by the detector are recorded, with the central slice of the Newton-sphere simply extracted from the data once the acquisition is complete. This flexibility at the data processing stage constitutes one of the principal advantages of the PImMS sensor, and removes the requirement to pulse the detector accurately at the precise time required to capture the central slice of the Newton-sphere. Furthermore, it is possible to collect slice images for multiple fragments of different mass-to-charge ratios in a single experimental acquisition, potentially reducing the time required to collect a comprehensive data set where ion images of multiple fragments are to be recorded.

Slice imaging using a fast silicon detector has been demonstrated previously by Jungmann et al. [12] using the TimePix sensor, which was mounted in-vacuum directly behind the MCPs of an ion imaging apparatus. The results presented in this chapter follow this approach, with the primary difference being that the in-vacuum TimePix sensor is replaced with the PImMS1 camera, which affords a multi-hit capability per pixel and the ability to interface directly with the MCP-phosphor screen detection system commonly used in ion imaging applications.

3.1.1 Ion Extraction Methods

A large number of ion extraction schemes have been developed to satisfy the requirements for VMI while simultaneously mapping the z -component of the initial fragment velocity onto the flight time of the ion. The most commonly used methods, and those relevant to imaging the full 3D Newton-sphere using a fast detector, fall broadly into one of two categories: delayed extraction, in which the ions are accelerated a short time after the initial reactive event; and dc-slicing, in which additional open electrodes and static potentials are used to achieve ion extraction.

3.1.1.1 Pulsed Extraction

Delayed extraction by pulsed electric fields is a commonly used technique in photofragment time-of-flight velocity analysis [13]. Gebhardt et al. [14] showed that by using a delayed pulsed extraction of the ions through a grid electrode, comprising an ultra-fine wire mesh, followed by velocity-mapping in the detector plane by a three-electrode Einzel lens, it was possible to substantially increase the tem-

poral spread of ion arrival times at the detector when compared to conventional Eppink and Parker-type ion extraction schemes [15]. The delayed extraction method relies on the differential potential energy imparted to the ions depending on their position in the extraction region when the potentials are pulsed on. Ions scattered towards the repeller plate achieve a higher terminal velocity than those scattered towards the extractor electrode, and therefore reach the detector at earlier times. The pulsed extraction method has since been adapted to incorporate exclusively open electrodes [4, 16], thus removing the issue of reduced transmittance and possibility of image distortion associated with the use of grid electrodes.

3.1.1.2 Direct Current Extraction

Arguably the simplest method of achieving the conditions required to effect 3D imaging is to add further electrodes to Eppink and Parker-type ion optics in order to achieve ion extraction using more conservative extraction fields. By using a reduced field gradient to achieve ion extraction, the turn-around time for backward-scattered ions is increased, resulting in a stretching of the Newton-sphere along the time-of-flight axis according to the initial z -component of the ion velocities. The use of further electrodes allows velocity-mapping of the ions to occur after the initial ion extraction. Since ion extraction relies on static electric fields, the term ‘direct current’ (or dc) slice imaging is used to describe these methods. The first such examples of dc slicing were reported independently by Townsend et al. [3] and Lin et al. [17]. Townsend et al. demonstrated that by adding either one or two additional open electrodes, Newton-sphere stretches on the order of hundreds of nanoseconds could be achieved, depending on the ion mass and initial kinetic energy. The approach of Lin et al. was similar, but their design comprised of 29 open electrodes linked by high precision resistors to provide a low extraction field gradient, followed by an acceleration region. The transition between the extraction and acceleration regions acts essentially as an electrostatic lens and results in velocity-mapping of the ions. Direct current methods work increasingly effectively if the initial kinetic energies and masses of the photofragments are large as this increases the turn-around time of the ions.

A disadvantage of dc slice imaging is that lower than normal extraction voltages are usually required to effect the required temporal spread of ion arrival times, which has implications for the detection efficiency of the ions when using MCP detectors [18]. Despite this limitation, the simplicity of the dc slice imaging approach is attractive and is the method used in the work presented in this chapter.

3.2 Simulations

To investigate the feasibility of performing slice and 3D imaging experiments with the PImMS camera, ion trajectory simulations were performed using SIMION 8.0. The ion optics are based upon those of Townsend et al. [3] and consist of four open

electrodes: a repeller, an extractor, a slicing lens, and a grounded electrode. Voltages were applied to all electrodes except the grounded plate. Panel B of Fig. 2.2 details the dimensions of the ion optics assembly. As in the experiment, a field-free flight tube extends 620 mm beyond the grounded electrode and terminates with a detector of diameter 78 mm. The simulated ions were generated halfway between the repeller and extractor electrodes in a cigar-shaped three-dimensional Gaussian distribution, with a standard deviation of 0.3 mm along the laser propagation axis (perpendicular to the time-of-flight axis) and $10\ \mu\text{m}$ in the remaining two dimensions. This range of starting positions was chosen to simulate as closely as possible the typical initial conditions in an ion imaging experiment, in which the molecular beam is intersected by the ionisation laser beam in a perpendicular manner. The length of the interaction volume along the laser propagation axis will largely be determined by the size of the aperture in the repeller plate, through which the target molecules enter the interaction region. The radius of the interaction volume will be determined by the tightness of focussing of the ionising laser beam and may be approximated by considering the ionising source as a Gaussian beam and calculating the beam waist diameter.

It is an important requirement for effective 3D imaging of the Newton-sphere that the initial z -component of the nascent photofragment velocity, v_z , maps straightforwardly onto the time-of-flight of the ion. Although it is not strictly a requirement that the relationship between the flight time of the ion and the initial z -velocity is linear and proportional, it is desirable for this to be the case so that v_z may be trivially determined from the experiment and so that the resolution with which v_z may be determined is invariant of its value.

The left-hand panel of Fig. 3.2 plots the simulated flight time, t , of the ions as a function of their initial z -velocity. The ions have a mass of 126.9 Da (that of atomic iodine) and a kinetic energy of 0.5 eV, with the ion velocities directed isotropically in a spherical distribution. From Fig. 3.2 it is clear that, in general, there is indeed a well-behaved linear relationship between v_z and the ion time-of-flight. A linear fit to the data is shown by the red line and the residuals of the data points are plotted as blue points, with the scale on the right-hand axis. The fit residuals show that

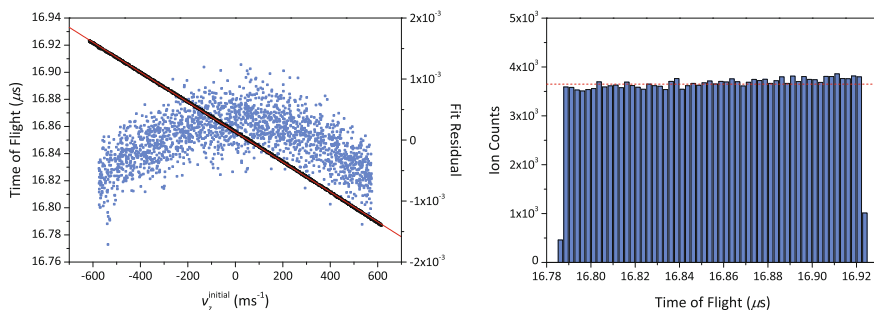


Fig. 3.2 *Left* The black points are a plot of the ion flight time, t , versus the initial z -velocity. The red line is a linear fit and the blue points are the fit residuals. *Right* Simulated time-of-flight histogram for I^+ ions illustrating the slight asymmetry in the time-of-flight peak when using dc slice imaging

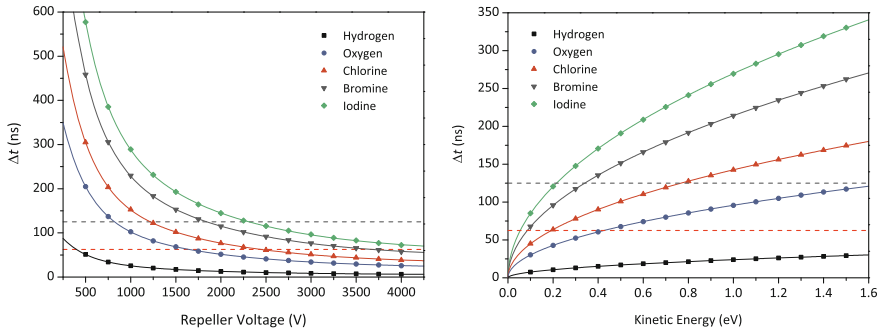


Fig. 3.3 *Left* Plot of the simulated spread of arrival times, Δt , as a function of the repeller voltage V_R for ions with an initial kinetic energy of 0.5 eV. *Right* Plot of the simulated spread of arrival times, Δt , as a function of ion kinetic energy for a repeller voltage of 1500 V

there is, in fact, a small amount of non-linearity in the $v_z - t$ relationship, but that the effect of this non-linearity is small, with the deviation from the linear fit rarely exceeding 1 ns in either direction. The uncertainty in the time-of-flight for a given initial z -velocity is also on the order of ± 0.5 ns, as determined from the breadth of the residual scatter. Since both of these values are small compared to the PImMS camera bin-width (12.5 ns), these effects can be ignored in the analysis of the data. The right-hand panel of Fig. 3.2 illustrates the effect of the non-linear relationship between v_z and the ion time-of-flight on the symmetry of the time-of-flight peak, with the peak skewed slightly towards later flight times.

Further simulations were performed to determine the degree to which the Newton-sphere could be temporally stretched using this particular variant of direct current extraction. The left-hand panel of Fig. 3.3 illustrates the effect of varying the repeller voltage (V_R) on the temporal spread of photofragment arrival times (Δt), while keeping the voltage ratios across all plates constant ($V_R : V_E : V_S = 1 : 0.886 : 0.775$). The ions were created with a kinetic energy of 0.5 eV with the ion velocities directed isotropically in three dimensions. The general trend for each ion mass is for the value of Δt to decrease as the repeller voltage increases. This is due to the reduced turn-around time of the ions as a steeper potential gradient is applied to the interaction region. It is also worth noting that, for a given V_R , Δt becomes larger upon increasing the mass of the ion. This is also a result of an increased turn-around time, in this case caused by the increased inertia of the heavier ions.

The right-hand panel of Fig. 3.3 illustrates how, for a given repeller voltage (in this case 1500 V), the value of Δt increases with increased photofragment kinetic energy, a trend once again explained by the increased turn-around time of the ions. In both panels of Fig. 3.3, broken horizontal lines represent the threshold at which the PImMS camera offers a time-resolution of 10% of the total Newton-sphere with both the current 12.5 ns (black) and the improved 6.25 ns (red) time bin widths. It is clear from these simulations that, even using a relatively simple, three electrode ion optics assembly and static extraction potentials, that the PImMS camera holds promise in slice imaging and low-resolution 3D imaging applications.

3.3 Experimental Results

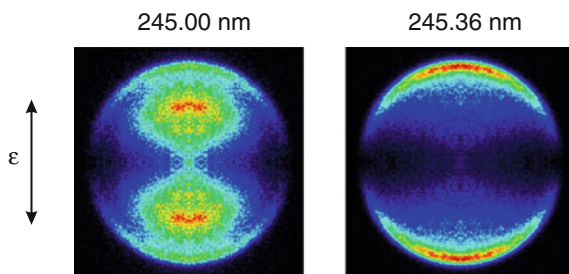
To test the performance of the PImMS camera in a 3D imaging application, data were recorded following the photodissociation of ethyl iodide ($\text{CH}_3\text{CH}_2\text{I}$) at around 245 nm. Figure 3.4 shows representative images of I^+ ions formed following the photodissociation of EtI at 245.00 and 245.36 nm, as recorded using the PImMS camera. The photodissociation of ethyl iodide is described in Sect. 2.5.4, where the origins of the various features present in the ion images are explained.

The two images at 245.00 and 245.36 nm contain complementary features for evaluating the 3D imaging capabilities of the PImMS camera. The image taken at 245.36 nm comprises a single, sharp ring at high velocities and is therefore ideal for evaluating the velocity-mapping performance of the PImMS camera in 3D imaging applications. The image at 245.00 nm, on the other hand, contains significant contributions from low-velocity photofragments and therefore offers an ideal test of the low-velocity performance of the PImMS camera, where the degree of slicing will be relatively poor in comparison to the higher velocity regions of the image. Furthermore, the iodine photofragments produced through photodissociation of ethyl iodide via the *A* band peak at 600 ms^{-1} , corresponding to a kinetic energy of approximately 0.237 eV. The ion trajectory simulation results, shown in the right-hand panel of Fig. 3.2, suggest that a Newton-sphere of approximately 140 ns should result from using a repeller voltage of 1500 V, which offers a degree of slicing of better than 10 %.

3.3.1 Experimental Conditions

A repeller voltage of 1500 V was selected to give a good compromise between imparting enough kinetic energy to the ions such that they were detected efficiently by the MCP detector, and achieving a long enough spread of ion arrival times to perform a good degree of slicing. It was also observed that using repeller voltages of less than 1500 V left the ion cloud susceptible to distortion by external fields. The ratio $V_R : V_E : V_S$ was set to 1 : 0.886 : 0.775, as determined by the ion trajectory simula-

Fig. 3.4 Images of the I^+ ions resulting from the photodissociation of ethyl iodide at 245.00 and 245.36 nm captured using the PImMS camera. The laser polarisation is *vertical*



tions, and verified in the laboratory, to give the best velocity-mapping performance. The detector was operated under high gain conditions, as this was demonstrated in Sect. 2.5.3 to yield the most accurate timing information when coupled with the PImMS camera. The voltage across the MCPs was set to 1800 V and the bias between the MCPs and the P47 phosphor screen set to 3200 V. The PImMS camera was fitted with a C-mount Nikon Nikkor lens ($f/0.9$).

3.3.2 PImMS Data Processing

As discussed in Sect. 2.5.3, the raw data from the PImMS camera must be intelligently processed in order to yield the highest quality information. In particular, for 3D imaging applications it is important that the time-of-flight information provided by the PImMS camera is highly accurate. For this reason, a minimum cluster size threshold was applied to the data at the centroiding stage, with any clusters below a certain threshold size removed from the data set. The rationale for applying such a filter is that larger clusters correspond to larger, and therefore brighter, flashes on the phosphor screen. The brighter the flash, the higher the photon flux experienced by each pixel of the PImMS sensor and the earlier the internal threshold is exceeded, resulting in a more accurate time code for the event. Conversely, smaller clusters will more commonly be associated with less intense flashes, and will therefore be associated with less accurate timing information.

Figure 3.5 plots the time-of-flight trace of the I^+ peak at both 245.00 and 245.36 nm, as recorded using the PImMS camera. The broken black traces plot the time-of-flight peak as determined from the raw PImMS data, whereas the red curves show the time-of-flight peaks after centroiding with varying cluster size thresholds applied to the data. The effect of centroiding is striking in all cases, with the peak shifted approximately 4 time codes (50 ns) earlier. The centroided data with no min-

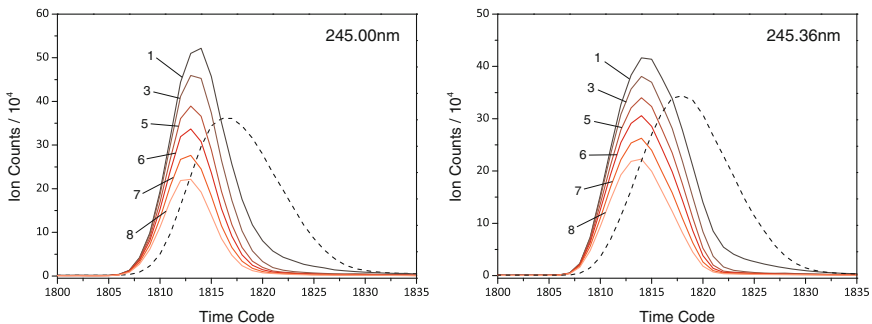


Fig. 3.5 Plots of the time-of-flight peaks of I^+ ions taken from the PImMS data. The time-of-flight of the raw data is plotted as a *broken black line*. The *red curves* are the time-of-flight peaks after centroiding with various minimum cluster size thresholds applied

imum cluster size threshold does, however, display a pronounced asymmetry, with the sharp rising edge of the left hand side contrasting with the more slowly decaying falling edge to the right. This asymmetry in the time-of-flight peak is reduced upon progressively increasing the minimum cluster size threshold, at the expense of signal intensity. Since the peak never fully reaches perfect symmetry, or indeed the small opposite skew that might be expected in light of the simulations shown in Fig. 3.2, it was decided that a minimum cluster size threshold of 6 pixels gave an acceptable compromise between peak symmetry and signal intensity.

3.3.3 PImMS Images

Figure 3.6 presents the images recorded using the PImMS camera at 245.36 nm. In the top left hand corner the I^+ time-of-flight peak is shown after centroiding with a minimum cluster size threshold of 6 pixels. The broken trace plots the same data, but reflected about the maximum time code to illustrate the small asymmetry in the peak. The yellow shading represents the range of time codes displayed in the

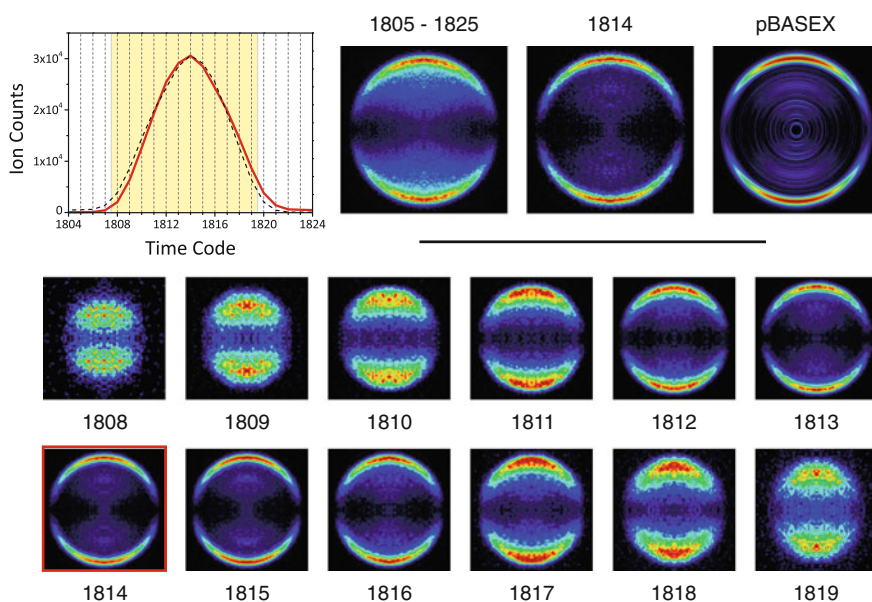


Fig. 3.6 Images of I^+ ions produced following photodissociation of ethyl iodide at 245.36 nm, recorded using the PImMS camera. The graph in the *top left corner* shows the time-of-flight peak of the I^+ ions (*red*) and the same peak reflected about time code 1814 (*broken black*). Images corresponding to individual time codes are shown in the *bottom half* of the figure. The three images across the *top* are, from *left*: the ion image integrated over time codes 1805–1825, the ion image corresponding to time code 1814, and the pBASEX inversion of the integrated ion image

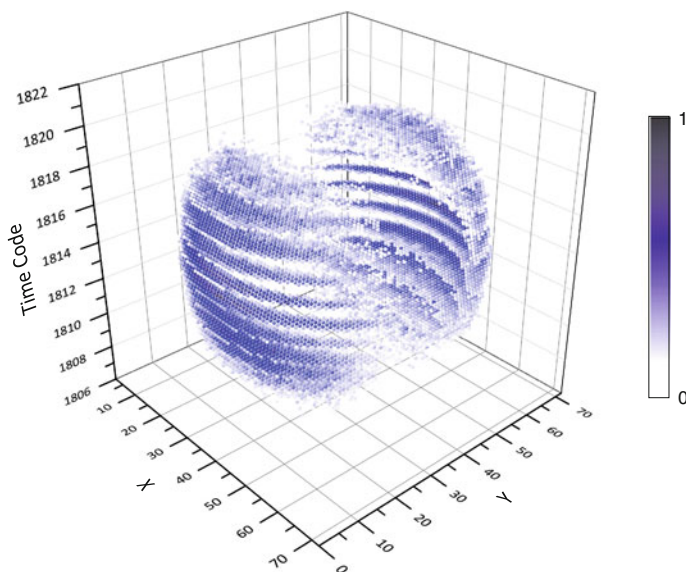


Fig. 3.7 A three-dimensional representation of the data shown in Fig. 3.6

sequence of images in the bottom half of the figure. The time code corresponding to the central slice of the Newton-sphere (1814) is shown in the centre of the top row of images, alongside the ‘crush’ image, which is obtained by integrated over the whole peak (time codes 1805–1825), and the pBASEX inversion of the integrated image. The sequence of single time code images clearly show that the product fragment distribution has been effectively time-sliced by the PImMS camera, with a slice being equal to approximately 7–8% of the full width of the peak. The velocity distributions of the images correspond to distinct and well-resolved slices through the product fragment Newton-sphere. A three-dimensional representation of the data is presented in Fig. 3.7 to further illustrate this point. From this data, it would appear that the PImMS camera has successfully captured the Newton-sphere in three dimensions, with each of the slices well-resolved in time.

Figure 3.8 presents the I^+ images recorded by the PImMS camera following the photodissociation of ethyl iodide at 245.00 nm. Once again, the sequence of single time code images demonstrates that the full I^+ Newton-sphere has been captured in three dimensions by the PImMS camera. Importantly, the lower velocity regions of the image also appear to be well-resolved, with the image corresponding to the central slice of the distribution comparing favourably in a qualitative sense with the pBASEX inversion. Furthermore, the central slice appears, in some sense, to be a truer representation of the product fragment distribution than the pBASEX inversion, which contains radial artefacts in the lower velocity regions of the image due to the radial basis functions used to achieve inversion.

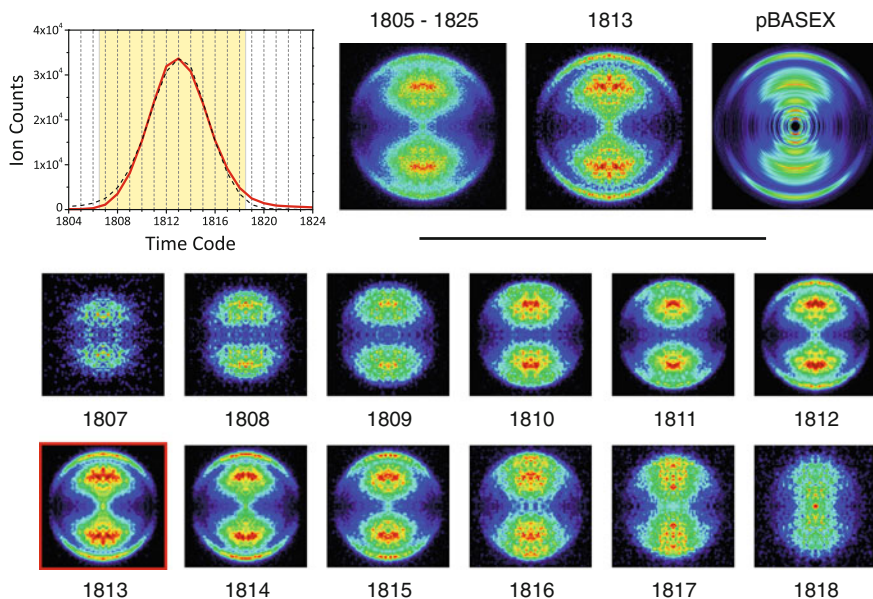


Fig. 3.8 Images of I^+ ions produced following photodissociation of ethyl iodide at 245.00 nm, recorded using the PImMS camera. The graph in the *top left corner* shows the time-of-flight peak of the I^+ ions (*red*) and the same peak reflected about time code 1813 (*broken black*). Images corresponding to individual time codes are shown in the *bottom half* of the figure. The three images across the *top* are, from *left*: the ion image integrated over time codes 1805–1825, the ion image corresponding to time code 1813, and the pBASEX inversion of the integrated ion image

While it would appear from a qualitative inspection of the ion images that the PImMS camera has been successful in accurately capturing the three-dimensional Newton-sphere, it is informative to compare the speed and angular parameters of the images with those calculated from an inversion of the ‘crushed’ image. Figure 3.9 compares the speed and angular parameters at the two wavelengths, as determined directly from the central slice of the distribution (red trace), and from the pBASEX inversion (broken blue trace). In general, both the speed and angular parameters are in good agreement, with a small discrepancy in the radius at which the features appear in the time-sliced and inverted data. This is likely to be caused by the finite width of the slice giving a non-zero solid angle over which the intensity is integrated. Encouragingly, the time-sliced parameters appear to be less affected by noise than those extracted through the pBASEX inversion, giving a greater confidence in the values extracted from the data. Crucially, the slice images reproduce well the features at low fragment velocities, despite the lower degree of slicing achievable when compared to the high-velocity regions of the images.

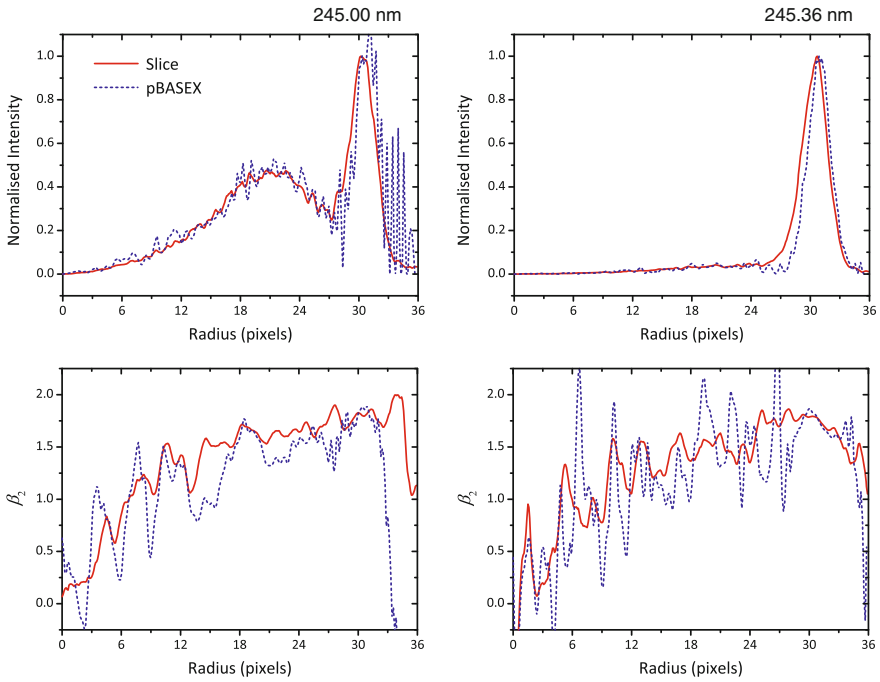


Fig. 3.9 The speed and angular parameters extracted directly from the slice images (*red*) and from a pBASEX inversion of the time integrated image (*broken blue*)

3.4 Discussion

This chapter has demonstrated the three-dimensional imaging capabilities of the PImMS camera when coupled with a simple dc slice imaging apparatus. The PImMS camera has been shown to be capable of recording well-resolved time slices through the product fragment Newton-sphere in a single experiment without the requirement to time-gate the acquisition. The ability to perform slice imaging without discarding any information represents an important advantage over conventional time-gating approaches. It is also important to note that the data presented in the preceding section were recorded under high-count rate conditions, in which several ions may reach the detector almost simultaneously. This approach would prove problematic for delay line detectors, which can typically accept only a single, or very few, particles at once. The PImMS camera may also be integrated trivially with any conventional ion imaging apparatus equipped with an MCP-phosphor detector. Additionally, since images of the phosphor screen are projected onto the PImMS sensor through a lens, it is possible to make maximum use of the PImMS sensor by focussing the image to fill the active area of the chip.

Not only do the results demonstrate effective slice imaging, they also show promise in the direction of full 3D imaging. Although, at present, the PImMS time-

resolution is 12.5 ns, it is expected that this will be halved to 6.25 ns in the near future. Furthermore, although the direct current ion extraction scheme used in this work is straightforward to implement, it does not afford the greatest degree of Newton-sphere stretch possible. More elaborate schemes that rely on large numbers of electrodes or pulsed extraction offer a greater spread of arrival times at the detector, which would have the effect of improving the effective v_z resolution offered by the PImMS camera.

Modifications to the PImMS sensor are also expected to improve the suitability of the device to full 3D imaging applications. Although not a limiting factor in this particular example, the pixel count of the PImMS1 sensor may be problematic in applications where a high resolution is required. This limitation will be largely overcome by the arrival of the PImMS2 sensor, with a resolution of 324×324 pixels.

In the experiments presented in this chapter, it was necessary to remove smaller clusters from the data during processing in order to ensure a high timing precision. While this approach largely succeeded in this case, it would be advantageous to retain the full set of events, especially in the case of coincidence experiments where a high detection efficiency is of high importance. For this to be possible, the light collection efficiency of the PImMS pixels must be improved so that the internal threshold is exceeded within the first time code after the flash occurs on the phosphor screen. One approach is to include microlenses [19] directly in front of the pixels. Light is collected by four photodiodes in each pixel, which constitute just 16.9% of the area of the PImMS sensor. By focussing the light from the phosphor screen into these four wells, it should be possible to significantly improve the sensitivity of the PImMS camera. An alternative strategy would be to back-thin the sensors [20]. This involves gradually reducing the thickness of the P-substrate layer until it become transparent to photons. The sensor can then be illuminated from the back side, which is unobscured by electronic circuitry, giving a theoretical light collection efficiency of 100%. It may also be possible to improve the sensitivity of the PImMS sensor without making any physical modifications to the chip through a more accurate calibration of the pixels. Since threshold must be set high enough such that even the most sensitive pixels are rarely triggered by background noise, a more consistent response over the entire sensor should yield a more uniform, and therefore higher, sensitivity. The PImMS2 sensor should, in theory, have an improved response to the four trim bits, thereby achieving a more accurate calibration than the current PImMS1 sensor.

Alternatively, the photon flux generated by the experiment could be increased through the use of a faster and/or brighter scintillator than the currently used P47 phosphor. While there are commercially available scintillators that offer both increased brightness and a faster response than P47 [21], it is difficult to achieve both of these requirements simultaneously. Recently, however, workers in the groups of Prof. Mark Brourd and Dr Claire Vallance have developed several new scintillators that offer both a faster response and increased brightness when compared to the current industry standards [22]. Testing of these materials with the PImMS camera is ongoing, but the new scintillators would seem to offer promise for an increased performance of the PImMS camera.

A more distant ambition is to couple single-photon avalanche diodes (SPADs) [11] with silicon-based sensors, such as PImMS. This marriage should, in principle, afford time-resolutions below 1 ns and a single-photon detection efficiency, which would represent a significant improvement over the currently realised technology.

References

1. A.I. Chichinin, K.-H. Gericke, S. Kauczok, C. Maul, *Int. Rev. Phys. Chem.* **28**, 607 (2009)
2. K. Tonokura, T. Suzuki, *Chem. Phys. Lett.* **224**, 1 (1994)
3. D. Townsend, M.P. Minitti, A.G. Suits, *Rev. Sci. Instrum.* **74**, 2530 (2003)
4. D.A. Chestakov, S.-M. Wu, G. Wu, A.T.J.B. Eppink, D.H. Parker, T.N. Kitsopoulos, *J. Phys. Chem. A* **108**, 8100 (2004)
5. T. Kinugawa, T. Arikawa, *J. Chem. Phys.* **96**, 4801 (1992)
6. K.T. Lorenz, D.W. Chandler, J.W. Barr, W.W. Chen, G.L. Barnes, J.I. Cline, *Science*, **293**, 2063 (2001)
7. A.V. Komissarov, M.P. Minitti, A.G. Suits, G.E. Hall, *J. Chem. Phys.* **124**, 014303 (2006)
8. I. Wilkinson, B.J. Whitaker, *J. Chem. Phys.* **129**, 154312 (2008)
9. J.J. John, M. Brouard, A. Clark, J. Crooks, E. Halford, L. Hill, J.W.L. Lee, A. Nomerotski, R. Pisarczyk, I. Sedgwick, C.S. Slater, R. Turchetta, C. Vallance, E. Wilman, B. Winter, W.H. Yuen, *JINST* **7**, C08001 (2012)
10. X. Llopert, R. Ballabriga, M. Campbell, L. Tlustos, *Nuc. Inst. Meth. Phys. Res.* **581**, 485 (2007)
11. C. Niclass, A. Rochas, P.A. Besse, E. Charbon, *IEEE J. Solid-State Circuits* **40**, 1847 (2005)
12. J.H. Jungmann, A. Gijssbertsen, J. Visser, J. Visschers, R.M.A. Heeren, M.J.J. Vrakking, *Rev. Sci. Instrum.* **81**, 103112 (2010)
13. M.A.J. Young, *J. Chem. Phys.* **102**, 7925 (1995)
14. C.R. Gebhardt, T.P. Rakitzis, P.C. Samartzis, V. Ladopoulos, T.N. Kitsopoulos, *Rev. Sci. Instrum.* **72**, 3848 (2001)
15. A.T. Eppink, D.H. Parker, *Rev. Sci. Instrum.* **68**, 3477 (1997)
16. V. Papadakis, T.N. Kitsopoulos, *Rev. Sci. Instrum.* **77**, 083101 (2006)
17. J.J. Lin, J. Zhou, W. Shiu, K. Liu, *Rev. Sci. Instrum.* **74**, 2495 (2003)
18. M. Krems, J. Zirbel, M. Thomason, R.D. DuBois, *Rev. Sci. Instrum.* **76**, 093305 (2005)
19. P. Nussbaum, R. Voelkel, H.P. Herzig, M. Eisner, S. Haselbeck, *Pure Appl. Opt. Eur. Opt. Soc. P. A* **6**, 617 (1997)
20. G. McMullan, A.R. Faruqi, R. Henderson, N. Guerrini, R. Turchetta, A. Jacobs, G. van Hoften, *Ultramicroscopy*, **109**, 1144 (2009)
21. G.F. Knoll, *Radiation Detection and Measurement*, 4th edn. (Wiley, Hoboken, 2010)
22. B. Winter, S.J. King, M. Brouard, C. Vallance, *Rev. Sci. Instrum.* (Manuscript in Preparation)

Chapter 4

Pulsed-Field Electron-Ion Imaging

This chapter presents a new method of extracting and velocity-mapping both the ions and electrons resulting from photoionisation onto a single detector in each acquisition cycle. It is demonstrated that it is possible to maintain a high velocity resolution using this approach through the simultaneous imaging of the photoelectrons and photoions resulting from the $(3 + 2)$ resonantly enhanced multi-photon ionisation of Br atoms produced following the photodissociation of Br_2 at 446.41 nm. Pulsed ion extraction represents a substantial simplification in experimental design over conventional photoelectron-photoion coincidence (PEPICO) imaging spectrometers and is an important step towards performing coincidence experiments using a conventional ion imaging apparatus coupled with a fast imaging detector. The performance of the PImMS camera in this application is investigated, and a new method for the determination of the photofragment detection efficiencies based on a statistical fitting of the coincident photoelectron and photoion data is presented.

4.1 Introduction

In many cases it is useful to detect both the photoelectrons and photoions resulting from a chemical process. The electrons often carry with them a wealth of complementary information relating to the dynamics of the processes under investigation and the electronic states from which they are ejected. Photoelectron-photoion coincidence (PEPICO) spectroscopy has proven an invaluable experimental tool, finding applications in fields as diverse as photoionisation [1–3], molecular photodissociation [4, 5], and measurements of molecular chirality [6]. A particularly interesting application of PEPICO is realised when time-resolved measurements on an ultrafast timescale are pursued using pump-probe techniques. Time-resolved coincidence imaging spectroscopy (TRCIS) involves the measurement of the fully correlated ion and electron momenta as a function of time, often affording a view of reactivity from the perspective of the molecule [7, 8].

A number of experimental techniques have been developed to simultaneously image photoions and their associated photoelectrons in coincidence [9–15]. The term ‘simultaneous’ is used here to mean the imaging of more than one species in a given acquisition cycle, such as that initiated by an photoionising radiation pulse. Despite the apparent diversity in techniques employed, a common theme linking the various approaches is that the photoelectrons and photoions are imaged on separate detectors. Although this would seem to be a logical corollary of the fact that the ions and electrons possess charges of opposite polarity, and that the method of their extraction generally proceeds through focussing by electric and/or magnetic fields, there are a number of non-trivial disadvantages associated with this method. In addition to the extra financial and spatial cost of building an apparatus equipped with two separate detectors, such arrangements have been shown to complicate the layout of the ion optics to accommodate fragments travelling in opposite directions towards separate detectors. Furthermore, as both the photoions and photoelectrons are focussed onto their respective detectors using the same set of extraction potentials, it is often necessary to compromise on image size, and therefore on image resolution, if the kinetic energy differences of the photoelectrons and photoions are significant. Experiments using pulsed extraction potentials have been developed that address this issue [12], with the most recent experiments demonstrating that it is possible to extract both the photoelectrons and photoions onto a single detector within each experimental cycle [16]. The work presented in this chapter demonstrates that it is possible to simultaneously image, with a high velocity resolution, both the photoelectrons and photoions on a single imaging detector during each acquisition cycle. The implication is that, with minor modifications, a conventional ion imaging apparatus equipped with a fast imaging detector has the potential for use as an effective photoelectron-photoion coincidence (PEPICO) imaging spectrometer, thereby removing the requirement for a dedicated apparatus for performing such experiments.

The method employed exploits the vastly different masses of the photoelectrons and the positively charged photoions. On each acquisition cycle, the extraction potentials of a standard time-of-flight ion imaging experiment are initially set to effect velocity-mapping of the photoelectrons. Once the photoelectrons have entered the field-free flight tube, the polarity and magnitudes of the optics are switched on a short timescale (~ 40 ns) by commercially available MOSFET switches (Behlke) in order to image the photoions. During the time taken for the electrons to enter the field-free region (5–10 ns) the ion trajectories are perturbed by only a small amount by the electron extraction fields, and may be subsequently velocity-mapped onto the detector with a high velocity resolution. The principle is illustrated in Fig. 4.1.

Whilst recent experiments by Lehmann et al. [16] have demonstrated the principle of pulsed ion/electron extraction using a fast imaging detector, the ion images were considered uninteresting due to their unstructured nature and only the time-of-flight information from the ion signals was analysed in detail. In this work, the simultaneous velocity-map imaging of both photoelectrons and photoions is demonstrated, representing a substantial increase in the information content of the data recorded.

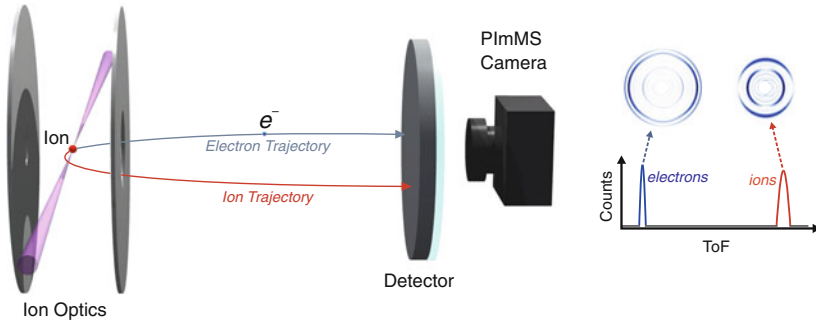


Fig. 4.1 Illustration of the principles of pulsed extraction. The voltages of the ion optics are initially set to effect electron extraction. After a short time (~ 10 ns) the electrons enter the field-free drift region and the potentials on the ion optics may be switched on a short time scale (~ 40 ns) to effect velocity-mapping of the ions. Images of both the photoelectrons and photoions are recorded using the PImMS camera on each acquisition cycle

4.2 Simulations

To investigate the feasibility of pulsed electron-ion extraction, simulations were undertaken using the SIMION 8.0 ion trajectory modelling package. Simulations were performed to investigate the performance of the fast switching extraction method over a range of ion masses and to investigate the effect of the electrode rise times on the velocity-mapping resolution. Two different electrode arrangements were investigated, both of which are shown schematically in Fig. 2.2. The first set-up, shown in Panel A of Fig. 2.2, and from here onwards referred to as configuration A, consists of a repeller, extractor and two grounded electrodes, as is typically used for crush velocity-map imaging experiments. The second ion optic set-up, referred to here as configuration B, is typical of that used in dc slice imaging experiments [17] and includes an additional focussing lens in place of the first grounded electrode, as shown in Panel B of Fig. 2.2. In both cases, the field-free flight tube extends 620 mm beyond the final grounded electrode, as is the case in the Oxford VMI spectrometer. During normal operation, using static extraction potentials, the optimum electrode potentials were found to be $V_R : V_E = 1 : 0.74$ for configuration A, and $V_R : V_E : V_S = 1 : 0.8855 : 0.7750$ for configuration B, where V_R , V_E , and V_S refer to the voltages applied to the repeller, extractor, and slice electrodes, respectively, as labelled in Fig. 2.2. The electrode potentials were modelled as a function of time, explicitly of the form

$$V(t) = \begin{cases} V_i, & t < t_s, \\ V_i + (V_f - V_i)(1 - \exp[-(t - t_s) \ln(100)/t_r]), & t \geq t_s, \end{cases} \quad (4.1)$$

where V_i and V_f are the initial and final electrode voltages, respectively, t is the flight time of the ions, as measured from the instant of their creation, and t_s and t_r are the switch time and rise time respectively, where the switch time is the time at which the electrode potentials are initially pulsed, and the rise time is the time it takes for the potentials to rise through 99% of the range ($V_f - V_i$). For all the simulations presented here, t_s was set to 20 ns after the formation of the ions as this was found to be more than sufficient for the photoelectrons to be extracted well into the field-free flight tube and is readily achievable from a practical standpoint. The ions were generated halfway between the repeller and extractor electrodes in a cigar-shaped three-dimensional Gaussian distribution, with a standard deviation of 0.4 mm along the laser propagation axis (perpendicular to the time-of-flight axis) and 0.2 mm in the remaining two orthogonal directions. The ions were formed with a kinetic energy of exactly 0.4 eV, with the velocities distributed isotropically in the plane perpendicular to the time-of-flight axis. In all of the simulations, the initial repeller electrode voltage, $V_{R,i}$, was set to either -2 or -5 kV, with the final repeller electrode voltage, $V_{R,f}$, set to $+2$ kV in all cases. The initially negative extraction potentials effect the velocity-map imaging of the photoelectrons, whereafter the ions are extracted following the pulsing of the electrode voltages.

Due to the large number of parameters that define each simulation, it is neither practical nor feasible to provide a comprehensive review of the performance of the pulsed extraction technique. Furthermore, the simulations presented here are limited to two basic electrode arrangements, with the optimisation of the ion optics a formidable challenge in its own right. For these reasons, these simulations are intended as a guide to illustrate some of the principles that may be of interest to the experimentalist intending to implement such a strategy, and are not meant as a comprehensive overview of the capabilities and limitations of pulsed electron-ion extraction.

Dependence on Rise Time

Figure 4.2 presents the results of ion trajectory simulations investigating the velocity-mapping performance of pulsed ion extraction over a range of rise times, t_r . In the results presented here, the velocity-mapping performance is characterised by the standard deviation of the radius (σ_r) of the ion impacts on the detector over 5000 ion trajectories, giving a standard error of 1% (1σ) for each data point. Perfect velocity-mapping is expected to yield a value of $\sigma_r = 0$, as each velocity maps onto a single impact radius in this case.

Panels (a) and (b) of Fig. 4.2 plot σ_r against t_r for ions carrying a single positive charge of mass 10, 20, and 40 Da for ion optic configurations A and B, respectively. The simulations were performed using $V_{R,i} = -5$ kV and $V_{R,f} = +2$ kV, with the potentials applied to the remaining electrodes independently optimised in each case to effect the most accurate velocity-mapping of the ions and electrons. Only the data corresponding to the velocity-mapping of the ions are shown, as the trajectories of the electrons are unaffected by the use of pulsed extraction, having entered the field-free flight tube before the electrodes are pulsed. At short rise times, the velocity-mapping performance upon pulsed extraction is either competitive with, or an improvement

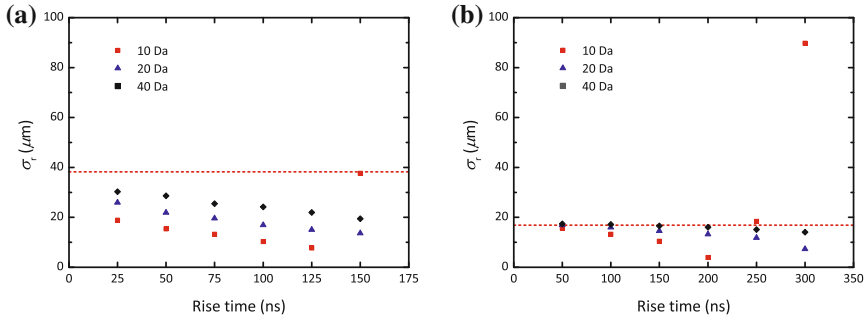


Fig. 4.2 Results of simulations investigating the effect of the electrode rise time on the velocity-mapping performance of the pulsed ion-electron extraction method. **Panel a** plots the results for electrode arrangement *A*, whereas **Panel b** plots the results for electrode arrangement *B*. In both cases, the results of simulations for ions of mass 10, 20, and 40 Da are plotted. The *horizontal broken red lines* indicate the velocity-mapping performance when using static extraction potentials. See text for further details

over, that achievable using static extraction voltages (broken red lines) using the same electrode configurations. As the rise time is progressively increased, the velocity-mapping performance of the apparatus improves in both cases, with the effect being most marked for ions of lower mass. At long rise times, the velocity-mapping resolution of the 10 Da ions begins to degrade, as witnessed by the increasing value of σ_r .

This behaviour may be understood by considering the trajectories of the ions during pulsed extraction. Initially, the ions will be drawn towards the repeller electrode under the influence of the electron extraction potentials. Upon pulsing, the extraction field is reversed in polarity and the ions are accelerated towards the detector. As the rise times are increased the ions travel closer to the repeller electrode before eventually being extracted towards the detector. As a consequence, the ions traverse an extended flight path during extraction using pulsed fields, allowing for a more precise manipulation of the ion trajectories, and therefore a more accurate velocity-mapping. However, as the rise time increases further, the ions travel too close to the repeller electrode and their trajectories are perturbed by the unevenness in the extraction field caused by the small (2 mm) aperture in the center of the plate, which causes a detrimental effect on the velocity-mapping performance. As the lighter ions are accelerated faster than heavy ions by a given potential gradient, this effect is observed for the ions of mass 10 Da before it is observed for those of 20 and 40 Da. Since the gradient of the extraction field of configuration *A* is steeper than that of configuration *B* for a given V_R , the timescales over which these effects manifest themselves are shorter when the apparatus is equipped with the crush imaging electrode arrangement. Crucially, however, the data presented in Fig. 4.2 demonstrate that the rise times afforded using commercially available high voltage switches (25–50 ns) fall comfortably within the range required to achieve simultaneous imaging of photoelectrons and photoions. Furthermore, the velocity-mapping resolution is

shown to be comparable to, and in some cases an improvement over, that achievable using static extraction potentials.

Dependence on Ion Mass

The effect of varying the mass of the ions is, in many ways, analogous to varying the rise times. This may be understood by considering that the trajectory of a heavier ion will be perturbed to a lesser extent by an electric field in a given time than will that of a lighter ion under the same conditions. This is equivalent to the heavier ion experiencing a shorter rise time than the lighter ion for a given extraction potential. The difference, however, is that during a given experimental cycle there will be only a single rise time, whereas there may be many ions of different mass, all of which must be imaged simultaneously and with an acceptable velocity resolution. It is therefore important to investigate how pulsed electron-ion extraction performs over a range of ion masses for a given set of extraction potentials.

Panel (a) of Fig. 4.3 plots σ_r for various ion masses when using electrode configuration A, with $V_{R,i} = -2$ kV, $V_{R,f} = +2$ kV, and a rise time of 50 ns. The results

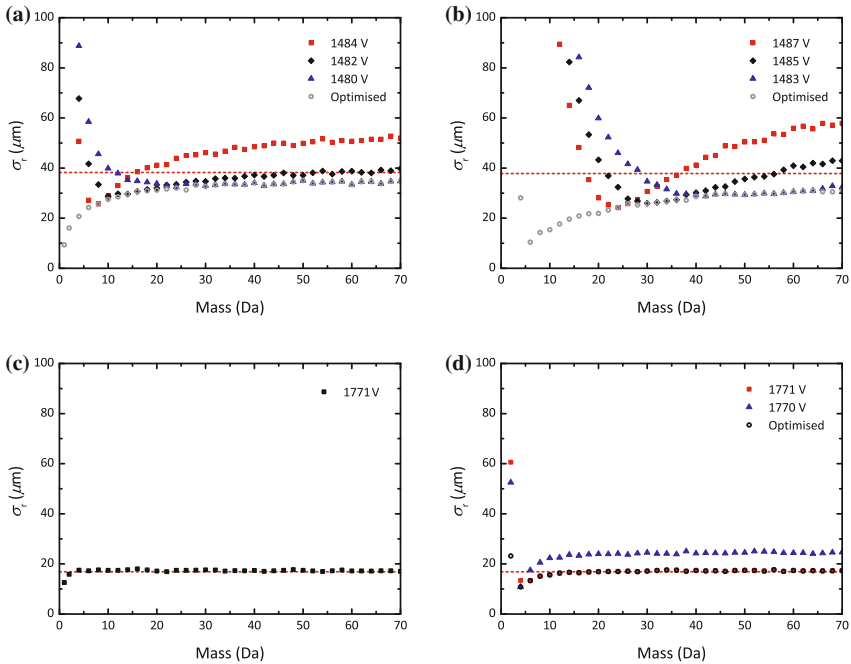


Fig. 4.3 Results of simulations investigating the effect of the ion mass on the velocity-mapping performance of the pulsed ion-electron extraction method using various extraction voltage ratios. **Panels a** and **b** plot the results of simulations performed using electrode arrangement A, whereas **Panels c** and **d** plot the results of simulations performed using electrode arrangement B. The *horizontal broken red lines* indicate the velocity-mapping performance when using static extraction potentials. See text for further details

demonstrate that, for a given ion mass, it is possible to optimise the extraction potentials to achieve a velocity resolution superior to that obtainable using a static extraction field, which is consistent with the data presented in Fig. 4.2a. The improvement is most marked for lower masses, which is analogous to the trend observed upon increasing the rise times, where a longer rise time corresponds to a lower mass in this case. Figure 4.3a also plots the velocity-mapping performance over a range of masses for three different extractor electrode voltages ($V_{E,f}$), optimised for the velocity-mapping of ions of mass 8, 16, and 32 Da, with $V_{E,f}$ set to 1482, 1483, and 1485 V, respectively (compared to 1480 V when using static extraction fields). The results show that it should be possible to simultaneously velocity-map ions over a range of masses during a single acquisition cycle, with the possible exception of very light ions (≤ 6 Da), depending on the mass range required. This limitation is largely overcome, however, when electrode configuration B is used, as demonstrated by the results presented in Panel (c) of Fig. 4.3. In this case, the optimised extraction voltages are identical for all masses, and are in fact the same as those used when using static extraction potentials. The relative insensitivity of electrode configuration B to the introduction of pulsed ion extraction is a consequence of the more conservative extraction field gradient in the vicinity of the laser interaction region, causing a smaller perturbation to the ion trajectories during the electron extraction phase.

Panels (b) and (d) of Fig. 4.3 investigate the effect of increasing the strength of the electron extraction fields on the velocity-mapping performance of the ions. In these simulations, $V_{R,i}$ was set to -5 kV, representing a 2.5-fold increase on the electron extraction field strength. Viewed from an alternative perspective, the increase in the field strength has a similar effect to reducing the mass of each ion by a factor of 2.5, which accounts neatly for the trends observed in the simulations. The data presented in Panel (b), which plot σ_r as a function of ion mass when using the higher electron extraction field and electrode configuration A, display a similar behaviour to those in Panel (a), with the dependence on ion mass scaled by a factor of 2.5. Additionally, the extractor voltages required to effect perfect velocity-mapping differ slightly from those required when $V_{R,i}$ is set to -2 kV. These small differences are explained by considering that the ion extraction voltages remain identical to those used previously and are not increased in magnitude, unlike those used to extract the electrons. The practical implication of this behaviour is that it becomes more difficult to effect accurate velocity-mapping over a broad range of ion masses using a single set of extraction potentials, with the range of masses over which a given voltage ratio is suitable becoming narrower as the electron extraction field is increased. Furthermore, the accurate velocity-mapping of very light ions (below 4 Da) becomes problematic, as these ions either travel too close to, or impact on, the repeller electrode during the electron extraction phase. However, despite these limitations, the independently optimised velocity-mapping resolution for ion masses of ≥ 5 Da is improved upon implementing pulsed extraction, satisfying the requirements when ions of only a single mass must be imaged in coincidence with the associated photoelectrons.

The results presented in Panel (d) illustrate that when the apparatus is equipped with electrode configuration B the use of a higher electron extraction field is tolerated far more favourably by the ions, due to the more conservative potential gradient

within the vicinity of the laser interaction region. All but the very lightest ions may be accurately velocity-mapped using a single set of electrode potentials, satisfying the requirements of the vast majority of PEPICO applications.

In summary, the performance of the pulsed extraction method is clearly dependent on the geometry of the electrodes, the rise times, and the extraction potentials used. However, the simulations presented here have shown that it should be possible to achieve velocity-mapping with an accuracy comparable to, and in some cases superior to, that obtainable using identical experimental apparatus under conventional velocity-mapping conditions. Furthermore, many of the values discussed above are comparable to the pore spacings of MCP detectors and are therefore of little to no practical significance. The simulations also suggest that it should be possible to design ion optics capable of fulfilling the requirements of a wide range of PEPICO experiments. In general, the use of a conservative extraction field is advantageous in pulsed ion-electron extraction applications.

4.3 Experimental Images

In light of the promising ion trajectory simulation results, experiments were performed to test the feasibility of the approach under laboratory conditions. The experimental apparatus used has been described in detail in Sect. 2.2. The ion optics arrangement employed was the same as that shown in Fig. 2.2a, and consisted of a repeller, extractor, and two grounded electrodes. Importantly, the potentials on the repeller and extractor electrodes required for velocity-mapping were supplied through two independent high-voltage MOSFET switches (Behlke; HTS 121, 12 kV, 30 A) so that the polarity and magnitude of the extraction field may be switched on a short timescale (~ 40 ns). Images of the photoelectrons and photoions produced following the photodissociation of Br_2 at 446.41 nm [18] were used to test the feasibility of the pulsed extraction method. Briefly, ground state ($X^1\Sigma_g^+$) molecular bromine is dissociated via a single photon transition at 446.41 nm to either the $A^3\Pi_u(1_u)$ or $B^3\Pi_u(0_u^+)$ electronically excited states, resulting in dissociation to $\text{Br} + \text{Br}$ and $\text{Br} + \text{Br}^*$, respectively (where Br^* refers to electronically excited bromine atoms in the $^2P_{1/2}$ state). The ground state ($^2P_{3/2}$) Br photofragments are subsequently ionised via a (3+2) resonantly enhanced multiphoton ionisation (REMPI) transition at the same wavelength to form the ground state ions in a variety of energetically excited states (3P_J , 1D_2).

The photodissociation of molecular bromine at 446.41 nm is an attractive system for the purposes of testing the pulsed extraction technique for a number of reasons. Firstly, both dissociation and subsequent ionisation of the atomic photofragments occur at the same wavelength. This is advantageous as the overlap of the pump and probe laser pulses is necessarily perfect, since they are provided by the same laser system, removing any potential for inconsistencies in the images caused by poor laser beam alignment. A further advantage is that the ionisation is via a REMPI

process at a relatively long wavelength, and hence low energy. The combination of resonant enhancement and low photon energy make the process very selective, with ionisation of other species by different processes very unlikely. This is particularly important for the determination of the detection efficiencies of the photofragments, as described in Sect. 4.4, but it is also advantageous for maintaining the consistency of the ion and electron images between acquisitions. Furthermore, the ion and electron images consist of well-resolved, narrow rings, providing an accurate measure of the velocity-mapping resolution.

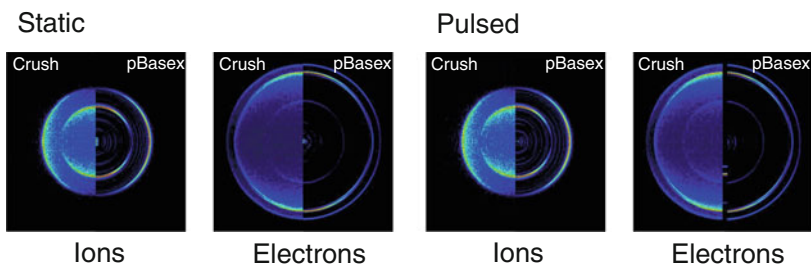
The correct pulsing time was determined using an iterative procedure. The Behlke switch trigger pulse was initially set to a time some tens of nanoseconds before the Q-switch of the Nd:YAG laser system. The trigger delay was then increased in 5 ns increments using a delay generator (Quantum Composer, 9520 series), while the photoelectron image was monitored in real-time. At the first signs of distortion in the photoelectron image, the delay was stepped back by approximately 10 ns to ensure that the photoelectrons were extracted well into the field-free flight tube before the ion optics were pulsed.

When using pulsed extraction it is often necessary to reoptimise the velocity-mapping voltages used to extract the ions. In this case it was found that the extractor plate voltage required for velocity-mapping shifted by 10 V, from 1485 V without pulsing to 1495 V when using pulsed extraction. This small difference is broadly in accord with the ion trajectory simulations presented in Sect. 4.2.

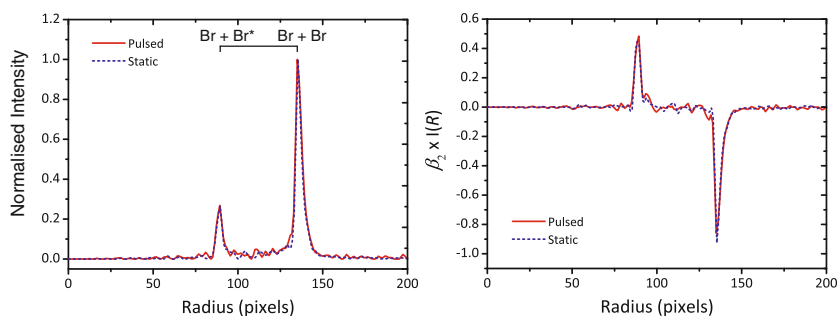
4.3.1 CCD Images

In order to accurately measure the effect of pulsed extraction on the velocity-mapping capabilities of the apparatus, a high-resolution CCD camera (Photonic Science, 576×768 pixels) was used to record images of both the photoelectrons and photoions. Representative photoelectron and ion images, obtained using both static and pulsed extraction fields and acquired with the Photonic Science CCD camera, are presented in Panel A of Fig. 4.4. The images were necessarily recorded on separate acquisitions due to the low frame rate of the CCD camera. The ion images contain contributions from both the ^{79}Br and ^{81}Br isotopes. The repeller electrode potential was set at -5 kV for imaging of the photoelectrons and $+2\text{ kV}$ for the photoions. The images obtained represent an improvement in the resolution achieved previously [18], and provide a useful benchmark against which to measure the success of pulsed extraction ion-electron velocity-map imaging. The ion images consist of two sharp rings, with the inner ring corresponding to production of $\text{Br} + \text{Br}^*$ via the $\text{B}^3\Pi_u(0_u^+)$ electronic state, and the outer ring corresponding to dissociation via the $\text{A}^3\Pi_u(1_u)$ electronic state, resulting in the production of $\text{Br} + \text{Br}$. The contrasting anisotropies of the two rings reflect the different symmetries of the A and B electronic states. The photoelectron images consist of four sharp rings, corresponding to ionisation of ground state bromine atoms to form ions in the $^1\text{D}_2$ and $^3\text{P}_J$ electronic states, as identified by the comb above the photoelectron speed distribution shown in Panel C of Fig. 4.4.

A: Images



B: Ion Parameters



C: Electron Parameters

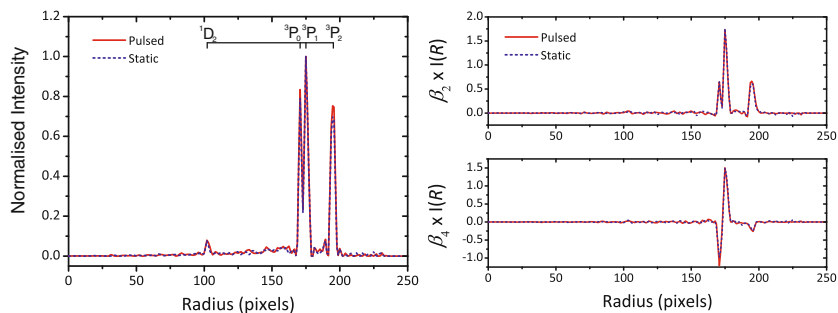


Fig. 4.4 **a** Images of the ions and electrons produced following the photodissociation of Br_2 at 446.41 nm, extracted using either static or pulsed fields and recorded using the high-resolution CCD camera. **b** Speed distributions and anisotropy parameters extracted from the ion images presented in **a**. **c** Speed distributions and anisotropy parameters extracted from the electron images presented in **b**

The two sets of images presented in Panel A of Fig. 4.4, acquired using pulsed and static extraction fields, appear very similar, with the two sets of images practically indistinguishable from one another. Furthermore, both the speed distributions and anisotropy parameters, obtained using the pBASEX algorithm and presented in

Panels B and C of Fig. 4.4, are in excellent agreement. The velocity-mapping condition appears to have been fully satisfied, with the velocity resolution of the ion image obtained with switching comparable to that obtained by conventional means.

4.3.2 PImMS Images

In order to capture images of both the photoelectrons and photoions on each acquisition cycle, it was necessary to replace the high-resolution CCD camera with a fast imaging device, in this case the PImMS1 camera. Since the ions are detected with a lower efficiency than the photoelectrons, due to their higher mass and lower kinetic energy, the voltages applied to the detector were pulsed slightly higher between the arrival of the electrons and ions in order to equalise the gain achieved for both species. For the photoelectrons, the detector was operated with 900 V applied across each MCP and 2500 V between the back face of the MCPs and the phosphor screen. For the detection of ions, the voltage applied across each MCP was increased to 950 V. At the time of acquisition, the clock cycle of the PImMS camera was limited to 25 ns. However, this time-resolution was easily sufficient to resolve not only the ion and electron images, but more impressively the two bromine isotopes, ^{79}Br and ^{81}Br . Figure 4.5 presents the time-of-flight spectrum, and ion and electron images recorded using the PImMS camera, demonstrating the concurrent acquisition of both the electrons and ions on a single detector with a good velocity-mapping resolution.

Whilst the PImMS camera significantly enriches the data available, the prototype PImMS1 sensor suffers from a relatively modest pixel resolution when compared to conventional CCD cameras. Figure 4.6 compares the ion and photoelectron images and associated parameters extracted using the pBASEX algorithm, as recorded using both the PImMS and CCD cameras. It should be noted that when these images were acquired the PImMS calibration was not so well implemented as it is now. As a result,

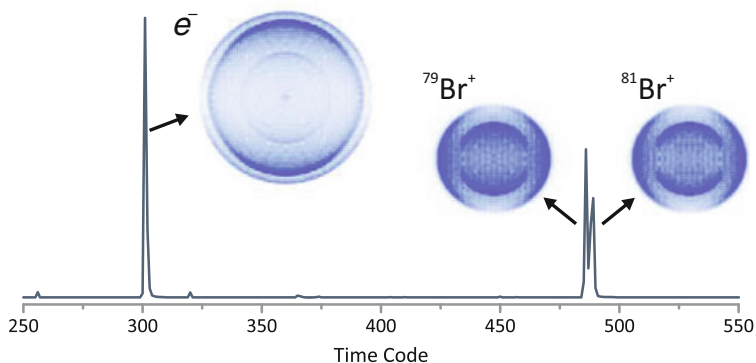


Fig. 4.5 Time-of-flight spectrum and images recorded using the PImMS camera and pulsed extraction of the ions and electrons

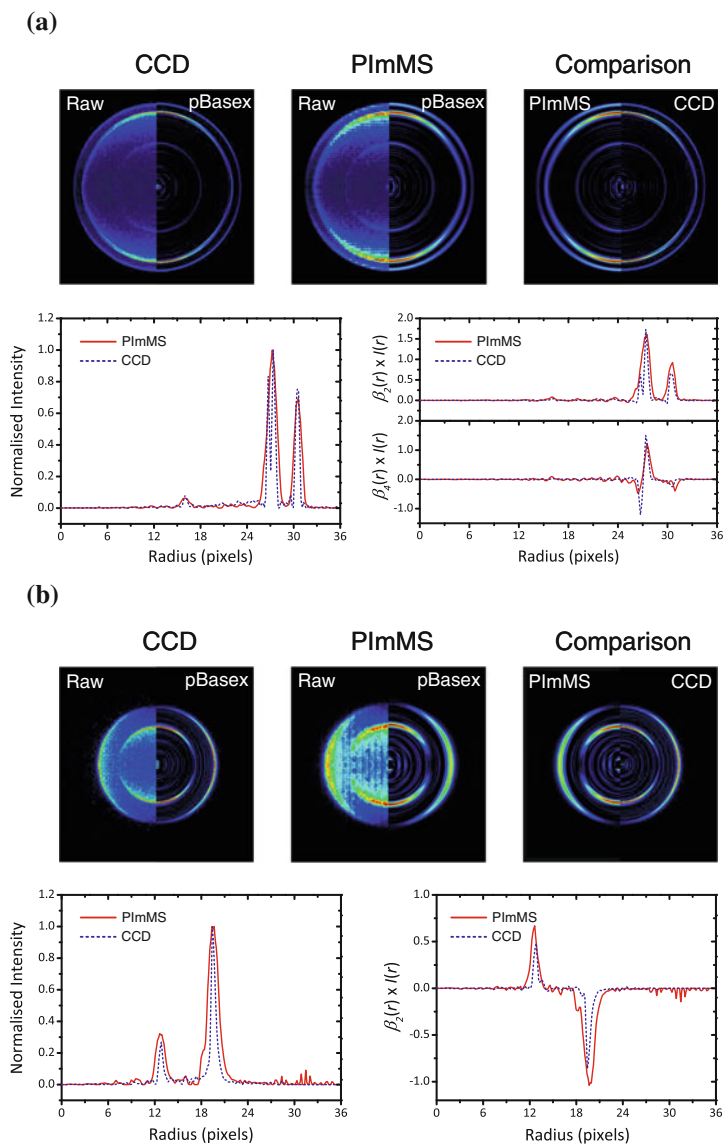


Fig. 4.6 Images of the electrons (a) and ions (b) produced following the photodissociation of Br_2 at 446.41 nm, extracted using pulsed fields and recorded using either the high-resolution CCD camera or the PImMS camera. The associated speed and anisotropy parameters, extracted from the images using pBASEX, are plotted below the images. The anisotropy parameters have been weighted by the normalised speed distributions in order to enhance the important features. The parameters extracted from the CCD camera have been rescaled to overlay with those extracted from the PImMS camera

the ion and electron images recorded using the PImMS camera contain some systematic artefacts due to the varying pixel-to-pixel sensitivity of the sensor. However, notwithstanding these limitations, the images are generally in very good agreement, with the major features of the images reproduced by both cameras. Perhaps unsurprisingly, the more limited resolution of the PImMS camera compared to the conventional CCD camera has led to a decreased velocity resolution in both the ion and electron images. In the photoelectron image, this has resulted in the two closely spaced peaks at a radius of approximately 27 pixels (corresponding to ionisation of ground state atomic bromine to ions in the 3P_0 and 3P_1 electronic states) becoming unresolved in the PImMS speed distribution. The two peaks are, however, still distinguishable through their anisotropy parameters, with the β_4 coefficient changing sign within the band. That the general agreement between the two data sets is good demonstrates that for many imaging purposes the resolution of the prototype PImMS1 sensor is sufficient to extract meaningful and scientifically pertinent information.

4.4 Measurement of the Detection Efficiency

The concurrent detection of both the photoelectrons and photoions resulting uniquely from a single photochemical process provides a useful opportunity to measure the efficiencies with which both photofragments are detected experimentally. The detection efficiencies of the photoions and photoelectrons may be determined through a statistical analysis of the shot-by-shot experimental data recorded using the PImMS camera, as follows.

Within each laser shot there will be a discrete number of photoionisation events, N_E . For a given N_E and a known detection probability, the number of photoions and photoelectrons detected within a single acquisition cycle may be described by a binomial probability distribution:

$$Bin(n_i, n_e; N_E, P_i, P_e) = \binom{N_E}{n_i} P_i^{n_i} (1 - P_i)^{N_E - n_i} \quad (4.2)$$

$$\times \binom{N_E}{n_e} P_e^{n_e} (1 - P_e)^{N_E - n_e}, \quad (4.3)$$

where n_i and n_e are, respectively, the number of detected ions and electrons, and P_i and P_e are their respective detection probabilities. Over a large number of acquisition cycles, the probability of detecting n_i ions and n_e electrons is given by

$$P(n_i, n_e; P_i, P_e) = \sum_{N_E} f(N_E) \times Bin(n_i, n_e; N_E, P_i, P_e), \quad (4.4)$$

where $f(N_E)$ is the probability of N_E events occurring within a single acquisition cycle. From the experimental data, the ratio of the detection efficiencies, P_i/P_e , may

be determined from the ratio of the number of ions and electrons detected, N_i/N_e . The unknown quantities are the absolute detection efficiencies, P_i and P_e , and the event frequency distribution, $f(N_E)$. By fitting Eq. 4.4 to the experimental data it is possible to determine the form of $f(N_E)$ and the values P_i and P_e .

The fitting of the experimental data to Eq. 4.4 was achieved by both global and local fitting methods. The global fitting procedure employs a genetic algorithm to optimise a set of $(N_{E,\max} + 2)$ coefficients, one describing the weighting of each term in Eq. 4.4 and a further two parameterising the values of P_i and P_e . This fitting procedure outputs a single, minimised set of coefficients, but does not provide any information on the shape of the parameter space. Therefore, a second, local fitting procedure was used in which the values of P_i and P_e were fixed, and a genetic algorithm was used to optimise the weighting of each term in Eq. 4.4. As the ratio of the detection efficiencies is known from the experimental data, by trialling different detection efficiencies and recording the converged best-fit on each occasion, a representation of the parameter space may be determined.

The results of fitting Eq. 4.4 to experimental data taken using the PImMS camera are presented in Figs. 4.7 and 4.8. Panels (a) and (b) of Fig. 4.7 plot, respectively, the experimentally observed and the fitted probability ($P(n_i, n_e)$) of observing a given number of electrons (n_e) and ions (n_i) in each laser shot. The agreement between the experimental and fitted distributions is so close as to make the two almost indistinguishable. Panel (c) plots the residuals between the fit and the experimental distribution, illustrating that there is, in fact, a small difference between the two distributions. The pattern of the residuals suggests that the true distribution is offset slightly along the vertical axis (n_e) and has a slightly lower gradient than the fitted distribution. This effect suggests that there is a small amount of background electron signal not belonging to Br^+ ions in the electron images, causing an imperfect fit of the data. This effect, however, is small and should not significantly affect the accuracy of the parameters extracted from the analysis. Figure 4.8 plots the results of both the local and global fitting routines. The local fitting points form a well-defined curve with a single minimum, representing the optimal detection efficiency of the electrons. The points are fitted to a polynomial curve ($N = 8$), with a minimum at 43.5 % (41.2 % for the ions). The global fitting returned a value of 43.6 ± 0.06 % for the electron detection probability (41.3 % for the ions), represented by the broken

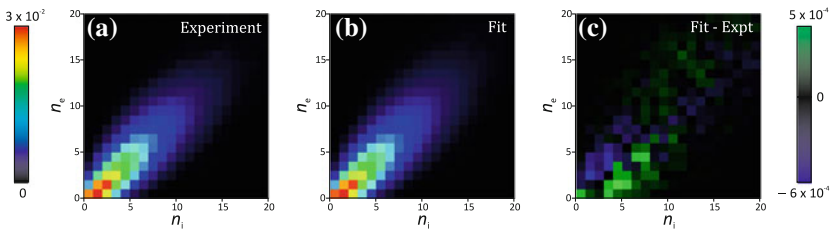


Fig. 4.7 Panels **a** and **b** show the experimental and fitted $f(n_i, n_e)$ distributions. Panel **c** plots the residuals between the fit and the experimental data

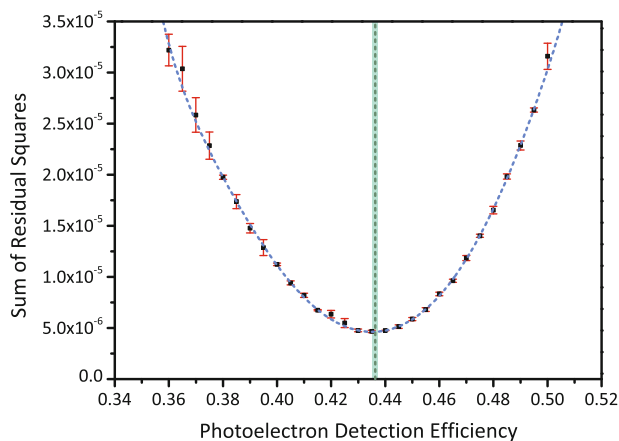


Fig. 4.8 The results of the local and global detection efficiency fitting procedures. The *black points* are the minimised sum of residual squares achieved for each detection efficiency using the local fitting method, with the error bars representing the 2σ uncertainty. The *broken blue curve* is a polynomial fit to the data. The *vertical green line* represents optimised detection efficiency as determined by the global fitting procedure, with the *green shading* representing the 2σ error

green vertical line in Fig. 4.8d. That the global and local fitting methods are in such close agreement is encouraging. Furthermore, the absolute values are physically very plausible, given the open area ratio of the MCPs (55.4%) and the use of high voltages on the detector to achieve high gain. It should be noted that the open area ratio of the MCPs generally represents the upper limit of the detection efficiency as charged particles must enter a pore in order to be detected. In this case the MCPs were obscured by a fine nickel mesh (95% transmittance), reducing the effective open area to 52.6%. The average value of the global and local fitting methods of 43.55% represents 83.1% of this effective open area ratio, suggesting that the PImMS camera is capable of recording events on the phosphor screen with a very high efficiency. This is particularly important in coincidence spectroscopy, where a high detection efficiency is desirable in order to maximise the number of genuine coincidences that are recorded.

4.5 Discussion

The work presented in this chapter has demonstrated that it is possible to extract and velocity-map both the ions and electrons produced following photoionisation onto a single detector in each acquisition cycle. The implication is that, with minor modifications, a conventional ion imaging apparatus equipped with a fast imaging detector, such as the PImMS camera, has the potential for use as an effective photoelectron-photoion coincidence (PEPICO) imaging spectrometer. Additionally, through the

concurrent detection of both the photoelectrons and photoions resulting from the photodissociation of molecular bromine at 446.41 nm and a statistical fitting of the data, the experimental detection efficiencies of the electrons and ions have been measured. The absolute detection efficiencies measured suggest that both the ions and electrons are detected with a relatively high probability, implying that the PImMS camera is ideally suited to the measurement of coincidences or correlations between photofragments.

References

1. T. Seideman, *J. Chem. Phys.* **107**, 10420 (1997)
2. K.L. Reid, J.G. Underwood, *J. Chem. Phys.* **112**, 3643 (2000)
3. Y. Arasaki, K. Takatsuka, K. Wang, V. McKoy, *J. Chem. Phys.* **112**, 8871 (2000)
4. K. McCulloh, T. Sharp, and H. Rosenstock, *J. Chem. Phys.* **42**, 3501 (1965)
5. J.A. Davies, J.E. LeClaire, R.E. Continetti, C.C. Hayden, *J. Chem. Phys.* **111**, 1 (1999)
6. N. Bhargava Ram, C.S. Lehmann, M.H.M. Janssen, *Eur. Phys. J. Web Conf.* **41**, 02029 (2013)
7. J.A. Davies, R.E. Continetti, D.W. Chandler, C.C. Hayden, *Phys. Rev. Lett.* **84**, 5983 (2000)
8. O. Geßner, A.M.D. Lee, J.P. Shaffer, H. Reisler, S.V. Levchenko, A.I. Krylov, J.G. Underwood, H. Shi, A.L.L. East, D.M. Wardlaw, E.t.H. Chrysostom, C.C. Hayden, and A. Stolow, *Science* **311**, 219 (2006)
9. U. Becker, *J. Electron Spectro. Relat. Phenom.* **112**, 47 (2000)
10. M. Lebeck, J.C. Houver, D. Doweck, *Rev. Sci. Instrum.* **73**, 1866 (2002)
11. A. Matsuda, M. Fushitani, A. Hishikawa, *J. Electron Spectrosc. Relat. Phenom.* **169**, 97 (2009)
12. A. Vredenburg, W.G. Roeterdink, M.H.M. Janssen, *Rev. Sci. Instrum.* **79**, 063108 (2008)
13. A. Bodi, M. Johnson, T. Gerber, Z. Gengeliczki, B. Sztray, T. Baer, *Rev. Sci. Instrum.* **80**, 034101 (2009)
14. X. Tang, X. Zhou, M. Niu, S. Liu, J. Sun, X. Shan, F. Liu, L. Sheng, *Rev. Sci. Instrum.* **80**, 113101 (2009)
15. F. Burmeister, L.H. Coutinho, R.R.T. Marinho, M.G.P. Homem, M.A.A. de Moraes, A. Mocellin, O. Bjrneholm, S.L. Sorensen, P.T. Fonseca, A. Lindgren, A. Naves de Brito, *J. Electron Spectrosc. Relat. Phenom.* **180**, 6 (2010)
16. C.S. Lehmann, N. Bhargava Ram, D. Irimia, M.H.M. Janssen, *Faraday Discuss.* **153**, 173 (2011)
17. D. Townsend, M.P. Minitti, A.G. Suits, *Rev. Sci. Instrum.* **74**, 2530 (2003)
18. P.C. Samartzis, T.N. Kitsopoulos, M.N.R. Ashfold, *Phys. Chem. Chem. Phys.* **2**, 453 (2000)

Chapter 5

Principles of Coulomb Explosion Imaging

This chapter introduces the concept of Coulomb explosion imaging (CEI), which is central to the work presented in Chaps. 6 and 7. The important principles upon which the technique is based are described, and the current capabilities and limitations of such experiments are discussed in the context of recent work.

5.1 Background and Motivation

The rapid development of the field of femtochemistry over recent years has revolutionised the study of molecular dynamics. A tantalising prospect is that of the ‘molecular movie’, in which the detailed structure of a chemical system is recorded as the reaction unfolds. However, achieving this level of insight is not without its challenges. It is a difficult undertaking to perform such measurements without significantly perturbing the structure of the target system as a direct result of performing the measurement itself. Furthermore, the structure of a molecular system represents a substantial amount of information, with three coordinates describing the position of each atom. Therefore, in order to determine the full structure of a molecule it is necessary to record a data set rich in information content.

The recent development of X-ray free-electron lasers (XFELs) [1] has brought closer the realisation of coherent diffraction imaging of non-crystalline materials on an ultrashort timescale. These new X-ray sources are capable of delivering optically coherent femtosecond pulses with a peak brilliance some nine orders of magnitude higher than that of conventional synchrotron sources. It has been suggested that these ultrashort, intense, and coherent light sources have the potential to generate diffraction signals from individual macromolecules on a femtosecond timescale, such that all structural information is collected before radiation damage can occur [2, 3].

This approach is known as ‘diffract before destroy’ and, if successful, holds much promise for the fields of structural biology, materials science, and potentially chemical dynamics. Although very much in its infancy (the world’s first XFEL facility, the Linac Coherent Light Source in Stanford, was only commissioned in 2009), promising proof-of-principle experiments demonstrating coherent diffraction imaging of single nanoscale particles have already been performed [4–7]. These initial successes have given rise to a new field of nanocrystallography on a femtosecond timescale [8–10].

The feasibility of performing diffraction experiments on individual molecules is still contentious and the subject of active study, with the timescales and mechanisms of radiation damage being of critical importance to the success of this approach [10, 11]. Additionally, as the size of the molecules is reduced, the probability of scattering photons in sufficient numbers to yield meaningful diffraction images becomes diminishingly small. For large biomolecules it may be possible to perform ultrafast X-ray diffraction on individual target molecules, but this is unlikely to be a realistic goal for smaller molecular systems, such as those of interest to the chemical dynamics community. For these reasons, alternative strategies have been investigated in the pursuit of the ultimate goal of deducing molecular structure on an ultrafast timescale. At the forefront of these efforts lies Coulomb explosion imaging.

5.2 Coulomb Explosion Imaging

Femtosecond Coulomb explosion imaging (CEI) aims to provide structural information of molecular systems on an ultrafast timescale through the investigation of the fragmentation dynamics of highly charged molecular ions. The first stage of CEI involves the rapid removal of several electrons from the target molecule, usually using an ultrafast radiation source, to produce a multivalent ion in a highly charged state. The resulting intramolecular Coulomb repulsion forces far outweigh the binding energy of this highly charged, unstable molecular ion, resulting in rapid break-up into several fragment ions. Since the forces governing the process of molecular dissociation are primarily Coulombic in nature, the dynamics of molecular dissociation may be described, to a good approximation, using classical laws of motion in a Coulomb potential.

Figure 5.1 illustrates the main principles of CEI and its application to pump-probe time-resolved studies of chemical dynamics. A non-stationary state is prepared through excitation of the ground state wavefunction by a pump laser pulse at time zero. The system is then allowed to evolve for some short time, Δt , whereafter the wave packet is projected onto a Coulomb potential energy surface, typically through rapid photoionisation, resulting in a Franck-Condon-type transition. Following ionisation, the system rapidly dissociates into atomic or fragment ions. The use of Coulomb explosion as a probe of molecular structure therefore depends upon three main assumptions. Firstly, the process of ionisation from the neutral to the highly charged molecular cation must occur on a timescale that is short compared to

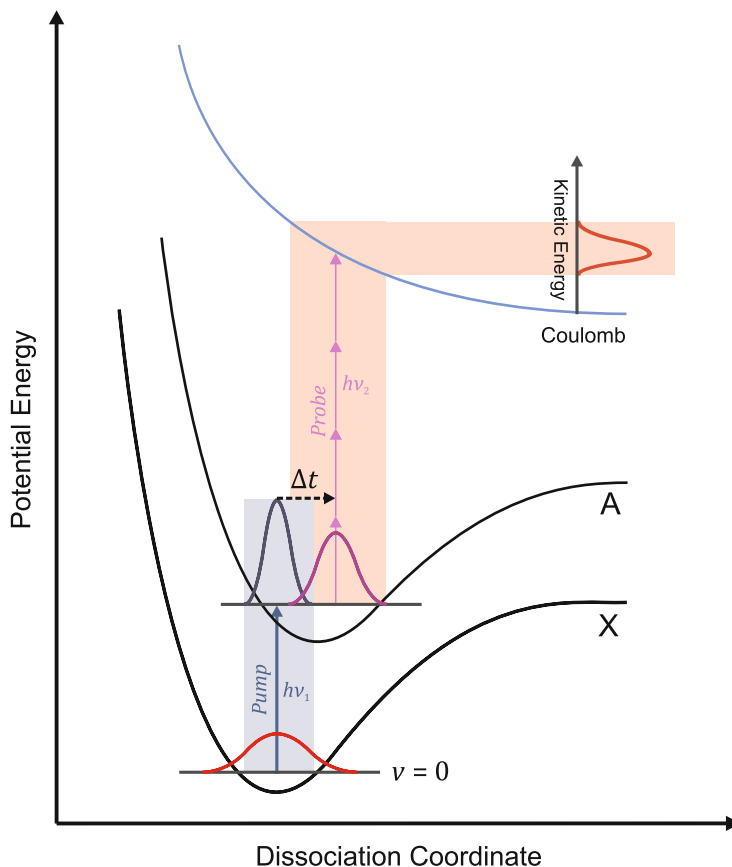


Fig. 5.1 Illustration demonstrating the principles of CEI when used in an ultrafast time-resolved pump-probe experiment. The initial ground state wavefunction is pumped into some excited potential energy surface, yielding a non-stationary state. The system is then left unobserved for a short time period, Δt , during which time the initially prepared wave packet evolves. A probe laser pulse then rapidly ionises the intermediate state to form a highly charged molecular ion. The transfer of the wave packet onto a Coulomb potential energy surface results in prompt dissociation of the system under the influence of electrostatic repulsion, yielding a number of fragment ions with velocities characteristic of the intermediate geometry of the system immediately prior to Coulomb explosion

the dynamics of the Coulomb explosion process, such that the initial coordinates of the atoms comprising the parent molecule are well-defined. Secondly, the potential energy surface upon which dissociation occurs is assumed to be entirely Coulombic in nature, and that the ions pursue classical trajectories according to Newton's laws of motion. Finally, it is assumed that the total charge of the molecular ion is partitioned between the constituent atoms at the instant of ionisation, and that the charges remain localised in this way throughout the Coulomb explosion. In this way, the final, experimentally observed charges of the ions map directly onto the initial

charge distribution in the nascent molecular ion. If significant charge redistribution occurs on a timescale comparable to molecular break-up, the interpretation of the dynamics becomes rapidly more complex. In general, if these conditions are satisfied, CEI may be considered a suitable probe of the molecular structure of the neutral system immediately prior to Coulomb explosion.

5.2.1 Methods of Ionisation

5.2.1.1 High-Energy Photon Sources

The technique of CEI was first demonstrated by firing a fast beam of singly charged molecular ions through a thin foil, stripping a large number of valence electrons from the molecule on a timescale of approximately 100 as to yield highly charged, multivalent molecular ions [12, 13]. Following this, an alternative method of inducing Coulomb explosion was developed that involves directing fast beams of atomic ions at targets of neutral molecules to induce multiple ionisation followed by Coulomb explosion [14]. However, the considerable interest in the development of time-resolved experiments capable of recording the ‘molecular movie’ have led to the development of optical means of inducing Coulomb explosion of neutral molecules on an ultrafast timescale.

Typically, photoabsorption of a single photon up to an energy of approximately 30 eV results in the removal of a single electron from the target system. However, absorption of photons exceeding this threshold tends to result in double, triple, or even higher order photoionisation as the dominant processes. For diatomic and triatomic molecules, these relatively low charge states are often highly unstable with respect to Coulomb explosion. Generation of photons of these energies is not within the capabilities of conventional laser systems and other light sources are therefore required. In the laboratory, fixed energy lines from atomic discharge lamps are capable of generating photons of up to about 50 eV in energy [15]. However, in order to achieve higher energies or tunable light sources it is necessary to use the output from large scale synchrotron facilities [1, 16].

Generally, photoionisation using VUV or soft X-ray light sources depends on core-hole formation followed by sequential ionisation through Auger-type cascades to yield highly charged molecular ions. Recently, the availability of XFELs has made multiphoton ionisation by high energy X-ray photons experimentally accessible. Through high energy multiphoton absorption, the creation of multiple core vacancies becomes possible, allowing higher charge states to be achieved through Auger-type processes than is possible using conventional synchrotron radiation sources. Double or multiple core-hole creation has been demonstrated for a wide range of target species, ranging from isolated atoms [17–19] to diatomics [20–22] and rare gas clusters [23], with charge states as high as 36+ observed for Xe atoms [19].

The Coulomb explosion of small molecular systems following multiphoton ionisation by XFEL light sources has only just begun to be explored. The most recently

reported work depends upon multiphoton absorption by a single atom of high mass within a molecule, such as selenium or iodine, to yield highly charged molecular ions following Auger-type cascade ionisation [24]. In these applications, the inclusion of high- Z atoms is desirable due to the large absorption cross section of heavy atoms, resulting in efficient multiphoton absorption and subsequent ionisation. Due to the localisation of charge build-up on the high- Z constituents, the mechanism of Coulomb explosion necessarily relies on some degree of charge redistribution to the rest of the molecular environment prior to break-up, somewhat complicating the dynamics of these processes. Measurement of the kinetic energies of the resulting ionic fragments reveals that the atomic nuclei are considerably displaced on a timescale comparable to the ionisation process [24], which is further compounded by the presence of local charge ‘hot spots’ in the vicinity of the high- Z constituents. Furthermore, the timescales of ionisation are defined by the XFEL pulse duration and the lifetime of the core-holes with respect to electronic relaxation through Auger decay. In atomic systems, these lifetimes range anywhere from 10 as to tens of fs [25]. However, in molecular systems the processes of relaxation will be affected by the local chemical environment, causing the lifetimes to differ from the values observed for isolated atomic species [26, 27].

5.2.1.2 Optical Laser Systems

The use of synchrotron and XFEL light sources to induce Coulomb explosion in highly charged molecules certainly has its advantages. Pulse durations as short as a few femtoseconds are possible and excitation energies are well-defined. A particularly attractive feature of ionisation by high energy photons is that the related absorption cross sections are insensitive to the relative molecular orientation with respect to the polarisation of the ionising light source, thereby removing spatial anisotropy effects that may complicate the interpretation of experimental data. However, despite these advantages, there are obvious impracticalities associated with the use of such facilities. Due to the incredibly high cost and limited number of synchrotron and XFEL light sources, beam time is severely restricted and highly competitive. The logistics of transporting experiments large distances to operate for short periods of time are far from trivial, and the pressures on time are necessarily a cause of compromise.

The most widespread Coulomb explosion method relies, therefore, on irradiation of neutral molecules by tabletop intense ultrashort laser pulses typically in the visible or near infrared region [28–32], most commonly using the output of a Ti:Sapphire laser system at around 800 nm. These laser systems are capable of producing pulse durations below 5 fs [33], with peak intensities high enough to induce substantial multiple ionisation almost universally. The use of ultrafast tabletop light sources obviates the need for storage ring based radiation sources, and renders Coulomb explosion possible for the vast majority of molecules in a conventional laboratory environment. Importantly, the use of ultrafast optical lasers also enables timing of

the Coulomb explosion event such that studies of time-resolved dynamics become possible through pump-probe measurements.

When Coulomb explosion is driven by ultrafast optical laser systems, the interpretation of the fragmentation dynamics depends crucially on the ionising pulse duration. The mechanism of ionisation proceeds via a sequential process, in which the charge state of the molecule is gradually increased through the stepwise removal of valence electrons. For small molecular systems, the removal of the first few electrons may be sufficient to trigger Coulomb explosion, which proceeds on a potential energy surface that is distorted by the ionising laser field. Depending on the pulse duration and intensity, further electrons may be removed from the molecule on a timescale comparable to the initial displacement of the atomic nuclei, potentially complicating the interpretation of the dissociation dynamics. Since ionisation in intense laser fields is a highly non-linear process, it is likely that the time window within which ionisation may occur will be far shorter than the actual pulse duration. Nevertheless, if meaningful conclusions pertaining to the structure of the neutral molecule prior to Coulomb explosion are to be drawn from the data, it is crucial that the pulse duration is kept as short as possible. Commercially available tabletop Ti:Sapphire oscillators are capable of generating pulses as short as 5 fs. However, during the amplification phase these pulses are broadened significantly and must be recompressed back to the original pulse length before they can be used effectively for CEI (as described in Sect. 2.3.6).

Although it is necessary to limit the duration of the ionising laser pulse, it has been experimentally observed that, even for pulse durations as long as 50 fs, precise measurements of dissociating wave packets, or ‘picostructures’, are possible for relatively heavy molecules such as I_2 [32]. Furthermore, few-cycle optical laser pulses of shorter than 10 fs in duration bring into reach to possibility of measuring elements of molecular structure for even the lightest molecules with an accuracy better than typical molecular bond lengths. Impressively, the evolution and recurrence of vibrational wave packets of H_2 [34] and D_2^+ [35] have been probed in remarkable detail using pulse durations of 7 fs. Corkum and co-workers have also compared the geometries calculated from CEI of D_2O and SO_2 using 8 and 40 fs laser pulses at 800 nm to the known ab initio structures and found a generally good level of agreement [36]. While the absolute values determined through a fitting to classical trajectory simulations were not in perfect agreement with the ab initio parameters, the general structures of the molecules were reproduced on a scale of considerably less than a molecular bond length, with the closest agreement observed when using the shorter pulse duration.

5.2.2 Ionisation by Intense Laser Fields

Strong field ionisation by intense laser pulses differs substantially from conventional multiphoton ionisation. Where the intensity of the ionising radiation source exceeds $\sim 10^{14} \text{ W cm}^{-2}$, the laser field becomes comparable in strength to the Coulombic

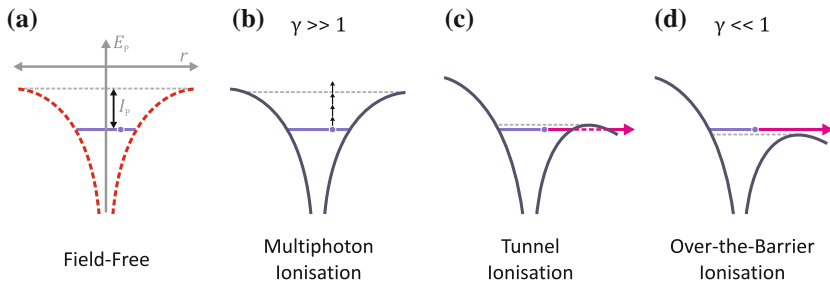


Fig. 5.2 Illustration of the various ionisation schemes in intense laser fields for an atomic Coulomb potential. The unperturbed potential is shown in **a**, where I_P denotes the field-free ionisation potential, or binding energy. **b–d** illustrate the distortion of the Coulombic potential by the external field, resulting in multiphoton, tunnelling, and over-the-barrier ionisation, respectively. See text for further details

interaction between the electrons and the nucleus. The effect of the ionising radiation can therefore no longer be considered using standard low-order perturbation theory, and a new theoretical framework must be sought.

Whenever the energy of a single photon is much less than the binding energy of the electrons, the process of photoionisation by intense laser fields may be divided into three regimes: multiphoton ionisation, tunnelling ionisation, and over-the-barrier ionisation. These three processes are illustrated schematically in Fig. 5.2. The three regimes may be understood rather simply by considering the relative magnitude of the laser field compared to the ionisation potential of the atom or molecule. If the external field is conservative compared to the binding energy of the electrons, the process may be treated using higher order perturbation theory, and ionisation proceeds via multiphoton absorption, as depicted in Fig. 5.2b. As the magnitude of the external field is increased, the potential experienced by the electrons becomes substantially deformed, lowering the barrier to ionisation sufficiently such that the tunnelling of bound electrons into the continuum becomes the dominant mechanism of ionisation. Eventually, when the external field becomes sufficiently strong, the barrier to ionisation is reduced below the binding energy of the electrons, resulting in over-the-barrier ionisation. An approximate indication of which of these three mechanisms is likely to dominate is given by the Keldysh parameter [37]:

$$\gamma = \sqrt{\frac{I_P}{2U_P}}, \quad (5.1)$$

where I_P is the field-free ionisation potential and U_P is the ponderomotive energy of the electron, defined as

$$U_P = \frac{e^2 E_0^2}{4m_e \omega^2}, \quad (5.2)$$

where E_0 and ω are the amplitude and angular frequency of the ionising radiation, respectively. The ponderomotive energy represents the energy imparted to the electron due to the oscillating, or quiver, motion at the frequency of the laser. The value of the Keldysh parameter may be used to infer the nature of ionisation in intense laser fields. For situations in which $\gamma \gg 1$, multiphoton ionisation dominates. In this case, either the binding energy far exceeds the magnitude of the external field or the frequency of the oscillations is much faster than the tunnelling rate of the electrons. In the case of $\gamma \ll 1$, strong field ionisation dominates, leading to tunnelling and over-the-barrier ionisation.

The theory outlined above relies on two main assumptions: the quasi-static, and single active electron (SAE) approximations. The quasi-static, or adiabatic approximation, assumes that the timescale of electron motion inside the atom or molecule is much faster than the periodic oscillations of the electric field. The electrons are therefore considered to respond instantaneously to the electric field, in a manner analogous to the well-known Born-Oppenheimer approximation [38]. The single active electron (SAE) approximation assumes that the laser field interacts with a single electron in the potential well. In atomic systems, these conditions are easily met under most conditions; the length scale of an atom is sufficiently short such that the electron may traverse the potential well on a timescale far shorter than the period of the laser field, and there are rarely accessible doubly excited electronic states below the ionisation limit. The SAE description has therefore been exceptionally successful in describing the behaviour of atoms [39, 40] and small molecules [41] in intense laser fields.

In the strong field ionisation of molecules, however, the adiabatic and SAE approximations often fail to account for the observations of experiment. The original Keldysh theory does not account for electron dynamics within the potential, assuming an instantaneous response to the laser field. As the path length of delocalised electron motion in conjugated systems lengthens, the timescales of electron motion within the potential become comparable to the laser frequency, causing a break-down of the quasi-static approximation. Furthermore, doubly excited states below the ionisation threshold are far more common in molecules than in atoms, particularly in the case of extended conjugated systems, rendering the SAE approximation invalid. As a result, where electron dynamics within the molecule become important, the Keldysh parameter becomes meaningless, and a more complex treatment is required based upon non-adiabatic multi-electron (NME) dynamics [42].

5.3 Molecular Alignment

The use of CEI to extract structurally pertinent information requires the measurement of the momenta of the ionic products of dissociation and their respective correlations in order that the absolute configuration of the system may be determined. The predominant method of achieving this has been the detection of the full three-dimensional (3D) momentum vectors of all fragments from each individual dissociation event. This is possible through the use of multiparticle 3D imaging detectors coupled with

coincidence analysis [43–45]. The information content accessible through such measurement schemes is extremely high and has recently enabled the determination of the absolute configuration of small chiral molecules [30]. However, there are limitations on the suitability of detecting the full 3D velocities of the product photoions when the structures of large, polyatomic molecules are to be measured. In these cases, the time-of-flight spectra will often be highly congested, with a large number of photofragments of different m/z arriving at the detector within a short time in each acquisition cycle. The requirement to stretch each ion peak in time according to the initial z -velocities of the photofragments renders the measurement of the full 3D velocities unsuitable as this unavoidably causes neighbouring peaks in the time-of-flight spectrum to overlap, resulting in ambiguity in the chemical identity of each ion detected. For this reason, in the experiments described in Chaps. 6 and 7 of this thesis, laser-induced alignment of the target molecules was exploited to increase the information content of two-dimensional photofragment velocity data.

5.3.1 Principles of Laser-Induced Alignment

The confinement of the spatial orientations of molecules using laser pulses was proposed by Friedrich and Herschbach in 1991 [46] and involves the fixing of one or more molecular axes in the laboratory frame using a linearly polarised non-resonant electromagnetic field. In a non-aligned ensemble the spatial orientation of each molecule will be randomly distributed, as shown in Fig. 5.3a. Through the application of non-resonant laser pulses, it is possible to induce either preferential alignment or orientation of the molecules, where alignment and orientation have separate and distinct definitions. In an aligned ensemble the primary axis of the molecules preferentially lies parallel to some spatial vector, but the distribution remains symmetric with respect to inversion with half the molecules pointing ‘up’ and half pointing ‘down’ (Fig. 5.3b). An oriented ensemble, on the other hand, has no such inversion symmetry, with the molecules being both aligned and preferentially pointing in the

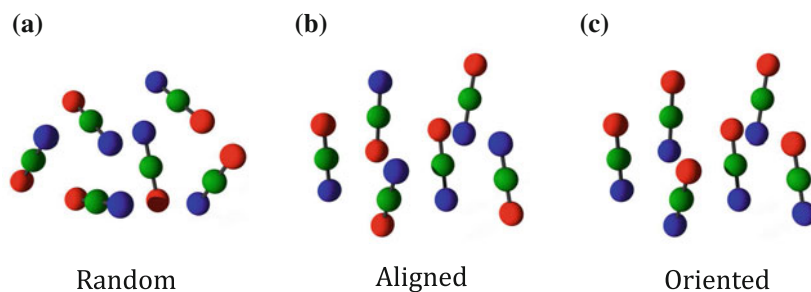


Fig. 5.3 Illustration of the differences between a non-aligned (a), aligned (b), and oriented (c) molecular ensemble. See text for further details

same direction, as illustrated by Fig. 5.3c. While it is possible to induce orientation of molecules using a combination of non-resonant laser irradiation and static electric fields [47], this was not exploited in the work described in this thesis and will therefore not be explored in any further detail here.

Broadly, laser-induced alignment may be categorised according to the duration of the pulse envelope into two regimes: adiabatic and non-adiabatic, as reported by Seideman [48] and Friedrich et al. [49]. In the case of adiabatic alignment, the laser pulse duration is long with respect to the molecular rotational period ($\tau_{\text{pulse}} > T_{\text{rot}}$) [50], and the pulse envelope varies slowly with time. The method of action depends on the anisotropic interaction of the induced dipole moment with the electric field vector of the laser pulse. This interaction causes the mixing of the molecular rotational quantum states, leading to the formation of pendular states directed along the laser field polarisation axis [49, 51]. Conversely, non-adiabatic alignment results from the use of laser pulses which are short compared to the natural rotational period of the molecules ($\tau_{\text{pulse}} < T_{\text{rot}}$). Non-adiabatic alignment results from the propagation of a rotational wave packet formed from a coherent superposition of several rotational eigenstates, which causes transient and recurrent alignment of the molecular ensemble.

In the experiments described in the following chapters, adiabatic alignment was achieved through irradiation of the target molecules by the fundamental output (1064 nm) of a seeded nanosecond Nd:YAG laser, while non-adiabatic alignment was observed following the application of a femtosecond ‘kick’ pulse to induce torsional motion in substituted biphenyl derivatives, as reported in Chap. 7.

5.3.1.1 Adiabatic Alignment

The mechanism of adiabatic alignment depends on the interaction of the anisotropic polarisability tensor of the molecules with the oscillating electric field of a non-resonant laser pulse with a duration that is long compared to the characteristic rotational period of the target molecules. This interaction results in the creation of directionally localised superpositions of the rotational eigenstates of the target molecules, confining the most polarisable axis (MPA) of the molecules to be parallel to the laser polarisation.

The electric vector of the alignment laser pulse is described in the time domain by

$$\mathbf{E}(t) = \boldsymbol{\varepsilon}(t) \cos(\omega t), \quad (5.3)$$

where ω is the frequency, and $\boldsymbol{\varepsilon}(t)$ is the time-dependent electric field vector, given by

$$\boldsymbol{\varepsilon}(t) = E_0 \boldsymbol{\epsilon} \varepsilon(t), \quad (5.4)$$

where E_0 is the magnitude of the electric field, ϵ is a unit vector along the polarisation axis, and $\varepsilon(t)$ describes the temporal evolution of the pulse envelope. The induced potential (V_{ind}) experienced by a molecule in a laser field described by Eq. 5.3 will be, to leading order, determined by the interaction of the polarisability and permanent dipole moment of the molecule with the oscillating electric field. However, since the electric field oscillates with a far higher frequency than the typical rotational period of the target molecules, and the pulse duration is long ($\tau_{\text{pulse}} > T_{\text{rot}}$), the interaction with the permanent dipole moment averages to zero [52]. In contrast, the interaction with the polarisability of the molecule relies on the coupling of the electrons, rather than the nuclear framework, to the oscillating field, resulting in a non-zero contribution to the induced potential. If it is assumed that the polarisability tensor of the molecule is diagonal in the same major axis system as the moment of inertia, the laser-induced potential is given by

$$V_{\text{ind}}(t) = -\frac{1}{2} \sum_i \alpha_{ii} |\mathbf{E}_i(t)|^2, \quad (5.5)$$

where α_{ii} is the ii polarisability component with respect to the molecular frame. Furthermore, in the limiting case where the evolution of the pulse envelope is slow compared to the natural rotational period of the target molecules, the explicit dependence of the rapid oscillations may be disregarded, reducing Eq. 5.5 to

$$V_{\text{ind}}(t) = -\frac{1}{4} \varepsilon^2(t) \sum_i \alpha_{ii} |E_{0,i}(t)|^2, \quad (5.6)$$

where the additional factor of $1/2$ results from the time average of $\cos^2(\omega t)$. For a molecule in a non-resonant laser field the total energy is given by

$$\hat{H} = \hat{H}_0 + V_{\text{ind}}, \quad (5.7)$$

where \hat{H} is the total Hamiltonian and \hat{H}_0 is the Hamiltonian in the absence of an applied laser field. If the polarisability tensor is anisotropic in the molecular frame, the value of V_{ind} will depend on the spatial alignment of the molecule with respect to the polarisation of the alignment laser pulse. Consequently, the laser field exerts a torque on the molecules, guiding them towards the most energetically favourable geometry, in which the interaction of the polarisability tensor with the oscillating electric field is greatest. This results in alignment of the target molecules in the laboratory frame, with the MPA aligned parallel to the major component of the oscillating electric field. Thus, the alignment of the molecules in the laboratory frame may be controlled through a manipulation of the polarisation axis of the electric field vector of the alignment laser pulse.

A more detailed understanding of the mechanism of adiabatic alignment may be sought by considering the relationship between the field-free rotational eigenstates of the molecules and their counterparts in the presence of an oscillating laser field.

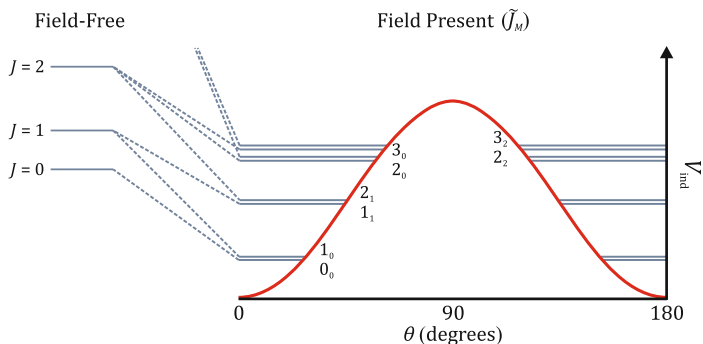


Fig. 5.4 Sketch of the lowest lying field-free rotational states and field-dressed pendular states for a linear molecule. The *broken lines* illustrate the adiabatic coupling between the field-free and field-dressed states, demonstrating that the lowest lying rotational states correspond to the lowest lying pendular states. The parameter θ refers to the angle between the MPA of the molecule and the polarisation vector of the alignment laser field. The energies of the levels are not shown to scale and the splitting of the near-degenerate pairs of pendular states has been enlarged for illustrative purposes. The notation of the pendular states is given as \tilde{J}_M , where \tilde{J} is the rotational angular momentum quantum number and $M\hbar$ is the projection onto the z -axis. Adapted from Ref. [53]

According to the adiabatic theorem, the slowly varying alignment pulse envelope transfers each of the field-free rotational eigenstates to separate pendular states in the presence of a rapidly oscillating electric field [54]. The pendular states may be expressed as superpositions of the field-free rotational eigenstates and, in the case of linear polarisation of the alignment pulse, correspond to librational motion of the MPA of the molecules about the electric field polarisation vector. Figure 5.4 illustrates the transfer of the field-free rotational eigenstates to the corresponding pendular states for the case of a linear molecule. From this sketch, some important principles of non-adiabatic alignment may be identified. Crucially, as a result of the adiabatic approximation, the occupation of the pendular states is identical to the initial rotational distribution. Since the lowest lying pendular states are the most tightly confined in their librational motion, the initial rotational temperature of the distribution is directly related to the degree of alignment that may be achieved for a given field strength [55]. Furthermore, the degree of alignment will be greatest when the perturbation of the field-free Hamiltonian is greatest, according to Eq. 5.7. Since the value of V_{ind} depends on both the polarisability and the magnitude of the alignment field strength, these parameters are crucially important in determining the degree of alignment possible. In the case of the polarisability tensor, it is not only the size, but also the relative magnitudes of the orthogonal components that determine the overall degree of alignment, with a greater anisotropy in the polarisability leading to a greater degree of alignment.

Adiabatic alignment has proved to be a very effective means of achieving highly aligned molecular ensembles [56]. However, since alignment depends on the presence of the laser field, the dynamics of the system under investigation may be influenced

somewhat as a result. This is an unavoidable consequence of the adiabatic coupling of the field-free rotational eigenstates and the field-dressed pendular states. In the absence of the external field, each of the pendular states is returned to their initial field-free rotational states, at which point no alignment of the ensemble remains.

5.3.2 *Non-adiabatic Alignment*

Non-adiabatic alignment refers to the confinement of the MPA of the target molecules in the laboratory frame using a linearly polarised laser pulse of short duration with respect to the rotational period ($\tau_{\text{pulse}} < T_{\text{rot}}$). A correct theoretical description of the mechanism of adiabatic alignment depends on a numerical solution to the time-dependent Schrödinger equation [57, 58]. However, it is possible to explain the process in a more intuitive sense, both quantum mechanically and classically, without recourse to such detailed mathematics.

The quantum mechanical description involves the preparation of a non-stationary state composed of a coherent superposition of rotational eigenstates through non-resonant stimulated Raman transitions [48]. Transient time-dependent alignment results from the periodic rephasing and dephasing of the rotational states comprising the wave packet. This recurrent alignment allows the possibility of performing experiments on aligned molecular ensembles in the absence of an external laser field.

A classical description of non-adiabatic alignment may be sought by considering the induced angular momentum imparted to the molecules as a result of a short kick pulse, which is known as the δ -kick model [59–61]. The salient result of this classical model is that, for small angles, the induced angular velocities of the MPA towards the linear polarisation vector of the non-adiabatic alignment pulse will be proportional to the value of θ , where θ is the initial angle between the MPA and the electric field polarisation vector. Therefore, at a certain time after the initial kick pulse, the MPA of the molecules in the ensemble will transiently align parallel to the electric field polarisation. The δ -kick model also correctly predicts that confinement of the MPA will be strongest for an initially prealigned distribution, such that the value of θ is already small and the above approximations become valid.

Non-adiabatic alignment is attractive primarily due to the recurrent nature of the alignment which allows for the possibility of measuring properties of molecules fixed in the laboratory frame in the absence of an external field. However, the degree of alignment achievable through non-adiabatic means is not as good as that afforded by adiabatic methods, either for the initial alignment or for the subsequent revivals.

5.3.3 *3D Alignment*

So far, the discussion has been restricted to confinement of the MPA of a molecule, with the remaining orthogonal axes having free rotation in the plane perpendicular

to the polarisation of the electric field. However, asymmetric top molecules have complex 3D structures and all three axes must be confined if the molecule is to be considered truly fixed in space. In the case of a rigid molecular framework, if two orthogonal molecular axes are controlled, this necessarily implies the confinement of the third. If this condition is achieved, the molecules may be considered to be 3D aligned.

To achieve 3D confinement, the electric field must have two orthogonal components. This may be achieved experimentally by a number of different schemes, using either adiabatic laser pulses [62], non-adiabatic laser pulses [63], or a combination of the two [64, 65]. Perhaps the simplest way of achieving 3D alignment is to use an elliptically polarised adiabatic laser field. In this case the induced potential depends on all three Euler angles, with a global minimum when the MPA and second most polarisable axis (SMPA) are confined parallel to the major and minor components of the electric field respectively [66]. Experimentally, 3D alignment using elliptically polarised nanosecond laser pulses has been demonstrated for substituted benzene rings [62, 67] and substituted biphenyl derivatives [68], and is the method employed to achieve 3D alignment of the substituted biphenyl molecules in Chaps. 6 and 7 of this thesis.

5.4 Summary

This chapter has introduced some of the important theoretical and experimental principles upon which the technique of Coulomb explosion imaging, as presented in this thesis, is grounded. While the Coulomb explosion dynamics of small molecules, particularly diatomic and triatomic species, has received much attention over the past couple of decades, comparatively little work has been targeted at understanding the behaviour of larger systems under similar conditions. To this end, the following chapter considers the Coulomb explosion dynamics of a substituted biphenyl molecule by a tabletop femtosecond pulsed laser, investigating the relationship between the structure of the parent molecule and the asymptotic recoil velocities of the fragment ions. Chapter 7 builds upon this work, using CEI to infer the instantaneous value of the dihedral angle following torsional excitation of the molecule by a femtosecond ‘kick’ pulse. This work demonstrates that it is indeed possible to use CEI as a sensitive probe of molecular structure on an ultrafast timescale.

References

1. J. Ullrich, A. Rudenko, R. Moshhammer, *Annu. Rev. Phys. Chem.* **63**, 635 (2012)
2. R. Neutze, R. Wouts, E. Weckert, D. van der Spoel, J. Hajdu, *Nature* **406**, 752 (2000)
3. S.P. Hau-Riege, R.A. London, A. Szoke, *Phys. Rev. E* **69**, 051906 (2004)
4. M.M. Seibert et al., *Nature* **470**, 78 (2011)
5. T. Gorkhover et al., *Phys. Rev. Lett.* **108**, 245005 (2012)

6. N.D. Loh et al., *Nature* **486**, 513 (2012)
7. S. Kassemeyer et al., *Opt. Express* **20**, 4149 (2012)
8. H.N. Chapman et al., *Nature* **470**, 73 (2011)
9. A. Barty et al., *Nature Photonics* **6**, 35 (2012)
10. L. Lomb et al., *Phys. Rev. B* **84**, 214111 (2011)
11. A. Barty et al., *Opt. Express* **17**, 15508 (2009)
12. E.P. Kanter et al., *Phys. Rev. A* **20**, 834 (1979)
13. Z. Vager, R. Naaman, E. Kanter, *Science* **244**, 426 (1989)
14. U. Werner, K. Beckord, J. Becker, H. Lutz, *Phys. Rev. Lett.* **74**, 1962 (1995)
15. P. Baltzer, L. Karlsson, *Phys. Rev. A* **38**, 2322 (1988)
16. H. Winick, *Synchrotron Radiation Sources: A Primer*, vol. 1, Series on Synchrotron Radiation Techniques and Applications (World Scientific, London, 1994)
17. L. Young et al., *Nature* **466**, 56 (2010)
18. G. Doumy et al., *Phys. Rev. Lett.* **106**, 083002 (2011)
19. B. Rudek et al., *Nat. Photonics* **6**, 858 (2012)
20. M. Hoener et al., *Phys. Rev. Lett.* **104**, 253002 (2010)
21. J.P. Cryan et al., *Phys. Rev. Lett.* **105**, 083004 (2010)
22. N. Berrah et al., *Proc. Natl. Acad. Sci. USA* **108**, 16912 (2011)
23. S. Schorb et al., *Phys. Rev. Lett.* **108**, 233401 (2012)
24. B.M.D. Erk, Fragmentation dynamics of small molecules upon multiple ionization by X-Ray free-electron laser pulses, Ph.D. thesis, Ruperto-Carola-University of Heidelberg, Germany 2013
25. J.L. Campbell, T. Papp, *At. Data Nucl. Data Tables* **77**, 1 (2001)
26. M. Covic, T.D. Thomas, *Phys. Rev. A* **43**, 6053 (1991)
27. I. Nenner, P. Morin, *VUV and Soft X-Ray Photoionization*, 1st edn. (Springer, New York City, 1996)
28. K. Codling, L. Frasninski, *J. Phys. B* **26**, 783 (1993)
29. J. Gagnon, K.F. Lee, D.M. Rayner, P.B. Corkum, V.R. Bhardwaj, *J. Phys. B* **41**, 215104 (2008)
30. M. Pitzer, M. Kunitski, A.S. Johnson, T. Jahnke, H. Sann, F. Sturm, L.P.H. Schmidt, H. Schmidt-Böcking, R. Dörner, J. Stohner, J. Kiedrowski, M. Reggelin, S. Marquardt, A. Schießer, R. Berger, M.S. Schöffler, *Science* **341**, 1096 (2013)
31. A. Hishikawa, A. Iwamae, K. Hoshina, M. Kono, K. Yamanouchi, *Chem. Phys. Lett.* **282**, 283 (1998)
32. J.H. Sanderson et al., *Phys. Rev. A* **59**, R2567 (1999)
33. A. Baltuska, Z. Wei, M.S. Pshenichnikov, D.A. Wiersma, *Opt. Lett.* **22**, 102 (1997)
34. A. Rudenko, Th Ergler, B. Feuerstein, K. Zrost, C.D. Schröter, R. Moshhammer, J. Ullrich, *Chem. Phys.* **329**, 193 (2006)
35. T. Ergler, A. Rudenko, B. Feuerstein, K. Zrost, C.D. Schröter, R. Moshhammer, J. Ullrich, *Phys. Rev. Lett.* **97**, 193001 (2006)
36. F. Légaré, K.F. Lee, I.V. Litvinyuk, P.W. Dooley, S.S. Wesolowski, P.R. Bunker, P. Dombi, F. Krausz, A.D. Bandrauk, D.M. Villeneuve, P.B. Corkum, *Phys. Rev. A* **71**, 013415 (2005)
37. L.V. Keldysh, *Sov. Phys. JETP* **20**, 1307 (1965)
38. M. Born, R. Oppenheimer, *Zur Quantentheorie der Molekeln* **84**, 457 (1927)
39. S. Augst, D. Strickland, D.D. Meyerhofer, S.L. Chin, J.H. Eberly, *Phys. Rev. Lett.* **63**, 2212 (1989)
40. B. Walker, B. Sheehy, L.F. DiMauro, P. Agostini, K.J. Schafer, K.C. Kulander, *Phys. Rev. Lett.* **73**, 1227 (1994)
41. A. Talebpour, S. Laroche, S.L. Chin, *J. Phys. B* **31**, L49 (1998)
42. M. Lezius, V. Blanchet, D.M. Rayner, D.M. Villeneuve, A. Stolow, M.Yu. Ivanov, *Phys. Rev. Lett.* **86**, 51 (2001)
43. A. Faibis, W. Koenig, E. Kanter, Z. Vager, *Nucl. Instrum. Meth. B* **13**, 673 (1986)
44. J.A. Davies, J.E. LeClaire, R.E. Continetti, C.C. Hayden, *J. Chem. Phys.* **111**, 1 (1999)
45. J. Ullrich, R. Moshhammer, A. Dorn, R. Dörner, L.P.H. Schmidt, H. Schmidt-Böcking, *Rep. Prog. Phys.* **66**, 1463 (2003)

46. B. Friedrich, D.P. Pullman, D.R. Herschbach, *J. Phys. Chem.* **95**, 8118 (1991)
47. J.J. Omiste, M. Gärttner, P. Schmelcher, R. González-Férez, L. Holmegaard, J.H. Nielsen, H. Stapelfeldt, J. Küpper, *Phys. Chem. Chem. Phys.* **13**, 18815 (2011)
48. T. Seideman, *J. Chem. Phys.* **103**, 7887 (1995)
49. J. Ortigoso, M. Rodríguez, M. Gupta, B. Friedrich, *J. Chem. Phys.* **110**, 3870 (1999)
50. H. Stapelfeldt, T. Seideman, *Rev. Mod. Phys.* **75**, 543 (2003)
51. W. Kim, P. Felker, *J. Chem. Phys.* **104**, 1147 (1996)
52. B. Friedrich, D. Herschbach, *Phys. Rev. Lett.* **74**, 4623 (1995)
53. J.L. Hansen, Imaging molecular frame dynamics using spatially oriented molecules, Ph.D. thesis, Aarhus University, 2012
54. D.J. Griffiths, *Introduction to Quantum Mechanics*, 2nd edn. (Pearson Education, New Jersey, 2005)
55. V. Kumarappan, C.Z. Bisgaard, S.S. Viftrup, L. Holmegaard, H. Stapelfeldt, *J. Chem. Phys.* **125**, 194309 (2006)
56. L. Holmegaard, J.H. Nielsen, I. Nevo, H. Stapelfeldt, F. Filsinger, J. Küpper, G. Meijer, *Phys. Rev. Lett.* **102**, 023001 (2009)
57. T. Seideman, E. Hamilton, *Adv. At. Mol. Opt. Phys.* **52**, 289 (2005)
58. C.Z. Bisgaard, Laser induced alignment; towards fixed-in-space molecules, Ph.D. thesis, University of Aarhus, Denmark, 2006
59. I.S. Averbukh, R. Arvieu, *Phys. Rev. Lett.* **87**, 163601 (2001)
60. M. Leibscher, I.S. Averbukh, H. Rabitz, *Phys. Rev. Lett.* **90**, 213001 (2003)
61. M. Leibscher, I.S. Averbukh, H. Rabitz, *Phys. Rev. A* **69**, 013402 (2004)
62. J.J. Larsen, K. Hald, N. Bjerre, H. Stapelfeldt, T. Seideman, *Phys. Rev. Lett.* **85**, 2470 (2000)
63. K.F. Lee, D.M. Villeneuve, P.B. Corkum, A. Stolow, J.G. Underwood, *Phys. Rev. Lett.* **97**, 173001 (2006)
64. S.S. Viftrup, V. Kumarappan, S. Trippel, H. Stapelfeldt, E. Hamilton, T. Seideman, *Phys. Rev. Lett.* **99**, 143602 (2007)
65. S.S. Viftrup, V. Kumarappan, L. Holmegaard, C.Z. Bisgaard, H. Stapelfeldt, M. Artamonov, E. Hamilton, T. Seideman, *Phys. Rev. A* **79**, 023404 (2009)
66. J.J. Larsen, Laser induced alignment of neutral molecules, Ph.D. thesis, University of Aarhus, Denmark, 2000
67. I. Nevo, L. Holmegaard, J.H. Nielsen, J.L. Hansen, H. Stapelfeldt, F. Filsinger, G. Meijer, J. Küpper, *Phys. Chem. Chem. Phys.* **11**, 9912 (2009)
68. J.L. Hansen, J.H. Nielsen, C.B. Madsen, A.T. Lindhardt, M.P. Johansson, T. Skrydstrup, L.B. Madsen, H. Stapelfeldt, *J. Chem. Phys.* **136**, 204310 (2012)

Chapter 6

Investigations of Coulomb Explosion Dynamics

This chapter demonstrates the application of the PImMS camera to laser-induced Coulomb explosion imaging (CEI) of a substituted biphenyl molecule. The multi-hit capabilities of the device allow the concurrent detection of individual 2D momentum images of all ionic fragments resulting from the Coulomb explosion of multiple molecules during each acquisition cycle. Correlations between the recoil directions of the fragment ions are determined through a covariance analysis. In combination with the ability to align the molecules in space prior to the Coulomb explosion event, the experimental results presented in this chapter demonstrate that it is possible to extract extensive information pertaining to the parent molecular structure and fragmentation dynamics following strong field ionisation. Preliminary simulations of the Coulomb explosion dynamics suggest that such an approach may hold promise for determining elements of molecular structure on a femtosecond timescale, bringing the concept of the ‘molecular movie’ closer to realisation.

The experiments presented in this chapter were performed at the University of Aarhus in collaboration with Prof. Henrik Stapelfeldt and his research group.

6.1 Introduction

As discussed in the preceding chapter, CEI using tabletop femtosecond laser systems in the visible or near-IR has shown much promise for the determination of molecular structure on an ultrafast timescale. So far, investigations of the usefulness of CEI as an effective probe of molecular structure have largely been confined to diatomic, triatomic, or small polyatomic systems, such as H_2 [1], SO_2 [2], and substituted methyl derivatives [3]. The experiments reported in this chapter explore the potential of CEI for determining elements of molecular structure of large polyatomic systems, using a substituted biphenyl molecule ($\text{RMM} = 373$) as an example of such a target. The conventional means of determining the configuration and absolute structure of a molecule following Coulomb explosion depends on the concurrent measurement of the individual 3D momenta of all fragment ions following molecular fragmentation.

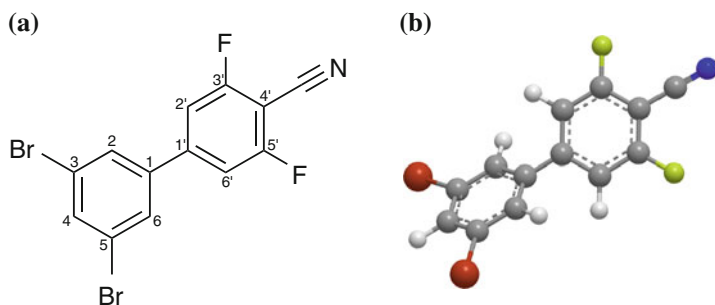


Fig. 6.1 **a** Skeleton and **b** ball and stick representations of 3,5-dibromo-3',5'-difluoro-4'-cyanobiphenyl

The relationships between these 3D momenta are determined through a coincidence analysis, thereby allowing inferences to be made on the parent molecular structure. However, due to the large number of fragment ions that are necessarily produced following Coulomb explosion of such extended structures, alternative strategies to 3D momentum imaging, based on a statistical correlation of 2D fragment ion momenta and prealignment of the spatial orientations of the target molecules, are investigated.

6.1.1 The Molecule

The target molecules used in this study were those of 3,5-dibromo-3',5'-difluoro-4'-cyanobiphenyl ($C_{13}H_5F_2Br_2N$, DBrDFCNBph), the structure of which is shown in Fig. 6.1. DBrDFCNBph is not commercially available and was synthesised specifically for these experiments following the procedure described in the appendix of Ref. [4]. The biphenyl molecules consist of two substituted phenyl rings linked by a single carbon-carbon (C–C) bond. The first phenyl ring is substituted with two bromine atoms at the 3 and 5 positions. The second phenyl ring is substituted with two fluorine atoms at the 3' and 5' positions and with a nitrile group (CN) at the 4' position. The molecules possess a stereogenic axis that lies along the C–C bond between the two phenyl rings, which is also the C_2 symmetry axis. Rotation about this axis takes place on a torsional potential energy surface, which has two equal minima when the angle between the rings is $\pm 39^\circ$ [4]. The two conformers that result from localisation around these minima are the R_a ($+39^\circ$) and S_a (-39°) enantiomers.¹ At room temperature, the molecules have sufficient energy to overcome the potential barrier between the two enantiomeric conformers, resulting in free rotation of the phenyl rings about the central C–C bond. However, at the low temperatures achieved

¹In this case, the angle refers to that between the two phenyl rings when observed along the stereogenic axis, with the ring of higher priority (the Br-substituted ring) pointing towards the observer.

through the supersonic expansion of the gaseous sample into the vacuum chamber (~ 1 K), the molecules are effectively frozen into one of the two enantiomeric forms.

The structure of DBrDFCNBph makes it an attractive target molecule for the study of Coulomb explosion dynamics for a number of reasons. Firstly, the inclusion of the CN group dramatically increases the permanent dipole moment of the molecule (4.4 Debye as opposed to 0.2 Debye without), thereby allowing for efficient deflection of the molecules according to their rotational states using the electrostatic deflector. By focussing the alignment and Coulomb explosion laser pulses onto the most deflected part of the molecular beam, which contains molecules that occupy the lowest rotational quantum states, it is therefore possible to achieve a high degree of alignment of the target molecules [4], which aids the interpretation of the measured ion trajectory correlations. As well as possessing a large permanent dipole moment, the molecule has a highly anisotropic polarisability, which is an important prerequisite for achieving efficient preferential alignment of the most polarisable axis (MPA) of the molecules in the laboratory frame. Furthermore, the MPA coincides with the C_2 symmetry axis of the molecules, thereby allowing a straightforward interpretation of the alignment of the molecules relative to the polarisation of the adiabatic alignment laser pulse. In addition to the molecules being highly amenable to efficient alignment, the biphenyl carbon skeleton provides a rigid framework upon which the peripheral substituents are arranged. The molecule therefore contains a number of well-defined structural coordinates that may be measured through CEI. For example, the two phenyl rings are easily distinguished through their substituents, and the CN group provides a useful probe of the orientation of the molecules. Finally, the molecule is composed of atoms spanning a wide range of different masses: from H atoms, with a mass of 1 Da, to Br atoms, with a mass of 81 Da. This allows for a relatively comprehensive study of the behaviour of a wide range of atoms under the conditions of Coulomb explosion.

6.1.2 Experimental Details

The experimental apparatus was described in detail in Sect. 2.3, so only the operational parameters will be considered in this section.

The voltages applied to the ion optics were $V_R = 7.5$ kV and $V_E = 5.0$ kV. The high extraction voltages were necessary in order to capture the majority of the high-velocity ions within the limits of the 40 mm detector. The use of such a high extraction field has the additional advantage that a large kinetic energy is imparted to the fragment ions, resulting in a high detection efficiency through efficient secondary electron production when the ions impact the surface of the microchannel plates [5]. To ensure efficient amplification of the ion signal by the detector, the MCPs were operated with a total potential difference across both plates of $V_{MCP} = 1.75$ kV. The effect of the phosphor screen voltage on the quality of the timing information using PImMS was investigated in detail in Sect. 2.5.3, where it was found that maintaining a high potential difference between the MCPs and the phosphor screen is desirable.

For this reason, the MCPs were operated at 4.75 kV to give a high photon yield without risking damage to the detector or causing each ion event to illuminate too many pixels of the PImMS camera. If the clusters were to become too large, there would be a significant risk of adjacent ion events overlapping, causing an incorrect counting and centroiding of the ions during post-processing (see Sect. 2.5.3 for details of the centroiding routine).

6.2 Adiabatic Alignment

To maximise the information content of the fragment ion momentum images, the molecules were 1D adiabatically aligned in space using a linearly polarized 10 ns (FWHM) pulse from an Nd:YAG laser (YAG pulse: $\lambda = 1064$ nm, $I_{\text{YAG}} = 8 \times 10^{11}$ W cm⁻²). When the YAG pulse is polarised perpendicular to the detector, the MPA of the molecules, which coincides with the C_2 symmetry axis, is confined along this direction. Thus, the molecules are imaged along the C_2 symmetry axis, as illustrated in Fig. 6.2a. Alternatively, with the YAG pulse polarised parallel to the detector, the molecules are imaged from a side-on perspective, as shown in Fig. 6.2b. In each case the molecules are 1D aligned and are free to rotate about the C_2 symmetry axis. Coulomb explosion was induced by a linearly polarised 30 fs (FWHM) probe pulse (probe pulse: $\lambda = 800$ nm, $I_{\text{probe}} = 3 \times 10^{14}$ W cm⁻²), which was overlapped in time and space with the YAG pulse. The polarisation of the probe pulse was parallel to the alignment laser pulse. The Nd:YAG laser system is limited to 20 Hz, which defines the maximum repetition rate of the experiment.

Experimentally, the degree of alignment may be assessed through inspection of the resulting ion images. Images of the N^+ and Br^+ fragments in both alignment geometries are presented in Fig. 6.2 to illustrate this point. A qualitative assessment of the degree of alignment may be gained through inspection of the general features of the ion images. In the case of perpendicular alignment the molecules are imaged along the C_2 -axis, as illustrated in Fig. 6.3a, whereas in the case of parallel alignment the molecules are imaged side-on, as illustrated in Fig. 6.3b. A reasonable approximation of the ion trajectories following Coulomb explosion may be made through the axial recoil approximation, in which the fragment ions corresponding to the peripheral substituents are considered to leave the molecule along the vector defined by their bond axis. Within this approximation, it is clear that the N^+ photofragments are ejected from the molecular parent ion parallel to the MPA since the $C\equiv N$ bond lies along the C_2 symmetry axis of the molecule. The ion images corresponding to the N^+ photofragments therefore represent an ideal probe of the alignment of the parent molecules prior to Coulomb explosion. In the case of perpendicular alignment, the N^+ ions will be ejected with the major component of velocity perpendicular to the plane of the detector. The N^+ ion image shown in Fig. 6.2a illustrates this clearly, with the N^+ ion intensity localised towards the centre of the image, corresponding to a low velocity in the xy -plane. Conversely, when the molecules are aligned parallel to the detector, the N^+ ion image (Fig. 6.2b) consists of two opposing maxima lying along

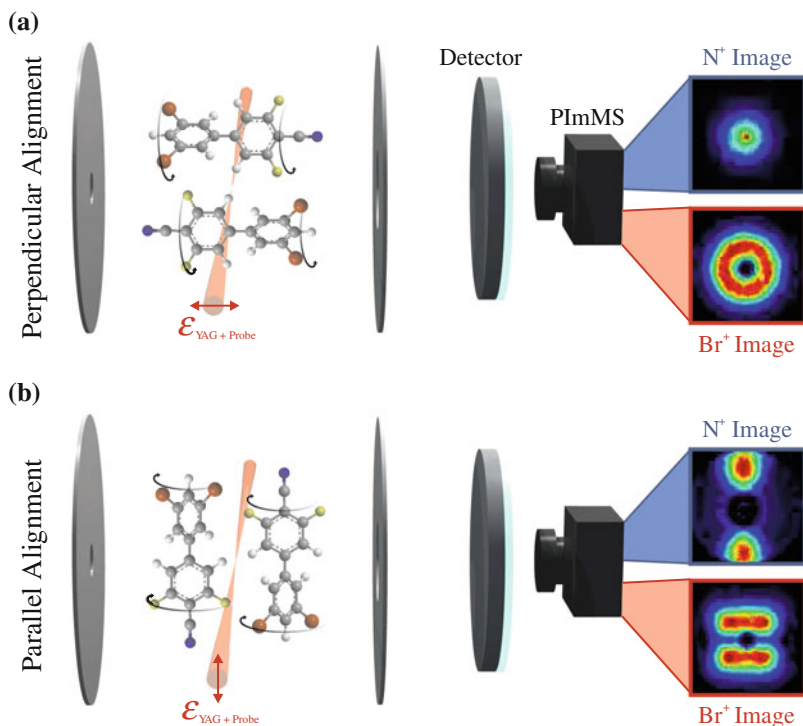


Fig. 6.2 Schematic illustration of **a** perpendicular and **b** parallel 1D laser-induced alignment, as used in the experiments described in this chapter. The molecules align with the MPA (in this case the C_2 symmetry axis) parallel to the polarisation of the alignment laser pulse. The alignment and probe pulses are both linearly polarised in the same direction. The laboratory frame images of the N^+ and Br^+ photofragments are shown in each case to illustrate the effect of alignment on the data. The alignment of the molecules is clear from the qualitative features of the images, as described in the text

the polarisation vector of the alignment laser pulse. The two maxima correspond to molecules that are oriented either ‘up’ or ‘down’ in the laboratory frame and are of equal intensity.

The signature of molecular alignment is also clearly present in the Br^+ ion images. According to the axial recoil approximation, in the laboratory frame the Br^+ ions will be ejected isotropically in two rings, or ‘doughnuts’, corresponding to the two orientations of the molecule when aligned. Figure 6.3 illustrates schematically the projection of these two rings of intensity onto the detector plane in the case of (a) perpendicular and (b) parallel alignment of the molecules under velocity-mapping conditions. In the case of perpendicular alignment, the two opposing orientations of the parent molecule are coincident in the plane of the detector, resulting in a single ring of intensity, as observed in the Br^+ ion image presented in Fig. 6.2a. When the molecules are aligned parallel to the detector plane, the two rings are imaged from a side-on perspective, resulting in two opposing bars

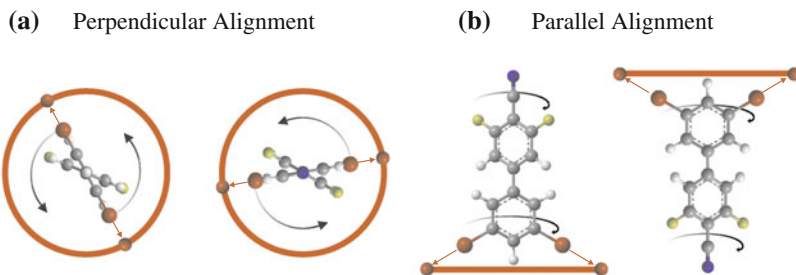


Fig. 6.3 Illustration of the alignment of the target molecules from the perspective of an observer located at the imaging detector for **a** perpendicular and **b** parallel 1D alignment. In both cases the molecules are aligned, not oriented. Therefore both orientations are equally likely and both are shown here. The *red arrows* illustrate the axial recoil trajectories of the Br^+ ions following Coulomb explosion. The *red shaded areas* illustrate schematically the expected ion impact coordinates of the bromine ions on the detector following ion extraction under velocity-mapping conditions

of intensity across the top and bottom of the images, as observed in the Br^+ ion image presented in Fig. 6.2b.

Whilst the above arguments demonstrate qualitatively that a strong degree of 1D alignment of the target molecules has been achieved, it is possible to extract a more quantitative measure of the degree of alignment through an analysis of the N^+ ion image taken with the molecules aligned parallel to the detector plane. The degree of alignment may be quantified through a calculation of the expectation value of $\cos^2 \theta$, where θ is the polar Euler angle between the C_2 symmetry axis of the molecule and the polarisation axis of the alignment laser pulse. A value of 0.5 corresponds to a totally isotropic distribution, whereas a value of 1 is the limiting value in the case of a perfectly aligned sample. From the N^+ ion image shown in Fig. 6.4a, $\langle \cos^2 \theta \rangle$

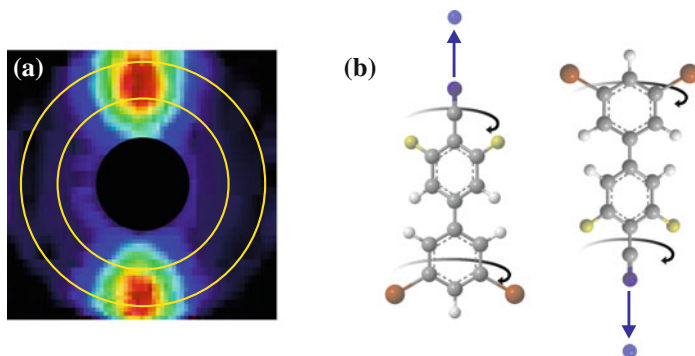


Fig. 6.4 a The N^+ ion image recorded following parallel alignment of the target molecules relative to the detector plane, as captured using the PImMS camera. The value of $\langle \cos^2 \theta \rangle$ for the area between the concentric *yellow circles* is calculated to be 0.87. **Panel b** shows the axial recoil of N^+ ions from the parent molecule, illustrating the usefulness of the N^+ ions as a probe of the degree of alignment

is calculated to be 0.87 when considering the intensity between the two concentric rings overlayed on Fig. 6.4a, which corresponds primarily to the contribution from N^+ ions. While this value is not as high as has been reported for iodobenzene, where a value of $\langle \cos^2 \theta \rangle$ of 0.96 has been observed [6], a high degree of alignment of the target molecules has clearly been achieved. The lower value of $\langle \cos^2 \theta \rangle$ measured in this case is likely due to a combination of factors. Firstly, in the work on iodobenzene only the most deflected ions, corresponding to the very lowest rotational states, were probed by Coulomb explosion. However, in the work presented here, the position of the probe pulse in the deflected beam was a compromise between achieving a good degree of alignment of the molecules and maintaining a high enough density in the target volume to yield the signal level required to achieve a satisfactory convergence of the covariance data in a limited time. A further reason for the reduced value of $\langle \cos^2 \theta \rangle$ is the overlap in the time-of-flight spectrum of the N^+ and C^+ peaks, resulting in a diffuse background signal corresponding to C^+ ions. Furthermore, such a measure of molecular alignment assumes complete axial recoil of the N^+ ions and takes no account of the dynamics of Coulomb explosion. The actual value of $\langle \cos^2 \theta \rangle$ corresponding to the N^+ ions alone will therefore likely be somewhat higher than the already favourable value of 0.87 reported here.

6.3 Time-of-Flight Spectra

The time-of-flight spectra following Coulomb explosion of DBrDFCNBph in parallel and perpendicular alignment, as recorded using the PImMS camera, are shown in Figs. 6.5 and 6.6, respectively. The data were recorded over 125,000 and 50,000

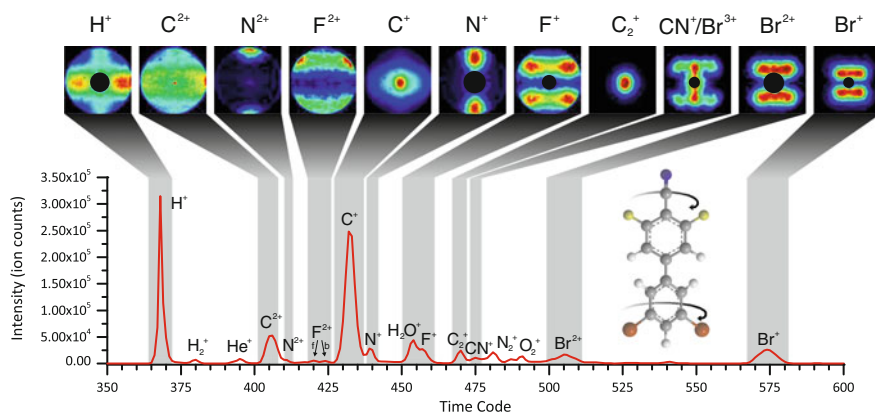


Fig. 6.5 Time-of-flight spectrum recorded using the PImMS camera following the Coulomb explosion of DBrDFCNBph aligned parallel to the detector plane. The peaks are assigned and images corresponding to a selection of fragment ions are shown above the time-of-flight spectrum. The *grey shading* identifies the range of time codes contributing to each image. Where appropriate, the forward- and backward-scattered peaks are identified by *arrows* labelled with ‘f’ and ‘b’, respectively

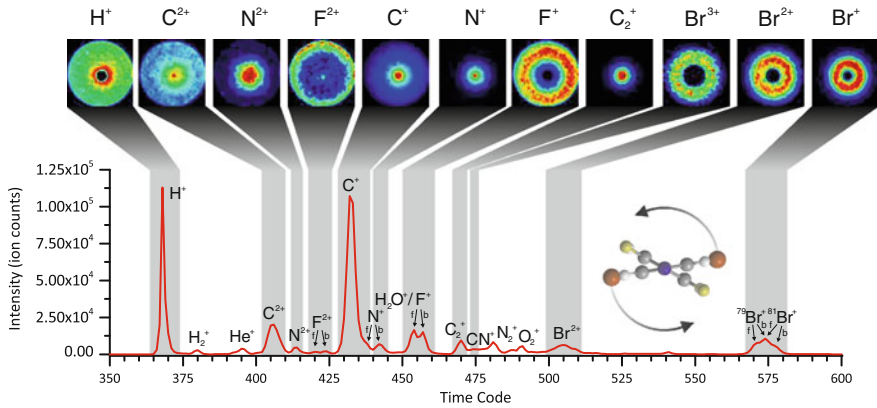


Fig. 6.6 Time-of-flight spectrum recorded using the PImMS camera following the Coulomb explosion of DBrDFCNBph aligned perpendicular to the detector plane. The peaks are assigned and images corresponding to a selection of fragment ions are shown above the time-of-flight spectrum. The grey shading identifies the range of time codes contributing to each image. Where appropriate, the forward- and backward-scattered peaks are identified by arrows labelled with ‘f’ and ‘b’, respectively

laser shots, respectively, and have been processed according to the scheme outlined in Sect. 2.5.3 in order to extract the most accurate timing information. Additionally, since the master trigger for the experiment was taken from the Ti:Sapphire laser system, it was necessary to trigger the PImMS camera from the previous laser shot. This is due to the delay between the PImMS camera receiving a trigger and the start of data acquisition by the sensor, which is on the order of $14 \mu\text{s}$. The time interval between successive laser shots is broadly consistent. However, a small amount of time jitter, on the order of a few PImMS time codes, was observed in the data. In order to reduce the effect of this time jitter, the time codes in each laser shot were shifted such that the H^+ signal was centred on time code 368. The H^+ peak was chosen for calibration as it is both intense and narrow, with $\sim 90\%$ of laser shots containing a signal from H^+ ions. The remaining $\sim 10\%$ of laser shots were left unshifted, which was the most probable correction applied to the data.

6.3.1 General Details of the Spectra

The data presented in Figs. 6.5 and 6.6 demonstrate the capabilities of the PImMS camera as an effective multi-mass imaging sensor. The spectra contain a large number of mass peaks, which are largely well-resolved and confidently assigned. The 12.5 ns timing resolution of the camera is clearly fully exploited, with features separated by only two or three time codes being clearly resolved. The mass spectra are highly congested in places, leading to the unavoidable overlap of some peaks. This is a

consequence of the high extraction voltages required to map the highly energetic ions onto the 40 mm detector. The use of such a high extraction field results in the entire mass spectrum spanning only 2.75 μs , somewhat restricting the mass-resolving capability of the experiment. Nevertheless, the majority of the important features are well-resolved and the additional velocity information provided by the spatial resolution of the camera aids the assignment of the peaks. In addition to the time-of-flight information, the overlapping ion signals often have significantly different velocity signatures, allowing their separation in the spatial domain. For example, the F^+ signal is coincident in the time domain with the signal from background water in the chamber. However, since the Coulomb explosion process imparts a substantial velocity to the fragment ions, the F^+ signal is easily separated from that of H_2O^+ , which has almost zero velocity and impacts exclusively on the centre of the detector. In several instances the contribution from background contaminants in the centre of the image has been removed. In addition to signal assigned to the Coulomb explosion of DBrDFCNBph, the time-of-flight spectra contain a number of peaks resulting from the ionisation of background gas in the target chamber, notably He^+ , H_2O^+ , N_2^+ , and O_2^+ . A further interesting observation is that several species exhibit a double peak structure, corresponding to forward- and backward-scattered ions, depending on the orientation of the molecules in the laboratory frame. This effect is particularly noticeable for the ions corresponding to N, F, and Br atoms in the case of perpendicular alignment.

From the mass spectra alone, some details of the Coulomb explosion process may be inferred. The most striking observation is that the vast majority of product fragments are atomic ions, with the contribution from diatomic or larger ionic fragments comprising the minority. The only non-atomic ion signals in the spectra are assigned to C_2^+ and CN^+ ions. It is possible that some minor contributions from other diatomic and larger fragment ions are present in the spectra, but these are so small as to be unassignable. The relatively low yield of CN^+ ions, when compared to the signal assigned to N^+ and N^{2+} ions, is perhaps surprising given the strength of the $\text{C}\equiv\text{N}$ bond in the parent molecule, which must be broken to yield nitrogen ions. These observations suggest that, in this case, Coulomb explosion is indeed dominated by the forces of Coulomb repulsion, with the majority of interatomic bonding destroyed during the process. Furthermore, the identification of doubly and triply charged atomic ions, including the highly energetically unfavourable F^{2+} and Br^{3+} , suggests that a substantial degree of charge is acquired by the parent molecule prior to fragmentation.

6.3.2 Ion Yields

Further insight into the mechanism of Coulomb explosion may be gained through an assessment of the relative yields of the various ionic photofragments, as presented in Table 6.1. The values in Table 6.1 were calculated from the integrals of the peaks in the time-of-flight spectrum, following Coulomb explosion of perpendicularly aligned

Table 6.1 Tabulated values of the ion intensities, as measured from the integrals of the peaks in the time-of-flight spectrum recorded following Coulomb explosion of perpendicularly aligned molecules

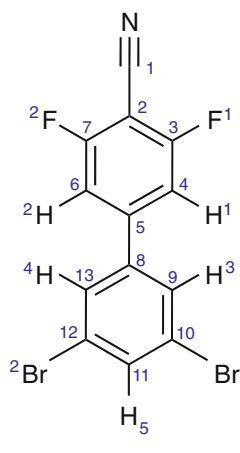
Parent atom	Ion	Cumulative I.E. (eV)	Intensity (Ion counts)	Total intensity	Relative intensity	Relative charge per atom	Calculated relative charge per atom		
							10+	14+	20+
H	H ⁺	13.6	195364	195364	5.00	1.00	1.00	1.00	1.00
	C ⁺	11.26	406006	499431	12.78	0.98	0.73	0.88	1.09
	C ²⁺	35.64	93425						
N	N ⁺	14.53	52740 ^a	81826	2.09	2.09	1.67	2.72	3.90
	N ²⁺	44.13	29086 ^a						
F	F ⁺	17.42	93766	105517	2.70	1.35	0.30	0.95	1.75
	F ²⁺	52.39	11751						
	Br ⁺	11.81	77973	149363	3.82	1.91	5.22	6.30	7.28
Br	Br ²⁺	33.4	51222						
	Br ³⁺	68.4	20168						

The cumulative ionisation energies are listed as an approximate guide to the energetics of production of each species. The calculated relative charge per atom is given for the ground state of three different total charge states of the molecule (10+, 14+, and 20+), and these values are calculated from the values presented in Fig. 6.7.

^aThe intensities quoted for the N peaks are double the integral of the backward-scattered peaks. This is due to the forward-scattered peaks being obscured in the time-of-flight spectrum.

target molecules. Since the atomic ions dominate the spectrum, only these have been considered in the ion yield calculations. The relative yields of the ions have been grouped according to the neutral parent and normalised such that the yield of H^+ ions is equal to 5, which corresponds to the stoichiometry of the parent molecule. From the data presented in Table 6.1, it is clear that the relative ion yields differ somewhat from those expected based on purely stoichiometric arguments. Although the relative yields of the hydrogen and carbon ions agree closely with the stoichiometry of the parent molecule (especially when it is noted that the contribution of the C_2^+ ions has been ignored, thereby reducing the relative yield of the carbon ions from the expected value of 13), the ion yields corresponding to the remaining substituents are somewhat higher than expected. The yield of the fluorine and bromine fragment ions is substantially higher than the value of 2 expected based purely on stoichiometric arguments, with observed yields of 2.70 and 3.82, respectively. The higher relative yield of bromine ions may be attributed to the much lower ionisation energy of bromine compared to fluorine, and the reduced collection efficiency of fluorine ions due to the limited size of the detector. However, the increased yield of fluorine ions relative to hydrogen and carbon ions is interesting, given the highly electronegative character of the atoms. The most pronounced enhancement in ion yield when compared to the stoichiometric ratios of the parent molecule is found for the nitrogen fragment ions, for which the ion yield is more than double that expected. The same trend is seen when the relative charges attributed to each substituent are calculated from the ion yields. By inference, the charge carried by ions corresponding to the peripheral N, F, and Br substituents is substantially higher than that calculated for the carbon skeleton.

The considerable enhancement of the ionisation yields of the peripheral substituents compared to the carbon skeleton is likely to be a reflection of the charge distribution in the nascent molecular ion immediately prior to Coulomb explosion. Therefore, electronic structure calculations were performed for various charge states of the molecular ion using a commercial software package (Gaussian Inc.) using Møller-Plesset perturbation theory (MP2) and the 6-311G** basis set. These calculations were performed on request by Dr C. Vallance. The geometry of the molecule was fixed as that of the equilibrium structure of the neutral parent molecule, calculated at density functional level of theory by colleagues at the University of Helsinki, according to the details presented in Refs. [7, 8]. The calculated equilibrium structure, along with the bond lengths, angles, and coordinates, are presented in Tables A.1 and A.2 of the Appendix. The partial charges on each atom in the ground electronic state was calculated for various total charge states of the molecule. The results of these calculations are summarised in Fig. 6.7 and Table 6.1. Table 6.1 compares the calculated relative charge per atom type for various charge states of the molecule with that observed from the experiment. The calculations are in reasonable agreement with the experimentally observed ion yields, predicting a disproportionately large charge build-up on the peripheral atoms compared to the core, increasingly so for higher charge states. In particular, the bromine atoms are predicted to carry far more charge than is observed experimentally, which, if correct, suggests a substantial degree of charge migration in the early stages of Coulomb explosion. In contrast,



Atom	1 Charge	10 Charges	14 Charges	20 Charges
N	-0.261	0.614	1.132	1.901
C1	0.178	0.903	0.983	1.365
C2	-0.135	-0.132	0.437	0.443
C3	0.430	0.682	0.651	0.635
C4	-0.136	0.441	0.513	0.668
C5	-0.011	-0.200	-0.175	0.374
C6	-0.136	0.441	0.513	0.671
C7	0.430	0.682	0.651	0.636
C8	-0.089	0.193	0.220	0.176
C9	0.104	0.394	0.533	0.655
C10	-0.126	-0.454	-0.400	-0.070
C11	0.019	0.615	0.703	0.820
C12	-0.126	-0.454	-0.400	-0.186
C13	0.104	0.394	0.533	0.680
F1	-0.270	0.109	0.395	0.853
F2	-0.270	0.109	0.395	0.856
Br1	0.215	1.915	2.619	3.584
Br2	0.215	1.915	2.619	3.504
H1	0.140	0.373	0.422	0.505
H2	0.140	0.373	0.422	0.506
H3	0.197	0.345	0.394	0.455
H4	0.197	0.345	0.394	0.455
H5	0.190	0.397	0.446	0.514

Fig. 6.7 The table on the *right* lists the calculated partial charges present on each atom of the parent molecule in the ground electronic state for various total charge states of the molecule. The geometry of the molecule is fixed at the equilibrium geometry of the neutral molecule in the ground electronic state. The electronic structure calculations were performed on request by Dr C. Vallance, using the Gaussian software package at the MP2 level of theory using the 6-311G** basis set. The representation of the molecule identifies each of the atoms, as labelled in the table

the predicted charge density localised on the fluorine atoms is generally less than observed experimentally, especially when it is noted that much of the contribution from the F^{2+} peak lies beyond the range of the detector and is therefore not counted in the experimental values reported.

It is worth bearing in mind, however, that ionisation of the neutral parent will not necessarily result in the formation of molecular ions exclusively in the ground electronic state. Furthermore, the charge density calculations neglect the presence of the ionising laser pulse, which will influence the electronic states of the parent ion to a substantial degree. An understanding of the distribution of charge in the parent ion must therefore consider the presence of this field and the mechanism of ionisation, which is likely to be highly complex in this case due to the highly conjugated and extended nature of the molecule.

6.3.3 Time-of-Flight Covariance

Acquisition of event-based data using the PImMS camera allows the measurement of the correlation between the various mass peaks through a covariance analysis of the data. The covariance may be formulated as

$$C(x, y) = \langle X(x)Y(y) \rangle - \langle X(x) \rangle \langle Y(y) \rangle \quad (6.1)$$

$$= \frac{1}{N} \sum_{i=1}^N X_i(x)Y_i(y) - \left[\frac{1}{N} \sum_{i=1}^N X_i(x) \right] \left[\frac{1}{N} \sum_{i=1}^N Y_i(y) \right], \quad (6.2)$$

where the expected values $\langle \rangle$ are calculated over N laser shots. Equation 6.2 may be applied to the measurement of correlations between the times of flight, as demonstrated by Frasinski et al. in 1989 [9]. In this case, X and Y are simply the same time-of-flight spectrum, where $X_i(x)$ is the value of spectrum X at time x on laser shot i . The calculation of the covariance in this way reveals correlations between the mass peaks, which are hidden in the time-averaged spectra so far considered.

Figure 6.8 plots the time-of-flight correlations following Coulomb explosion of the molecules in perpendicular alignment as a two-dimensional covariance map. It is worth noting at this point that in a conventional covariance map, of the sort presented in Fig. 6.8, a diagonal line of autocovariances is normally present, which represents the necessarily perfect correlation of each ion with itself. However, in the calculation of the data presented here, these autocorrelations have been excluded by neglecting the correlation of each ion with itself. This is possible since each discrete ion event is identified as such and may be treated individually. The covariance map is rich in information and reveals some interesting details pertaining to both the experiment and the dynamics of the Coulomb explosion process.

From the shape of the peaks in the covariance map, it is clear that the effect of time jitter due to triggering the camera from the previous laser shot has not been completely removed. Each of the peaks has a diagonal profile with a gradient of 1, indicating that late events in one peak correlate with late events in another, and vice versa. As a consequence, the features corresponding to the various photofragments are somewhat better resolved in the covariance map than in the conventional time-of-flight data, demonstrating that the time-resolution of the PImMS camera itself is not the limiting factor in determining the sharpness of the time-of-flight spectrum.

The most striking features of the covariance map are related to the various correlations between the forward- and backward-scattered peaks of the various photofragments. This is highlighted particularly clearly in Fig. 6.9, which shows a section of the full covariance map corresponding to the correlations of the F^+ ions with all other charged photofragments. It is clear that the forward- (backward-) scattered F^+ ions are correlated exclusively with both forward- (backward-) scattered fluorine (F^+ , F^{2+}) and nitrogen (N^+ , N^{2+}) fragment ions, as highlighted by the yellow rings superimposed on the covariance data presented in Fig. 6.9. Conversely, the forward- (backward-) scattered F^+ ions are correlated with the backward- (forward-) scattered bromine (Br^+ , Br^{2+}) ions, as highlighted by the red rings. These asymmetric correlations allow inferences to be made about the structure of the parent molecule. Firstly, it is clear that since the F and N ions are scattered in the same direction they must reside on the same end of the molecule, with the opposite true for the relationship between F and Br. From the structure of the target molecules, this is known to be the case and it is encouraging that these relationships manifest themselves in the correlation spectrum. It is also possible to deduce, through the existence of correlations

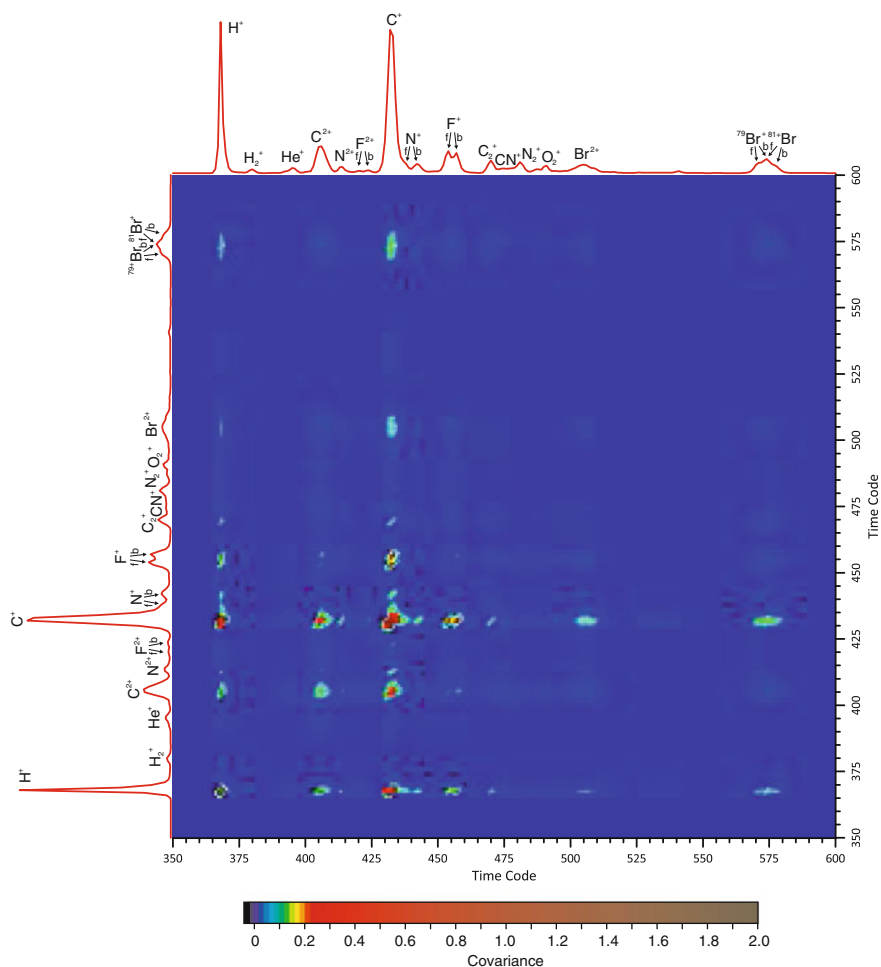


Fig. 6.8 Plot of the covariance between the time codes, as calculated from the PIMMS data. The autocorrelation normally present in such measurement is not present as the correlation of each particle with itself has been ignored. The diagonal nature of the correlation peaks suggests that the effect of time jitter has not been completely removed from the data

between F^+ ions and other fluorine photofragments, that there is necessarily more than one fluorine atom in the parent molecule. If this were not the case then it would be impossible for F^+ to correlate with either itself or F^{2+} as there would be no remaining fluorine atoms from which the partner ions could be produced.

While the covariance map presented in Fig. 6.8 clearly contains a wealth of information, it is difficult to accurately assess some of the more subtle, but nonetheless important features present in the data. In order to undertake a more detailed analysis of the correlations between the various time-of-flight peaks, it is perhaps more

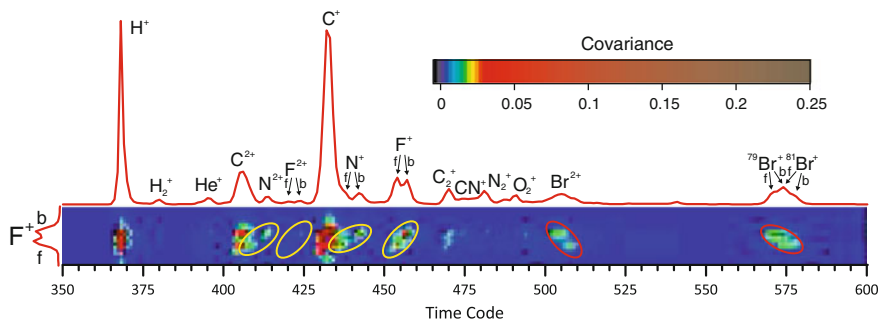


Fig. 6.9 Section of the time-of-flight covariance data corresponding to the correlations of F^+ ions to all others in the spectrum. The red and yellow rings highlight asymmetric correlations in the data

informative to consider the covariance profiles of carefully selected individual time codes corresponding to the different ion species, as presented in Figs. 6.10 and 6.11. The subtle differences between the individual covariance profiles corresponding to different product ions reveal much about the Coulomb explosion dynamics and the relationships between the various ionic photofragments. Encouragingly, it is universally observed that contribution of signal from ions attributed to background gas in the target chamber is almost entirely removed. The peaks corresponding to H_2^+ , He^+ , N_2^+ , and O_2^+ are effectively absent in each trace, confirming their lack of association with the target molecules. Furthermore, in the cases where a backward-scattered peak has been selected, the asymmetric relationships discussed above are clearly reproduced in the data. This is particularly pronounced in the traces corresponding to backward-scattered N^+ and N^{2+} , which correlate almost exclusively with backward-scattered F^+ . Inferences on the composition of the parent molecule may also be made through inspection of the correlation spectra of N^+ and N^{2+} . In these traces, correlations to N^+ and N^{2+} ions are largely absent, suggesting that only a single N atom is present in each parent molecule, which is indeed the case.

A perhaps more subtle feature of the data is the disproportionately strong positive correlation between the doubly charged ions C^{2+} , N^{2+} , and Br^{2+} . In the covariance traces corresponding to these species the relative abundance of other doubly charged ions is significantly higher than in the 1D time-of-flight spectrum. In particular, the ion signal assigned to C^{2+} shows a particularly strong correlation to other doubly charged ions, displaying a markedly increased intensity in the correlation spectra of C^{2+} , N^{2+} , and Br^{2+} . Similarly, the singly charged photofragments show a strong correlation to other singly charged species. For example, the correlation spectrum of C_2^+ is weighted heavily in favour of itself and the Br^+ ion, whereas the correlation of C_2^+ to the doubly charged species C^{2+} , N^{2+} , and Br^{2+} is so small as to be almost negligible. These trends are reproduced consistently across each of the correlation spectra presented in Figs. 6.10 and 6.11, suggesting that highly localised charge accumulation in the parent ion is unlikely. If the charge imparted to the parent molecule through strong field ionisation is relatively low, the fragment ions released following

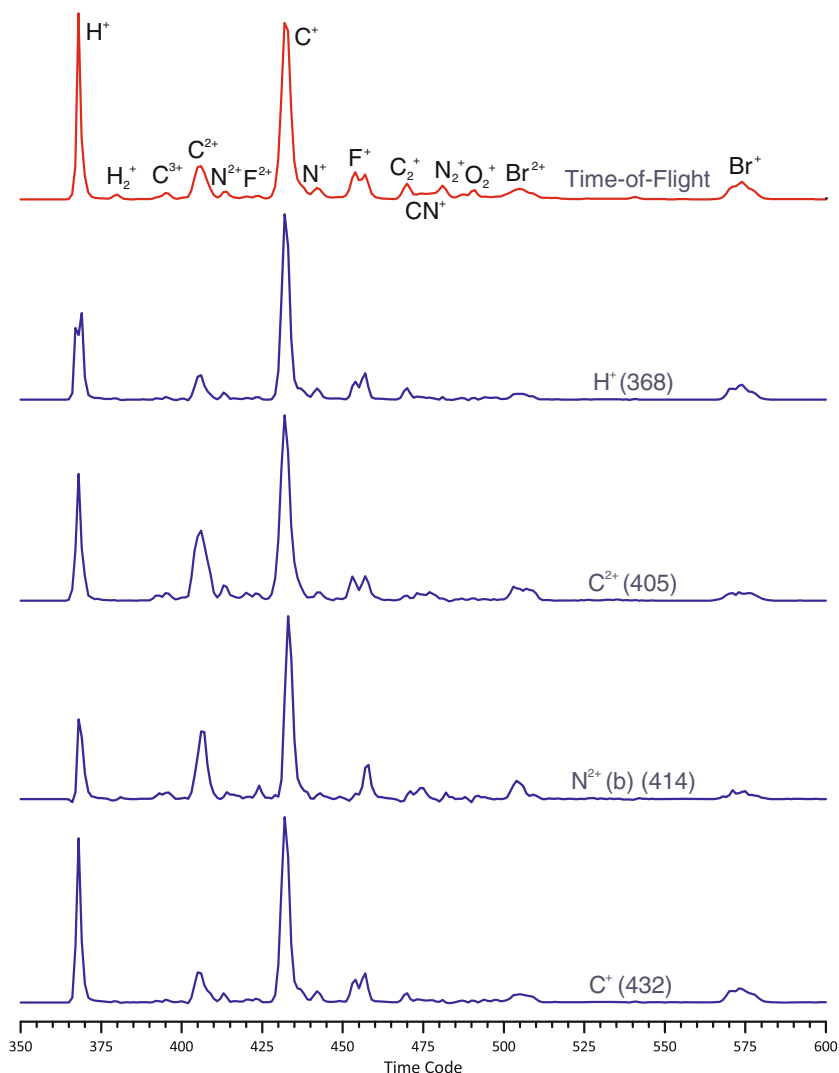


Fig. 6.10 A selection of covariance profiles corresponding to individual time codes, as labelled. The ion species to which each trace corresponds is labelled along with the time code. The addition of a (b) indicates that a backward-scattered peak has been selected for. The top trace is the integrated time-of-flight spectrum, which is included for comparison. The vertical scales represent the covariance and have been normalised such that the most intense peak in each trace has a maximum value of 1

Coulomb explosion will themselves carry a low charge. In this case, it is unlikely that sufficient charge will become localised on any individual atom to yield a doubly charged fragment ion, as observed in the correlation spectrum of C_2^+ in Fig. 6.11. Conversely, where charge build-up in the parent ion is significant, the probability

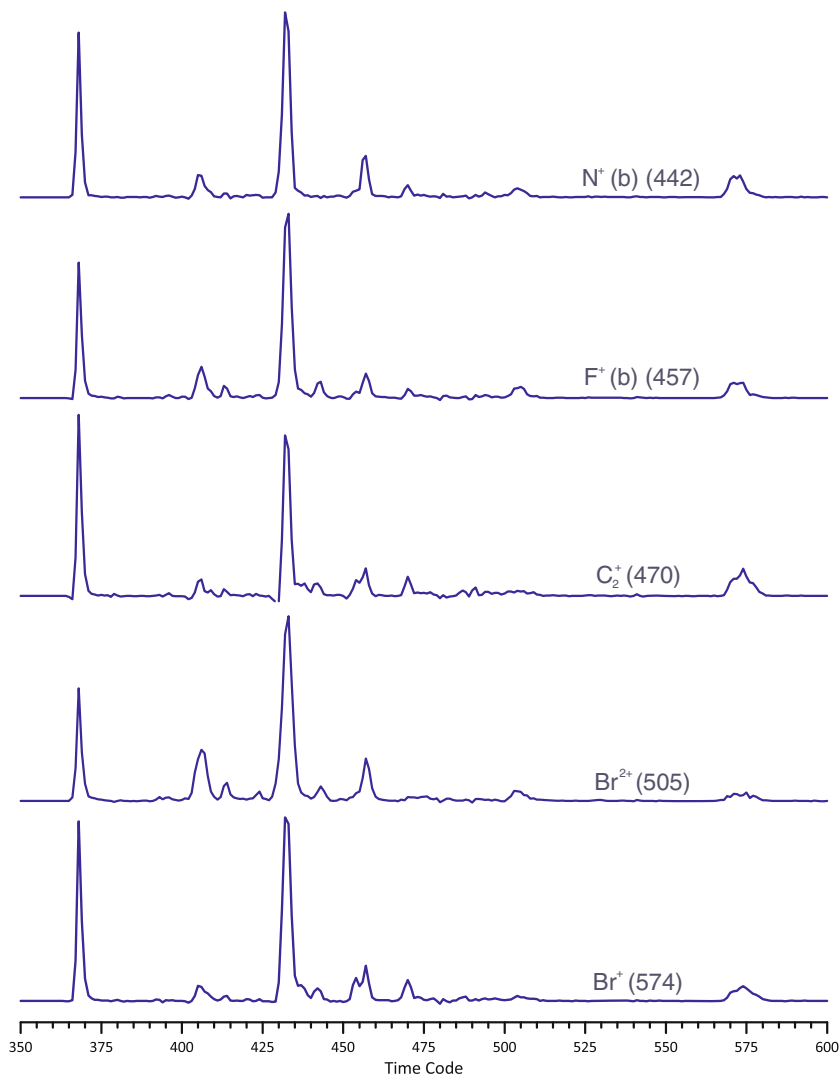


Fig. 6.11 A selection of covariance profiles corresponding to individual time codes, as labelled. The ion species to which each trace corresponds is labelled along with the time code. The addition of a (b) indicates that a backward-scattered peak has been selected for. The vertical scales represent the covariance and have been normalised such that the most intense peak in each trace has a maximum value of 1

of forming singly charged fragment ions diminishes, with doubly charged species becoming increasingly common. It is important to note that this is not to say that charge is uniformly distributed amongst the atoms of the parent molecule (the ion yield calculations presented earlier in this chapter demonstrate clearly that this is not the case), but that significant localised charge build-up is unlikely.

6.4 Recoil Frame Covariance Images

From the above discussion, it is clear that the dynamical insight that may be gained from the time-of-flight information is substantial. Details of ion yields, ionisation mechanism, charge distribution, and structural properties of the parent molecule may be inferred to some degree from either the raw time-of-flight information or through an analysis of the correlations between the various photofragments. However, the covariance method is not limited to measuring correlations between the time coordinates of the ion events recorded by the PImMS camera, but may also be applied to the measurement of correlations in the full x, y, t coordinate space recorded by the sensor. In this way, it is possible to simultaneously measure correlations between both the velocities and times-of-flight of the recorded ion events. Using the full event coordinate information provided by the PImMS camera, the covariance may be expressed as

$$C(c_1, c_2) = \frac{1}{N} \sum_{i=1}^N X_i(c_1)X_i(c_2) - \left[\frac{1}{N} \sum_{i=1}^N X_i(c_1) \right] \left[\frac{1}{N} \sum_{i=1}^N X_i(c_2) \right], \quad (6.3)$$

where $X_i(c_j)$ is the value of the PImMS data set at coordinate c_j on laser shot i , where c_j is identified by the coordinates (x_j, y_j, t_j) . In this formulation, if an ion event is recorded at coordinate c_j on laser shot i , then a value of 1 is assigned to $X_i(c_j)$; otherwise $X_i(c_j) = 0$.

In practice, the full, x, y, t correlation map is difficult to process analytically due to the vast amount of information contained within the data. The situation becomes somewhat more manageable if the ion events are grouped according to the ion species attributed to each time code. Following this approach, the t coordinate is replaced by an ion identification. For example, any event that occurs within the time window 567–581 in the perpendicularly aligned data set is identified as a Br^+ ion. In the present example, this reduces the 4095 individual time codes present in the PImMS data down to fewer than 10 ion species of interest. In this case, Eq. 6.3 becomes

$$C(X, Y) = \frac{1}{N} \sum_{i=1}^N X_i(x)Y_i(y) - \left[\frac{1}{N} \sum_{i=1}^N X_i(x) \right] \left[\frac{1}{N} \sum_{i=1}^N Y_i(y) \right], \quad (6.4)$$

where $X_i(x)$ is the value of the PImMS data set for the ion species X at the spatial coordinate x , as recorded on laser shot i . Using this formulation, the covariance analysis can be applied to the signal variations recorded by each pixel of the sensor for either the same or two different ionic photofragments, X and Y . However, for each pair of ions between which the covariance is measured, there still exists an overwhelming amount of covariance data. For each pair of ions there will exist $N^4/2$ individual correlation measurements for a sensor comprising $N \times N$ pixels, where the factor of 2 accounts for the reciprocal nature of the covariance. It is therefore necessary to develop methods of condensing the data into a more manageable form.

A particularly intuitive representation is to transform the coordinate system of the measurements, such that the data are presented in the recoil frame of one of the ion species between which covariances are being measured. In this approach, one ionic species is designated as the ‘reference’ ion, and the covariance between each pixel in the reference ion time window and each pixel in the partner ion time window is calculated. In this way, each pixel of the sensor has an associated ‘covariance map’, showing the correlations of the reference ions at that pixel to the partner ions recorded by each pixel of the sensor. The covariance maps for each pixel are then rotated such that the reference pixels all lie along a common vector, and summed together. This results in a ‘recoil frame’ covariance ‘image’, in which the trajectories of the reference ions are confined along a single vector, and the covariances with the partner ions are shown relative to this vector. This visual representation of the 2-vector correlations is a useful and intuitive tool through which the features and trends of the data can be readily appreciated.

Figure 6.12 illustrates schematically the various stages involved in the production of a recoil frame covariance image. In this case, reference ion signals (to which the correlations are measured) are rotated such that the x component of the velocity is zero and the y component is positive, i.e. the frame of reference has the reference ions travelling vertically along a vector from the centre of the image to the top edge. For each of the recoil frame covariance images presented in this thesis, this is the frame of reference that is used.

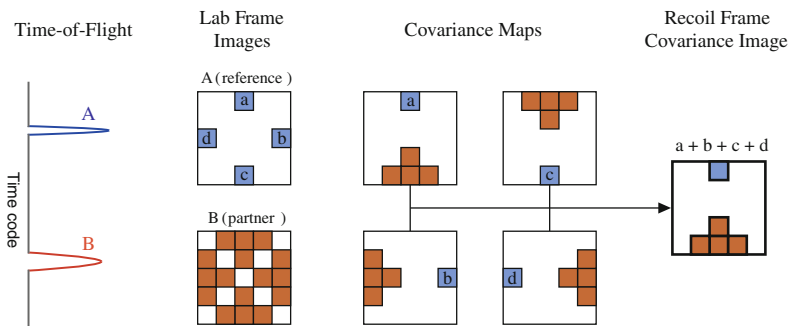


Fig. 6.12 Illustration of the various stages involved in the generation of a recoil frame covariance image. First, two time windows corresponding to two ion species, A and B , are identified. One of the ions is designated the ‘reference’ ion, in this case ion A . The covariance maps plotting the correlation of each pixel in the reference frame (pixels $a-d$) to each pixel in the partner frame are generated. Each of these covariance maps is rotated so that the velocity of the reference ion is confined to a single vector, and summed together to produce a recoil frame covariance image

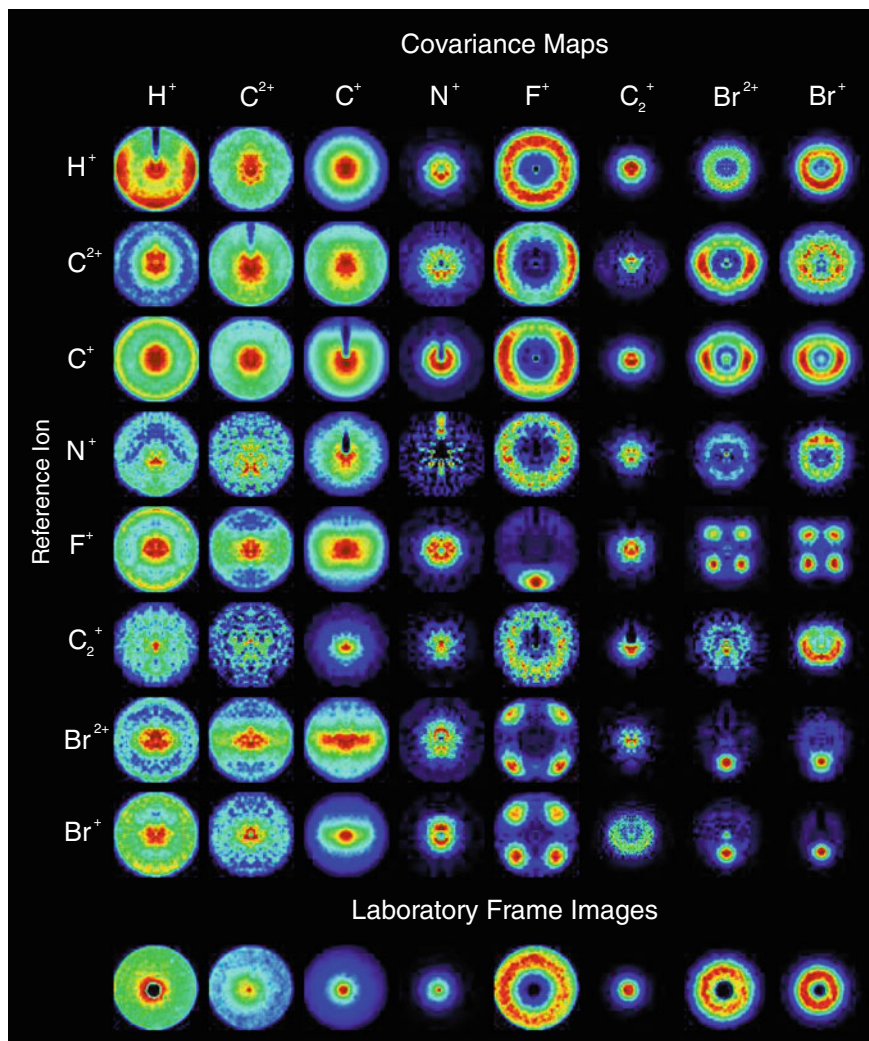


Fig. 6.13 Covariance images of each ion species (labelled at top) relative to various reference ions (labelled left), compared to the laboratory frame ion images (bottom row), as recorded following alignment of the target molecules perpendicular to the detector plane. In each case the reference ion is confined to a vertical vector from the centre of the covariance image to the top edge

6.4.1 Overview of Covariance Images

Figures 6.13 and 6.14 show the complete set of recoil frame covariance images for the eight most prominent peaks in the mass spectrum for both perpendicular and parallel alignment, respectively. The columns plot the correlated velocities of the individual

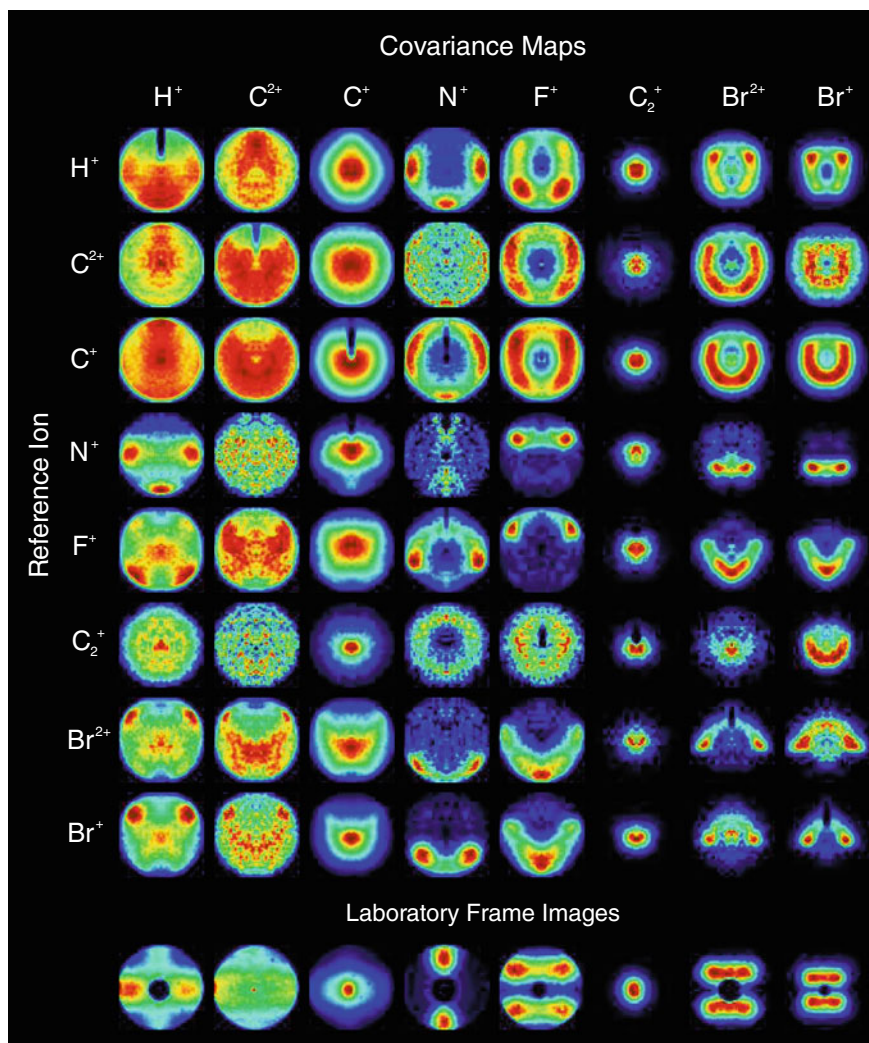


Fig. 6.14 Covariance images of each ion species (*labelled at top*) relative to various reference ions (*labelled left*), compared to the laboratory frame ion images (*bottom row*), as recorded following alignment of the target molecules parallel to the detector plane. In each case the reference ion is confined to a vertical vector from the centre of the covariance image to the top edge

ion species in the recoil frame of various reference ions, with the laboratory frame ion images for each of the photofragments displayed in the bottom row of each figure for comparison. The quantity of information contained in the covariance images is striking. Each geometry yields 64 individual covariance maps, representing the 2-vector velocity correlations between each pair of product ions. When compared to the information content of the uncorrelated laboratory frame measurements, the

advantage of considering the velocity vector correlations is clear. The majority of the covariance images show distinctly anisotropic distributions, which relate directly to the structure of the molecules prior to Coulomb explosion and to the dynamics of the dissociation process.

Before exploring the details of the covariance images fully, it is worth noting the absence of false correlation artefacts in the data. In the case of a well-behaved experiment operating under Poisson statistics, all positive covariances will be caused by genuinely coincident events; i.e. where the photofragments are correlated due to their common provenance from a single parent ion. However, if experimental factors cause systematic fluctuations in signal level, such as may be caused by a variable shot-to-shot laser intensity or target gas density, all recorded signals will be correlated to some extent. For example, if the photon flux is higher than average on a given laser shot, all ion signals have an enhanced probability of being recorded, causing some degree of false correlation to be measured. Various schemes have been developed to address this issue, such as the calculation of the partial covariance [10–12], in order to remove the contributions of these false correlations. Such schemes depend on the measurement of various experimental parameters, usually the laser power, on each laser shot so that the correct number of false covariances may be calculated and subtracted. However, the covariance maps presented in Figs. 6.13 and 6.14 appear to be almost entirely unaffected by such effects, with artefacts caused by systematic correlations largely absent from the data. For example, in the parallel geometry covariance maps of F^+ and Br^+ measured with N^+ as the reference ion, one would expect to see the ‘shadow’ of the laboratory frame ion image superimposed on the covariance map if false correlations were present in the data. This is because the N^+ ions are already tightly confined to the vertical y -axis in the laboratory frame, and because the laboratory frame ion images possess reflective symmetry about the x -axis. However, such artefacts are either not observed in the covariance maps, or are very minor in their contribution, suggesting that the experiment operates under Poisson statistics, with a consistent laser power and a consistent target molecule density in the laser interaction region. The application of corrective procedures was therefore not deemed necessary, and the raw covariance data are considered.

Returning to the discussion of the covariance images themselves, there are some interesting general trends that are worth noting before a more detailed interpretation of the data is pursued. The most striking feature is the sheer wealth of information represented by the full collection of covariance images in both geometries. It is perhaps unsurprising that clear and distinct anisotropies are present in some of the covariance images, particularly those between peripheral substituents occupying a limited number of positions in the molecule. However, it is interesting that even the covariance images corresponding to the 13 carbon atoms comprising the molecular skeleton (C^+ and C^{2+}) are highly structured. In the case of H^+ ions, each covariance image has a unique and complex structure, containing important information pertaining to the connectivity of the atoms in the parent molecule, and to the process of Coulomb explosion itself.

It is interesting to compare the details of the covariance images corresponding to the singly charged C^+ and Br^+ ions and their doubly charged counterparts C^{2+}

and Br^{2+} . In the case of bromine, the covariance images of the doubly charged ions resemble almost exactly those of the singly charged photofragment, but with an increased kinetic energy of the ions, as witnessed by the larger radius of the features in the Br^{2+} covariance images. That the more highly charged species acquires a greater kinetic energy is an unsurprising and expected result of the larger magnitude of the pairwise Coulomb forces acting on the Br^{2+} ion. It was suggested in Sect. 6.3.3 that highly charged ions are more likely to be released from highly charged parent molecular ions. This assertion is supported by comparing the covariance maps of other ionic photofragments measured relative to Br^+ and Br^{2+} . In all cases the kinetic energies of the photofragments recorded in coincidence with Br^{2+} are greater than those recorded in coincidence with Br^+ , implying a greater initial potential energy and therefore a more highly charged molecular parent ion. This observation lends further support to the argument that the localised charge build-up required to produce highly charged photofragments such as Br^{2+} is unlikely unless the charge state of the molecular parent ion is sufficiently high, suggesting a relatively even build-up of charge across the whole molecule prior to Coulomb explosion.

In the case of the carbon ions (C^+ and C^{2+}), while a similar effect is observed, wherein the covariance images corresponding to the more highly charged species are broadly similar to those of the singly charged counterpart but with a larger kinetic energy, the differences between the C^+ and C^{2+} covariance images is more pronounced. For example, the C^+ and C^{2+} covariance images recorded relative to H^+ ions in parallel geometry both peak in the forward-scattered direction (where forward-scattered here refers to both ions travelling in the same direction). However, the C^{2+} covariance image shows a greatly increased preference for forward-scattering than the covariance image of the C^+ counterpart. This particular example is perhaps suggestive of interesting details of the Coulomb explosion process. It would seem highly likely that the forward-scattered component of the C^+ and C^{2+} covariance images comprises primarily of carbon atoms connected directly to H atom substituents in the parent molecule. This is due to the proximity of the nascent ions and the similar Coulomb forces that will therefore result, guiding them onto similar final trajectories. The enhancement of the forward-scattered signal in the C^{2+} covariance map therefore suggests that charge is more likely to reside on the carbon atoms adjacent to H atom substituents in the more highly charged states of the molecular ion, resulting in an increased yield of C^{2+} ions from these positions relative to the remaining carbon atoms. The charge density calculations for various charge states of the molecular parent ion lend support to this argument. Figure 6.15 compares the calculated percentage of the total charge carried by carbon atoms either with or without an H atom substituent for various charge states of the ion. It would appear from these calculations that in the lower charge states of the molecule the charge is more likely to be located on carbon atoms without H atom substituents. As the total charge carried by the molecule increases, the greater proportion of the overall charge is calculated to reside on the carbon atoms bonded to H atom substituents, which is in accordance with the vector correlations presented in the covariance images. Although this agreement between calculation and experiment is indeed promising, it should be stressed that the charge density calculations have been performed for the ground electronic

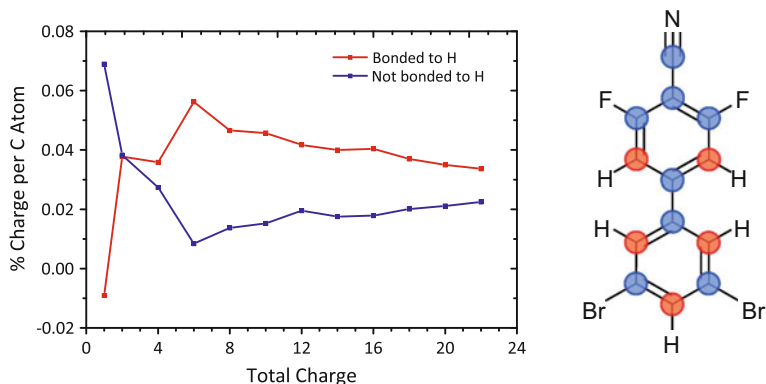


Fig. 6.15 *Left* Plot of the average charge carried by carbon atoms with (*red*) and without (*blue*) H atom substituents. *Right* The carbon atoms with (*red*) and without (*blue*) H atom substituents are identified in the context of the molecular structure

state, and in the absence of the ionising laser field, and so must be treated with caution. The laboratory frame ion image also supports this hypothesis, with the C^{2+} ion image in parallel alignment resembling much more closely the H^+ ion image than that corresponding to C^+ ions.

A further possible explanation for the differences observed between the covariance images measured relative to C^+ and C^{2+} stems from the location of the carbon atoms in the core of the molecule, consisting as they do of the skeleton on which the remaining constituents are arranged. While an additional charge to a peripheral substituent, such as a bromine atom, is unlikely to influence to any significant extent the trajectories of the remaining ions, the presence of a highly charged ion in the core of the molecule is far more likely to perturb the Coulomb explosion process.

6.4.2 Detailed Analysis of Selected Covariance Images

The general trends identified in the discussion thus far are certainly interesting and help to further our understanding of the Coulomb explosion mechanism. However, the covariance data contains within it a vast amount of detailed information relating to the structure of the parent molecule prior to dissociation. In particular, the two orthogonal projections of the ion trajectories afforded by the adiabatic alignment of the target molecules provide complementary information pertaining to various structural coordinates of the parent. In this section a more detailed analysis of selected covariance images is undertaken with a view to extracting quantitative structural measurements of DBrDFCNBph.

6.4.2.1 Perpendicular Alignment: Measurement of the Dihedral Angle

In perpendicular alignment, the relationship between the velocities of the bromine and fluorine ions is indicative of the dihedral angle of the parent molecule prior to Coulomb explosion, and of the details of the dissociation process itself. As an example, Column I of Fig. 6.16 shows ‘raw’ ion images of (a) F^+ and (b) Br^+ recorded following perpendicular alignment of the molecules. Both images show a cylindrically symmetric distribution around the alignment axis, as expected, due to free rotation about the C_2 -axis. However, it is not possible to determine the relationship between the two fragments from the raw ion images alone; it is necessary to refer

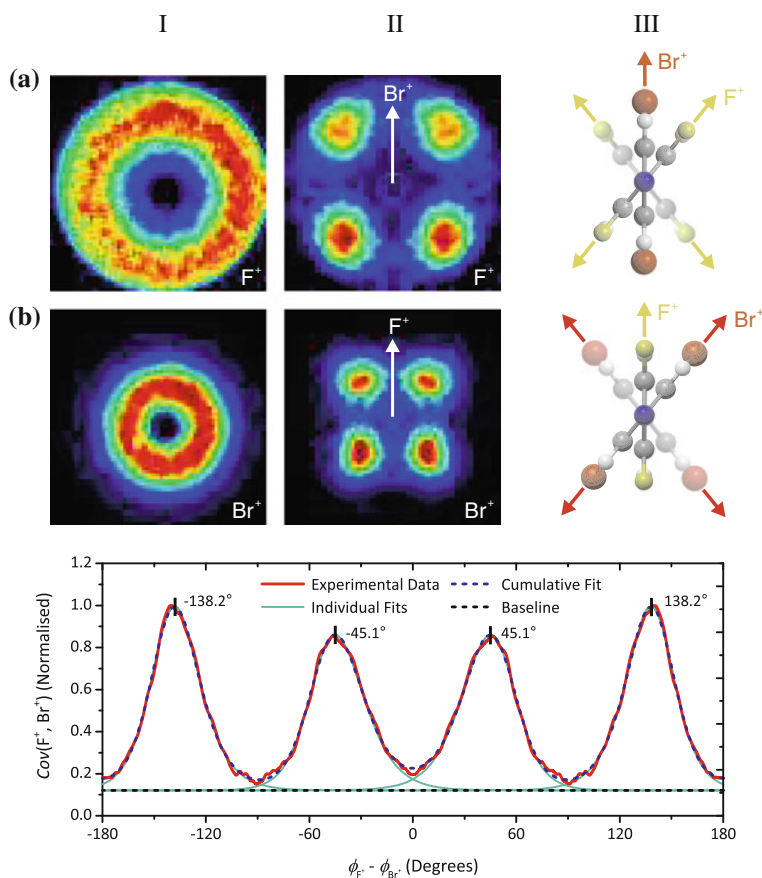


Fig. 6.16 Ion images (I) of **a** F^+ and **b** Br^+ , and covariance images (II) of **a** F^+ relative to Br^+ , and **b** Br^+ relative to F^+ for perpendicular alignment of the target molecules. The molecular reference frames resulting in the covariance maps shown in column II are illustrated on the right. The bottom panel shows the corresponding covariance plotted as a function of the relative angle of F^+ to Br^+ . The peaks are fitted to four asymmetric sigmoidal peak functions

to the covariance images, which correlate the velocity vectors of the F^+ ions with respect to Br^+ , or vice versa.

The covariance images shown in column II of Fig. 6.16 clearly reveal the relationship between the velocities of the F^+ and Br^+ ions. The covariance images consist of four peaks of intensity, with the relative positions of the peaks being determined by the combination of the dihedral angle between the two phenyl rings in the parent molecule and the Coulomb explosion dynamics. The lower panel of Fig. 6.16 plots the signal intensity from the covariance images as a function of the relative angle between the two ion trajectories. In the limit of axial recoil, the angles of the peaks should be characteristic of the dihedral angle between the two phenyl rings. The equilibrium dihedral angle, computed at density functional theory level (see Refs. [7, 8] for details), is 39.0° , which is in reasonable quantitative agreement with the values extracted from the covariance images, especially considering the rather shallow minima on the potential energy surface in the torsional coordinate. The peaks in the covariance images are fitted to four asymmetric sigmoidal peak functions in order to identify the angles of peak intensity. The fitted maxima are observed at approximately $\pm 138.2^\circ$, which corresponds to a dihedral angle of $41.8 \pm 1.3^\circ$, and $45.1 \pm 0.4^\circ$ (where the errors represent 2σ statistical errors from fits to the data).

The increased recoil angles obtained from the covariance images relative to that calculated for the parent molecules suggest that the ion trajectories are somewhat affected by Coulomb repulsion between the measured fragment ion pairs. Furthermore, it is interesting to note that the peaks of the near side (proximal) Br^+/F^+ ion pairs ($\pm 45.1^\circ$, $FWHM = 36.96^\circ$) are broader and have a larger relative recoil angle than those corresponding to Br^+/F^+ ion pairs originating from opposite sides (distal) of the molecule ($\pm 138.2^\circ$, $FWHM = 33.21^\circ$). This suggests that the mutual Coulomb repulsion between Br^+ and F^+ is greater when the ion pairs originate from the same side of the molecule, which is likely to be due to the closer proximity of the nascent ions resulting in a larger pairwise Coulombic interaction. Nevertheless, the results show convincingly that the covariance analysis is a good probe of the dihedral angle, a characteristic structural coordinate of the molecule, to within a few degrees of the calculated value.

6.4.2.2 Parallel Alignment: Bonding Angles of F and Br

Whilst the perpendicular geometry allows the measurement of the dihedral angle of the molecules, the orthogonal alignment, wherein the molecules are aligned parallel to the detector plane, arguably offers a richer source of structural information. In particular, the unique position of the nitrogen atom in the parent molecule makes the measurement of covariances relative to N^+ ions an especially useful probe of the relative coordinates of the various constituents of the system. Furthermore, that the trajectories of the N^+ ions are preferentially confined parallel to the C_2 symmetry axis of the parent molecule and therefore the axis of free rotation makes the covariance images recorded relative to N^+ particularly amenable to straightforward interpretation.

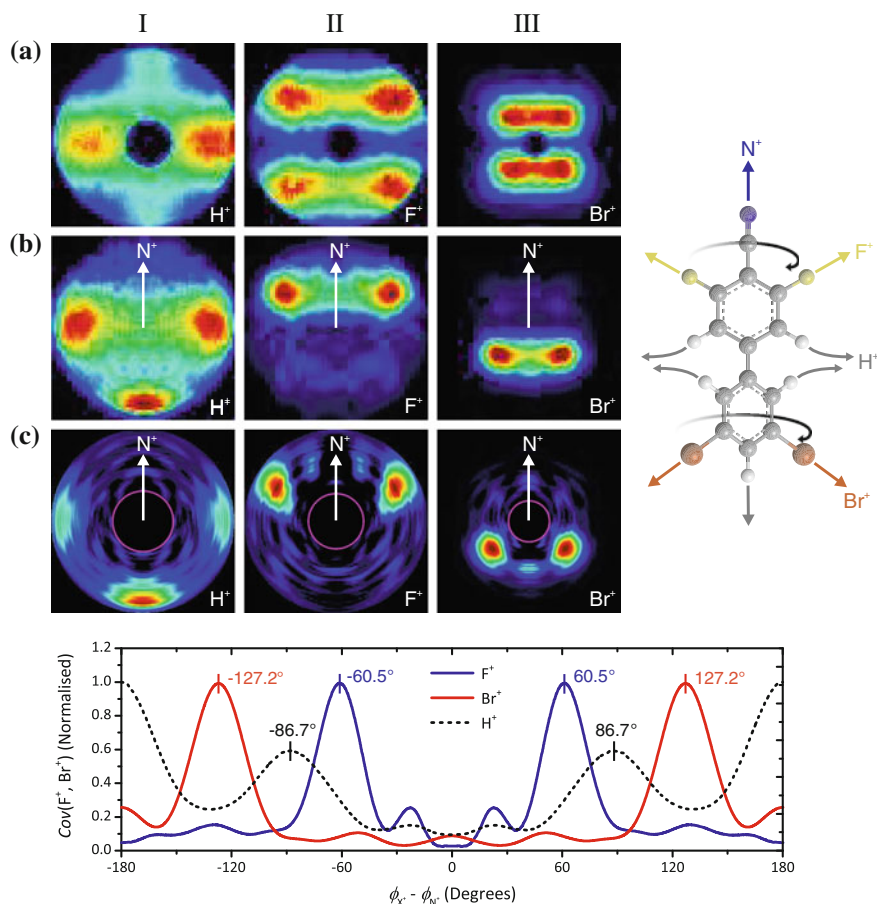


Fig. 6.17 Row (a) plots the laboratory frame ion images of (I) H^+ , (II) F^+ , and (III) Br^+ following parallel alignment of the target molecules. Row b plots the corresponding recoil frame covariance images with respect to N^+ . Row c plots the pBASEX inversions of the recoil frame covariance images presented in Row b. The molecular reference frame to which the covariance images correspond is illustrated on the right hand side. The bottom panel plots the covariance as a function of the recoil angle of H^+ (black dashed), F^+ (blue), and Br^+ (red) relative to N^+ . The maxima in each of the traces are identified with vertical markers

To illustrate this point, Row (a) of Fig. 6.17 shows raw ion images of H^+ , F^+ , and Br^+ recorded following parallel alignment of the target molecules. To some degree, the positions of the substituents within the molecule are reflected in the ion images. However, due to the four-fold symmetry of the images, it is not possible to identify, for instance, whether Br or F substituents are located adjacent to the CN group in the molecule, or on the second phenyl ring. In order to ascertain more precisely the positions of the substituents in the molecule it is once again necessary to refer to

the recoil frame covariance images. Row (b) of Fig. 6.17 presents the recoil frame covariance images of H^+ , F^+ , and Br^+ with respect to N^+ . It is immediately clear that these covariance images bear a striking resemblance to the molecular structure of the parent: Br^+ is observed on the opposite side of the images relative to N^+ , while F^+ is located adjacent to N^+ , as intuitively expected. Furthermore, the equatorial positioning of the H atoms in the parent molecule is highlighted, and the unique location of the remaining H atom opposing the CN group is revealed.

The information obtained from the covariance images can be increased by exploiting the cylindrical symmetry resulting from the 1D alignment of the molecules, which allows free rotation around the alignment axis. The 3D correlated velocity distributions were retrieved through an inverse Abel transform, using the pBASEX algorithm. The Abel inverted ion images are displayed in Row (c) of Fig. 6.17, with the resulting angular distributions of the H^+ , F^+ , and Br^+ ions, as measured relative to N^+ , plotted in the lower panel. From an inspection of the Abel inverted covariance images, it would appear that the inversion has been successful, with the features attributed to free rotation about the MPA of the molecule largely removed. Some artefacts do, however, remain in the images. In particular, the pBASEX routine allows the fitting of Legendre polynomials up to a maximum of $L = 10$, which results in small periodic oscillations in the angular coordinate. Furthermore, although the x - and y -components of the N^+ ion velocities have been confined to a single vector in the covariance images, the out-of-plane component (z) is confined only by the degree of alignment of the target molecules in the laboratory frame. This results in some contributions to the covariance images from out-of-plane molecules, breaking the strict requirements of cylindrical symmetry necessary to perform a clean Abel inversion. However, in the cases of the N^+ to F^+ and Br^+ , the out-of-plane component consists of a slight bulge in the line of covariances linking the two maxima, resulting from a side-on projection of the ‘doughnut’ of covariances at a slightly oblique angle. In the inverted covariance images for F^+ and Br^+ , the out-of-plane contribution manifests itself as a peak at either 0 or 180° , respectively, and is therefore easily identified and distinct from the important features.

From the peaks in the angular profiles of each of the recoil frame covariance images, the recoil angles relative to the N^+ ions are determined to be $\pm 60.5^\circ$ for F^+ , $\pm 127.2^\circ$ for Br^+ , and $\pm 86.7^\circ$ and 180.0° for H^+ . The recoil angle measured between the N^+/F^+ ion pairs is exceptionally close to the bonding angle between the C–CN and the C–F bonds in the parent molecule (60.0°), suggesting almost axial recoil of the N^+ and F^+ ions from the nascent molecular ion. In contrast, the relative recoil angles of the N^+/Br^+ ion pairs corresponds to a relative leaving angle of 52.8° for the Br^+ ions with respect to the para C–H bond, which is substantially smaller than the calculated 60.0° bonding angle between the para C–H and the C–Br bonds in the parent molecule. This discrepancy is perhaps surprising given the heavier mass of the bromine atoms, which should relax the requirement for impulsive parent ionisation in order for straightforward conclusions to be drawn from the resulting ion trajectories. The greater deviation from axial recoil observed for the Br^+ ions may be due to a variety of factors. One possibility is that the slower velocities of

the bromine ions compared to the remaining constituents of the parent molecule is likely to result in the Br^+ ions being ‘overtaken’ by ions generated in the core of the molecule, namely those derived from the carbon skeleton. This would result in substantially non-axial components contributing to the overall forces experienced by the Br^+ ions, causing their trajectories to deviate from those expected from the axial recoil approximation. A further possibility is that the higher-than-average charge build-up in the vicinity of the bromine ions suggested by the electronic structure calculations may also lead to more complicated mechanisms than those described by the simple model in which the charges are assigned at time zero and remain localised throughout the dissociation process.

The above discussion demonstrates that it is possible to infer details of the Coulomb explosion process directly from the covariance images themselves. When combined with the laboratory frame ion images and the time-of-flight covariance maps, an increasingly detailed picture of the explosive dynamics is revealed. However, it is clear that in order to pursue a more accurate and complete interpretation of the data, in terms of both the structure of the parent molecule and the dynamics of ionisation and subsequent explosion, some model of the system must be constructed to guide and support more detailed inferences. The remainder of this chapter therefore explores the application of a simple classical model of Coulomb explosion to the experimental data.

6.5 Classical Simulations of Coulomb Explosion

Coulomb explosion is a highly complex process, involving ionisation, charge redistribution, and molecular break-up, all occurring on competing timescales of a few tens of femtoseconds. Furthermore, the presence of the intense laser field used to induce ionisation may have unintended consequences for the structure of the target molecules beyond simple removal of valence electrons. However, as an initial approximation, the Coulomb explosion process may be modelled through simple classical trajectory calculations of point charges following instantaneous ionisation of the parent molecule. While such an approximation ignores many of the important details of ionisation, charge transfer, and structural deformation that may occur during the initial phases of Coulomb explosion, the success, or otherwise, of this simple model in simulating the experiment is useful as a guide towards a more detailed interpretation of the data and the underlying processes that characterise Coulomb explosion.

The simulation code has been adapted from that developed as part of a collaboration between the author, Dr C. Vallance, and a selection of mathematicians who attended a ‘Maths in Chemistry Study Group’ hosted by the Mathematical Institute at the University of Oxford.

6.5.1 Computational Details

In general, the inverse problem (that is starting with the final velocities of the fragment ions and working back to the initial molecular structure through a reverse Coulomb explosion) is intractable for polyatomic systems. A far more realistic approach is to use an iterative procedure in which the initial conditions of the system are somehow assumed and the forward process simulated. The results of the ion trajectory simulation may then be compared to the experimentally observed velocities, and the starting conditions refined until a satisfactory agreement between simulation and experiment is achieved.

The motion of the ions is assumed to be entirely governed by the inter-ionic forces of Coulomb repulsion, with no contribution from the bonding characteristics of the molecule. The trajectories propagate according to Newton's second law of motion ($\mathbf{F} = m\mathbf{a}$), allowing the problem to be formulated as a series of coupled second order differential equations, corresponding to the equations of motion of the charged particles. More explicitly, for a molecule consisting of N atoms, the equations of motion are of the form

$$M_i u \frac{d^2 \mathbf{x}_i}{dt^2} = z_i e \mathbf{E}_i(\mathbf{x}_i), \quad (6.5)$$

for $i = 1, \dots, N$, where M_i , z_i , and \mathbf{x}_i are the mass number, integer charge, and position of atom i respectively, and u and e are the atomic mass unit and elementary charge, respectively. $\mathbf{E}_i(\mathbf{x})$ is given by

$$\mathbf{E}_i(\mathbf{x}) = E_0 \mathbf{e}_z + \sum_{j \neq i}^N \frac{z_j e (\mathbf{x} - \mathbf{x}_j)}{4\pi \epsilon_0 |\mathbf{x} - \mathbf{x}_j|^3}. \quad (6.6)$$

The ions are assumed to be initially stationary at time zero ($t = 0$) at the coordinates calculated for the equilibrium geometry of the parent molecule. The equilibrium structure used in this case was that calculated at density functional level of theory by colleagues at the University of Helsinki, according to the details presented in Refs. [7, 8]. The calculated equilibrium structure, along with the bond lengths, angles, and coordinates, are presented in Tables A.1 and A.2 of the Appendix. The initial conditions of the system are therefore

$$\mathbf{x}_i(0) = \mathbf{x}_{i,0}, \quad \frac{d\mathbf{x}_i}{dt}(0) = 0. \quad (6.7)$$

The first term on the right hand side of Eq. 6.6 defines the ion extraction field of the ion imaging experiment (considering only the dominant z -component of the field, where the z -axis is defined as the time-of-flight coordinate), whereas the second term defines the pairwise Coulomb interaction of ion i with all other ions in the exploding system. The problem may be reformulated in dimensionless quantities using

$$\mathbf{x}_i = L\mathbf{x}_i^*, \quad t = \tau t^*, \quad \mathbf{E}_i = \frac{e}{4\pi\epsilon_0 L^2} \mathbf{E}_i^*, \quad (6.8)$$

where L and τ are the characteristic length and timescales of the Coulomb explosion process. By solving Eq. 6.5 for a pairwise Coulombic term only, the non-dimensional timescale is identified as

$$\tau = \sqrt{\frac{4\pi\epsilon_0 L^3 u}{e^2}}. \quad (6.9)$$

Using a value of 2×10^{-10} m as a typical interatomic separation, this gives a characteristic timescale of $\sim 7.6 \times 10^{-15}$ s. The non-dimensionalised formulation may then be written as (dropping the stars)

$$M_i \frac{d^2 \mathbf{x}_i}{dt^2} = z_i \lambda \mathbf{e}_z + \sum_{j \neq i}^N \frac{z_i z_j (\mathbf{x}_i - \mathbf{x}_j)}{|\mathbf{x}_i - \mathbf{x}_j|^3}, \quad (6.10)$$

with

$$\lambda = \frac{4\pi\epsilon_0 L^2}{e} E_0. \quad (6.11)$$

Using a typical value of 2.5×10^5 V m⁻¹ for E_0 gives a value of $\lambda \simeq 6.9 \times 10^{-6}$. If the non-dimensionalised charges and interionic separations are of order 1, as is the case at $t = 0$, it is clear that the Coulomb term in Eq. 6.10 dominates the explosion dynamics, and the extraction field may be considered an insignificant perturbation of order λ . The effect of the external field becomes comparable to the Coulomb force only once the ions are of order $\lambda^{-\frac{1}{2}}$ apart. However, at this separation (~ 750 Å) the Coulomb potential is too small to significantly alter the ion trajectories. CEI may therefore be considered as a two-step process, in which the ions initially explode exclusively under the influence of the Coulomb potential, whereafter they are extracted onto the detector according to their asymptotic recoil velocities. Since the experiments were performed under velocity-mapping conditions, the extraction of the ions by the static electric field is well-formulated. For this reason, the extraction field was ignored during the ion trajectory calculations and the asymptotic recoil velocities of the ionic fragments were projected onto a two-dimensional plane simulating the detector. Explicitly, the coupled second order differential equations to be solved are of the form

$$M_i u \frac{d^2 \mathbf{x}_i}{dt^2} = \sum_{j \neq i}^N \frac{z_i z_j e^2 (\mathbf{x} - \mathbf{x}_j)}{4\pi\epsilon_0 |\mathbf{x} - \mathbf{x}_j|^3}, \quad (6.12)$$

These equations are solved numerically using an ordinary differential equation (ODE) solver contained in the library of commercially available MATLAB[®] software

to yield $\mathbf{x}_i(t)$. The simplest method of approximately solving differential equations of this sort is through an iterative procedure, such as Euler's method, wherein the function is solved at a discrete time, t , and the system allowed to evolve for a short time step, Δt . This procedure is repeated in order that the trajectory of the particles may be determined as a function of time. However, following such a procedure is generally insufficiently accurate for most applications as the cumulative error involved in the iterative procedure becomes too large. The ODE solver used here implements a more sophisticated Runge-Kutta formulation to increase the computational accuracy of the calculations. Within this method, the solution is calculated over a given time interval, combining several values determined using Euler's method at different time steps within the interval being processed. These values are then fitted to a Taylor series expansion, which significantly increases the accuracy of the approximate solutions. For purposes of computational efficiency, the algorithm uses variable time intervals, which are chosen intelligently by the ODE solver. The algorithm is able to calculate approximately 300 Coulomb explosion events per minute on a desktop PC, allowing for a relatively rapid convergence of the simulated data.

6.5.2 Details of the Ion Trajectories

Figure 6.18 plots the trajectories of the ions following Coulomb explosion of DBrD-FCNBph carrying a single positive charge on each atom. While this particular charge configuration is unlikely to be representative of the actual charge distribution in the molecule, the trajectories that result are a useful guide for understanding the dynamics of the Coulomb explosion process and the interactions between the various ionic

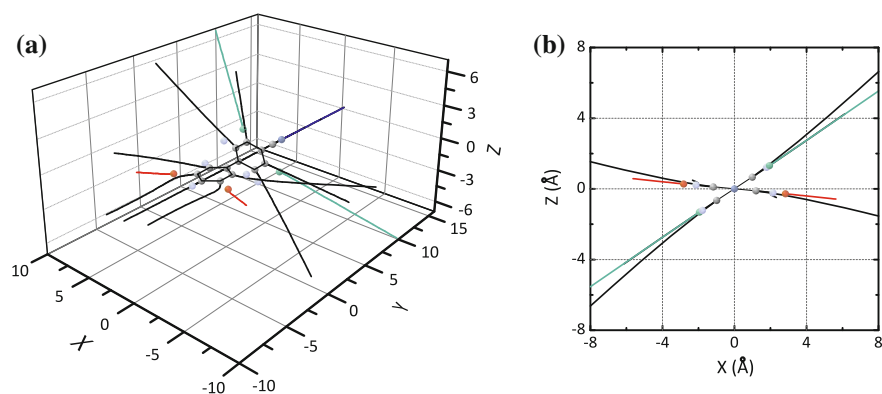


Fig. 6.18 Plots of the trajectories of the fragment ions following Coulomb explosion of DBrD-FCNBph carrying a single positive charge on each atom in three dimensions (a) and as projected onto the xz -plane (b), where the y -axis is coincident with the C_2 symmetry axis of the molecule. The trajectories are plotted up to 70 fs after the start of the simulation

photofragments. The calculated ion trajectories illustrate that, while for some atoms (such as the peripheral substituents N, F, and Br) axial recoil does indeed serve as a reasonable approximation, for a number of the constituent atoms, particularly those from the core of the parent molecule, the trajectories depart substantially from the axial recoil scheme. A particularly interesting example of this behaviour is seen in the trajectories of carbon atoms 10 and 12, which are bonded directly to the Br substituents on the first phenyl ring. The relatively large mass, and therefore inertia, of bromine causes the Br^+ ions to accelerate significantly slower than the C^+ ions to which they are bonded in the parent molecule. The carbon atoms at positions 10 and 12 initially depart the molecule on an axial trajectory, approximately parallel to the C–Br bond axis, but encounter an obstruction in the form of the Br^+ ions after a short time. The larger inertia of the Br^+ ions relative to C^+ causes the C^+ ions to deviate substantially from their initial path, resulting in their departure from the molecule along trajectories approximately parallel to the C_2 symmetry axis. In addition to deviations caused by obstructed ion trajectories, it is generally observed that ions formed from atoms located around the waist of the molecule are ejected almost perpendicular to the C_2 symmetry axis.

Figure 6.18b shows plots the projection of the ion trajectories onto the xz -plane, where the y -axis is coincident with the MPA of the molecule. Interestingly, the halogen substituents leave the molecule along trajectories largely confined to the planes of the phenyl rings to which they are originally bonded. This suggests that the relative recoil of the Br^+ and F^+ , as imaged in the xz -plane, is indeed indicative of the dihedral angle, as postulated in the discussion of Fig. 6.16.

Although the integrated ion trajectories plotted in Fig. 6.18 provide a highly intuitive representation of the fates of the various fragment ions following Coulomb explosion, they fail to convey the timescales of the process. Figure 6.19 plots the displacement and velocities of the various fragment ions as a function of time after the start of the simulation. Again, each atom in the parent molecule is allocated a single positive charge, so the values in Fig. 6.19 are intended as a guide to the range of timescales involved in the Coulomb explosion process. It is clear from this data that the ions are displaced to a significant extent during the pulse duration of the ionising laser (30 fs). By 30 fs the majority of ions have travelled between 0.8–4.5 Å, with the H^+ ions having effectively left the parent molecule long before this time. In fact, the H^+ ions effectively leave the molecule instantaneously, becoming displaced by 10 Å within ~ 13 fs. The remaining ions, however, move very little during the first 10 fs, becoming displaced by less than 1 Å. By 70 fs the ions are reaching their asymptotic trajectories, with slight increases in their velocities the only perturbations beyond this time. Additionally, the obstructed trajectories of carbon atoms 10 and 12 are readily identified in Fig. 6.19a.

Given the large displacements calculated for the ions within the time period corresponding to the ionising laser pulse, it would seem unlikely that detailed insights into the structure of the parent molecule should be possible through the use of CEI as a probe in this case. It is therefore interesting that the parameters extracted from the covariance images presented in Figs. 6.16 and 6.17 are in such close agreement with those calculated for the target molecules. This suggests that either the actual time

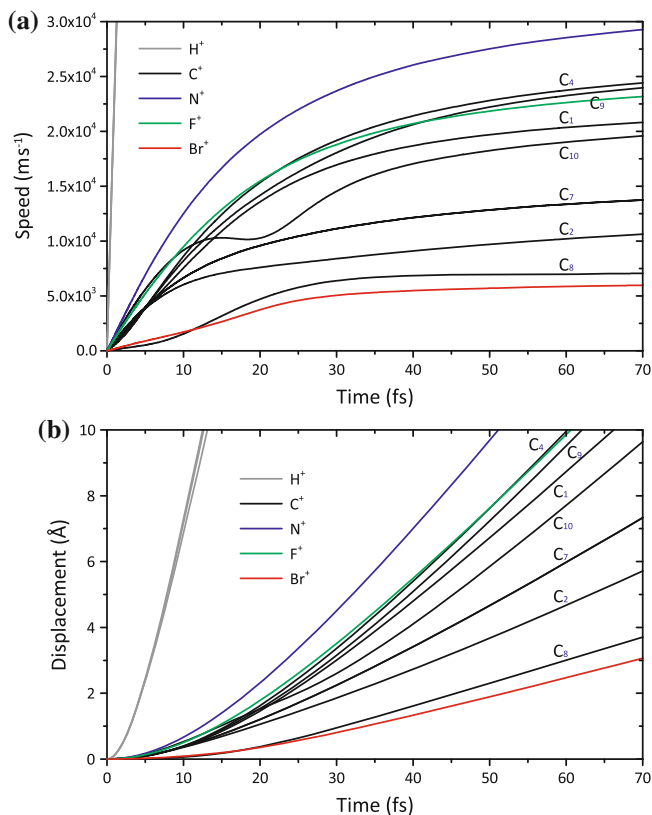


Fig. 6.19 Plots of the simulated displacement (a) and velocities (b) of the fragment ions as a function of time after the start of the simulation, at which time the ions are at rest at their equilibrium positions. The carbon ions are labelled according to the parent atom, as defined in Fig. 6.7. Each atom in the parent molecule is assigned a single positive charge

during which the ionisation of the parent molecule occurs is much shorter than the total pulse duration of the ionising laser, occurring only during the period when the pulse reaches near maximum intensity, or that the trajectories are not greatly affected by the gradual build-up of charge within the molecule. It is perhaps conceivable that such an extended molecule is able to support a substantial degree of charge before the Coulomb explosion of the system occurs. This would have the effect of allowing charge to accumulate gradually, with Coulomb explosion being triggered only when a threshold of total charge has been reached. From a slightly different perspective, this may be considered a break-down at early times of the assumption that the trajectories of the ions are determined solely by the Coulombic interactions. With respect to the timescales of parent ionisation, it is likely that ionisation proceeds via some sort of tunnelling or over-the-barrier mechanism, which will have an exponential dependence on the height of the barrier to ionisation. It is therefore plausible that

ionisation occurs only during the period of peak laser intensity, which will be substantially shorter than the 30 fs pulse duration. Of course, the actual dynamics of the Coulomb explosion process are not yet well understood, and these are merely suggestions of the possible reasons for the observed well-behaved nature of the Coulomb explosion process.

6.5.3 Comparison to Experimental Data

While the simulated data presented in Figs. 6.18 and 6.19 aid in the interpretation of the Coulomb explosion process, it is perhaps more useful to consider the final velocities of the ions in the plane of the detector, as these are the observable quantities from the experiment. Figure 6.20 shows the simulated velocity-map ion image following the Coulomb explosion of a single molecule of DBrDFCNBph with a single positive charge allocated to each atom. This idealised ‘ion image’, corresponding to a molecule with the F^+ phenyl ring confined to the plane of the detector, allows the relationships between the various ion velocities to be clearly identified. These velocity relationships are effectively being measured in the recoil frame covariance images extracted from the experimental data. Although the simulated ion image presented in Fig. 6.20 corresponds to only a single initial charge distribution and a single initial alignment of the parent molecule relative to the detector plane, it is worth comparing the velocity vector correlations measured from the experiment with those predicted by this simple simulation.

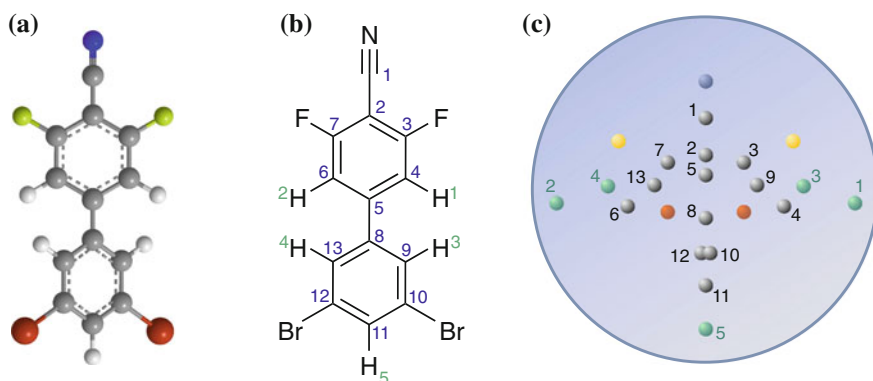


Fig. 6.20 Ball and stick (a) and skeleton (b) representations of DBrDFCNBph, alongside a simulated ‘ion image’ resulting from the Coulomb explosion of a single parent molecule originally in the geometry represented in **Panel (a)**, and in which each atom is assigned a single positive charge. The ions in **Panel (c)** are by colour according to their type (H^+ , green C^+ , black N^+ , blue F^+ , yellow Br^+ , red). The C^+ and H^+ ions in the ion image are identified according to the parent atom, as labelled in **Panel (b)**

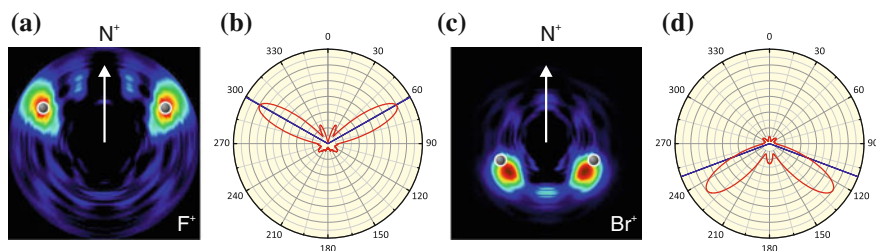


Fig. 6.21 Panels **a** and **c** show the simulated velocities of F^+ and Br^+ relative to N^+ superimposed on the corresponding pBASEX inverted recoil frame covariance images. The simulated data have been rescaled to overlay with the main features of the experimental data. Panels **b** and **d** plot in red the integrated intensities of the covariance images as a function of the relative recoil angle between the N^+ and the F^+ and Br^+ ions, respectively. The radial blue lines represent the predictions of the simulations

Figure 6.21 overlays the simulated relative velocities on the pBASEX inverted covariance images of F^+ and Br^+ , as measured relative to N^+ , following parallel alignment of the target molecules, as previously presented in Fig. 6.17. The simulated ion images have been rescaled to approximately match the velocities observed in the experimental images. The agreement between the simulation and the experimental data is exceptional in the case of F^+ relative to N^+ . The simulated data predict a relative recoil angle of 60.5° , the exact value extracted from the inverted covariance images. In the case of Br^+ relative to N^+ , however, the agreement is qualitatively good, but the discrepancy between the simulation and experimental data is pronounced. The simulated ion trajectories predict a relative recoil angle between the N^+ and Br^+ of 112.5° , which differs substantially from the experimentally determined value of 127.2° . This difference, wherein the Br^+ ions are predicted to have a tighter relative recoil angle with respect to N^+ , may be caused by the exaggerated effect of the obstructed C^+ ion trajectories, which act to push the Br^+ away from the path predicted by axial recoil. In reality, it is possible that the likelihood of yielding a C^+ ion from the 10 or 12 positions is lower than assumed in the simple model used in these simulations. This hypothesis is supported by the electron density calculations presented in Fig. 6.7, which suggest that the carbon atoms at the 10 and 12 positions carry a net negative charge, even for very highly charged states of the molecule. If the simulation is run with zero charge assigned to these carbon atoms, the relative recoil angle between the Br^+ and N^+ increases significantly to 150.6° , suggesting that the actual situation lies somewhere between these two extremes.

The interpretation of the covariance images of the halogens relative to N^+ is rather straightforward, and the simulations act to provide a more quantitative appreciation of the factors governing the ion trajectories. However, the covariance images corresponding to the more abundant constituents of the parent molecule, in particular those of the H^+ and C^+ fragments, are more complex in their composition and are therefore more difficult to interpret. The simulated ion trajectories in these cases offer a valuable insight into the relationship between the structure of the parent molecule

and the features of the experimentally measured covariance images. To illustrate this point, Fig. 6.22 presents the covariance images of H^+ and C^+ plotted relative to N^+ , F^+ , and Br^+ , overlaid with the appropriately transformed simulated H^+ and C^+ ion images. In the covariance images where correlations are measured relative to ions located at two positions in the molecule, as is the case for the measurements relative to F^+ and Br^+ , the contributions from the second reference ion are circled in red.

Row (a) of Fig. 6.22 compares the simulated and experimental covariance images of H^+ relative to N^+ , F^+ , and Br^+ , while Row (b) plots the integrated intensities of the experimental covariance images as a function of relative scattering angle between the plotted and reference ions. At first glance, it is clear that the simulated ion trajectories reproduce reasonably well the main features of each of the experimental covariance images. The measurement relative to N^+ illustrates clearly that the strong perpendicular feature corresponds to the equatorial H^+ ions, whereas the antiparallel component corresponds to the H^+ ion originating from the end of the molecule opposite to the CN group. Given the speed at which the H^+ ions are calculated to escape the influence of the parent molecular ion, it is perhaps surprising that the simulated and experimental ion trajectories are in such close agreement. This strong agreement between the simulations and experiment is reproduced for the measurements of H^+ relative to F^+ and Br^+ , where the origin of the different relative intensities of the major angular features of the covariance images is revealed. The four main peaks in the angular intensity profiles plotted in Panels II(b) and II(c) of Fig. 6.22 each contain contributions from the equatorial H^+ ions. The different intensities of the forward- and backward-scattered peaks results from the contribution, or otherwise, of H atom 5, coincident with the C_2 axis of the molecule.

Rows (c) and (d) of Fig. 6.22 show the C^+ analogues of the H^+ data presented in Rows (a) and (b). The somewhat higher abundance of carbon in the parent molecule leads to rather more congested, and therefore more difficult to interpret, covariance images. However, in each case, the simulations appear to reproduce to some extent the main features of the experimental data, offering a valuable insight into the relationship between the structural composition of the parent molecule and the resulting relative recoil of the fragment ions. The covariance image of C^+ relative to N^+ presented in Panel I(c) is composed primarily of a large lobe of intensity scattered preferentially in the forward direction. In addition there exists a localised peak in intensity in the backward-scattered direction, corresponding to C^+ ions travelling in an antiparallel manner following Coulomb explosion. The simulated ion trajectories overlay favourably with the experimental data, revealing the origins of each feature in the covariance image. It would appear that the backward-scattered tail is composed of contributions from C^+ ions originating from the 10, 11, and 12 positions. The experimental covariance image appears to lend strong support to the prediction that the carbon ions originating from the 10 and 12 positions in the parent molecule follow an initially obstructed trajectory which causes a substantial deviation in their flight path from that expected according to axial recoil assumptions. The remaining carbon ions contribute to the dominant forward-scattered component of the covariance

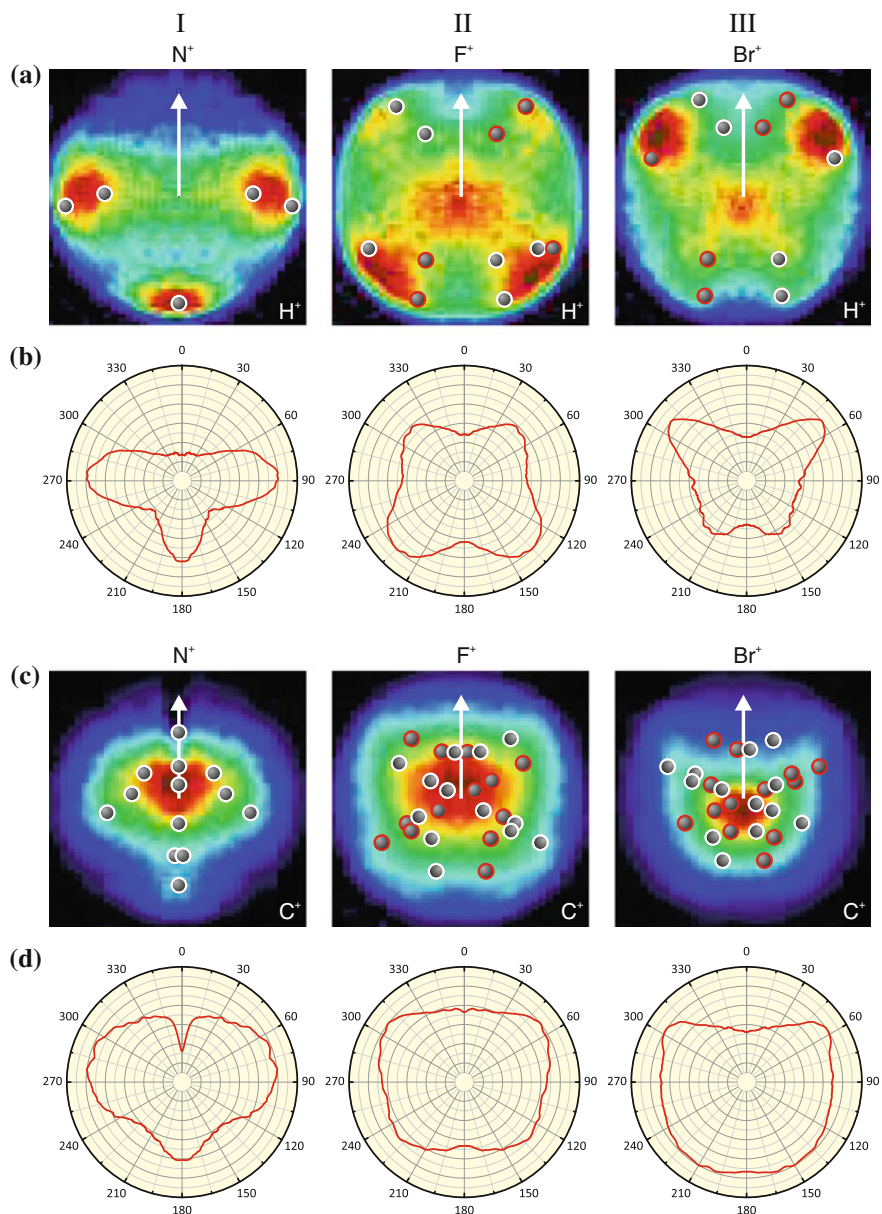


Fig. 6.22 Rows **a** and **c** show, respectively, the covariance images of H^+ and C^+ relative to N^+ (**I**), F^+ (**II**), and Br^+ (**III**), as recorded following parallel alignment of the MPA with the detector plane, overlaid with the simulated relative recoil velocities. The simulated data have been rescaled to overlay with the main features of the experimental data. Rows **b** and **d** plot the integrated intensities of the covariance images as a function of the relative recoil angle between the fragment ions. Where the covariance images contain contributions as measured relative to ions located at two distinct positions in the molecule, as is the case for the measurements relative to F^+ and Br^+ , the contributions from the second reference ion are circled in *red*

image, with the two small lobes at approximately 105° and 255° corresponding to the carbon atoms at the 4 and 6 positions.

The general agreement between the experimental data and the simulated ion trajectories, and resulting structural insight demonstrated in the above discussion is repeated in Panels II(c) and III(c). Where the C^+ recoil velocities are plotted relative to the F^+ ions, the peaks at approximately $\pm 50^\circ$ and $\pm 130^\circ$ are predicted by the simulated ion trajectories. These peaks in intensity correspond to the increased density of simulated ion trajectories across the diagonal of the images, resulting from the large number of C^+ ions that are ejected parallel to the MPA of the parent molecule. Similarly, the prominent features at approximately $\pm 55^\circ$ in the experimental covariance image of C^+ relative to Br^+ are reproduced by the simulated ion trajectories. Once again, it is the contribution of the C^+ ions originating from positions 10, 11, and 12 that are responsible for the sharp features observed.

Although the covariance images obtained following parallel alignment of the target molecules relative to the detector plane are arguably richer in structural information than those recorded following perpendicular alignment, there are nonetheless a number of covariance images recorded in the latter geometry that display distinctly anisotropic features worthy of further investigation. The top Row (a) of Fig. 6.23 shows, respectively, the covariance images of H^+ , C^+ , and F^+ , relative to F^+ (Columns I and II), and Br^+ (Column III), as recorded following perpendicular alignment of the MPA to the detector plane, overlaid with the simulated relative recoil velocities of the ions. Once again, the simulated ion trajectories in each case are generally suggestive of the features seen in each of the covariance images. However, although the agreement is indeed strong between the simulated ion trajectories and the covariance images, there are some interesting points of difference present, which may be suggestive of details of the Coulomb explosion dynamics. For example, in the recoil frame covariance image of C^+ relative to F^+ , the contribution of the C^+ ions corresponding to the carbon atoms 4 and 6 in the parent molecule is under-represented when compared to that suggested by the simulated ion trajectories. This suggests that either the carbon atoms at the 4 and 6 positions carry little charge in general or that there is a reduced probability of charge build-up at these positions if the fluorine atom carries a positive charge. Since features corresponding to C^+ ions originating from the 4 and 6 positions in the parent molecule have been identified previously, it would seem likely that the reduced contribution of these atoms to this particular covariance image is caused by correlations in electron density in the parent ion. This is, of course, highly speculative, but would appear to be plausible in light of the evidence presented here.

Panel III (a) plots the simulated and experimental relative recoil angle between the Br^+ and F^+ fragments, which is suggested to be indicative of the dihedral angle of the molecule. The value predicted by the simulations is 40.9° , which is in fairly close agreement with the values extracted from the experimental data of $41.8 \pm 1.31^\circ$, and $45.1 \pm 0.39^\circ$. This simple model appears to overestimate the relative recoil angle by between 0.9° and 4.2° , which represents a good level of agreement in the context of the absolute values.

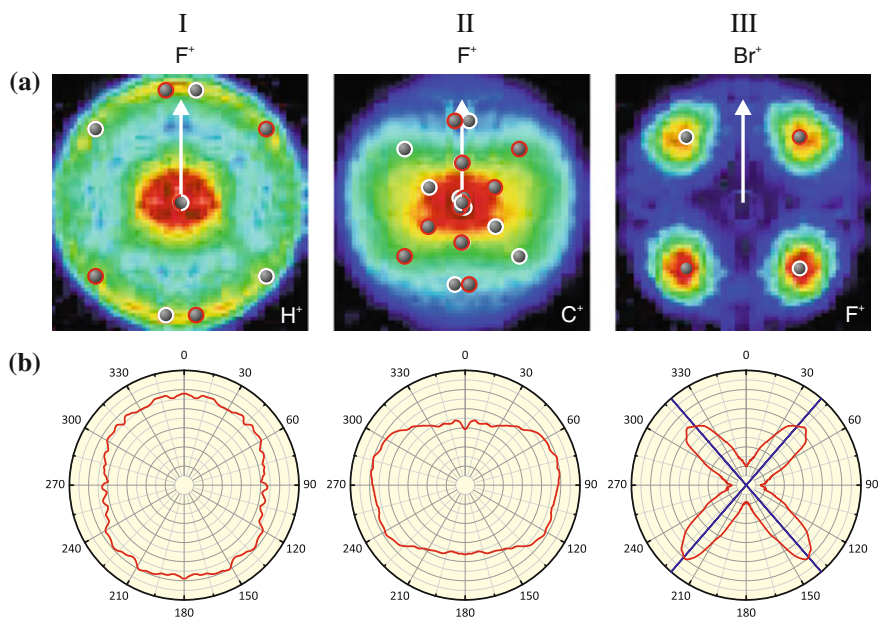


Fig. 6.23 Row **a** shows, respectively, the covariance images of H^+ , C^+ , and F^+ , relative to F^+ (**I** and **II**), and Br^+ (**III**), as recorded following perpendicular alignment of the MPA to the detector plane, overlaid with the simulated relative recoil velocities. The simulated data have been rescaled to overlay with the main features of the experimental data. Row **b** plots the integrated intensities of the covariance images as a function of the relative recoil angle between the fragment ions. Where the covariance images contain contributions as measured relative to ions located at two distinct positions in the molecule, as is the case for the measurements relative to F^+ and Br^+ , the contributions from the second reference ion are *circled in red*

6.6 Simulation of Experimental Data

The simple model of Coulomb explosion presented in the previous section has been demonstrated to provide many valuable insights on the behaviour of the fragment ions during Coulomb explosion, and has proved to be remarkably effective in reproducing the primary features of the recoil frame covariance images. In particular, the understanding of the relationship between the structure of the parent molecule and the asymptotic recoil velocities of the fragment ions that is afforded is promising. However, this simple model neglects many of the factors important in the experiment, which must be included if a more complete and accurate simulation of the experimental data is to be pursued.

6.6.1 Details of the Simulations

In order to simulate more closely the experiments described in this chapter, several modifications were made to the simulation routine. The simulations presented thus far have been concerned with the Coulomb explosion of a single parent molecule, which is to neglect the vast number of initial starting conditions that are possible, in terms of the total charge held by the parent molecule and its distribution amongst the constituent atoms. To more accurately reflect this in the simulations, each molecule is assigned an integer number of positive charges, in units of elemental charge (q), according to a Poisson distribution. The charges are randomly localised amongst the atoms, weighted according to the experimentally observed relative charge per atom type, as listed in Table 6.1. Additionally, each atom type has a maximum number of charges that it may support, as informed by the time-of-flight data (H = 1; C, N, F = 2; Br = 3). A further layer of averaging that has been ignored in the simulations thus far is that related to the precise orientation of the target molecule relative to the imaging plane. Since the molecules are only one-dimensionally aligned in the experiment, rotation about the C_2 symmetry axis is unrestricted. To accurately reproduce this rotational averaging in the calculation of the simulated ion trajectories, each target molecule is rotated through an arbitrary angle about the C_2 symmetry axis of the molecule prior to Coulomb explosion. Additionally, the imperfect degree of alignment observed in the experiment is approximated using a $\cos^4 \theta$ weighted distribution of the MPA of the target molecules, where θ is the angle between the electric vector of the alignment laser pulse and the C_2 symmetry axis of the molecule. With additional layers of averaging included in the ion trajectory simulation routine, it becomes possible to attempt a full simulation of the experiment. Each simulation is run over 30,000 trajectories in order to achieve a satisfactory convergence of the data, and the covariance maps generated on each iteration are summed together to yield the final output.

6.6.1.1 Limitations of the Approach

Although the simulation routine has been adapted to incorporate some of the averaging present in the physical experiment, it is important to note that the inherent model remains fundamentally the same: that the ions are assigned charge when at rest in their equilibrium positions and the trajectories calculated using the forces of Coulomb repulsion and Newtonian mechanics. More complex phenomena likely to be important in the process, such as the gradual ionisation of the parent molecule and charge redistribution during dissociation, are still ignored. Furthermore, some assumptions must still be made regarding the range of initial conditions over which the system must be averaged in order to closely simulate the experiment. In particular, the degree of alignment of the target molecules has been approximated to a $\cos^4 \theta$ distribution, where the exponent value of 4 has been used as an initial estimation, which reproduces relatively closely the features observed experimentally. An exact

determination of the true degree of the target molecules in the experiment is difficult as the observed alignment of the molecule, as calculated from the observed ion signals, is influenced by both the degree of alignment of the target molecules and the deviation from axial recoil of the ionic product fragments caused by the influence of the Coulomb explosion process on the ion trajectories.

A further approximation must be made in determining the average charge carried by each of the parent molecules prior to Coulomb explosion. Simulations have been performed using average charge states of 10+, 15+, and 20+ in order to gain some understanding of the initial conditions present in the experiment. From these investigations it was observed that an initial average charge of 15+ gave the closest qualitative agreement to the experimental data and was therefore the value used in the following simulations. Ideally, a calibration of the ion fragment kinetic energies would allow a direct comparison between the absolute experimental and simulated velocities. This may seem an attractive route towards determining the total charge state of the parent molecule prior to fragmentation since the final kinetic energies of the fragment ions will be determined by the geometry and charge distribution in the parent ion, according to Eq. 6.12. However, such assumptions have been shown to be rather inadequate in the case of Coulomb explosion since a small displacement in the initial positions of the atoms during the ionisation process will cause large differences in the final kinetic energies of the ions [2]. As the ion trajectory calculations in this chapter have shown, the atomic nuclei are likely to become displaced on the timescale of parent ionisation (see Fig. 6.19). Furthermore, in the present case, the precise distribution of charge amongst the constituent atoms of the parent molecule is not yet well understood. For these reasons, the absolute velocities of the simulated covariance images were deemed an unsuitable route to determining the charge state of the parent ion prior to Coulomb explosion. Instead, the charge state of the parent ion was estimated through a qualitative comparison of the simulated and experimental data, and the simulated covariance images appropriately scaled to overlay favourably with the experimental data.

For future experiments, one possibility is that a knowledge of the total number of ions, and therefore charges, recorded on each laser shot may be statistically fitted from the experimental data to yield the distribution of initial charge states of the parent molecules. The parameters to be fitted include the average number of molecules undergoing Coulomb explosion on each acquisition cycle and the statistical probabilities of a given number of charges being supported by each target molecule prior to break-up. In the current experiment this approach is difficult, however, due to the highly condensed time-of-flight spectrum and the number of ions that travel beyond the limits of the MCPs and are therefore not detected. However, there are no fundamental practical reasons why an experiment could not be designed to allow such measurements to be taken.

6.6.2 Simulation Results

6.6.2.1 General Details

The full set of experimental and simulated recoil frame covariance images for all singly charged ions, as recorded following parallel alignment of the target molecules, is presented in Fig. 6.24. It is immediately obvious that the agreement between the simulated and experimental data is, at least qualitatively, very good. In general, the majority of the experimentally observed features are clearly reproduced in the simulated recoil frame covariance images. The strength of the agreement is perhaps surprising, given the basic assumptions of the model and the relatively long duration of the probe laser pulse, providing further support for the assertion that CEI provides a means of determining structural parameters of large polyatomic molecules on a femtosecond timescale. The simulations suggest that the variable initial charge states of the target molecules is largely responsible for the broad nature of the features present in the experimental covariance images, with further broadening caused by the finite degree of alignment of the target molecules and free rotation about the MPA.

Figure 6.25 compares the experimentally measured and simulated recoil frame covariance images recorded following perpendicular alignment of the molecules relative to the imaging plane. Although the radial properties of the simulated covariance images are generally in good agreement with the experimental data, the angular properties are somewhat less convincing than in the case of parallel alignment. The

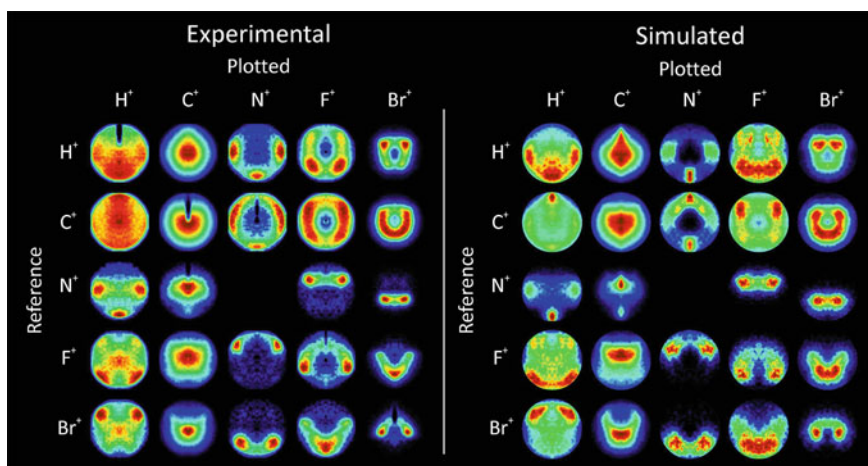


Fig. 6.24 Experimental (*left*) and simulated (*right*) recoil frame covariance images, as recorded following Coulomb explosion of molecules aligned parallel to the detector plane. In each case the ion species plotted is labelled at the top of the column, with the reference ion labelled to the left of the rows. In each case the reference ion is confined to a vertical vector from the centre of the covariance image to the top edge

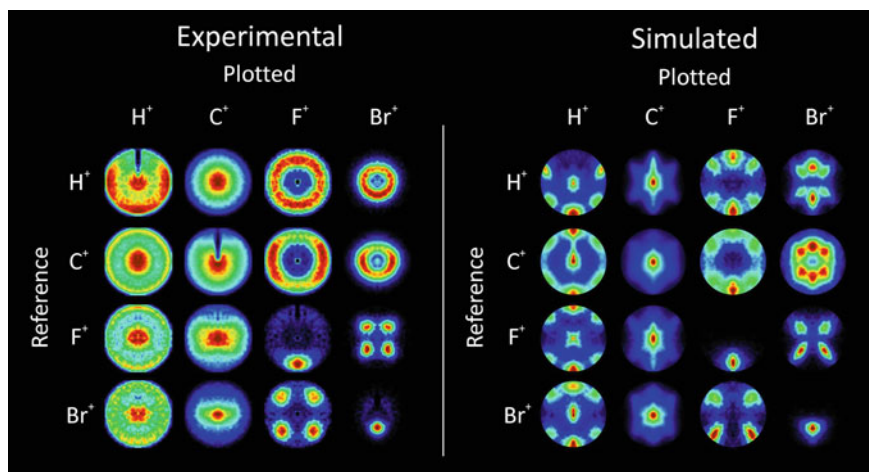


Fig. 6.25 Experimental (*left*) and simulated (*right*) recoil frame covariance images, as recorded following Coulomb explosion of molecules aligned perpendicular to the detector plane. In each case the ion species plotted is labelled at the top of the column, with the reference ion labelled to the left of the rows. In each case the reference ion is confined to a vertical vector from the centre of the covariance image to the top edge

features of the simulated covariance images are considerably more localised than those present in the experimental data, suggesting a far higher degree of angular correlation between the fragment ions than is observed experimentally. The relatively low level of angular correlation observed experimentally is perhaps suggestive of deformation of the parent molecule out of the planes defined by the phenyl rings during the early stages of Coulomb explosion. This result should perhaps be expected given that the phenyl rings are initially planar to facilitate the delocalisation of π -electrons, which are likely to be removed during the process of ionisation preceding molecular explosion. With the stabilising effect of conjugation lost, the molecule is free to relax into a non-planar conformation. Such a relaxation of the initially rigid carbon skeleton would have the result of reducing the strength of the angular correlations between the trajectories of the fragment ions, as observed in the experimental data. The angular correlations observed following alignment of the MPA perpendicular to the imaging plane are far more sensitive to the planarity, or otherwise, of the phenyl rings than the measurements taken in a parallel geometry, hence the somewhat poorer agreement between the simulated and experimental data in this case. Nevertheless, certain covariance images show a clear similarity between the simulated and experimental data. In particular, the covariance images describing correlations between and amongst F^+ and Br^+ resemble closely those predicted by the simulations. Since these correlations are indicative of the dihedral angle between the two phenyl rings, it is promising that the simulations successfully reproduce the experimental data in these cases.

Fig. 6.26 Relative average scaling factors used for the simulated recoil frame covariance images of each ion species. See text for details

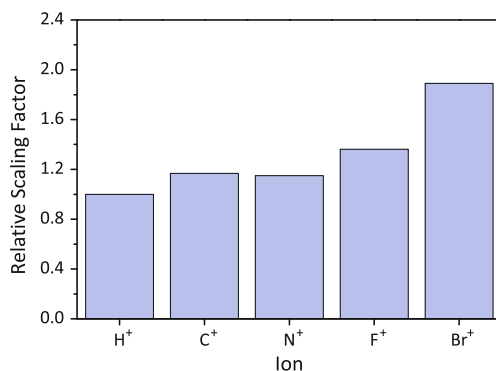


Figure 6.26 summarises the average relative scaling factors used to fit the simulated data to the experimental covariance images for each ion species. The scaling factors reveal some interesting discrepancies between the simulated and experimental data. Clearly, the bromine ion velocities observed experimentally are far in excess of those predicted through simulation. This is again suggestive of substantial charge migration during the early stages of Coulomb explosion. In the ion trajectory calculations the initial charge state of each ion is conserved throughout the simulation. In order to account for the experimentally observed bromine ion velocities, it would appear that the ions must initially carry a far higher charge than is observed at the detector such that the ions possess sufficient Coulombic potential energy to account for their final recoil velocities. This hypothesis is supported by the electron density calculations presented in Table 6.1, which predict exceptionally high partial charges on each of the bromine ions, far in excess of that observed experimentally from the ion yields. The evidence therefore suggests that in the molecular ion the positive charge is supported to a substantial degree by the bromine atoms, which becomes redistributed during the early stages of fragmentation to yield the observed charge states of the bromine ions. The H⁺ scaling factors are the lowest of all ions. This may be explained by considering that the hydrogen ions are expected to become substantially displaced on the timescale of molecular ionisation due to their low mass (see Fig. 6.19), thereby reducing the final velocities of the ions from those expected based on an impulsive ionisation model. That the scaling factor is not so much smaller than the other ions is perhaps surprising, and suggests that the hydrogen atoms remain bound to the molecule for a substantial time during the process of ionisation. The scaling factors of the remaining ions lie somewhere between these two limits. The slightly higher scaling factors applied to the fluorine ion images are perhaps suggestive of some degree of charge redistribution akin to that observed for the bromine ions, but to a far lesser extent.

6.6.2.2 Detailed Analysis of Selected Data

The data presented in Figs. 6.24 and 6.25 demonstrate that there is a good qualitative agreement between the simulated and experimental data. However, since the experimental covariance data have been used to extract quantitative measurements of the molecular structure, namely the dihedral angle between the two phenyl rings and the bonding angles of the fluorine and bromine atoms relative to the CN group, it is possible to gain a quantitative assessment of the agreement between the simulated and experimental data by measuring the same coordinates from the simulated covariance images.

Figure 6.27 compares the simulated and experimental covariance images of F^+ and Br^+ to N^+ , as viewed parallel to the C_2 symmetry axis of the parent molecule,

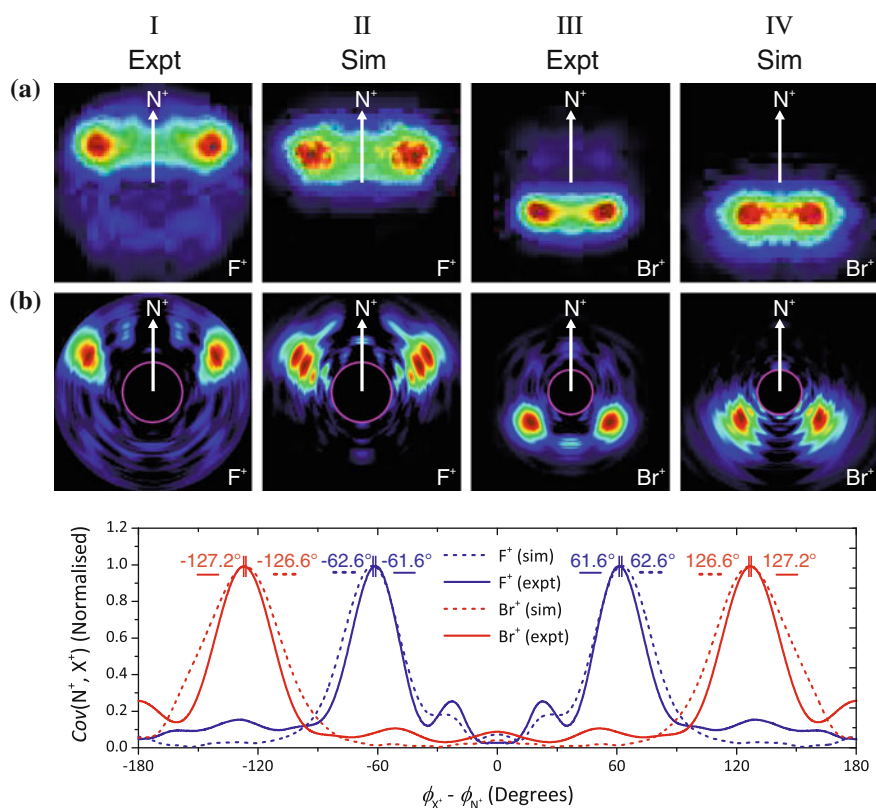


Fig. 6.27 Presented in **Row a** are the experimental (**I** and **III**) and simulated (**II** and **IV**) recoil frame covariance images of F^+ relative to N^+ (**I** and **II**) and Br^+ relative to N^+ (**III** and **IV**). **Row b** presents the pBASEX inversions of the covariance images displayed in **Row (a)**. The lower panel compares the simulated and experimental covariance as a function of the relative recoil angle of the partner fragment ions, as determined from the pBASEX inverted data

alongside the pBASEX inversions of the data. The lower panel of the figure plots the angular intensities of the inverted images for both the simulated and experimental data. It is clear from this comparison that the parameters extracted from the simulated and experimental data are in excellent agreement. The most probable relative recoil angle between the F^+ and N^+ fragment ions, as measured experimentally and predicted by the simulation, differs by only 1.0° , with the simulated data predicting an angle of 62.6° compared to the experimentally observed value of 61.6° . The agreement in the case of Br^+ improves upon that observed for the F^+ ions, with a simulated value of 126.6° comparing very favourably to the experimentally determined most probable relative recoil angle of 127.2° . The level of agreement between the experimental and simulated data is striking, given the simplicity of the model employed and the approximations involved. Nonetheless, this is not to say that the agreement is perfect, and there remains some significant differences between the experimental and simulated data; most notably in the relative spread of recoil velocities of the photofragments and the degree of confinement about the most probable relative recoil angles.

Of particular interest is the measurement of the dihedral angle between the two phenyl rings of the parent molecule, which represents perhaps the most characteristic coordinate of the parent structure. Figure 6.28 compares the simulated and experimental covariance images corresponding to the recoil of F^+ and Br^+ relative to one another, as viewed along the C_2 symmetry axis of the parent molecule. Panel (b) of Fig. 6.28 compares the angular intensities of the simulated and experimental covariance images, with Panel (c) showing the fitting of the simulated data to four asymmetric sigmoidal peak functions. From the simulated data, the relative recoil angles between the F^+ and Br^+ ion fragments are predicted to be $48.3 \pm 2.3^\circ$ for the near side peaks, and $137.2 \pm 1.5^\circ$ for the far side peaks, corresponding to a dihedral angle of $42.8 \pm 1.5^\circ$. These values are in good agreement with those measured from the experimental data, where the maxima are observed at $45.1 \pm 0.4^\circ$ for the near side peaks, and at $138.2 \pm 1.3^\circ$ for the far side peaks, which corresponds to a dihedral angle of $41.8 \pm 1.3^\circ$.

In addition to accurately predicting the relative recoil angles of the F^+ and Br^+ product ions, the differences observed between the near side and far side peaks are also reproduced in the simulated data, with the far side peaks being considerably narrower and implying a smaller dihedral angle than their near side counterparts. In Sect. 6.4 it was suggested that the differences between the proximal and distal ion pair trajectories is largely due to the increased pairwise Coulomb repulsion experienced between the F^+ and Br^+ fragment ions when the two ions originate from the same side of the molecule, influencing the trajectories of the ions during the early stages of Coulomb explosion. Since the present model considers exclusively Coulombic forces, the reproduction of this effect in the simulated data appears to support this assertion. However, in the model system, unlike in the experiment, it is possible to investigate precisely the effect of each ion on the rest of the system. In particular, it is possible to ignore terms in Eq. 6.12, describing the pairwise Coulomb repulsion between specific ions. Ion trajectories were therefore simulated with the terms describing the pairwise interaction between the F^+ and Br^+ fragments ignored.

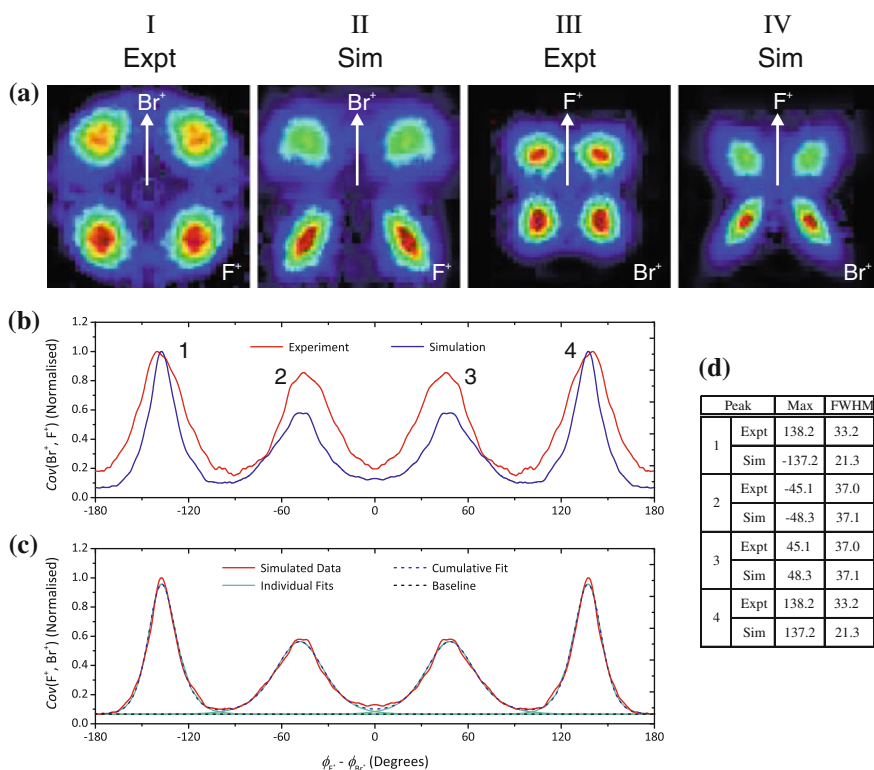


Fig. 6.28 Presented in **Row a** are the experimental (**I** and **III**) and simulated (**II** and **IV**) recoil frame covariance images of F^+ relative to Br^+ (**I** and **II**) and Br^+ relative to F^+ (**III** and **IV**). **Panel b** compares the simulated and experimental covariance as a function of the relative recoil angle of the partner fragment ions. **Panel c** illustrates the fitting of the simulated data to four asymmetric sigmoidal peak functions. The table presented in **Panel d** summarises the properties of the four peaks labelled in **Panel (b)**, as determined from the fits to the data

The resulting recoil frame covariance image of F^+ relative to Br^+ is shown in Panel II of Fig. 6.29. Interestingly, the covariance image in the absence of pairwise interactions between F^+ and Br^+ is almost identical to that calculated using the full model, as presented in Panel I. Although the proximal peaks are narrowed slightly in the absence of direct F^+/Br^+ repulsions, they remain far broader than their distal counterparts. However, closer inspection of the angular dependence of the correlated ion trajectories, as presented in Panel (b) of Fig. 6.29, reveals that the implied dihedral angle, as measured from both the proximal and distal peaks, is reduced when compared to the full simulation. The relative recoil angles between the F^+ and Br^+ are measured as 44.4° and 39.8° , from the proximal and distal ion pairs, respectively. These values are in closer agreement to the actual dihedral angle of the molecule of 39.0° than those extracted from the full simulation, implying that the pairwise interactions between the F^+ and Br^+ , while not the primary cause of the differences

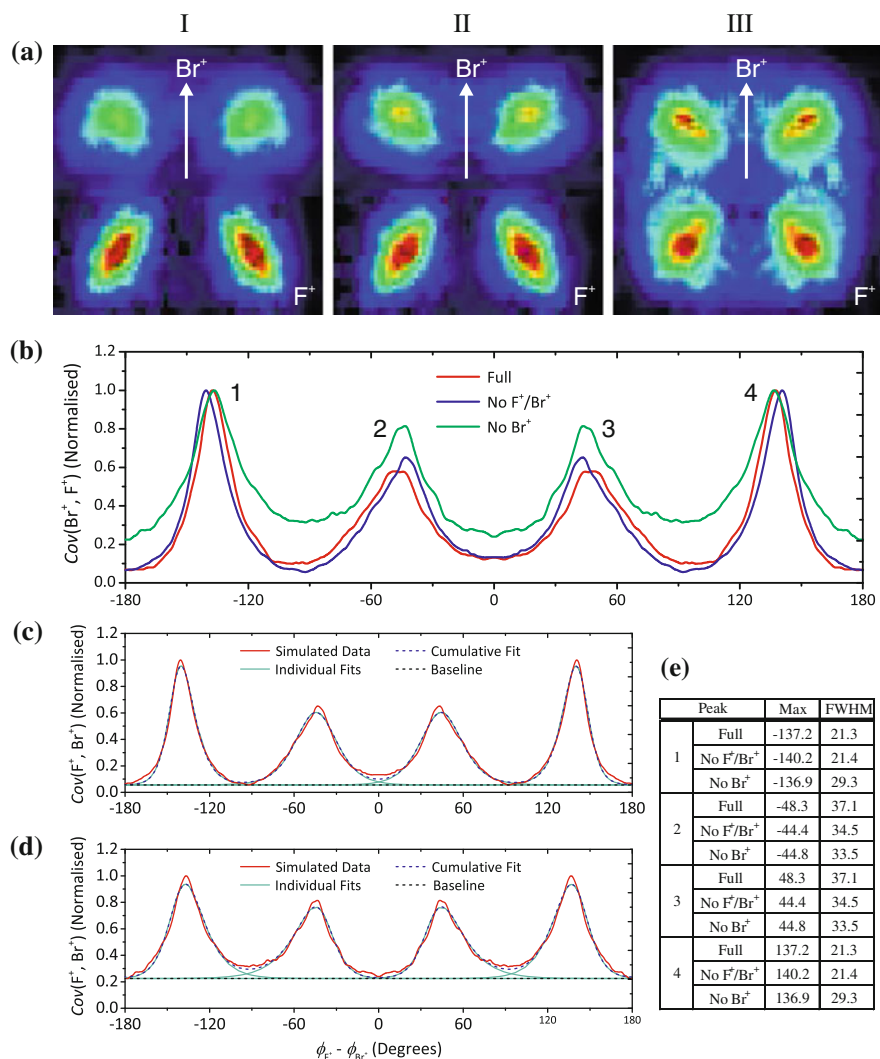


Fig. 6.29 Row **a** presents the simulated covariance images of F^+ relative to Br^+ in the case of (I) all Coulomb terms included, (II) the exclusion of the pairwise repulsion of F^+ and Br^+ , (III) the exclusion of repulsive forces resulting from interactions with Br^+ as the second body. Panel **b** compares the covariance plotted as a function of the relative recoil angle between the partner ions for each of the cases presented in Row **(a)**. Panels **c** and **d** illustrate the fitting of the simulated data presented in Panels **II** and **III**, respectively, to four asymmetric sigmoidal peak functions. The table presented in Panel **e** summarises the properties of the four peaks labelled in Panel **(b)**, as determined from the fits to the data

observed between the proximal and distal peaks, do influence the ion trajectories to a measurable extent.

The logical corollary of these findings is that the repulsive interactions between the F^+ and Br^+ ions are largely mediated through third parties, rather than through the simple pairwise interaction initially postulated. To investigate this assertion, a further simulation was run in which the trajectories of all ions were unaffected by the Coulomb terms corresponding to interactions with Br^+ ions. The trajectories of the Br^+ ions themselves were calculated as in the full simulation, with all Coulombic terms included. The resulting recoil frame covariance image is shown in Panel III of Fig. 6.29. The removal of the Br^+ terms from the equations of motion noticeably alters the ion trajectory correlations with the features of the covariance image becoming markedly broader. This observation suggests that the presence of the Br^+ ions acts to restrict the possible range of trajectories of the other product ions. With the repulsive influence of the Br^+ ions removed, the remaining ions are free to explore a greater range of possible ion trajectories, resulting in the broadening of the features observed in the covariance image. Interestingly, although there are still differences between the peaks corresponding to the distal and proximal ion pairs, these differences are markedly less pronounced than in the full simulation. The proximal ion pair peaks are still slightly broader than their distal counterparts, but this is to be expected as the Br^+ ions are still subject to repulsions caused by the F^+ ions, both directly and indirectly.

6.7 Summary

This chapter has demonstrated the considerable advantages conferred through the application of the PImMS camera to the recording of multi-mass velocity-map images following the Coulomb explosion of a large polyatomic molecule. The information content of the data upon concurrent acquisition of the full set of product fragment ion images on each acquisition cycle is compelling, allowing inferences on the structure of the parent molecule and the dynamics of Coulomb explosion to be made through analysis of the correlated fragment ion trajectories. The data presented are suggestive of many details of the Coulomb explosion process, including the mechanism of ionisation, charge localisation and migration, and rearrangement of the parent structure following ionisation. Furthermore, the measured and simulated fragment ion trajectories suggest that it is indeed possible to measure to a reasonable degree of accuracy various characteristic structural coordinates of the parent system on a femtosecond timescale.

The unique properties of the PImMS camera are crucial to the success of these measurements. While there are alternative devices that are capable of recording ion events to a high degree of temporal and spatial accuracy, the unique ability of the PImMS camera to record a large number of ion events simultaneously and without an appreciative loss of data is decisive in this application. The use of a delay line detector would place severe constraints on the number of ions that may be

detected concurrently, rendering the technology unsuitable for the recording of data following the Coulomb explosion of moderately large polyatomic systems containing a number of identical constituent atoms. Alternative silicon-based detectors, such as the TimePix/MediPix family, overcome this limitation, but at the expense of an imperfect and non-uniform collection efficiency of late-arriving ions. This is a direct consequence of each pixel containing only a single memory register, resulting in shadowing of later mass peaks by those occurring at earlier times. Where a large variety of product fragments are yielded spanning a large range of mass and charge states, this limitation has the potential to systematically reduce the fidelity of the experimental data.

Having stated the considerable and unique advantages of the PImMS camera, it is important to note that the present experiment is not without its limitations. For example, due to the size of the ion detector, a number of fragment ions of high velocity are unrecorded, skewing the calculated ion yields and resulting in an incomplete representation of the system under investigation. Moreover, the small size of the ion detector requires the use of high extraction voltages, thereby condensing the mass spectrum and reducing the overall effective mass resolution of the experiment. This has implications for the assignment of the various peaks in the time-of-flight spectrum. The experiments presented in this chapter utilise the 1D adiabatic alignment of the target molecules prior to Coulomb explosion to aid the interpretation of the experimental data. While it is arguably not entirely necessary to pursue such a scheme, the advantages of this approach are clear. In the present example, the MPA of the molecules coincides with the primary molecular axis, allowing for a straightforward interpretation of the resulting ion images and covariance information. However, while it is generally likely that the polarisability tensor is diagonal in the molecular frame, this is by no means guaranteed, which has implications for the range of systems for which the combination of alignment and CEI is suitable. The relatively long ionising laser pulse is also likely to cause a reduction in the information content of the resulting data, with minor rearrangements of the parent structure possible on the timescale of the ionisation. Commercial systems are currently available that provide laser pulses as low as a few femtoseconds, which limits the possibilities for atomic displacement during the ionising step of Coulomb explosion. Employing such laser systems to similar experiments should allow for a more accurate determination of the structural coordinates of the parent system, including the possibility of measuring bond lengths in addition to bond angles and molecular configuration.

The success of a simple model in the simulation of the ion trajectories is encouraging. The details of the simulations reveal much about the dynamics of Coulomb explosion, and are informative of the relationship between the structure of the parent molecule and the final trajectories of the various fragment ions. The refinement of this simple model to include, for example, the effects of the finite ionisation period and charge migration during the early stages of the Coulomb explosion should further our understanding of this interesting and complex phenomenon. That such a simple model has proved capable of reproducing many of the characteristic features present in the experimental data suggests that there is much promise in the suggestion that CEI combined with ion trajectory calculations represents a relatively straightforward

and accessible means of monitoring changes to the structural parameters of molecular systems on a femtosecond timescale. Furthermore, that the simulations predict to a reasonable degree of accuracy the trajectories of even the lightest ions following Coulomb explosion by a relatively long probe laser pulse is surprising. The success of the model is strongly suggestive that either ionisation occurs on a much shorter timescale than the duration of the probe laser pulse or that a more complex scheme of ionisation and dissociation is followed. For example, it is possible that the parent molecule remains bound until such time as a threshold level of charge is reached, after which molecular break-up proceeds rapidly, thereby reducing the effect of the finite duration of the ionisation step. In order to understand better the early time behaviour of the system, it will be necessary to gain a clearer understanding of the range of initial charge states of the parent molecule prior to break-up, and how these relate to possible bound states of the system.

The strategy introduced in this chapter holds much promise for the measurement of characteristic structural parameters, particularly those relating to bond angles, of relatively large polyatomic systems on a femtosecond timescale. In the following chapter, this potential is explored through the time-resolved measurement of the dihedral angle following following excitation of the torsional mode by a femtosecond kick pulse.

References

1. A. Rudenko, Th Ergler, B. Feuerstein, K. Zrost, C.D. Schröter, R. Moshhammer, J. Ullrich, *Chem. Phys.* **329**, 193 (2006)
2. F. Légaré, F. Kevin, I.V. Lee, P.W. Litvinyuk, S.S. Dooley, P.R. Wesolowski, P. Bunker, F. Dombi, A.D. Krausz, D.M. Bandrauk, Villeneuve, P.B. Corkum, *Phys. Rev. A*, **71**, 013415 (2005)
3. M. Pitzer, M. Kunitski, A.S. Johnson, T. Jahnke, H. Sann, F. Sturm, L.P.H. Schmidt, H. Schmidt-Böcking, R. Dörner, J. Stohner, J. Kiedrowski, M. Reggelin, S. Marquardt, A. Schießer, R. Berger, M.S. Schöffler, *Science* **341**, 1096 (2013)
4. J.L. Hansen, J.H. Nielsen, C.B. Madsen, A.T. Lindhardt, M.P. Johansson, T. Skrydstrup, L.B. Madsen, H. Stapelfeldt, *J. Chem. Phys.* **136**, 204310 (2012)
5. M. Krems, J. Zirbel, M. Thomason, R.D. DuBois, *Rev. Sci. Instrum.* **76**, 093305 (2005)
6. L. Holmegaard, J.H. Nielsen, I. Nevo, H. Stapelfeldt, F. Filsinger, J. Kpper, G. Meijer, *Phys. Rev. Lett.* **102**, 023001 (2009)
7. C.B. Madsen, L.B. Madsen, S.S. Viftrup, M.P. Johansson, T.B. Poulsen, L. Holmegaard, V. Kumarappan, K.A. Jorgensen, H. Stapelfeldt, *Phys. Rev. Lett.* **102**, 073007 (2009)
8. C.B. Madsen, L.B. Madsen, S.S. Viftrup, M.P. Johansson, T.B. Poulsen, L. Holmegaard, V. Kumarappan, K.A. Jorgensen, H. Stapelfeldt, *J. Chem. Phys.* **130**, 234310 (2009)
9. L.J. Frasinski, K. Codling, P.A. Hatherly, *Science* **246**, 1029 (1989)
10. T.W. Anderson, *An Introduction to Multivariate Statistical Analysis* (Wiley, New York, NY, USA, 2003)
11. L.J. Frasinski, A.J. Giles, P.A. Hatherly, J.H. Posthumus, M.R. Thompson, K. Codling, *J. Electron Spectrosc. Relat. Phenom.* **79**, 367 (1996)
12. L.J. Frasinski et al., *Phys. Rev. Lett.* **111**, 073002 (2013)

Chapter 7

Time-Resolved Studies of Induced Torsional Motion

This chapter reports the application of the PImMS camera to the imaging of laser-induced torsional motion of axially chiral biphenyl molecules through femtosecond Coulomb explosion imaging (CEI). The target molecules are initially one-dimensionally (1D) or three-dimensionally (3D) aligned in space using a nanosecond laser pulse, and torsional motion is induced using a femtosecond ‘kick’ pulse. Instantaneous measurements of the dihedral angle of the molecules are inferred from the correlated F^+ and Br^+ ion trajectories following photoinitiated Coulomb explosion at various time delays after the initial kick pulse. The technique is extended to include a second kick pulse, in order to achieve either an increase in the amplitude of the oscillations or to damp the motion, representing a substantial degree of control of the system. Measurements out to long kick-probe time delays (200 ps) reveal that the initially prepared torsional wave packet periodically dephases and rephases, in accordance with the predictions of recent theoretical work. Finally, the potential of such schemes for preparing samples with an enantiomeric excess from racemic mixtures are considered.

The experiments presented in this chapter were performed at the University of Aarhus in collaboration with Prof. Henrik Stapelfeldt and his research group.

7.1 Introduction

Torsional modes in polyatomic molecules represent a fascinating intermediary between overall molecular rotation and internal vibration. Often characterised by shallow potential energy surfaces and timescales comparable to those normally expected of rotational motion, torsional modes exhibit complex time-dependent dynamics due to their unique energy eigenvalue spectra (see Fig. 7.1). In addition to being of significant fundamental interest, torsional modes have been observed to influence a wide range of interesting chemical phenomena, including charge transfer [1], energy flow and redistribution [2], electrical conductivity of molecular junctions [3–5], and molecular chirality [6–12]. The manipulation of torsional motion

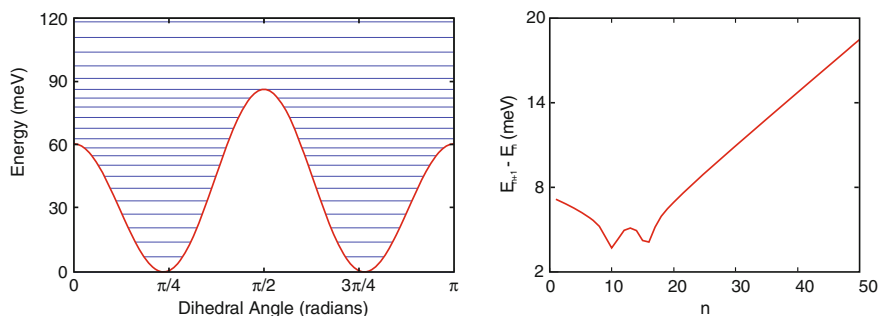


Fig. 7.1 *Left* The torsional potential and first 26 torsional eigenstates of biphenyl as a function of the dihedral angle, where a zero angle corresponds to the conformation in which the two phenyl rings are in a coplanar arrangement. *Right* The energy level spacings between adjacent torsional eigenstates for biphenyl. (Figure adapted from Ref. [13])

in polyatomic molecules therefore represents a possible means of controlling an interesting variety of fundamental molecular processes in a time-resolved manner.

In particular, the dependence of electrical conductivity on the dihedral angle in molecules such as biphenyl, diphenylacetylene, and their derivatives is especially interesting from a practical perspective [14, 15]. Since the manipulation of torsional motion in such systems necessarily translates into control over the electrical conductivity, it has been proposed that the study of torsional dynamics may lead to potentially interesting applications in the field of nanomaterials and molecular junctions [16–20]. A particularly enticing proposition is that such molecules may be placed between two electrodes, allowing optical control of the conductivity on a picosecond timescale. Through careful preparation of the torsional wave packet, it should, in theory, be possible to precisely dictate the pattern of torsional motion, and therefore the time-dependent current flow through the junction. If realised, such schemes would complement currently available technologies such as mechanical break junctions [21] and molecular junctions driven through resonant photon absorption [22, 23].

The control of torsional motion also has potentially interesting implications for the stereochemical properties of a particular subset of molecules, which owe their chirality to the presence of a stereogenic axis of symmetry. Such molecules are described as ‘axially chiral’, and interconversion between the two enantiomeric forms is often possible through rotation about the stereogenic axis. Substituted derivatives of biphenyl, which consist of two phenyl rings linked by a single C–C bond, are prime examples of such axial chirality in which an asymmetric offset equilibrium angle between the two phenyl rings gives rise to two energetically confined conformers, which constitute the two enantiomeric forms of the molecule. The characteristic dihedral angle between the phenyl rings results from the interplay between the conflicting tendency of the system to favour planarity, which maximises the extent of delocalisation of the π -electrons within the ring systems, and the steric repulsion of the substituents at the ortho positions, which favours a perpendicular alignment of the phenyl rings. The

reaction path corresponding to interconversion between the two enantiomeric forms is therefore a rotation about the central C–C bond linking the two phenyl rings.

The stereochemical control of axially chiral molecules by laser fields has been the subject of much theoretical attention in recent years. This interest is largely driven by the relatively low barrier separating the two enantiomers, allowing the use of moderate laser intensities to achieve interconversion without causing substantial ionisation and fragmentation of the molecules. The first theoretical study directed towards achieving an enantiomeric excess from a racemic mixture of axially chiral target molecules considered the use of circularly polarised continuous monochromatic light [24]. While the study predicted that it should indeed be possible to pursue deracemisation using such an approach, the enantiomeric excess predicted by the theory fell far short of anything that would be experimentally detectable or of serious practical merit (50.0001:49.9999 %). However, subsequent theoretical studies, based on the use of linearly or elliptically polarised laser pulses, have suggested that it should be possible to achieve a far more pronounced deracemisation of an initially achiral sample using laser radiation. Using oriented molecules of phosphinothioic acid (H_2OPSH) as a target, Fujimura et al. [25] proposed that the use of elliptically polarised picosecond shaped laser pulses could drive an ensemble from a 50:50 racemate to a nearly pure 100:0 ratio of a single enantiomer through a pump-dump process, which exploits the asymmetric shift in the permanent dipole moment upon rotation about the torsional coordinate.

Following this initial success, several further schemes have been developed to achieve enantiospecific control of torsional motion in axially chiral systems. For example, the probability of exciting one enantiomer over the other may be enhanced by coupling the ground state to a superposition of two excited states of opposite parities. Such schemes depend on quantum interference effects present in a three-level system, allowing for a gradual population transfer from one enantiomer to the other through laser distillation [26] or cyclic population transfer [27]. Alternatively, the relationship between the molecular handedness and the direction of the transition dipole moment vector may be exploited to achieve population transfer from one enantiomer to the other, causing deracemisation of the ensemble. Pump-dump schemes based on this approach depend on the optimised alignment of the polarisation vectors of the pump and dump pulses relative to the molecule such that the interaction with one of the enantiomers vanishes, resulting in exclusive transfer of population from one conformer to the other [28]. Similarly, the preferential asymmetric excitation of a single enantiomer in a racemic mixture may be followed by removal of molecules in the excited state from the population. This is achieved by, for example, pumping to a dissociative state which leads to fragmentation of the excited molecules, or through ionisation and acceleration by static electric fields [29].

Since torsional modes exhibit many similarities with molecular rotation, it is natural to look to the concepts of laser-induced alignment to provide alternative approaches towards manipulating torsional motion. As with laser-induced alignment, the various strategies may be divided into two broad regimes: that where the pulse envelope is long with respect to the timescale of field-free torsional motion ($\tau_{\text{pulse}} \gg T_{\text{tor}}$), known as the adiabatic regime, and that where the pulse envelope is

much shorter than the torsional period ($\tau_{\text{pulse}} \ll T_{\text{tor}}$), known as the non-adiabatic regime. Adiabatic control of the torsional coordinate of a biphenyl derivative may be understood on a qualitative level by treating the phenyl rings as two distinct moieties that interact classically with one another and an applied electric field. For the case in which the stereogenic axis and the MPA of the biphenyl coincide, it has been suggested that the torsional coordinate may be manipulated adiabatically using a single, elliptically polarised nanosecond laser pulse. This pulse simultaneously acts to induce 3D alignment of the target molecule through an interaction of the major and minor axes of polarisation with the MPA and SMPA of the molecule, respectively, and to modify the torsional coordinate of the system through an interaction of the minor axis of the polarisation ellipse with the two phenyl rings, reducing the dihedral angle between them and eventually forcing them into a coplanar arrangement [30, 31]. The extension of this scheme to manipulating molecular systems comprising more than two planar components, and to forcing the dihedral angle to an arbitrary value, is conceptually straightforward [10]. Quantum mechanically, as the pulse envelope increases in amplitude, the population of each field-free torsional eigenstate gradually transfers adiabatically into the corresponding eigenstate of the field-dressed Hamiltonian. As the laser field turns off, the system adiabatically evolves back into the original field-free state. Adiabatic torsional alignment therefore serves to modify the system only during the period in which the laser pulse is present, with the effect vanishing thereafter. Although attractively intuitive and apparently straightforward to implement, the feasibility of achieving adiabatic torsional control has recently been disputed due to the strong coupling between the torsional modes and molecular rotation, which results in a substantial degree of delocalisation in the torsional coordinate and therefore a break-down of the torsional confinement [32].

Non-adiabatic excitation of torsional motion, where the pulse duration is short with respect to the timescale of the field-free torsional period ($\tau_{\text{pulse}} \ll T_{\text{tor}}$), proceeds via a coherent excitation of the ground state to a non-stationary superposition of excited torsional eigenstates through a series of non-resonant stimulated Raman transitions. The resulting torsional wave packet evolves such that the peak alignment of the two phenyl rings occurs a short time after the laser pulse, under field-free conditions, whereafter dephasing of the wave packet occurs. Provided that the coherence of the system is maintained to some degree, a non-periodic partial revival structure will be observed at later times, with the precise details of the beat structure being a consequence of the energy eigenvalue spectrum of the torsional motion and the relative populations and phases of the contributing eigenstates. Non-adiabatic excitation is therefore predicted to exhibit a far more complex behaviour than adiabatic control schemes, making it a far more attractive target for experimental investigation. Furthermore, since the torsional dynamics persist long after the initial excitation pulse, non-adiabatic control is more appealing for most practical applications as these will benefit from the field-free torsional revivals that result.

While much theoretical work has been devoted to investigating the potential for strong field control of torsional motion, comparatively few experimental studies have sought to validate the predictions of this theory. This is largely due to the considerable challenges involved in the necessary preparation of the target mole-

cules in the correct alignment or orientation, and the ultrafast real-time monitoring of the system following the initial torsional excitation. Of particular relevance to the work presented in this chapter are the experimental papers of Stapelfeldt and co-workers, who have combined the principles of adiabatic laser alignment with non-adiabatic excitation of torsional motion in substituted biphenyl derivatives. In the work described in Refs. [11] and [12], 1D adiabatic alignment by a 9 ns laser pulse was used to achieve spatial confinement of the stereogenic axis of molecules of 3,5-dibromo-3',5'-difluorobiphenyl (DBrDFBph). The equilibrium dihedral angle between the two planar, differentially substituted phenyl rings is calculated to be 39° . The aligned molecules were subsequently irradiated by a linearly polarised 700 fs, moderately intense, non-resonant laser pulse, resulting in non-adiabatic excitation of motion about the torsional coordinate. Since the 'kick' pulse was polarised perpendicular to the nanosecond alignment pulse, the torsional motion was accompanied by overall rotation of the molecules about the stereogenic axis, which causes transient non-adiabatic 3D alignment of the sample. The torsional dynamics were probed by an intense 25 fs probe pulse, delayed by a known time after the initial kick pulse, which was used to induce rapid Coulomb explosion of the parent molecules. By measuring the recoil velocities of the F^+ and Br^+ fragments in the laboratory frame through velocity-map ion imaging, the period (1 ps) and amplitude (0.6°) of the torsional motion was determined. While the measured torsional period was in reasonable qualitative agreement with the theoretically predicted 1.2 ps, there remained a large discrepancy between the predicted amplitude of the torsional motion (2.45°) and that observed experimentally.

In an attempt to resolve this discrepancy between the theoretically predicted and experimentally observed amplitude, further experiments were performed by Stapelfeldt et al. [33]. The general principle of the experiments was largely similar to the previous work, with two important elements altered or improved to achieve an enhanced resolution of the torsional motion. The target molecule was exchanged for a very similar, but crucially different molecule. The new target was identical to the previous one, but with the addition of a nitrile group at the 4 position on the Br-substituted phenyl ring (3,5-dibromo-3',5'-difluoro-4-cyanobiphenyl). The inclusion of the nitrile group has a negligible effect on the torsional dynamics of the molecule as it is coincident with the stereogenic axis, but has the crucial effect of increasing the permanent dipole moment of the molecule from 0.2 to 4.4 Debye. The increased permanent dipole moment of the molecules allowed the use of an electrostatic deflector to select for molecules occupying the lowest rotational states, thereby increasing the degree of adiabatic alignment possible using the nanosecond laser pulse. The most important modification to the experiment, however, was the use of an elliptically polarised alignment laser pulse to achieve full 3D alignment of the molecules in space [34, 35] prior to the interaction with the femtosecond kick pulse. Following this approach, the discrepancy between theory and experiment was largely resolved, with the amplitude and period of the torsional motion measured experimentally as $\sim 3^\circ$ and 1.25 ps, respectively.

The success of these experiments in measuring the real-time torsional dynamics of a biphenyl system to an unprecedented level of accuracy is impressive. However, a

common feature of the experiments so far reported is their dependence on the spatial alignment of the target molecules in order to measure the torsional motion through laboratory frame measurements of the ion fragment velocities. Unfortunately, due to the transient nature of the alignment induced by the impulsive interaction with the kick laser pulse, the alignment of the SMPA of the molecules is rapidly lost past a kick-probe time delay of 4 ps, making it impossible to measure the torsional dynamics out to longer time delays. The experiments reported in this chapter aim to overcome this limitation by removing the dependence of the time-resolved measurements on the confinement of the SMPA of the target molecules, thereby allowing the evolution of the torsional wave packet to be followed with a high degree of accuracy out to long time delays.

7.2 Experimental Details

With the exception of the optical systems, the experimental set-up is identical to those reported in Sect. 6.1.2 and will therefore not be reviewed in detail. The molecules were 3D adiabatically aligned in space using an elliptically polarized 10 ns (FWHM) pulse from an Nd:YAG laser (YAG pulse: $\lambda = 1064$ nm, $I_{\text{YAG}} = 8 \times 10^{11}$ W cm⁻²). The major and minor components of the elliptical field were in a ratio of 3:1, with the major component aligning the MPA and the minor component acting to confine the SMPA of the molecules, as illustrated in Fig. 7.2. In DBrDFCNBph the MPA is coincident with the stereogenic axis of the molecules, whereas the SMPA lies orthogonally to the MPA, bisecting the dihedral angle between the two phenyl rings at an offset of 11° with respect to the Br-phenyl ring and 28° with respect to the F-phenyl rings. While it is not necessary to achieve 3D alignment for the purpose of measuring the dihedral angle, the preparation of the torsional wave packet is sensitive to the relative alignment of the molecules with respect to the polarisation of the kick pulse. Excitation of the torsional motion was achieved through irradiation of the molecules at precisely determined times by either one or two femtosecond kick pulses, each with a duration of 130 fs (kick pulse: $\lambda = 800$ nm, $I_{\text{probe}} = 2 \times 10^{13}$ W cm⁻²). The kick pulses were linearly polarised perpendicular to the major component of the alignment laser pulse. The timings of the two pulses were independently controlled using two independent delay stages. Coulomb explosion was induced by a linearly polarised 30 fs (FWHM) probe pulse (probe pulse: $\lambda = 800$ nm, $I_{\text{probe}} = 3 \times 10^{14}$ W cm⁻²). The polarisation of the probe pulse was parallel to the major component of the alignment laser pulse, and therefore to the stereogenic axis.

The target molecules were 3,5-dibromo-3',5'-difluoro-4'-cyanobiphenyl (C₁₃H₅F₂Br₂N, DBrDFCNBph), which was described in detail in Sect. 6.1.1.

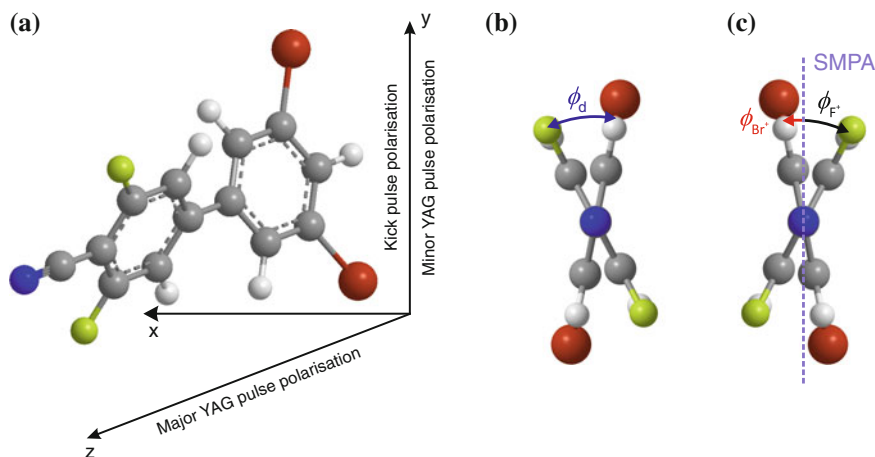


Fig. 7.2 **a** Ball and stick representation of DBrDFCNBph illustrating the three-dimensional alignment of the molecules in space. In the coordinate system used the z -axis is parallel to the time-of-flight axis and perpendicular to the detector plane. **Panels b** and **c** identify the dihedral angle of the molecule (ϕ_d) and the relative angles of the fluorine and bromine phenyl rings relative to the SMPA of the molecule. In the ground torsional state $\phi_{F^+} = 28^\circ$ and $\phi_{Br^+} = -11^\circ$

7.3 Single Kick Torsional Dynamics

7.3.1 Theoretical Treatment

The experimental data presented in this chapter allow the torsional dynamics to be parameterised in terms of the period and amplitude of the beating motion. These values are compared to the predictions of a previously developed theoretical model which concerns the torsional motion of a similar substituted biphenyl derivative (DBrDFBph) [11, 12]. Since the primary focus of this work is therefore on the predictions of the model and their comparison to the experimental data, only a brief description of the theory is presented.

It is convenient from a theoretical standpoint to describe the system in terms of two parameters: the dihedral angle, $\phi_d = \phi_{Br} - \phi_F$, where ϕ_F and ϕ_{Br} are the angles of the two phenyl rings with respect to the kick laser pulse, and the overall rotation about the stereogenic axis, which is described by the weighted azimuthal angle, $\Phi = (1 - \eta)\phi_{Br} + \eta\phi_F$, where the parameter η is formulated in terms of the rotational moments of inertia of the two phenyl rings, $\eta = I_F/(I_F + I_{Br})$.

The torsional motion evolves according to the time-dependent Schrödinger equation, which, in atomic units ($e = \hbar = m_e = a_0 = 1$), may be formulated as

$$i \frac{\partial}{\partial t} \Psi(\Phi; \phi_d, t) = [T_d + V_{\text{tor}}(\phi_d) + V_{\text{kick}}(\Phi; \phi_d, t)] \Psi(\Phi; \phi_d, t), \quad (7.1)$$

where V_{tor} is the torsional potential energy surface, T_{d} is the rotational kinetic energy due to torsional motion, given by

$$T_{\text{d}} = -\frac{I_{\text{Br}^+} + I_{\text{F}^+}}{2I_{\text{Br}^+}I_{\text{F}^+}} \frac{\partial^2}{\partial \phi_{\text{d}}^2}, \quad (7.2)$$

and V_{kick} is the polarisability interaction between the kick pulse and the molecule, given by

$$\begin{aligned} V_{\text{kick}}(\Phi; \phi_{\text{d}}, t) = & -\frac{1}{4}E_0^2(t)[\alpha_{xx}(\phi_{\text{d}})\cos^2(\Phi + \eta\phi_{\text{d}}) \\ & + \alpha_{yy}(\phi_{\text{d}})\sin^2(\Phi + \eta\phi_{\text{d}}) \\ & + \alpha_{xy}(\phi_{\text{d}})\cos(\Phi + \eta\phi_{\text{d}})\sin(\Phi + \eta\phi_{\text{d}})]. \end{aligned} \quad (7.3)$$

Here, E_0 is the amplitude of the electric component of the kick pulse, and the α_{ij} coefficients are the dynamic polarisability components of the molecule.

Equation 7.1 has previously been solved for molecules of DBrDFBph using a close coupling method for interaction with a kick pulse polarised parallel to the SMPA, which starts with a wavefunction localised in the ground torsional state. The kick pulse is predicted to excite the system to a coherent superposition of the ground and first excited torsional eigenstates, separated by 3.42 meV. This superposition behaves essentially as a classical harmonic oscillator, resulting in periodic oscillatory motion. Although the molecule used in the work presented here contains an additional nitrile group compared to that for which calculations have previously been performed, quantum mechanical calculations have shown that the torsional potentials of the two molecules are very similar [33]. Therefore, the values calculated for DBrDFBph are those to which the experimental data are compared.

7.3.2 Alignment Dynamics

The initial proof-of-principle experiments, demonstrating the feasibility of measuring the dihedral angle of the molecules as a function of time through a covariance analysis of the F^+ and Br^+ recoil velocities, were performed using a single 130 fs kick pulse to initiate torsional motion. The time of the kick pulse defined time zero (t_0), from which the 30 fs probe pulse was delayed by various predetermined intervals (t_{probe}).

Figure 7.3 shows the full set of laboratory frame ion images of both F^+ and Br^+ recorded at various kick-probe time delays, from -1.00 to 10.00 ps. The target molecules of DBrDFCNBph were three-dimensionally adiabatically aligned using an elliptically polarised nanosecond laser pulse according to the principles described in Sect. 5.3.3, whereby the MPA and SMPA are confined in space by the major and minor components of the polarisation ellipse. In this case, the major component of the polarisation ellipse is aligned perpendicular to the page and the minor component aligned vertically in the ion images.

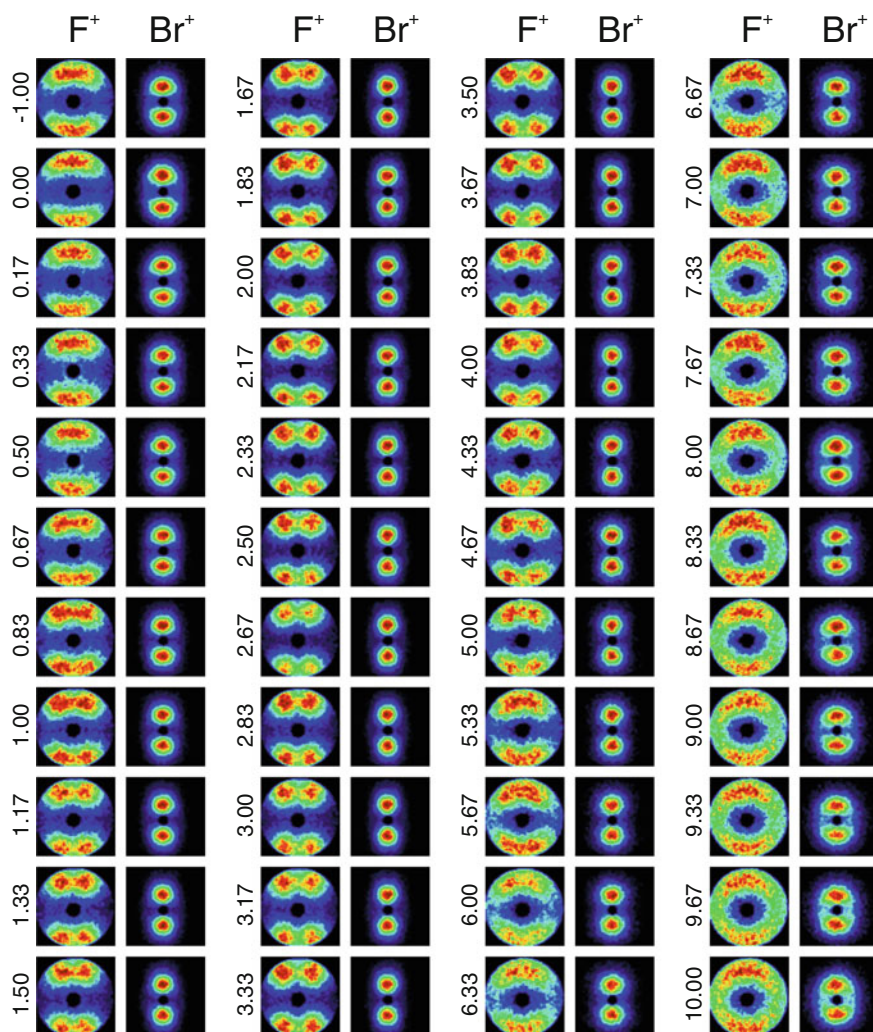


Fig. 7.3 Laboratory frame ion images of F^+ and Br^+ recorded at various kick-probe time delays, as indicated by the values alongside the images. The target molecules were adiabatically 3D aligned in space prior to interaction with a 130 fs kick pulse, which induced torsional motion about the stereogenic axis, and were subsequently Coulomb exploded by a 30 fs probe pulse. The nanosecond alignment laser pulse was elliptically polarised with the major component of the polarisation ellipse perpendicular to the detector plane and the minor component polarised vertically. Each data set from -1.00 to 4.00 ps was recorded over 20,000 laser shots. The remaining data sets contain 10,000 laser shots each

7.3.2.1 Three-Dimensional Adiabatic Prealignment

The success of the three-dimensional adiabatic alignment scheme is confirmed through an inspection of the ion image corresponding to a negative kick-probe delay of -1.00 ps, which displays the unmistakable signatures of three-dimensional confinement of the target molecules. The central regions of the ion images are largely devoid of intensity, suggesting that the ions are aligned with the MPA perpendicular to the detector plane (note: a small region at the very centre of each image has been masked in order to remove the contribution from contaminants in the reaction chamber). The localisation of the signal intensity around the vertical axis is a direct result of the confinement of the SMPA of the molecules parallel to the minor component of the polarisation ellipse of the alignment laser pulse. The signal intensity of Br^+ is more tightly localised about the vertical axis than the corresponding F^+ ion image due to the smaller offset angle of the Br-phenyl ring from the SMPA in the torsional ground state ($\phi_{\text{Br}^+} = 11^\circ$, $\phi_{\text{F}^+} = 28^\circ$).

7.3.2.2 Non-adiabatic Alignment

While the purpose of the kick laser pulse is primarily to induce torsional motion, an inevitable secondary consequence of exposing the molecules to a short, intense, non-resonant femtosecond laser pulse is the preparation of a coherent superposition of rotational eigenstates, resulting in transient non-adiabatic alignment of the molecules. Since the kick pulse is polarised parallel to the minor axis of the nanosecond laser polarisation ellipse, the kick pulse acts to sharpen the alignment of the SMPA of the molecules. This effect is obvious from an inspection of the ion images presented in Fig. 7.3. The degree of alignment of the F^+ and Br^+ ion images gradually increases from $t_{\text{probe}} = 0$, reaching a maximum at around 2 to 3 ps after the initial kick pulse. In the case of the Br^+ images, the two peaks of intensity become noticeably more localised about the vertical axis, whereas in the F^+ ion images the contributions from molecules with the F-phenyl rings aligned at $+28^\circ$ and -28° relative to the SMPA become increasingly well-resolved. It is possible to discern the beating of the torsional motion from an inspection of the F^+ ion images, with the four peaks in intensity periodically oscillating towards and away from the central vertical axis of the images. From approximately 4 ps, the alignment of the ion images begins to degrade as the rotational wave packet dephases, eventually reducing the degree of alignment far below that observed before the introduction of the kick pulse.

As described in Chap. 6, the alignment dynamics of the system may be quantified through a measurement of $\langle \cos^2 \theta \rangle$ in each of the ion images, where θ is the angle between the ion velocity vector in the xy -plane and the polarisation axis of the kick pulse. Figure 7.4 plots the value of $\langle \cos^2 \theta \rangle$ as a function of kick-probe time delay, as measured from the F^+ and Br^+ ion images. From the traces in Fig. 7.4, the effect of the kick pulse on the alignment of the target molecules is clear. The initially adiabatically aligned distributions of F^+ and Br^+ become increasingly strongly aligned in the direction of the kick laser polarisation, reaching a maximum alignment at

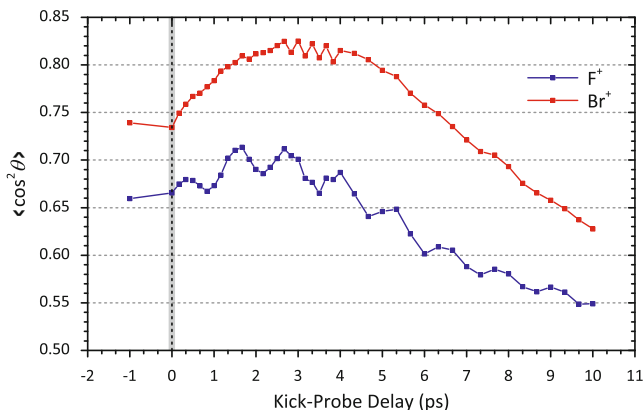


Fig. 7.4 Plot of the value of $\langle \cos^2 \theta \rangle$ as a function of kick-probe delay time, as measured from the F^+ and Br^+ ion images, where θ is the angle between the ion velocity vector in the xy -plane and the polarisation axis of the kick pulse

around 1.5 ps in the case of the F^+ and 3 ps in the case of Br^+ . The combination of adiabatic and non-adiabatic laser alignment schemes clearly enhances the degree of confinement of the target molecules, as expected based on previous studies [36, 37]. Following the attainment of peak alignment, the coherent superposition of rotational eigenstates dephases, resulting in a reduction in the degree of alignment observed. The alignment of the F^+ ion images falls below that initially achieved using exclusively adiabatic alignment shortly after 4 ps, with the same effect observed for Br^+ at approximately 6 ps.

Importantly, the disalignment of the SMPA of the molecules renders the measurement of the dihedral angle from the laboratory frame ion images impossible past these times. This represents a fundamental limitation of the previously reported experimental strategies [33]. An additional and highly interesting feature of the data presented in Fig. 7.4 is the presence of periodic oscillations superimposed on the alignment trace of the F^+ ions. This regular beating behaviour is a consequence of the induced torsional motion, which periodically reduces and increases the dihedral angle between the two phenyl rings. As the dihedral angle closes, the two phenyl rings become increasingly well aligned with the SMPA of the molecule, enhancing the degree of alignment observed. This effect is not observed in the case of Br^+ due to the far larger amount of rotational inertia of the heavier moiety, and the closer initial alignment of the Br-phenyl rings relative to the SMPA.

7.3.3 Time-Resolved Torsional Motion

While the phenomenon of non-adiabatic alignment is indeed interesting, the primary aim of this study is to observe the torsional dynamics of the system through

time-resolved measurements of the dihedral angle. In Sect. 6.4.2 it was demonstrated that the relative recoil angle between the F^+ and Br^+ ions following Coulomb explosion of the parent molecule is indicative of the dihedral angle of the system. Although it was observed that there is a small discrepancy of a few degrees between the measured relative recoil angle and the generally accepted dihedral angle of the parent molecule, for the most part, the torsional dynamics of the system may be described in terms of the amplitude and period of the oscillations, which should be largely unaffected by this small discrepancy. As in Sect. 6.4.2, the relative recoil angle between the F^+ and Br^+ ions was determined through a covariance analysis of the data. The resulting recoil frame covariance images of F^+ relative to Br^+ are shown alongside the laboratory frame F^+ ion images in Fig. 7.5. The covariance images clearly display a well-resolved four peak structure, with a significantly improved resolution when compared to the laboratory frame ion images. Crucially, the resolution of the covariance images is invariant of the laboratory frame alignment of the molecules, with the four distinct peaks preserved throughout the period of the measurements. Furthermore, since the covariance images represent the measurement of the F^+ ion velocities in the recoil frame of the Br^+ ions, the angular intensity translates directly into a measurement of the dihedral angle.

Figure 7.6 plots the angular intensities of the recoil frame covariance images as a function of kick-probe time delay. In this plot the torsional dynamics are manifested in the periodic oscillations of the peak intensities of the four major features. The middle two features, at an approximate relative recoil angle of 45° , correspond to ions ejected from the same side of the molecule, whereas the features at approximately 140° correspond to ion pairs originating from opposite sides of the molecule. In order to achieve a more quantitative description of the torsional dynamics, the angular intensities of the covariance images were fitted to four Gaussian functions and the peak intensities interpreted as representing the instantaneous dihedral angle of the molecule at a given time delay. The resulting data are presented in Fig. 7.7, where the most probable recoil angles are plotted as a function of kick-probe time delay.

The periodic torsional motion is immediately obvious from inspection. The sinusoidal oscillations are clearly resolved to a high degree of precision for both the proximal and distal ion pairs. The data corresponding to the distal ion pairs (i.e. that oscillating about a mean value of approximately 140°) represent a more reliable measure of the dihedral angle due to the reduced Coulombic effects on the ion trajectories, as reasoned in Sect. 6.4.2. The evolution of the torsional motion was therefore parameterised according to a damped sine curve fitted to this data. The fit to the data, as shown in Fig. 7.7, closely follows the observed measurements of the dihedral angle, allowing for a confident parameterisation of the torsional dynamics. The period of the oscillations was determined to be 1.253 ± 0.006 ps, with an amplitude of $1.63 \pm 0.23^\circ$, about a mean dihedral angle of $40.02 \pm 0.10^\circ$. The period of the motion is in almost perfect agreement with that predicted by theory, as is the mean dihedral angle which differs by 1° from that expected. However, the amplitude is slightly lower than the expected 2.45° . Given the quality of the data and the close agreement of the other parameters to that predicted by theory, this discrepancy is perhaps a little

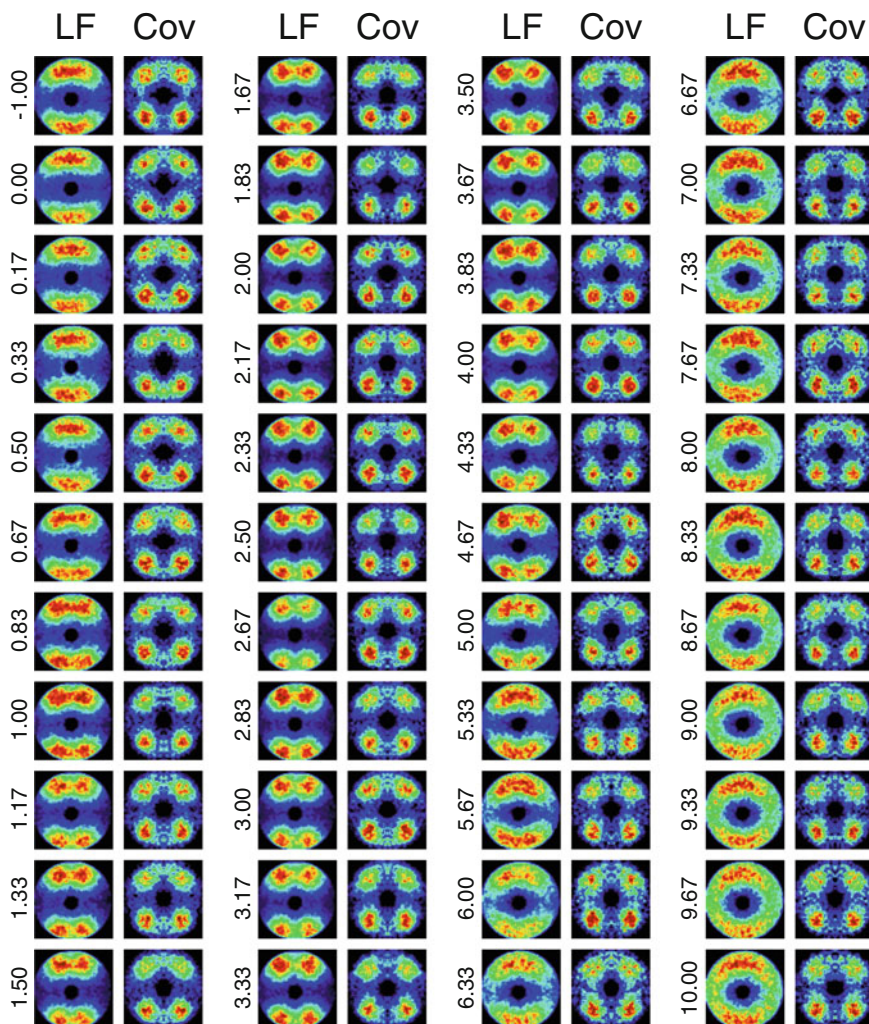


Fig. 7.5 Laboratory frame (*LF*) ion images of F^+ recorded at various kick-probe time delays alongside the corresponding recoil frame covariance images (*Cov*) of F^+ relative to Br^+ . The target molecules were adiabatically 3D aligned in space prior to interaction with a 130 fs kick pulse, which induced torsional motion about the dihedral angle, and were subsequently Coulomb exploded by a 30 fs probe pulse. The nanosecond alignment laser pulse was elliptically polarised with the major component of the polarisation ellipse perpendicular to the page and the minor component vertical in the plane of the page. Each data set from -1.00 to 4.00 ps was recorded over 20,000 laser shots. The remaining data sets contain 10,000 laser shots.

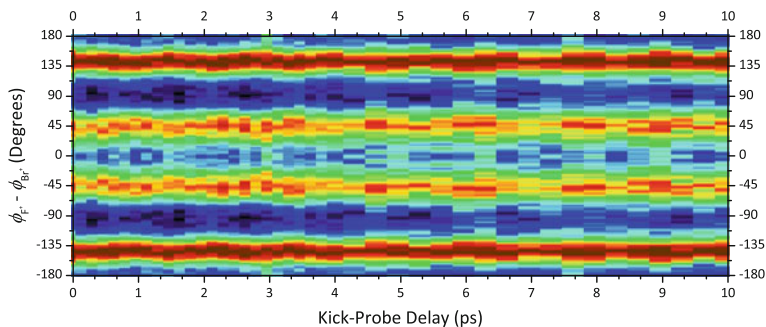


Fig. 7.6 Plot of the angular intensities of the recoil frame covariance images as a function of kick-probe time delay

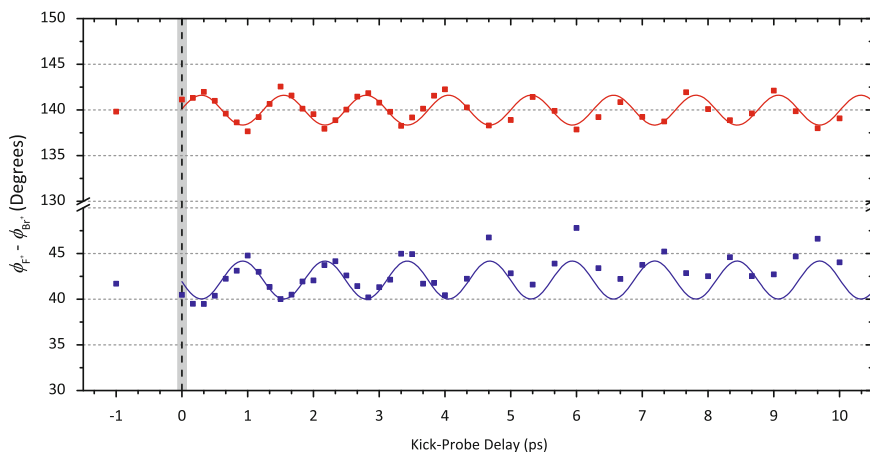


Fig. 7.7 Plot of the most probable relative recoil angle between the F^+ and Br^+ ions, as determined from a fit to the angular profiles of the recoil frame covariance images presented in Fig. 7.5. The standard errors of the fits are generally $<0.5^\circ$, and are therefore not shown. The *red* and *blue* lines represent fits to the data of a damped sine wave. See text for more details

surprising. One possibility is that the kick pulse intensity was not exactly matched to that used in the theoretical calculations, causing the lower amplitude observed.

Interestingly, the decay time constant of the fitted damped sine curve was effectively infinite, suggesting that the phase relations between the various eigenstates comprising the torsional wave packet are maintained indefinitely. The spectral bandwidth of the kick pulse is sufficient to excite the torsional ground state to either the first or second excited state through a stimulated Raman process. This modest degree of torsional excitation gives rise to the rather small amplitude of the vibrations. The states that contribute to the torsional wave packet will therefore exist within the deepest regions of the torsional potential, where the motion is largely harmonic in nature. Since it is the anharmonic terms in the potential that cause the phase relations

between the various eigenstates to become unmatched, the absence of these terms results in persistent torsional motion, as observed experimentally.

7.3.4 Torsional Dynamics of 1D Prealigned Molecules

So far, the investigation of torsional dynamics has been restricted to the case in which the SMPA and the electric vector of the kick laser pulse are aligned in a parallel arrangement. However, inspection of Eq. 7.3 reveals that the interaction between the kick pulse and the molecule depends upon the weighted azimuthal angle, Φ , which has so far been limited to values close to zero. It is therefore interesting to consider molecules aligned in a variety of spatial arrangements relative to the kick laser pulse. By reducing the degree of alignment of the target molecules, such that the SMPA is free to rotate about the stereogenic axis, the experiment necessarily probes molecules sampled over a range of geometries with respect to the kick laser pulse. By selecting the appropriate subset of ions between which the correlations are measured, the possibility of investigating the torsional dynamics of molecules following excitation by an arbitrarily aligned kick laser pulse becomes experimentally accessible.

Figure 7.8 presents the laboratory frame ion images of both F^+ and Br^+ recorded at various kick-probe time delays, from -1.00 to 10.00 ps, following 1D adiabatic alignment of the target molecules. At negative times, before the application of the kick pulse, the images are circularly symmetric, demonstrating the free rotation of the molecules about the stereogenic axis. Following the interaction of the femtosecond kick pulse, the molecules exhibit a gradually increasing degree of non-adiabatic alignment around the vertical axis of the images, which coincides with the axis of polarisation of the kick pulse. The 3D alignment that results is transient, with the tight confinement of the minor polarisation axis of the molecules persisting for only a short time, on the order of a few picoseconds. Figure 7.9 plots the alignment parameter $\langle \cos^2 \theta \rangle$ as a function of kick-probe time delay for both the F^+ and Br^+ ion images. The quantification of the degree of alignment reveals some interesting features, which are not obvious from an inspection of the ion images alone. Firstly, although the impulsive kick pulse induces transient 3D alignment of the molecules, the maximum degree of confinement is less than that achieved through a combination of adiabatic and non-adiabatic pulses. Of more direct interest to the present study is the observation of the torsional beat superimposed on the time-resolved F^+ alignment parameter, as was observed in the 3D aligned case. However, the torsional beat persists for a far shorter time in the 1D aligned case, with the oscillations becoming damped to such an extent that they are not observable by 4 ps.

The strategy employed for achieving a quantitative measurement of the torsional dynamics in the case of 1D alignment follows the same principles as used previously. The covariance is used as a measure of correlation between the F^+ and Br^+ signals, which allows a determination of the relative recoil angle between the fragment ions, and by extension a measurement of the instantaneous dihedral angle. In a minor modification, the covariance analysis is confined to considering only pixels that fall

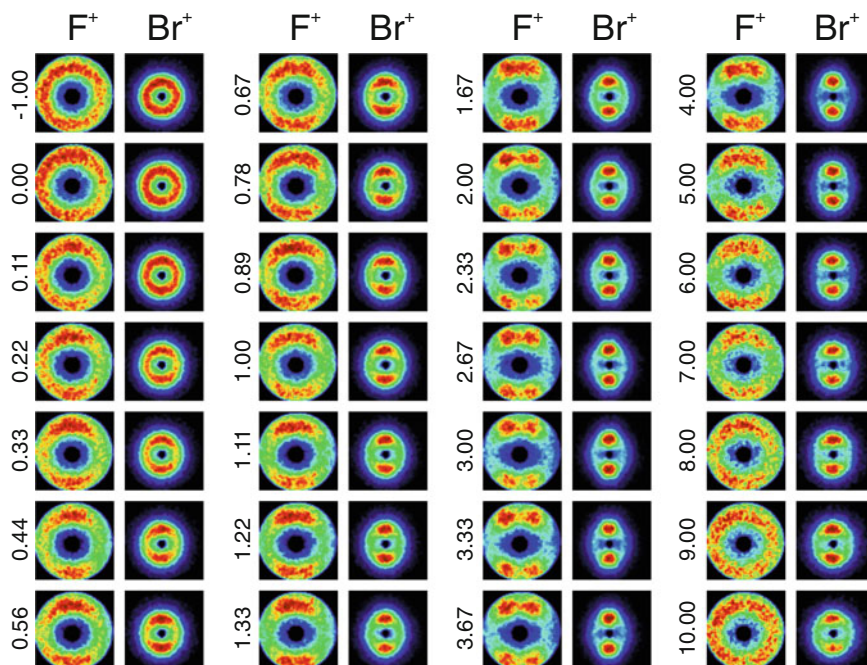


Fig. 7.8 Laboratory frame ion images of F^+ and Br^+ recorded at various kick-probe time delays, as indicated by the values alongside the images. The nanosecond alignment laser pulse was linearly polarised perpendicular to the detector plane. Each data set from -1.00 to 4.00 ps was recorded over 40,000 laser shots. The remaining data sets contain 20,000 laser shots each

within the bounds of certain angular limits, in order that molecules may be identified according to their alignment with respect to the kick laser pulse.

Figure 7.10 plots the most probable relative recoil angle between the F^+ and Br^+ ions, as determined from Gaussian fits to the angular profiles of the recoil frame covariance data, for two subsets of the data. In Panel (a) the covariance is measured relative to Br^+ ions with a final velocity within $\pm 15^\circ$ of parallel to the kick pulse polarisation axis, whereas Panel (b) considers only covariances to Br^+ ions with a final velocity within $\pm 15^\circ$ of perpendicular to the kick pulse polarisation axis. At negative time delays, before the application of the femtosecond kick pulse, these subsets correspond to molecules with the SMPA aligned approximately parallel and perpendicular to the polarisation of the kick laser pulse, respectively, since the the Br -phenyl ring is offset by just 11° from the SMPA. The evolution of the dihedral angle in the case of parallel alignment therefore resembles the torsional dynamics following 3D alignment of the molecules, as discussed in the previous section. The dihedral angle is initially observed to decrease, as the kick laser pulse modifies the torsional potential in such a way as to coerce the rings into a more coplanar geometry, whereafter the system oscillates at a characteristic frequency. Conversely, in the case of molecules aligned with the SMPA perpendicular to the femtosecond kick pulse, the

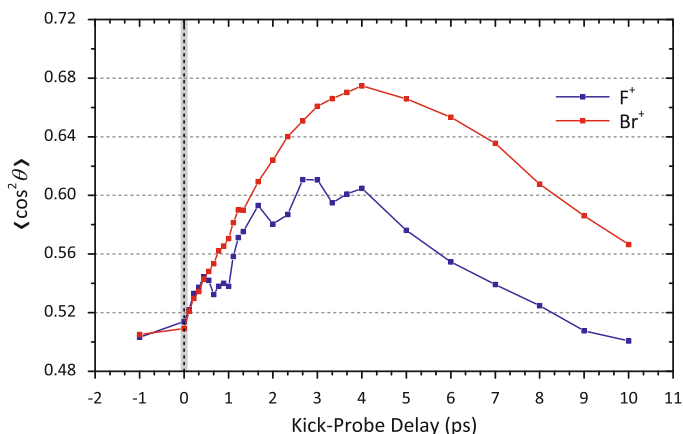


Fig. 7.9 Plot of the value of $\langle \cos^2 \theta \rangle$ as a function of kick-probe delay time, as measured from the F^+ and Br^+ ion images, where θ is the angle between the ion velocity vector in the xy -plane and the polarisation axis of the kick pulse

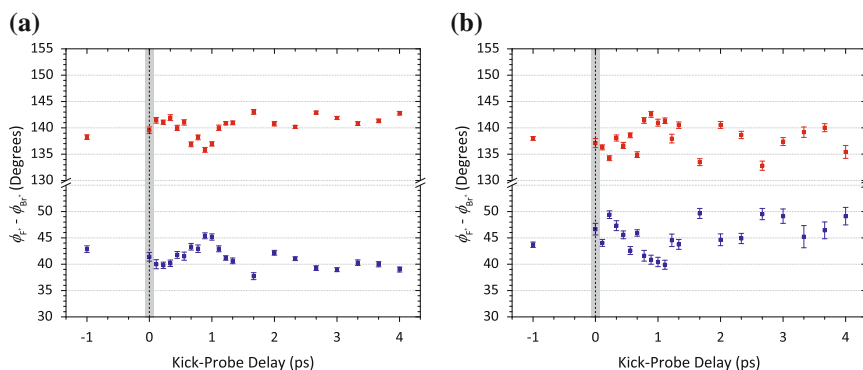


Fig. 7.10 Plot of the most probable relative recoil angle between the F^+ and Br^+ ions, as determined from Gaussian fits to the angular profiles of the recoil frame covariance data, for molecules with the SMPA aligned initially **a** parallel and **b** perpendicular to the polarisation axis of the kick laser pulse

opposite effect is observed. The dihedral angle is observed to increase immediately following exposure to the kick pulse, with the subsequent oscillations offset by half a torsional period relative to the parallel alignment case.

The data demonstrate clearly the dependence of the wave packet preparation on the initial alignment of the molecules relative to the kick pulse polarisation. The torsional dynamics unfortunately become obscured at relatively short delays following the kick laser pulse, with the periodic oscillations becoming considerably damped, especially in the case of parallel alignment. This is a result of the transient non-adiabatic 3D alignment of the system, induced by the femtosecond kick pulse,

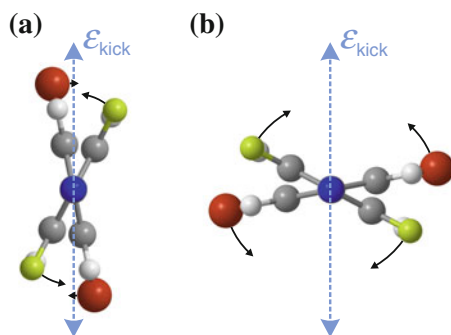


Fig. 7.11 Illustration of the torque induced in the phenyl rings resulting from **a** parallel and **b** perpendicular alignment of the SMPA with respect to kick pulse polarisation vector. A minimum energy conformation exists with the two phenyl rings in a coplanar arrangement in the presence of the kick pulse, pulling the rings away from their equilibrium angle under field-free conditions

which acts to align the SMPA of the molecules about the vertical axis. The induced rotation of the molecules about the stereogenic axis results in a greater uncertainty in the initial alignment of the SMPA at time zero for a given laboratory frame recoil angle as the kick-probe time delay increases. At later times, when a high degree of 3D alignment is observed in the laboratory frame images, many of the molecules that were initially aligned with the SMPA perpendicular to the kick laser pulse have become aligned along the axis of the kick laser polarisation. Since these molecules will be oscillating in anti-phase with the molecules initially aligned with the SMPA parallel to the kick laser pulse, this results in a substantial damping of the observed torsional motion at parallel geometries.

Although a complete description of the mechanism of the kick pulse requires a quantum mechanical treatment, the torsional dynamics may be understood on a qualitative level using simple classical arguments. The opposing phase of the torsional oscillations in the two cases considered here may be understood by considering the torque experienced by each phenyl ring upon exposure to the kick pulse, as illustrated schematically in Fig. 7.11. As individual moieties, the two phenyl rings favour alignment with the kick pulse, resulting in a torque which acts to draw the system away from the equilibrium dihedral angle under field-free conditions. When the kick pulse is removed, the rings experience a restorative force in the opposite direction, which results in the periodic torsional motion observed.

7.4 Double Kick Torsional Dynamics

The torsional motion observed thus far has been relatively modest, with typical amplitudes of around $2\text{--}3^\circ$ inferred from the measurement of the relative recoil angles of the F^+ and Br^+ fragment ions. In the introduction to this chapter, the prospect

of photoinduced deracemisation was discussed, which would clearly require a much greater degree of torsional excitation to be induced in the target molecules in order that the barrier to interconversion between the two enantiomeric conformers may be overcome. In principle, this may be achieved using a higher intensity, a longer pulse duration, or a train of synchronised kick pulses optimised to amplify the torsional motion.

The two single pulse strategies, while attractive due to their apparent simplicity, are less straightforward than they initially appear. The intensity of the kick pulse is limited by the ionisation threshold of the target molecules. If this threshold is exceeded, ionisation and subsequent Coulomb explosion will occur, resulting in the destruction of the system that is to be controlled. In the present experiments, the intensity of the kick pulse was optimised to induce the maximum torsional excitation without inducing Coulomb explosion of the target molecules, leaving little scope for increasing the pulse intensity. As discussed previously, the use of a longer kick pulse is complicated by the strong coupling between overall rotation and torsional motion, which results in a large degree of delocalisation in the torsional coordinate, and therefore a break-down of the torsional confinement [32]. Furthermore, since the coherence of the torsional wave packet depends on the duration of the kick pulse, the use of longer pulse envelopes is likely to have a detrimental effect on the coherence of the resulting torsional motion. As the pulse duration is lengthened, the initial coherence of the torsional wave packet will weaken, ultimately destroying the coherence of the system entirely as the pulse length becomes comparable to the torsional period.

In light of these considerations, the more attractive strategy for achieving a greater degree of torsional excitation would appear to be the use of multiple kick pulses that are synchronised in such a way so as to successively amplify the torsional motion. The remaining experimental work presented in this chapter investigates the feasibility of this approach by introducing a second kick pulse to modify the torsional wave packet following the initial excitation. Extending this approach to include a train of kick pulses delivered to the experiment at optimised time delays should be relatively straightforward using conventional femtosecond pulse shaping techniques [38].

The experimental details are largely identical to those used previously, with the important addition of a second kick pulse, identical to the first, to the optical scheme. A further difference to the experiments was the use of a slightly different target molecule, 3,5-dibromo-3',5'-difluoro-4-cyanobiphenyl ($C_{13}H_5F_2Br_2N$, DFDBrCNBph). The new target molecule is almost identical to that used previously, but the nitrile group has been moved to the 4 position of the Br-phenyl ring from its original location at the 4' position on the F-phenyl ring. The reason for the change of target molecule is the higher purity of the DFDBrCNBph sample following synthesis, which results in a reduced contribution to the ion images from impurities and byproducts. The molecules were adiabatically 3D aligned in space prior to interaction with the initial kick pulse.

Figure 7.12 presents the measurement of the relative recoil angle between the F^+ and Br^+ ions as a function of time after the initial kick pulse for three different pulse sequences. Panel (a) presents the results following torsional excitation using a single

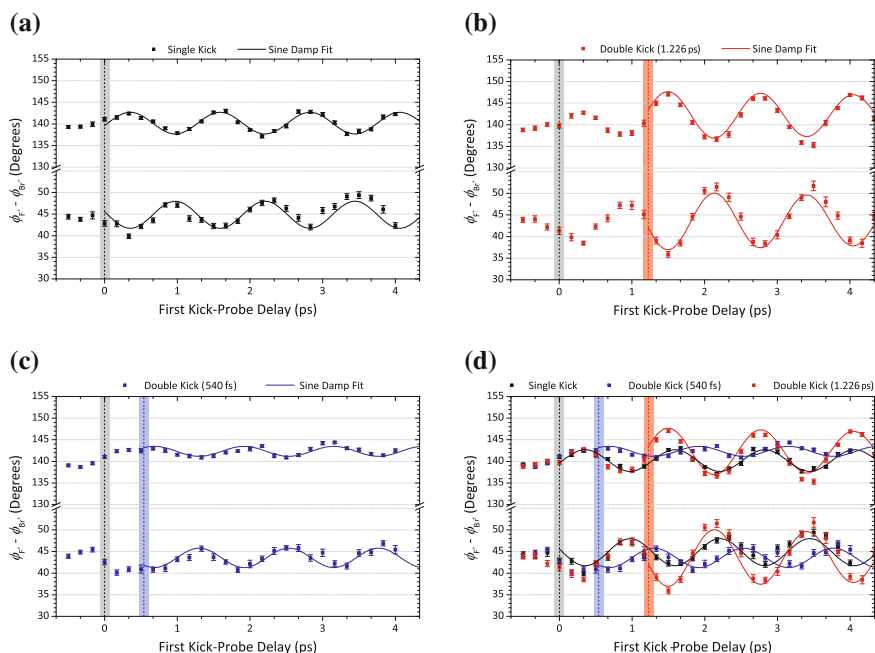


Fig. 7.12 Plots of the most probable relative recoil angle between the F^+ and Br^+ ions, as determined from Gaussian fits to the angular profiles of the recoil frame covariance data. The data are plotted as a function of initial kick-probe time delay, following **a** a single kick pulse, **b** two identical kick pulses separated by 1.226 ps, and **c** two identical kick pulses separated by 540 fs. **Panel d** overlays the results presented in **Panels a** to **c** for comparison. The *solid lines* are fits of a damped sine function to the data. Each data set consists of 10,000 laser shots

kick pulse, as previously reported in Sect. 7.3.3 for DBrDFCNBph. The period (1.236 ± 0.015 ps) and amplitude ($2.50 \pm 0.14^\circ$) are in good agreement with the predicted values and those measured in Sect. 7.3.3 for DBrDFCNBph. Panel (b) presents the results following excitation by two kick pulses separated by 1.226 ps. The delay of the second pulse relative to the first is optimised to achieve maximum amplification of the torsional motion, which results when the molecules pass through the equilibrium geometry as the dihedral angle closes. The amplitude of the torsional beat is increased to $5.95 \pm 0.40^\circ$, almost exactly double that observed following excitation by a single kick pulse, while the period (1.274 ± 0.002) remains relatively unaffected. Panel (c) presents the results following interaction of the target molecules by two kick pulses separated by 540 fs. In this case, the timing of the second kick pulse relative to the first is optimised to achieve the maximum damping of the induced torsional motion, occurring almost exactly half a phase earlier than the kick pulse used in Panel (b) so as to exert a torque on the rings opposing their angular velocity. A considerable damping of the motion is observed, with the amplitude of the oscillations reducing to $1.15 \pm 0.21^\circ$, with the period (1.233 ± 0.049 ps) again remaining largely unaffected by the second kick pulse. From the progression of the torsional motion inferred from the

data in Panel (c), it would appear that the kick pulse was applied slightly prematurely in this instance, with the effect that the motion is over-damped by the second kick pulse, such that the direction of the torsional motion is reversed rather than stopped. By applying the kick pulse slightly later, at exactly half a period before the timing of the amplifying kick pulse, it should therefore be possible to enhance the effect of the damping kick pulse, potentially stopping the torsional motion completely.

Long Time Behaviour

In Sect. 7.3.3 the invariance of the covariance method to the laboratory frame alignment of the molecules was demonstrated to allow the measurement of the instantaneous dihedral angle out to kick-probe delays of 10 ps with a high precision. Provided the alignment of the stereogenic axis is preserved, there is no fundamental limit on the range of kick-probe delays over which measurements may be taken, offering the possibility of monitoring the long time behaviour of the torsional dynamics. As discussed previously, the torsional wave packet is prepared from a coherent superposition of torsional eigenstates, which occupy a complex ladder of energy eigenvalues exhibiting characteristics of both rotational and vibrational motion. The time evolution of the torsional motion is therefore expected to exhibit a rich revival structure, periodically damping and amplifying as the eigenstates successively dephase and rephase [13].

Figure 7.13 plots the evolution of the dihedral angle following an amplifying double kick pulse (kick-kick delay = 1.226 ps) out to 20 ps. The periodic beating of the torsional motion persists throughout the measured time window, with the gradual dephasing of the excited torsional eigenstates manifested in the decaying amplitude of the oscillations. Interestingly, the coherence of the torsional wave packet

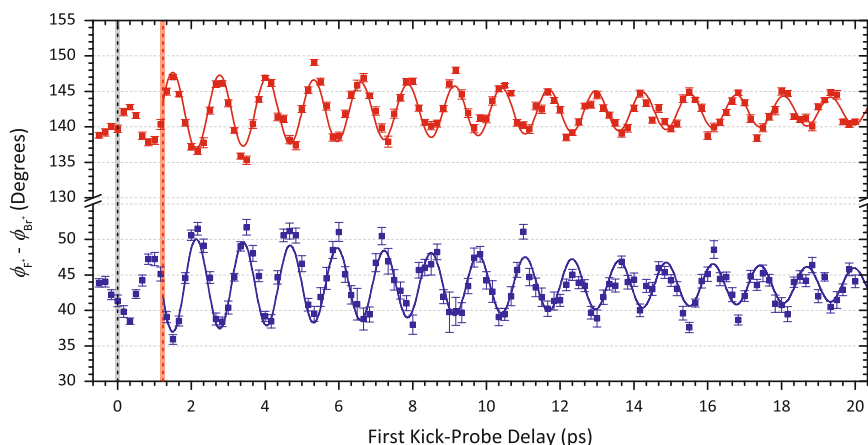


Fig. 7.13 Plot of the most probable relative recoil angle between the F^+ and Br^+ ions, as determined from Gaussian fits to the angular profiles of the recoil frame covariance data. The data are plotted as a function of initial kick-probe time delay, following two identical kick pulses separated by 1.226 ps. Each data set consists of 10,000 laser shots

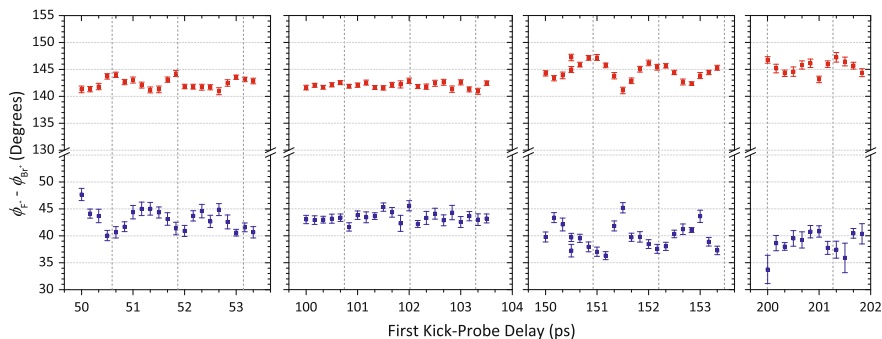


Fig. 7.14 Plot of the most probable relative recoil angle between the F^+ and Br^+ ions, as determined from Gaussian fits to the angular profiles of the recoil frame covariance data. The data are plotted as a function of initial kick-probe time delay, following two identical kick pulses separated by 1.226 ps. Each data set consists of 10,000 laser shots. The *vertical drop lines* are spaced by the period of the torsional motion (1.274 ps), and are included as a guide to the eye

appears to reduce noticeably faster than that observed following a single kick, as reported in Sect. 7.3.3 for DBrDFCNBph. In contrast to the practically infinite decay time constant parameterising the single kick torsional dynamics, the damping of the torsional motion following two synchronised kick pulses is noticeable within a few torsional periods. This contrasting behaviour may be understood by considering the composition of the initially prepared torsional wave packet in each case. The second kick pulse acts to further excite the torsional motion through the inclusion of higher lying torsional eigenstates, accessed via a second tranche of non-resonant stimulated Raman transitions. Since the anharmonic nature of the system increases as the torsional ladder is climbed, the energy spacings, and therefore the phase relations, between successive eigenstates become increasingly non-uniform.

Although the coherence of the system is clearly decreasing, the torsional progression observed in Fig. 7.13 is suggestive of a rather long revival time. In order to confirm that the damping of the torsional motion is caused by the dynamics of the torsional wave packet, and not through other processes such as intramolecular vibrational redistribution (IVR), measurements were taken at several short time windows between 50 and 200 ps. The results of these measurements are shown in Fig. 7.14. These data offer an intriguing glimpse of the full time-dependent torsional dynamics of the system. At 50 ps, although significantly damped, the signature of torsional motion is still clearly present, suggesting that the coherence of the system is still, to some degree, intact. However, by 100 ps the periodic beating of the dihedral angle is no longer measurable, with the system exhibiting complete decoherence. The revival of the torsional motion is unmistakable at 150 ps, with an amplitude of approximately 3° and a period consistent with that observed at earlier times. By 200 ps the torsional motion is once again damped; however, the torsional beat is still just about discernable above the level of the noise.

Although the data are not sufficiently complete to pursue a more quantitative assessment of the torsional dynamics, they give at least an impression of the long time behaviour of the system. It is clear that torsional motion persists for an extended period of time, with the energy localised in the torsional coordinate of the molecule for at least 200 ps. Due to the anharmonicity of the torsional potential, the torsional mode undergoes coherent dephasing following initial excitation, and subsequently exhibits at least one wave packet revival. It may be possible that there are more revivals within the first 200 ps. However, from the current data it is not possible to draw strong conclusions on the precise details of the revival structure. It is also difficult to derive any firm conclusions from the data on the role of IVR in the torsional dynamics. It appears that the energy persists in the torsional mode for an extended period of time, certainly compared to the normal timescales of IVR, which are generally on the order of femtoseconds or picoseconds. However, due to the complicated revival structure it is not possible to determine the contributions of IVR in any quantitative manner. The localisation of energy in the torsional coordinate is consistent with the low frequency nature of torsional motion, which couples more strongly to overall rotation of the molecule than to other vibrational modes.

7.5 Summary and Outlook

The experimental work presented in this chapter has demonstrated the extension of Coulomb explosion imaging to the real-time monitoring of photoinduced torsional motion in substituted biphenyl derivatives. The measured torsional dynamics are in good agreement with both theory and previous experimental results, suggesting that a high confidence may be ascribed to the findings. Crucially, the measurement of the instantaneous dihedral angle depends only on the confinement of the stereogenic axis and is invariant of the degree of alignment of the SMPA, allowing the study of the torsional dynamics to be extended far beyond the first few picoseconds following the initial kick pulse. In this work, measurements were recorded at a kick-probe time delay of 200 ps, compared to the 4–5 ps range possible through measurements of the laboratory frame F^+ and Br^+ signal intensity. Furthermore, the insensitivity of the measurements to the alignment of the SMPA allowed the measurement of the torsional dynamics of molecules aligned perpendicularly to the kick pulse polarisation following 1D adiabatic alignment of the molecules.

Building on the success of the measurements following torsional excitation by a single kick pulse, the optical scheme was extended to include a second kick pulse at different, user-defined time delays after the first, in order to either damp or amplify the amplitude of the torsional motion. Following amplification of the torsional motion, snapshots of the torsional revival structure were recorded, providing the first experimental observation of revival phenomena in a torsional mode. A possible direction for future work is the measurement of a more complete data set, although it should be noted that this will take some time due to the low repetition rate (20 Hz) of the experiment. Complementary to this, *ab initio* calculations of the torsional dynamics

are currently being performed by Lauge Christensen in the group of Prof. Henrik Stapelfeldt, in order that the experimental results may be more accurately compared to the predictions of theory.

More generally, the success of CEI using a tabletop light source in measuring small amplitude molecular motion on a femtosecond timescale provides direct evidence of the feasibility of recording a ‘molecular movie’ using such a strategy. It is therefore proposed that CEI, when combined with a fast imaging sensor, provides a means of monitoring photoinduced processes on the natural timescale of molecular motion. It is possible that the experimental principles introduced in this chapter could be extended to the study of the structural transformations following photoabsorption in a variety of interesting systems. For example, the photoinitiated cis-trans isomerisation of alkenes could be studied, where substituted derivatives of stilbene would be attractive candidates for study.

7.5.1 Towards Larger Amplitude Torsional Motion

The torsional motion observed in this work has been relatively modest, with a peak amplitude of around 5° induced following amplification by a second kick pulse. In principle, larger amplitude torsional motion may be achieved using a higher intensity, a longer pulse duration, or a train of synchronised kick pulses optimised so as to amplify the torsional motion, as discussed previously. The use of higher intensity kick pulses is rather unattractive, however, due to the increased likelihood of ionisation and fragmentation of the target system following exposure to high intensity femtosecond laser pulses. An extension of the double kick strategy to include a train of kick pulses delivered to the experiment at optimised time delays should be relatively straightforward using conventional femtosecond pulse shaping techniques [38], and represents a more feasible means of inducing larger amplitude torsional motion while avoiding significant ionisation and fragmentation of the target molecules.

An alternative route towards achieving larger amplitude torsional motion is to instead exchange the target molecules for systems with a shallower torsional potential energy surface. Suitable candidates include phenylpyrroles and ortho-substituted biphenylacetylene derivatives, for which the barrier to stereochemical interconversion is lowered compared to the substituted biphenyl molecules considered in this work.

An interesting extension of the current work would be to monitor the torsional motion induced upon resonant $\pi-\pi^*$ excitation. Such a transition is expected to be associated with large amplitude torsional motion as the equilibrium dihedral angle is significantly different in the excited state compared to that of the ground state. A potential complication of such an experiment is the influence of the YAG laser on the system, since the absorption spectrum of the molecule will be red-shifted following a $\pi-\pi^*$ transition, potentially increasing the risk of ionisation by the YAG laser pulse.

7.5.2 Prospects for Photoinduced Deracemisation

The introduction to this chapter discussed the prospect of photoinduced deracemisation for molecules in which torsional motion corresponds to the coordinate by which the enantiomers may be interconverted. The experimental results demonstrate that the application of a train of synchronised kick pulses has the potential to induce a well-defined degree of torsional motion, potentially allowing the torsional barrier to be crossed if the optical scheme is extended to include further kick pulses. Alternatively, it may be possible to induce a sufficient degree of torsional excitation using a longer kick pulse. However, it must be stressed that an important prerequisite for all photoinduced deracemisation schemes so far proposed is that the molecules may be oriented in space, rather than simply aligned as has been considered in this work. The requirement of orientation may be understood by considering Eq. 7.3, which describes the interaction of the kick pulse and the target molecules. Close inspection of the terms present in Eq. 7.3 reveals that the kick pulse interaction is sensitive only to the projection of the rings in the xy -plane, which will be identical for oppositely oriented R_a and S_a enantiomers. It is therefore inevitable that in an aligned ensemble the interconversion of the two enantiomers will proceed with equal probabilities in both directions, resulting in no net deracemisation.

The orientation of such molecules using mixed-field orientation schemes has been investigated in previous studies [39], where it was found that a modest degree of orientation of the target molecules could be achieved (45:55). Clearly, if deracemisation is to be seriously pursued, a far higher degree of orientation must be realised than has been demonstrated thus far, either by significantly increasing the static field strength, or through alternative strategies such as the use of terahertz pulses [40, 41] or two-colour fields [42]. However, in an aligned ensemble the interaction of the two enantiomers with the kick pulse is reversed in the two orientations. Therefore, although net deracemisation of the ensemble is not expected, deracemisation of each orientation should occur, with the opposing molecules consisting of a greater proportion of either the R_a or S_a enantiomer, depending on their orientation. While this is arguably of little practical use, the process of photoinduced deracemisation is interesting from a theoretical perspective, and it would therefore be interesting to monitor this process experimentally. Using the current experimental set-up, this should be possible as the signature of molecular orientation is present in the time-of-flight spectrum. In Sect. 6.3 it was shown that the two opposing orientations of the molecule split the peaks of the fluorine ions into forward- and backward-scattered components. By selecting either the forward- or backward-scattered ions, the orientation of the molecule is therefore selected for, and the enantiomeric composition of the sample may be assessed by measuring the contributions from each of the four peaks present in the recoil frame covariance images, as illustrated by Fig. 7.15.

Recent theoretical work has investigated the feasibility of performing photoinduced deracemisation using a similar scheme to that reported in this thesis. In Ref. [12] calculations were performed using the time-dependent torsional potential of DFDBrBph, as determined from quantum chemical calculations, but reduced by a

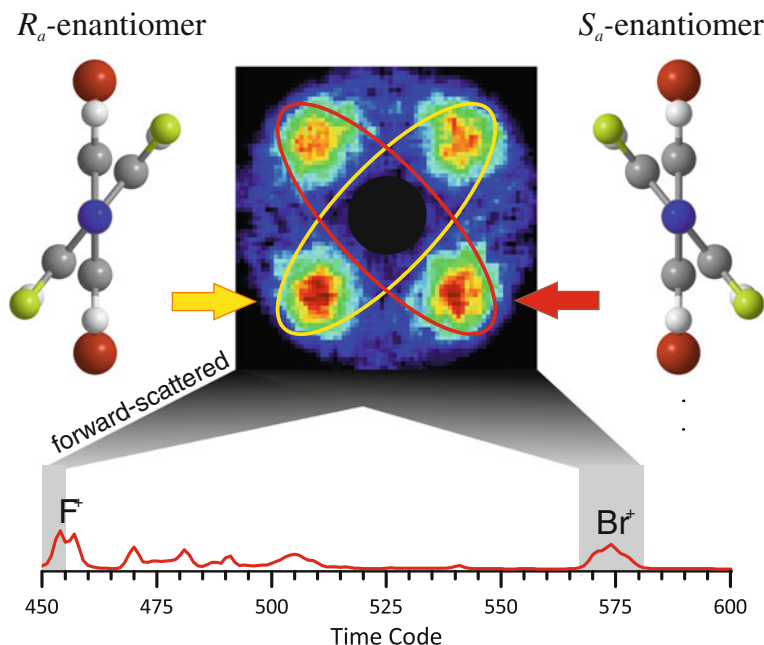


Fig. 7.15 Illustration of the principles of enantiospecific identification. Using the forward-scattered F^+ time-of-flight peak to determine the orientation of the molecules, it is possible to deduce the chirality of the molecules contributing to the recoil frame covariance image

factor of 1/4. Such a reduction in the torsional barrier should be possible through structural modifications to the molecule; for example, by modifying the phenyl rings or by using a halogen substituted diphenylacetylene. In these calculations, torsional motion was initiated by a kick pulse with a peak intensity of $1.2 \times 10^{13} \text{ W cm}^{-2}$ and a duration of 1 ps, polarised at an angle of 13° relative to the SMPA of the molecules. In order to achieve this alignment experimentally, it would be necessary to introduce the kick laser pulse at an angle of 13° relative to the alignment pulse, rather than in the collinear fashion currently used. The results of the simulations are summarised in Fig. 7.16. The potential energy surface plot presented in Panel (a) illustrates some important features of the kick pulse interaction. Firstly, for a perfectly oriented ensemble, the effect of the kick pulse on the torsional potential energy surface is clearly asymmetric with respect to the two conformationally restricted enantiomers, causing a differential behaviour of molecules originally confined within the two potential wells. Secondly, the potential barrier separating the two enantiomers is substantially reduced during the kick pulse envelope, facilitating interconversion between the R_a and S_a conformers.

In order to investigate the extent of deracemisation that would result from such an interaction, the torsional dynamics of molecules initially of purely S_a and R_a character were calculated under identical experimental conditions. The results of these calculations are presented in Panels (b) and (c) of Fig. 7.16, and illustrate the strongly

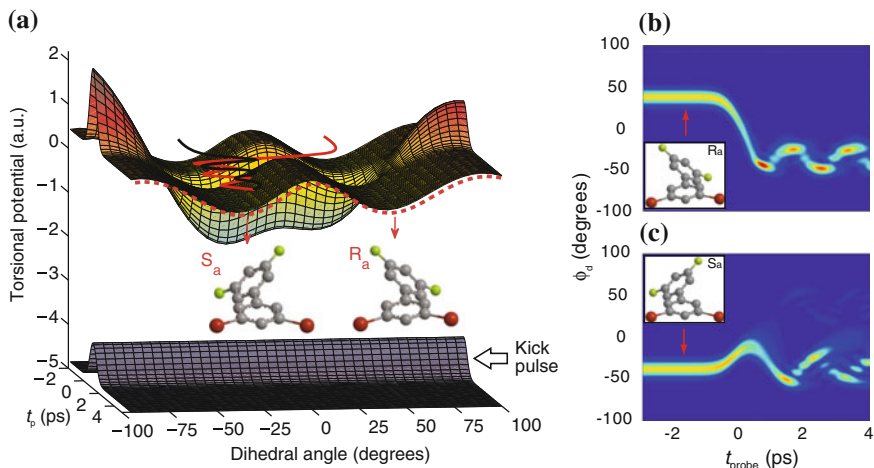


Fig. 7.16 Panel a shows the calculated torsional potential energy surface of oriented molecules of DBrDFBph as a function of kick-probe delay in the presence of a kick laser pulse with a peak intensity of $1.2 \times 10^{13} \text{ W cm}^{-2}$ and a duration (FWHM) of 1 ps, polarised at an angle of 13° relative to the SMPA of the molecules. The broken red line at later times represents the field-free torsional potential. The red and black traces above the PES illustrate the motion of molecules initially confined to the R_a and S_a potential wells, respectively. Panels b and c plot the probability density of the torsional wavefunction as a function of kick-probe delay when starting with 100% R_a and S_a molecules, respectively. (Figure adapted from Ref. [12])

differential response of the two enantiomers to the kick laser pulse. For molecules initially confined to the R_a potential well, the kick pulse drives the population over the potential barrier separating the two enantiomers, resulting in a permanent change in conformation. In contrast, the S_a enantiomer responds to the kick pulse in a less dramatic fashion due to the higher potential barrier to conformational interconversion, resulting in a modest oscillatory motion confined within the S_a potential well. A quantitative analysis of the results reveals that 99% of the molecules initially of R_a character are converted to the S_a form following the kick pulse, whereas only 13% of the S_a enantiomers cross the barrier to become R_a in symmetry. The enantiomeric excess that results is therefore calculated to be 0.86, which corresponds to a mixture in which 86% of the molecules are S_a , and 14% of the molecules consist of a racemic mixture of S_a and R_a .

The theoretical calculations therefore demonstrate that it should be possible to induce a significant e.e. from an initially racemic mixture of oriented molecules. Furthermore, since the effect is reversed upon inversion of the orientation of the molecules, in an aligned ensemble the two oriented components will become deracemised to an equal and opposite extent, which should be observable using the current experimental scheme.

References

1. M. Maus, W. Rettig, *J. Phys. Chem. A* **106**, 2104 (2002)
2. F. Sterpone, R. Martinazzo, A.N. Panda, I. Burghardt, *Z. Phys. Chem.* **225**, 541 (2011)
3. L. Venkataraman, J. Klare, C. Nuckolls, M. Hybertsen, M. Steigerwald, *Nature* **442**, 904 (2006)
4. D. Vonlanthen, A. Mishchenko, M. Elbing, M. Neuburger, T. Wandlowski, M. Mayor, *Angew. Chem. Int. Ed.* **48**, 8886 (2009)
5. A. Mishchenko, D. Vonlanthen, V. Meded, M. Burkle, C. Li, I. Pobelov, A. Bagrets, J. Viljas, F. Pauly, F. Evers, M. Mayor, T. Wandlowski, *Nano Lett.* **10**, 156 (2010)
6. D. Kroner, B. Klaunzner, T. Klamroth, *J. Phys. Chem. A* **112**, 9924 (2008)
7. F. Grossmann, L. Feng, G. Schmidt, T. Kunert, R. Schmidt, *Europhys. Lett.* **60**, 201 (2002)
8. B. Dietzek, B. Brüggemann, T. Pascher, A. Yartsev, *Phys. Rev. Lett.* **97**, 258301 (2006)
9. S. Belz, T. Grohmann, M. Leibscher, *J. Chem. Phys.* **131**, 034305 (2009)
10. M. Parker, M.A. Ratner, T. Seideman, *Mol. Phys.* **110**, 1941 (2012)
11. C.B. Madsen, L.B. Madsen, S.S. Viftrup, M.P. Johansson, T.B. Poulsen, L. Holmegaard, V. Kumarappan, K.A. Jorgensen, H. Stapelfeldt, *Phys. Rev. Lett.* **102**, 073007 (2009)
12. C.B. Madsen, L.B. Madsen, S.S. Viftrup, M.P. Johansson, T.B. Poulsen, L. Holmegaard, V. Kumarappan, K.A. Jorgensen, H. Stapelfeldt, *J. Chem. Phys.* **130**, 234310 (2009)
13. B.A. Ashwell, S. Ramakrishna, T. Seideman, *J. Chem. Phys.* **138**, 044310 (2013)
14. J.M. Seminario, A.G. Zacarias, J.M. Tour, *J. Am. Chem. Soc.* **120**, 3970 (1998)
15. F. Anariba, J.K. Steach, R.L. McCreery, *J. Phys. Chem. B* **109**, 11163 (2005)
16. Z.J. Donhauser, *Science* **292**, 2303 (2001)
17. A. Nitzan, M.A. Ratner, *Science* **300**, 1384 (2003)
18. A.L. Sobolewski, *Phys. Chem. Chem. Phys.* **10**, 1243 (2008)
19. S.Y. Quek, M. Kamenetska, M.L. Steigerwald, H.J. Choi, S.G. Louie, M.S. Hybertsen, J.B. Neaton, L. Venkataraman, *Nat. Nanotechnol.* **4**, 230 (2009)
20. F. Leyssner, S. Hagen, L. Ovari, J. Dokic, P. Saalfrank, M.V. Peters, S. Hecht, T. Klamroth, P. Tegeder, *J. Phys. Chem. C* **114**, 1231 (2010)
21. S. Wu, M.T. González, R. Huber, S. Grunder, M. Mayor, C. Schönenberger, M. Calame, *Nat. Nanotechnol.* **3**, 569 (2008)
22. C. Zhang, M.-H. Du, H.-P. Cheng, X.-G. Zhang, A. Roitberg, J. Krause, *Phys. Rev. Lett.* **92**, 158301 (2004)
23. S. Loudwig, H. Bayley, *J. Am. Chem. Soc.* **128**, 12404 (2006)
24. J. Shao, P. Hänggi, *J. Chem. Phys.* **107**, 9935 (1997)
25. Y. Fujimura, L. González, K. Hoki, J. Manz, Y. Ohtsuki, *Chem. Phys. Lett.* **306**, 1 (1999)
26. D. Gerbasi, M. Shapiro, P. Brumer, *J. Chem. Phys.* **115**, 5349 (2001)
27. P. Král, M. Shapiro, *Phys. Rev. Lett.* **87**, 183002 (2001)
28. K. Hoki, L. González, Y. Fujimura, *J. Chem. Phys.* **116**, 2433 (2002)
29. D. Kröner, M.F. Shibl, L. González, *Chem. Phys. Lett.* **372**, 242 (2003)
30. S. Ramakrishna, T. Seideman, *Phys. Rev. Lett.* **99**, 103001 (2007)
31. S.M. Parker, M.A. Ratner, T. Seideman, *J. Chem. Phys.* **135**, 224301 (2011)
32. L.H. Coudert, L.F. Pacios, J. Ortigo, *Phys. Rev. Lett.* **107**, 113004 (2011)
33. J.L. Hansen, J.H. Nielsen, C.B. Madsen, A.T. Lindhardt, M.P. Johansson, T. Skrydstrup, L.B. Madsen, H. Stapelfeldt, *J. Chem. Phys.* **136**, 204310 (2012)
34. J.J. Larsen, K. Hald, N. Bjerre, H. Stapelfeldt, T. Seideman, *Phys. Rev. Lett.* **85**, 2470 (2000)
35. I. Nevo, L. Holmegaard, J.H. Nielsen, J.L. Hansen, H. Stapelfeldt, F. Filsinger, G. Meijer, J. Kpper, *Phys. Chem. Chem. Phys.* **11**, 9912 (2009)
36. S.S. Viftrup, V. Kumarappan, S. Trippel, H. Stapelfeldt, E. Hamilton, T. Seideman, *Phys. Rev. Lett.* **99**, 143602 (2007)
37. S.S. Viftrup, V. Kumarappan, L. Holmegaard, C.Z. Bisgaard, H. Stapelfeldt, M. Artamonov, E. Hamilton, T. Seideman, *Phys. Rev. A* **79**, 023404 (2009)
38. A.M. Weiner, *Rev. Sci. Instrum.* **71**, 1929 (2000)
39. J.L. Hansen *Imaging Molecular Frame Dynamics Using Spatially Oriented Molecules* Ph.D. thesis, Aarhus University (2012)

40. S. Fleischer, Y. Zhou, R.W. Field, K.A. Nelson, *Phys. Rev. Lett.* **107**, 163603 (2011)
41. K. Kitano, N. Ishii, J. Itatani, *Phys. Rev. A* **84**, 053408 (2011)
42. S. De, I. Znakovskaya, D. Ray, F. Anis, N.G. Johnson, I.A. Bocharova, M. Magrakvelidze, B.D. Esry, C.L. Cocke, I.V. Litvinyuk, M.F. Kling, *Phys. Rev. Lett.* **103**, 153002 (2009)

Appendix A

Calculated Structural Parameters

See (Tables A.1 and A.2).

Table A.1 The coordinates and bond lengths of 3,5-dibromo-3',5'-difluoro-4'-cyanobiphenyl, as calculated at density functional level of theory by colleagues at the University of Helsinki, according to the details presented in Refs. [1, 2]

Atom	Coordinates(Å)			Bond	Length (Å)
	x	y	z		
N	0.00	0.00	7.03	Br1-C10	1.91
C1	0.00	0.00	5.88	Br2-C12	1.91
C2	0.00	0.00	4.46	C10-C9	1.39
C3	-0.99	-0.66	3.72	C11-C10	1.39
C4	-1.00	-0.67	2.34	C12-C11	1.39
C5	0.00	0.00	1.63	C13-C12	1.39
C6	1.00	0.67	2.34	C13-C8	1.40
C7	0.99	0.66	3.72	C2-C1	1.42
C8	0.00	0.00	0.15	C3-C2	1.40
C9	-1.20	0.11	-0.56	C4-C3	1.38
C10	-1.18	0.11	-1.95	C5-C4	1.40
C11	0.00	0.00	-2.66	C6-C5	1.40
C12	1.18	-0.11	-1.95	C7-C2	1.40
C13	1.20	-0.11	-0.56	C7-C6	1.38
F1	-1.94	-1.31	4.38	C8-C5	1.48
F2	1.94	1.31	4.38	C9-C8	1.40
Br1	-2.83	0.28	-2.90	F1-C3	1.34
Br2	2.83	-0.28	-2.90	F2-C7	1.34
H1	-1.78	-1.22	1.83	H1-C4	1.08
H2	1.78	1.22	1.83	H2-C6	1.08
H3	-2.14	0.22	-0.03	H3-C9	1.08
H4	2.14	-0.22	-0.03	H4-C13	1.08
H5	0.00	0.00	-3.74	H5-C11	1.08
				N-C1	1.15

Table A.2 The bond angles of 3,5-dibromo-3',5'-difluoro-4'-cyanobiphenyl, as calculated at density functional level of theory by colleagues at the University of Helsinki, according to the details presented in Refs. [1, 2]

Bond Pair	Angle (Degrees)	Bond Pair	Angle (Degrees)
Br1-C10-C11	119.0	C7-C2-C3	116.2
Br1-C10-C9	119.3	C7-C6-C5	119.7
Br2-C12-C11	119.0	C8-C5-C4	120.4
Br2-C12-C13	119.3	C8-C5-C6	120.4
C10-C9-C8	119.7	F1-C3-C2	118.2
C11-C10-C9	121.8	F1-C3-C4	119.1
C12-C11-C10	117.9	F2-C7-C2	118.2
C12-C13-C8	119.7	F2-C7-C6	119.1
C13-C12-C11	121.8	H1-C4-C3	118.7
C13-C8-C9	119.2	H1-C4-C5	121.6
C1-C2-C3	121.9	H2-C6-C5	121.6
C1-C2-C7	121.9	H2-C6-C7	118.7
C2-C1-N23	180.0	H3-C13-C8	120.4
C4-C3-C2	122.7	H3-C9-C10	119.9
C5-C4-C3	119.7	H3-C9-C8	120.4
C5-C8-C13	120.4	H4-C13-C12	119.9
C5-C8-C9	120.4	H5-C11-C10	121.1
C6-C5-C4	119.1	H5-C11-C12	121.1
C6-C7-C2	122.7		

Dihedral Bond Linkage	Angle (Degrees)
C4-C5-C8-C9	39.0

References

1. C.B. Madsen, L.B. Madsen, S.S. Viftrup, M.P. Johansson, T.B. Poulsen, L. Holmegaard, V. Kumarappan, K.A. Jorgensen, H. Stapelfeldt, *Phys. Rev. Lett.* **102**, 073007 (2009)
2. C.B. Madsen, L.B. Madsen, S.S. Viftrup, M.P. Johansson, T.B. Poulsen, L. Holmegaard, V. Kumarappan, K.A. Jorgensen, H. Stapelfeldt, *J. Chem. Phys.* **130**, 234310 (2009)